STP 651

TOUGHNESS AND FRACTURE BEHAVIOR OF TITANIUM

Ti

AMERICAN SOCIETY FOR TESTING AND MATERIALS

TOUGHNESS AND FRACTURE BEHAVIOR OF TITANIUM

A symposium
presented at
May Committee Week
AMERICAN SOCIETY FOR
TESTING AND MATERIALS
Toronto, Ontario, Canada, 1-6 May 1977

ASTM SPECIAL TECHNICAL PUBLICATION 651
R. G. Broadwell and C. F. Hickey, Jr.
symposium co-chairmen

List price $28.50
04-651000-30

AMERICAN SOCIETY FOR TESTING AND MATERIALS
1916 Race Street, Philadelphia, Pa. 19103

Copyright © by American Society for Testing and Materials 1978
Library of Congress Catalog Card Number: 78-55313

NOTE
The Society is not responsible, as a body,
for the statements and opinions
advanced in this publication.

Printed in Baltimore, Md.
July 1978

Foreword

The symposium on Toughness and Fracture Behavior of Titanium was presented at May Committee Week of the American Society for Testing and Materials held in Toronto, Ontario, Canada, 1-6 May 1977. Committee J-1 on Effect of Temperature on the Properties of Metals, which is a joint committee of the American Society for Testing and Materials, American Society of Mechanical Engineers, and Metal Properties Council, sponsored the symposium. R. G. Broadwell, TIMET, and C. F. Hickey, Jr., Army Materials and Mechanics Research Center, presided as symposium chairmen.

Related
ASTM Publications

Fatigue and Fracture Toughness, STP 556 (1974), $20.25, 04-556000-30

Fractography-Microscopic Cracking Process, STP 600 (1976), $27.50, 04-600000-30

Cracks and Fracture, STP 601 (1976), $51.75, 04-601000-30

A Note of Appreciation to Reviewers

This publication is made possible by the authors and, also, the unheralded efforts of the reviewers. This body of technical experts whose dedication, sacrifice of time and effort, and collective wisdom in reviewing the papers must be acknowledged. The quality level of ASTM publications is a direct function of their respected opinions. On behalf of ASTM we acknowledge their contribution with appreciation.

ASTM Committee on Publications

Editorial Staff

Jane B. Wheeler, *Managing Editor*
Helen M. Hoersch, *Associate Editor*
Ellen J. McGlinchey, *Senior Assistant Editor*
Sheila G. Pulver, *Assistant Editor*
Susan Ciccantelli, *Assistant Editor*

Contents

Introduction

The publication of the papers presented at this symposium represents a significant contribution to the literature in the current state of the art of toughness and fracture behavior of commercially available and experimental titanium alloys. Parameters considered include the influence of composition, microstructure, heat treatment, and specimen geometry on the toughness and fracture-related properties. Various material forms such as castings, forgings, extrusions, plate, thin sheet, and titanium-aluminum laminates are considered.

Since fracture behavior of the design and maintenance of aerospace and other critical industrial and military components recently has become a primary engineering criterion, concern is shown for both static and dynamic fracture considerations. Relevant inferences to current problems regarding fracture toughness can be drawn from these papers, enriching the data bank for future problem solving relative to new techniques, processes, and tests in titanium and titanium alloys.

The authorship includes cognizant and highly qualified personnel from government, academe, and industry to provide a well rounded coverage of the most recent studies in the area of titanium.

R. G. Broadwell
TIMET, Toronto, Ohio 43964;
symposium co-chairman.
C. F. Hickey, Jr.
Department of the Army, Army Materials and Research Center, Watertown, Mass.; symposium co-chairman.

Copyright© 1978 by ASTM International www.astm.org

C. F. Fiftal,[1] *D. A. Bolstad,*[2] *and M. S. Misra* [3]

Fracture Resistance of Ti-5Al-2.5Sn Extra-Low Interstitial Castings

REFERENCE: Fiftal, C. F., Bolstad, D. A., and Misra, M. S., **"Fracture Resistance of Ti-5A1-2.5Sn Extra-Low Interstitial Castings,"** *Toughness and Fracture Behavior of Titanium, ASTM STP 651,* American Society for Testing and Materials, 1978, pp. 3–16.

ABSTRACT: Fracture toughness and cyclic crack propagation data for Ti-5A1-2.5Sn extra-low interstitial (ELI) castings, 0.51 and 2.54 cm (0.20 and 1.00 in.) thick, at 394, 294, 77, and 20 K (250, 70, −320, and −423° F), are presented. Both surface flaw and compact tension geometries were tested. Comparison is made with other titanium alloys in both wrought and cast forms. Crack propagation resistance is comparable to wrought Ti-5A1-2.5Sn ELI, even with the extremely coarse as-cast grain size encountered.

KEY WORDS: titanium, fracture properties, crack propagation, surface defects, compact tension, castings

A space shuttle is designed to reduce cost and increase effectiveness of using outer space for commercial, scientific, and defense needs by virtue of its versatility and reusability. The space shuttle referred to in the present paper is composed of a winged spacecraft with three main propulsion engines (the Orbiter), an external tank that contains the ascent propellants (liquid oxygen (LO_2) and liquid hydrogen (LH_2)) to be used by the Orbiter engines, and two solid rocket boosters (SRB).

During launch, the external tank serves as structural support for the Orbiter and SRBs. The Orbiter and SRB support struts are joined to the external tank by means of attachment fittings. In selecting the attachment fittings, Ti-5A1-2.5Sn extra-low interstitial (ELI) castings were preferred over forgings for economical reasons and their amenability to design

[1] Materials staff engineer, Martin Marietta Aerospace, Denver, Colo. 80201.
[2] Senior materials staff engineer, Martin Marietta Aerospace, New Orleans, La. 70189.
[3] Materials staff engineer, Martin Marietta Aerospace, Los Angeles, Calif. 90509.

Copyright© 1978 by ASTM International www.astm.org

changes. However, because castings usually are associated with reduced standards of acceptability due to possible porosity, the less widely used, lower strength Ti-5A1-2.5Sn alloy was preferred over the more widely used, higher strength Ti-6A1-4V alloy because it has a higher fracture toughness. The ELI grade for the alloy was selected because it retains its superior fracture toughness down to very low temperatures. This is necessary since the attachment fittings are in direct contact with the tank shell that contains the cryogenic propellants. The objective of this program was to quantify the fracture resistance of Ti-5A1-2.5Sn ELI castings as part of a comprehensive fracture control plan for the space shuttle external tank.

Procedure

The Ti-5A1-2.5Sn ELI panels, 10.16 to 15.24 cm (4 to 6 in.) wide, 0.51 and 2.54 cm (0.20 and 1.00 in.) thick, were prepared by centrifugal casting in a rammed graphite mold. The chemical analyses for all heats were within the specified composition limits for ELI material as shown in Table 1. All panels were annealed at 1116 K (1550°F) for 2 h in vacuum, fan cooled with argon to 811 K (1000°F), and air cooled. After heat treatment, a minimum of 0.013 cm (0.005 in.) was removed from all surfaces by chemical milling.

Two types of flaw geometries were used for both fracture toughness and cyclic crack growth testing: (*a*) the surface flaw geometry (shape ratio $a/2c = 0.4$ to 0.5), and (*b*) the compact tension geometry. These flaws were produced by fatigue extension of an appropriately machined starter notch. All specimens were polished before machining of the starter notch so that surface fatigue extension could be easily observed. Polishing consisted of rough sanding with oil lubricated 320-grit paper, fine sanding with oil lubricated 600-grit paper, and buffing with a polishing compound. The starter notch for the surface flaw geometry was machined by electric-discharge machining (EDM) using a 0.038-cm (0.015-in.) thick tungsten-copper electrode. The slot for the compact tension geometry was sharpened using a slitting saw having a 45-deg bevel edge and 0.013-cm (0.005-in.) tip radius. Fatigue extension was done in tension at room temperature at a stress intensity of 27 $MN/m^{3/2}$ (25 $ksi\sqrt{in.}$) corresponding to approximately ¼ K_{Ic}. For the surface flaw geometry, this was equivalent to 345 MN/m^2 (50 ksi). The starter notches were monitored optically for measurement of flaw initiation and extension on the surface. For the surface flaw geometry, growth along the surface (ΔC) was approximately equal to growth in the depth direction (Δa). A minimum Δa of 0.127 cm (0.050 in.) was considered to be adequate for the fracture toughness tests and also for each growth increment in the cyclic flaw growth tests. A photomicrograph showing fatigue extension from an EDM notch is shown in Fig. 1.

TABLE 1—*Chemical composition of Ti-5Al-2.5Sn ELI cast material, weight percent.*

Designation	Al	Sn	C	H	N	O	Fe	Others	Ti
Martin Marietta Corp. specification STM-5640	4.50 to 5.75	2.0 to 3.0	0.05 max	0.0125 max	0.035 max	0.12 max	0.25 max	0.30 max	remainder
Howmet Corp. Heat No. TB-041	5.05	2.40	0.012	0.0030	0.010	0.104	0.07	<0.05	remainder
Titech International, Inc. Heat No. 5-25-3256	5.24	2.67	0.019	0.0028	0.007	0.100	0.14	<0.30	remainder

Notice that there is considerable wandering of the flaw above and below the plane of the notch that is caused by the extremely large as-cast grain size. This high relief of the fatigue zone effectively prevents delineation from the rest of the fracture surface by "natural" fatigue marking. Therefore, heat tinting at 727 K (850°F) for 5 to 30 min was used to distinguish the fatigue zones. Typical heat tinted surface fatigue flaws introduced in 0.51 and 2.54-cm (0.20 and 1.00-in.) thick cast Ti-5A1-2.5Sn ELI are shown in Figs. 2 and 3, respectively. Flaw depth ratios (a/t) were in the range 0.5 to 0.9 for 0.51-cm (0.20-in.) material and 0.2 to 0.6 for 2.54-cm (1.00-in.) material.

Fracture toughness and cyclic crack propagation specimens were tested at 394, 294, 77, and 20 K (250, 70, −320, and −423°F) in various servohydraulic tensile fatigue machines with load capacities ranging from 156 to 4448 kN (35 to 1000 kips). Liquid hydrogen tests were accomplished by total specimen immersion in a 722 kN (50-kip) cryostat. Liquid nitrogen tests were accomplished by the use of a special freeze-on cryostat that surrounded only the reduced gage section of the specimen. This permitted greater flexibility because remote liquid handling was not a consideration as was true with liquid hydrogen testing. High temperature testing was accomplished using a clam-shell quartz tube furnace. This type of furnace provided ease of accessibility for fatigue crack growth monitoring without having to unclamp the specimen.

Stress intensity values (K) for fracture toughness and cyclic crack propagation surface flaw specimens were calculated from gross section stress (σ) using the stress intensity expression for a semielliptical surface

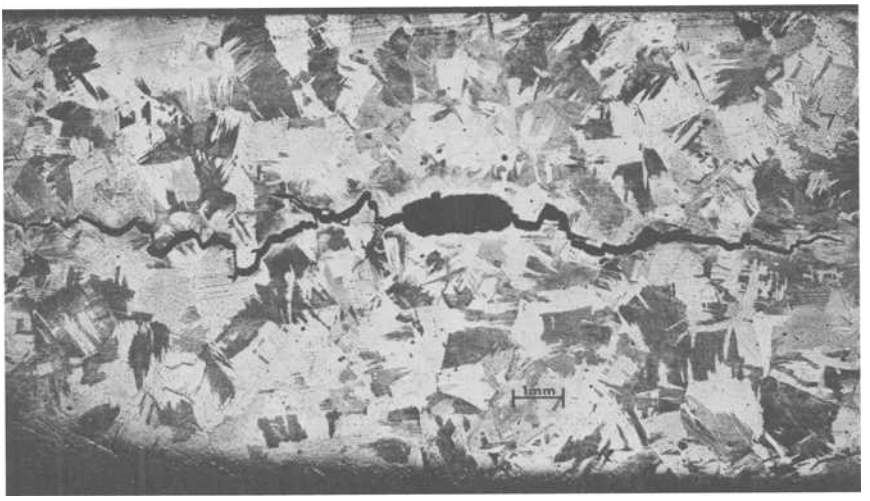

FIG. 1—*Fatigue flaw extension from EDM notch.*

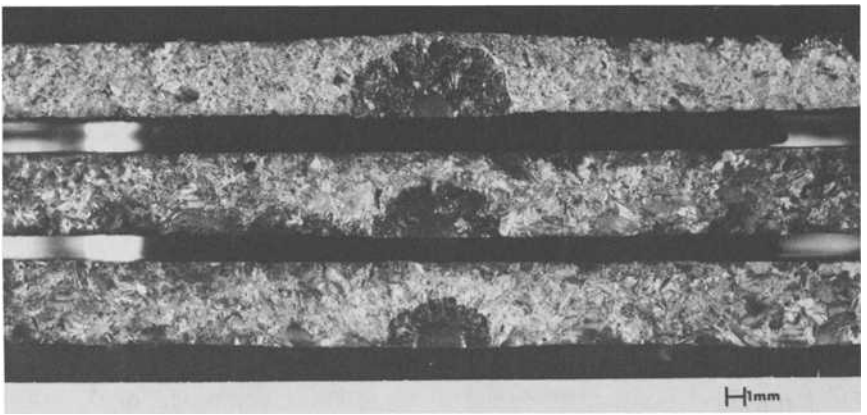

FIG. 2—*Typical surface fatigue flaws introduced in 0.51-cm (0.20-in.) thick cast Ti-5Al-2.5Sn ELI.*

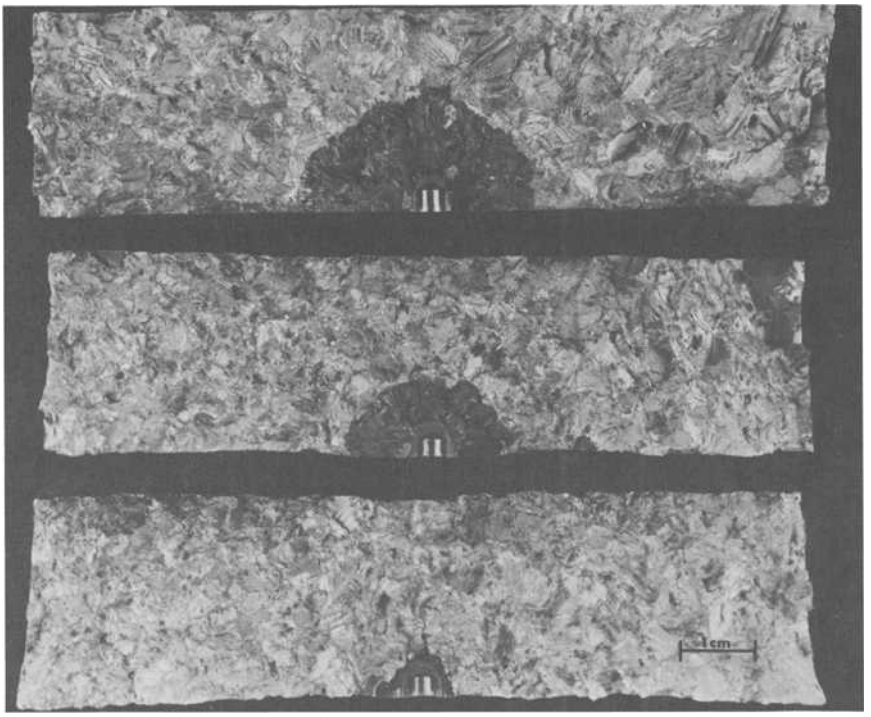

FIG. 3—*Typical surface fatigue flaws introduced in 2.54-cm (1.00-in.) thick cast Ti-5Al-2.5Sn ELI.*

flaw, $K=M_K\ \sigma\sqrt{\pi a/Q}$ where M_K is Shah and Kobayashi's [*1*] [4] combined front surface and back surface stress intensity magnification factor, and Q is the flaw shape parameter. Stress intensity values for fracture toughness and cyclic crack propagation compact tension specimens were calculated using ASTM Test for Plane-Strain Fracture Toughness of Metallic Materials (E 399) data reduction procedures from $K=YP/BW^{1/2}$, where Y is the stress intensity coefficient. Cyclic stress intensity levels were selected to obtain growth rates of 25 to 5080 nm/cycle (1 to 200 μin./cycle) and ranged from 22 to 77 MN/m$^{3/2}$ (20 to 70 ksi $\sqrt{\text{in.}}$).

Metallographic specimens were prepared by conventional techniques. Polishing was accomplished in two stages, rough and final. Rough polishing was performed using 6-μm diamond paste on a nylon covered wheel. Final polishing was accomplished using a slurry composed of 0.05 μm alumina and Kroll's reagent. Macroetching was performed with a hydrofluoric (5 ml)/nitric (10 ml)/lactic (30 ml) acid solution. Macroetching was carried out using a two-step process: a 5-s Kroll's reagent etch was used, followed by a 5-s electrolytic anodization in an oxalic/citric/orthophosophoric/lactic acid solution. Macrofractography was performed using oblique lighting to enhance the grain structure. Microphotography was performed using polarized light, which together with the anodic film defined grain structure more dramatically than using conventional hydrofluoric etchants alone.

Results and Discussion

The alpha grain structure in cast Ti-5A1-2.5Sn ELI is shown in Fig. 4. The acicular grains shown are extremely large with an average diameter of 0.80 mm (0.030 in.) corresponding to an ASTM macrograin size number of M-11. This large grain size is contributed sometimes to a tendency for irregular crack front curvature as can be seen in Fig. 5. However, for these cases, stress intensity was still calculated for the maximum flaw depth as if the shape were semielliptical. Even though the grain size is very large, the grain boundary strength remains high so that flaw growth is predominantly transgranular as shown in Fig. 6.

During fatigue cycling of the artificially introduced defect it was not an unusual occurrence to find natural fatigue flaws that were in the same size range as the artificial defects. These natural flaws may have initiated from casting gas holes. The occurrence of these natural flaws was more of an annoyance than a serious problem since in most cases these flaws were not on the same plane as the artificial defect and were usually somewhat smaller. A typical natural flaw formed during fatigue cycling is shown in

[4] The italic numbers in brackets refer to the list of references appended to this paper.

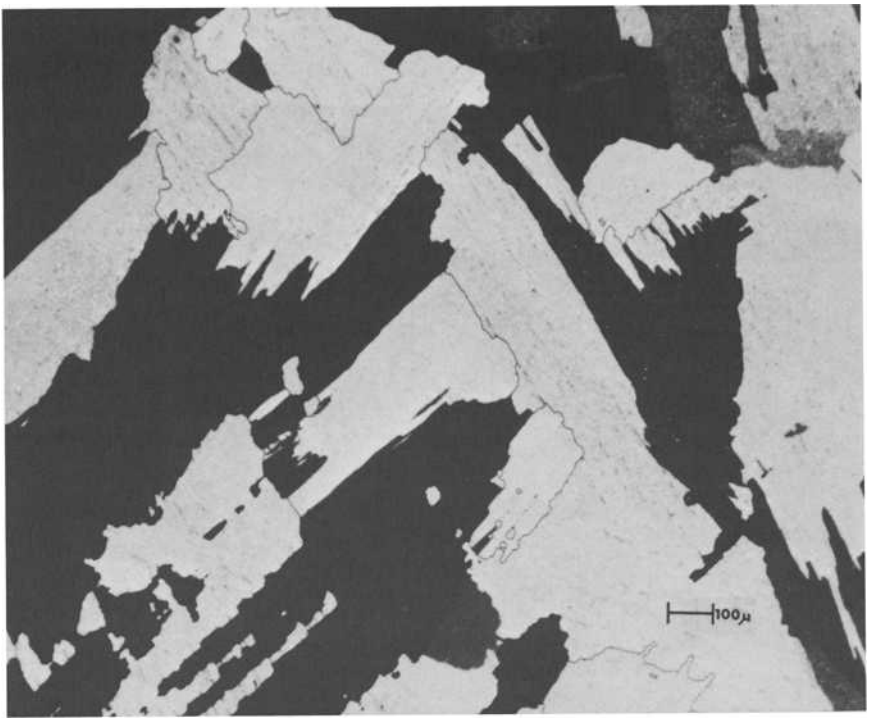

FIG. 4—*Photomicrograph of alpha grain structure in cast Ti-5Al-2.5Sn ELI.*

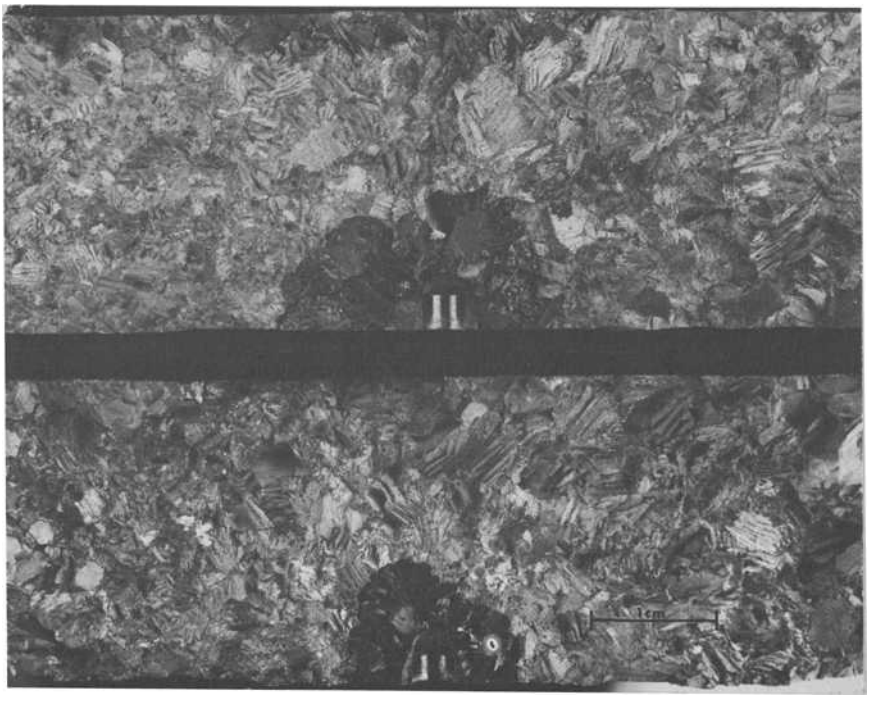

FIG. 5—*Nonuniform flaw growth in large grained Ti-5Al-2.5Sn ELI cast material.*

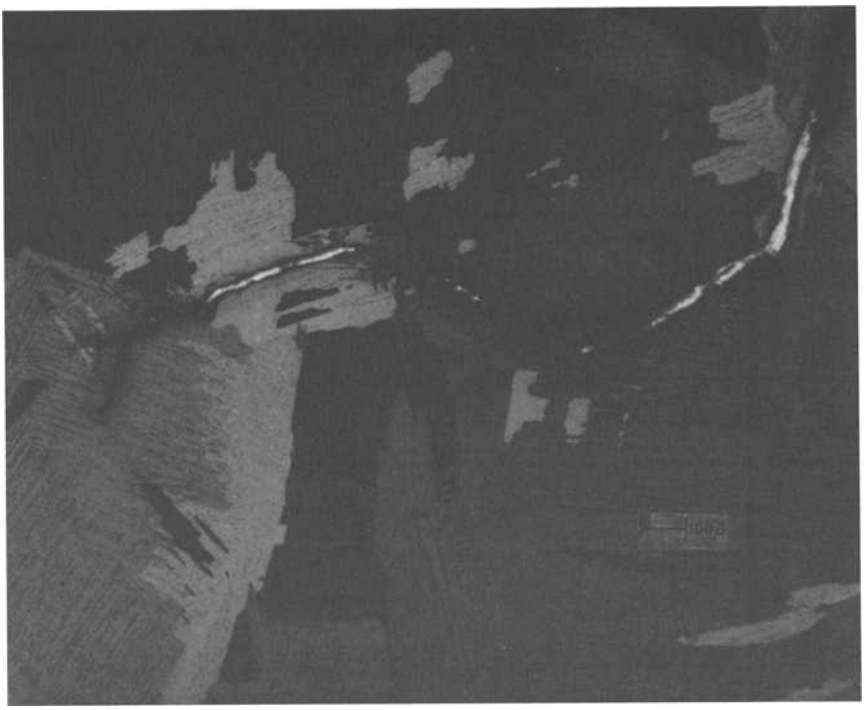

FIG. 6—*Predominantly transgranular fatigue flaw growth in cast Ti-5Al-2.5Sn ELI.*

Fig. 7. An atypical natural flaw that occurred on the same plane and was the same size as the artificially introduced defect is shown in Fig. 8.

Tensile properties of 0.5 and 2.5-cm (0.2 and 1.0-in.) thick Ti-5A1-2.5Sn ELI cast material at 394, 294, 77, and 20 K (394, 294, 77, −320 and −423°F) are given in Table 2. Note that the as-cast properties are not markedly affected by thickness and are fairly close to typical values for wrought material with the strength level of Ti-5A1-2.5Sn being approximately 15 percent lower than for Ti-6A1-4V.

The fracture resistance of Ti-5A1-2.5Sn ELI cast material containing surface flaws of shape ratio $(a/2c)$ 0.4 to 0.5 is shown in Fig. 9 where fracture stress-to-yield stress ratio (σ_f/σ_y) is plotted as a function of crack depth. Since critical stress intensity (K_Q) remains constant with increasing flaw size at (σ_f/σ_y) ratios of 0.9 and below, this level was chosen as the boundary between valid and invalid K_{Ic} data. Note that at 20 K (−423°F) a thickness of 0.5 cm (0.2 in.) is sufficient for valid K_{Ic} data corresponding to a thickness ratio $[t/(K_{Ic}/\sigma_y)^2]$ of 1.2, while at 77 K (−320°F) a thickness of 2.5 cm (1.0 in.) is sufficient corresponding to a thickness ratio of 2.6. ASTM Test Method E 399 indicates that a minimum thickness ratio

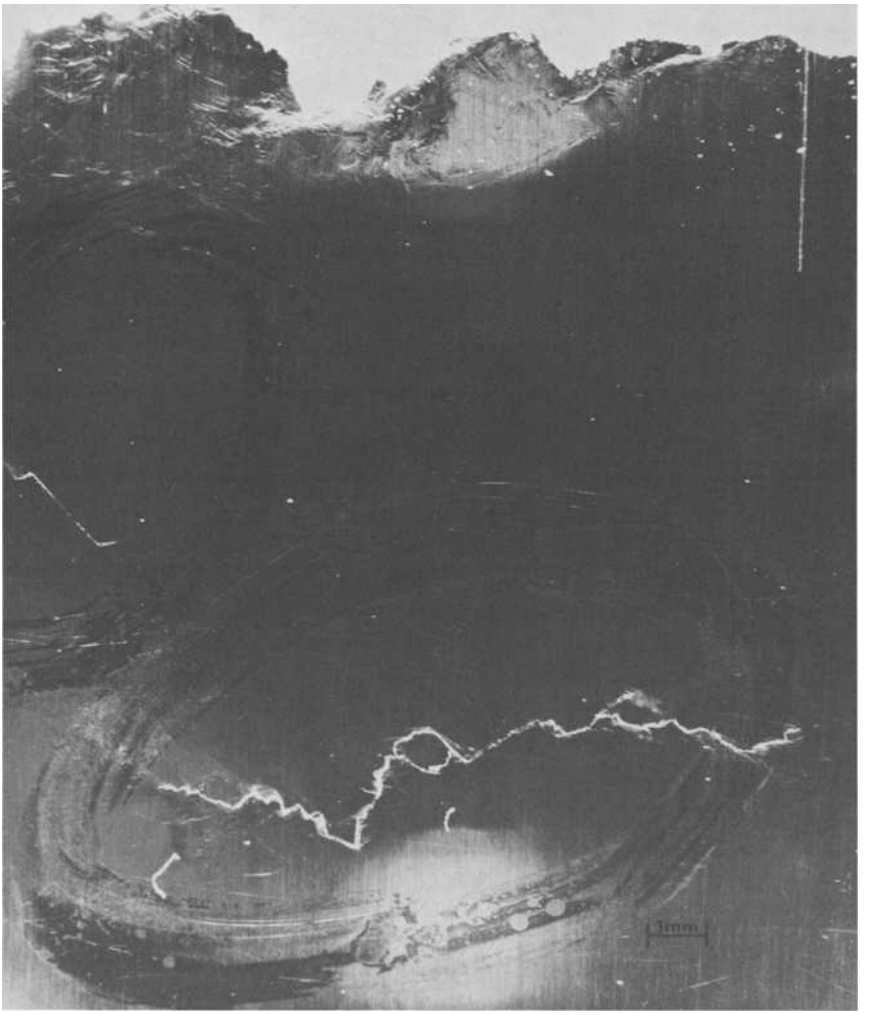

FIG. 7—*Natural fatigue flaw formed during fatigue cycling of artificial defect.*

of 2.5 usually is required for valid data when using through-flaw geometries. It is apparent, then, that this ratio may sometimes be overconservative when applied to other geometries such as the surface flaw. The fracture toughness of Ti-5A1-2.5Sn ELI cast material is high, being equal to 82 $MN/m^{3/2}$ (75 ksi $\sqrt{in.}$) at 20 K (−423°F) and 109 $MN/m^{3/2}$ (99 ksi $\sqrt{in.}$) at 77 K (−320°F). At 294 K (70°F) the toughness probably approaches 120 to 130 $MN/m^{3/2}$ (110 to 120 ksi $\sqrt{in.}$) but it would require a thickness in excess of 8 cm (3 in.) for valid fracture toughness

TABLE 2—*Tensile properties of Ti-5Al-2.5Sn ELI cast material.*

Thickness, t		Temperature, T		Number	Average Yield Strength, σ_y		Average Ultimate Strength, σ_u		Elongation,
cm	(in.)	K	(°F)	of Tests	MN/m^2	(ksi)	MN/m^2	(ksi)	%
0.51	(0.20)	394	(250)	9	572	(83)	627	(91)	14.5
0.51	(0.20)	294	(70)	18	724	(105)	758	(110)	12.0
0.51	(0.20)	77	(−320)	10	1145	(166)	1248	(181)	9.0
0.51	(0.20)	20	(−423)	6	1269	(184)	1386	(201)	3.5
2.54	(1.00)	294	(70)	28	696	(101)	731	(106)	...
2.54	(1.00)	77	(−320)	3	1110	(161)	1220	(177)	9.0
Wrought Ti-5Al-2.5Sn-ELI (typical)		294	(70)	...	758	(110)	793	(115)	10.0
Wrought Ti-6Al-4V ELI (typical)		294	(70)	...	862	(125)	931	(135)	10.0

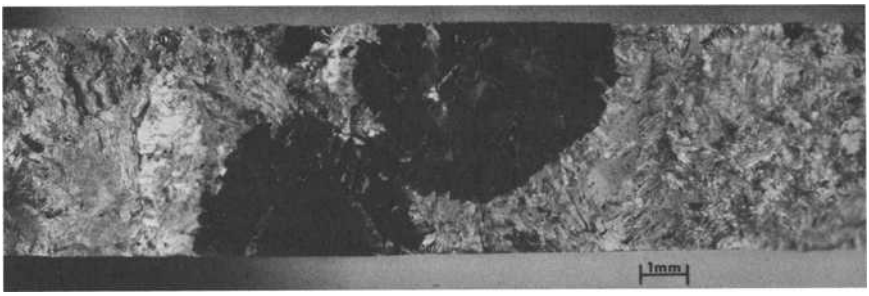

FIG. 8—*Natural fatigue flaw occurring on same plane as artifically introduced defect.*

measurement. Compact tension tests at 294 K (70°F) for 2.5-cm (1.0-in.) cast material resulted in highly scattered K_Q values in the range 90 to 119 MN/m$^{3/2}$ (83 to 108 ksi $\sqrt{\text{in.}}$), but these are not valid since the validity ratio, P_{max}/P_Q, was greater than 1.1. The fracture stress ratio-flaw size curves in Fig. 9 that have stress ratios (σ_f/σ_y) greater than 0.9, though invalid as K_{Ic} data, are useful as simulated service data for determining the defect acceptance limits for the SRB attachment fittings on the space shuttle external tank provided that specimen and fitting thicknesses are similar.

A fracture toughness comparison between Ti-5A1-2.5Sn ELI and Ti-6A1-4V ELI material in both wrought and cast forms is shown in Fig. 10. In general, the fracture toughness of cast Ti-5A1-2.5Sn ELI was found to

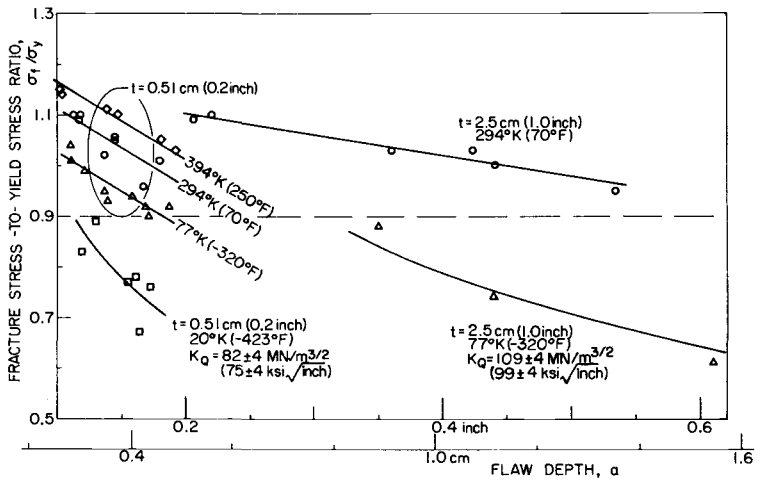

FIG. 9—*Fracture resistance of Ti-5Al-2.5Sn ELI cast material containing surface flaws of shape ratio (a/2c) 0.4 to 0.5.*

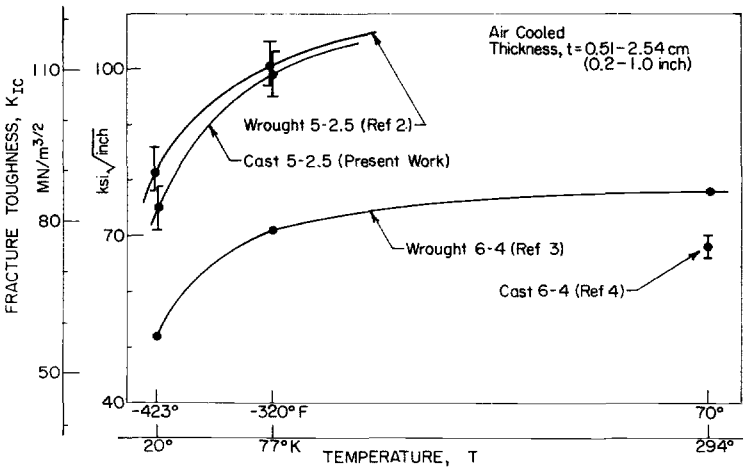

FIG. 10—*Fracture toughness comparison between Ti-5Al-2.5Sn ELI and Ti-6Al-4V ELI annealed material.*

be 5 percent lower than for wrought Ti-5A1-2.5Sn ELI, but approximately 40 percent higher than wrought Ti-6A1-4V ELI.

Crack growth rate data for Ti-5A1-2.5Sn ELI castings from compact tension and surface flaw tests are given in Fig. 11. These flaw growth data are unnecessary to the design of the SRB attachment fittings because the required useful life of the space shuttle external tank is only four pres-

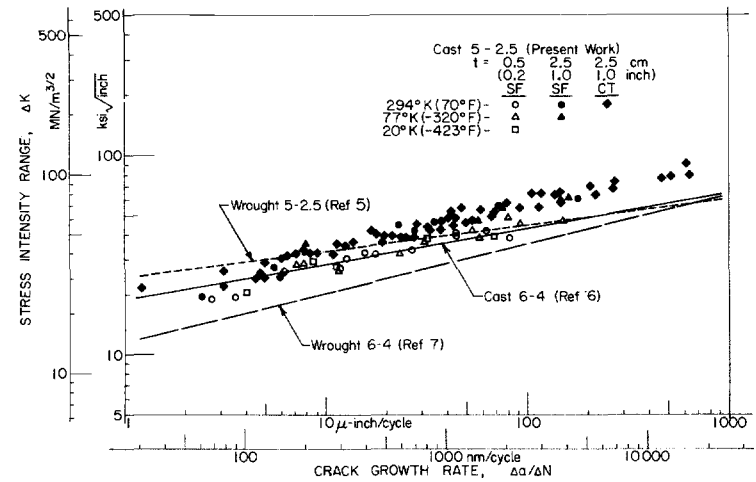

FIG. 11—*Crack growth comparison between Ti-5Al-2.5Sn ELI and Ti-6Al-4V ELI annealed material.*

surization cycles. The results were generated to provide comparative data with wrought Ti-5A1-2.5Sn ELI and cast and wrought Ti-6A1-4V ELI. The crack propagation resistance for cast 5-2.5 is somewhat higher than for both cast and wrought 6-4, but about the same as for wrought 5-2.5. It is relatively independent of temperature over the range 20 to 294 K (−423 to 70°F). The crack growth rates for 2.5-cm (1.0-in.) material are approximately half as much as those for 0.5-cm (0.2-in.) material over the stress intensity range 27 to 49 $MN/m^{3/2}$ (25 to 45 ksi $\sqrt{in.}$).

Conclusions

In general, cast Ti-5A1-2.5Sn ELI has comparable fracture toughness and crack propagation resistance to the wrought material. In short lifetime applications, such as the space shuttle external tank attachment fittings, the as-cast material is an adequate alternative when the use of forged material may not be desired for economical reasons. However, for long lifetime applications, where high cycle fatigue is a consideration, the as-cast form may not be a reliable alternative because of its propensity to initiate readily natural flaws. Since the use of cast Ti-5A1-2.5Sn ELI in long lifetime applications remains attractive because of its high fracture toughness and crack propagation resistance, future development must consider ways of reducing the propensity for initiation of natural flaws so that the cost effectiveness of using castings rather than forgings is not negated by the expense involved in nondestructive qualification of the castings to a high acceptability level.

Acknowledgments

This work was sponsored by NASA-Marshall Space Flight Center under Space Shuttle External Tank Contract NAS8-30300.

We sincerely wish to thank Dennis Karsten, Jerry Busto, and Ted Kiefer for conducting the fracture toughness and crack propagation testing.

Special thanks go to Richard Gibb for conducting the metallography and fractography.

References

[*1*] Shah, R. C. and Kobayashi, A. S. in *The Surface Crack: Physical Problems and Computational Solutions,* American Society of Mechanical Engineers, Nov. 1972, pp. 79-124.

[*2*] Van Stone, R. H., Low, J. R., and Shannon, J. L., "The Effect of Microstructure on the Fracture Toughness of Titanium Alloys," NASA Technical Report No. 2-Ti for Research Grant NGR39-087-047, Carnegie-Mellon University, Pittsburgh, Pa., Dec. 1974.

[*3*] Hall, L. R. and Finger, R. W., "Fracture and Fatigue Growth of Partially Em-

bedded Flaws," The Boeing Company, Seattle, Wash., paper presented at the Air Force Conference on Fatigue of Aircraft Structures and Materials, Miami Beach, Fla., 15-18 Dec. 1969.

[4] Bass, C. D., "Evaluation of Ti-6A1-4V Castings," AFML-TR-69-116, Air Force Materials Laboratory, Sept. 1969.

[5] Tiffany, C. F., Lorenz, P. M., and Hall, L. R., "Investigation of Plane-Strain Flaw Growth in Thick-Walled Tanks," NASA CR-5420 for Contract NAS3-4194, The Boeing Company, Seattle, Wash., 1966.

[6] Amateau, M. F., *Proceedings,* International Conference on Mechanical Behavior of Materials, Kyoto, Japan, 15-20 Aug. 1971.

[7] Harrigan, M. J., "B-1 Fracture Mechanics Data for Air Force Handbook Usage," Report TFD-72-501-1, North American Rockwell, Los Angeles Division, Los Angeles, Calif., June 1972.

M. G. Ulitchny,[1] *H. J. Rack,*[2] *and D. B. Dawson* [3]

Mechanical and Microstructural Properties Characterization of Heat-Treated, Beta-Extruded Ti-6Al-6V-2Sn

REFERENCE: Ulitchny, M. G., Rack, H. J., and Dawson, D. B., **"Mechanical and Microstructual Properties Characterization of Heat-Treated, Beta-Extruded Ti-6Al-6V-2Sn,"** *Toughness and Fracture Behavior of Titanium, ASTM STP 651,* American Society for Testing and Materials, 1978, pp. 17–42.

ABSTRACT: The mechanical behavior of β-extruded Ti-6A1-6V-2Sn has been examined after a variety of subtransus heat treatments. Increasing strength has been found to result in a gradual decrease in fracture toughness. The fracture toughness that may be achieved at any given strength level is also a function of prior solution treatment. Optimum toughness at intermediate strength levels (yield strength of approximately 1035 MPa) is associated with lower solution treatment temperatures, while at high strength levels (yield strength of approximately 1200 MPa), the use of higher solution temperatures appears to enhance the maximum achievable toughness. Comparison of the present results with those previously obtained for α-β processed Ti-6A1-6V-2Sn also indicates that, at any given strength level, β processing will result in a higher fracture toughness and a somewhat lower tensile ductility.

Finally, microscopic evidence suggests that the ordering in the primary α phase which occurs after high temperature aging does not play a predominant role in limiting the fracture toughness of high strength α-β titanium alloys; indeed, the deformation limiting characteristics of the interface α phase may be the principal factor controlling the toughness of these alloys.

KEY WORDS: titanium, mechanical properties, extrusions, titanium alloys, heat treatment, fracture properties, microstructure, metallography

Although Ti-6A1-6V-2Sn and Ti-6A1-4V alloys are similar age hardenable, α-β titanium alloys, the former is generally thought to possess greater through-thickness hardenability. This increased hardenability is typically

[1] Staff engineer, Materials Engineering, The Bendix Corp., Kansas City, Mo. 64141.
[2] Member of technical staff, Sandia Laboratories, Albuquerque, N. Mex. 87115.
[3] Member of technical staff, Sandia Laboratories, Livermore, Calif. 94550.

Copyright© 1978 by ASTM International www.astm.org

associated with more uniform mechanical behavior in heavier section sizes. Prior investigations [*1-10*] [4] have shown that processing variations can have a marked influence on mechanical properties. Procedures which involve either β working or heat treatments above the β transus temperature can result, at a given strength level, in improved fracture toughness and stress corrosion cracking resistance [*3,5,11-17*]. These improvements, when compared to those obtained by wholly α-β processing, are achieved at the expense of a slight reduction in the maximum strength achieved and a more significant reduction in tensile ductility. Previous studies of the mechanical properties of β processed titanium alloys have been concentrated on Ti-6A1-4V [*11-16*] with very little attention being given to other alloy systems [*5*].

The objective of this work therefore was to characterize the mechanical and microstructural properties of heat-treated, β-extruded Ti-6A1-6V-2Sn. The alloy was examined in both the duplex-annealed and the solution-treated-and-aged conditions.

Experimental Procedures

The chemical analysis of the Ti-6A1-6V-2Sn evaluated in this study is given in Table 1. The material was α-β blocked at 900°C (1650°F) prior to being β extruded at 985°C (1800°F). This procedure resulted in a final extrusion ratio of 4.4:1. All specimens were removed from 140 to 152-mm-long (5.5 to 6-in.) prolongations taken from predetermined location along the extrusion length as shown in Fig. 1. Figure 2 shows the relationship between the ring prolongation and the various specimen orientations examined.

Table 2 summarizes the heat treatment conditions investigated to date.

TABLE 1—*Chemical analysis of Ti-6Al-6V-2Sn alloy.*

Element	Weight Percent
Al	5.7
O	0.155
Cu	0.77
V	5.7
Sn	2.1
Fe	0.75
N	0.011
C	0.02
H	45 ppm[a]

[a] Hydrogen concentration actually varied from 30 ppm on the inside diameter to 60 ppm on the outside diameter.

[4] The italic numbers in brackets refer to the list of references appended to this paper.

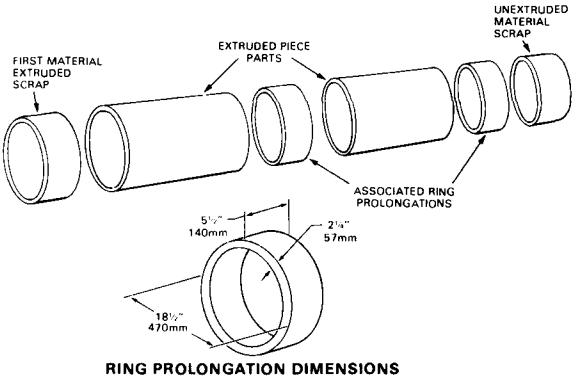

FIG. 1—*Relationship of piece parts and ring prolongations to β-extruded pipe with ring prolongation dimensions.*

TABLE 2—*Heat-treat schedules.*

Solution-treat-and-age schedule
1. Solution treat 1 h at 850° C, water quench, age 4 h at each of the following temperatures, and air cool: 400, 450, 500, 550, 600, 650, and 700° C.
2. Same as 1, except age 8 h at each temperature.
3. Same as 1, except solution treat 1 h at 900° C.
4. Same as 3, except age 8 h at each temperature.
Duplex-anneal schedule
5. Anneal 2 h at 900° C, air cool, anneal 2 h at 785° C, and air cool.

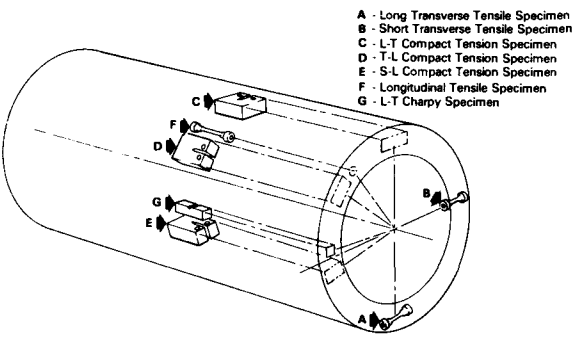

FIG. 2—*Orientation and nomenclature of specimens within ring prolongations.*

Duplex-annealed specimens were prepared from 152-mm (6-in.) arcs of the ring prolongation while the solution-treatment-and-aged specimens were machined from 32-mm (1¼-in.) arcs.

The evaluation of the mechanical behavior of the beta-extruded Ti-6Al-6V-2Sn included both tensile and fracture toughness measurements. Tension specimens were tested according to ASTM Tension Testing of Metallic Materials (E 8-69). The rate of strain was maintained at 0.005/min through the 0.2 percent offset yield strength and then increased to produce failure in approximately one additional minute. The fracture toughness measurements included both compact tension specimens tested according to ASTM Test for Plane-Strain Fracture Toughness of Metallic Materials (E 399-74) and instrumented, precracked Charpy specimens which had been machined according to ASTM Notched Bar Impact Testing of Metallic Materials (E 23-72). For the latter, the Charpy V-notch was initially sharpened by electrical discharge machining and then precracked, the final a/w (crack depth to specimen width ratio) for these specimens being between 0.45 and 0.55. Charpy-type specimens were impact tested at a velocity of 1 m/s which is equivalent to 11.1 J (8.2 ft·lbf) of energy at impact, and the output was fed into and recorded by a digital oscilloscope. Compact tension specimens were also precracked and tested. All specimen orientation nomenclature corresponded to that given in ASTM Test E 399-74.

Because of the very large number of similar heat treatments and tests, some conventions of nomenclature should be established. First, a short hand notation for the solution-treated-and-aged material. These heat treatments will be designated according to the following example: 850/450/8, where the first number is the solutionizing temperature (°C), the second number is the aging temperature (°C), and the third number is the aging time in hours. Solutionizing is for 1 h, followed by water quenching, and aging is followed by air cooling. Second, "Charpy testing" will correspond to tests from which dynamic fracture toughnesses, K_{Id}, were calculated. Finally, "fracture toughness testing" will be referred to when compact tension specimens from which static fracture toughnesses, K_{Ic}, were calculated are being considered.

The microstructural characterization portion of this study generally utilized material removed from previously failed mechanical specimens. Optical metallography used standard techniques with a final etchant of 1.5 volume percent hydrofluoric acid (HF), 3.5 volume percent nitric acid (HNO_3), and the balance water (H_2O). The measurements of the volume fraction primary α, the prior β grain size, and the grain boundary primary α thickness reported herein were performed on an image analyzing computer using quantitative metallographic procedures summarized elsewhere [*18*]. Since the microstructures observed were essentially equiaxed, no dif-

ferentiation will be made between the measurements obtained on the three orthogonal surfaces (that is, longitudinal, and long and short transverse).

Texture determination was in accordance with ASTM Preparing Quantitative Pole Figures of Metals (E 81-63 (1974)) with CuK_α radiation and a nickel filter. The X-ray pole figures were obtained by the Schulz technique on a texture goniometer, background corrections being performed prior to automatic plotting of the pole figure [*19*].

Finally, transmission and scanning electron microscopy observations were made utilizing, respectively, an electron microscope operated at 200 kV and a scanning electron microscope operated at 25 kV. Transmission specimens were prepared as detailed elsewhere [*20*]. It is to be noted that all fractographic examinations were normal to the original fracture surface.

Experimental Results and Discussion

Textural Analysis

Figure 3 illustrates a $(0002)_\alpha$ pole figure obtained from the central region of the extrusion. Each contour line in this figure represents an intensity increment of 10. Unfortunately, no quantitative comparison with a random specimen can be made since no such specimen was available at the time the measurements were made. A qualitative comparison of this figure with those previously obtained by other investigations [*21*] does however indicate that it is typical of α-β titanium alloys which have been β worked and transformed from the β to α phase upon cooling; that is, a concentration of basal planes is observed to be at an angle of approximately 40 deg from both the long transverse direction and the specimen surface.

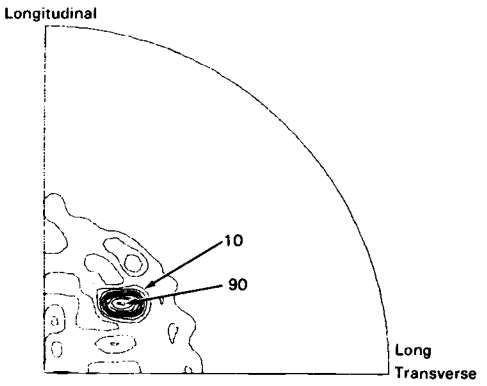

FIG. 3—*Pole figure of as-β-extruded Ti-6Al-6V-2Sn. Material examined was from center of extrusion thickness. Each contour line represents an intensity increment of ten. Figure shows a concentration of basal planes at an angle of 40 deg to both long transverse direction and specimen surface.*

Optical and Transmission Microscopy

As-Extruded Condition—Optical examination (Fig. 4) of the as-extruded condition revealed an essentially equiaxed β grain structure with a prior β grain size and primary α volume fraction of 216.3 μm and 0.49, respectively. The prior β grain boundaries also contained an almost continuous layer of primary α, the latter having a mean thickness of 4.7 μm. In addition, isolated areas were observed wherein the normally acicular primary α tended to be rounded (see arrow in Fig. 4). Electron microprobe examination showed that the primary αs contained within these regions, as well as the primary α located at the prior β grain boundaries, did not contain as high a concentration of vanadium and iron when compared with the more general Widmanstätten (α plus β) matrix. This observation suggests that both these areas and the grain boundary primary α layer form first when the extrusion is cooled from the β extrusion temperature. Further examination showed that the aforementioned regions of localized concentration differences were not materially affected by any of the subsequent solution or duplex-annealing treatments.

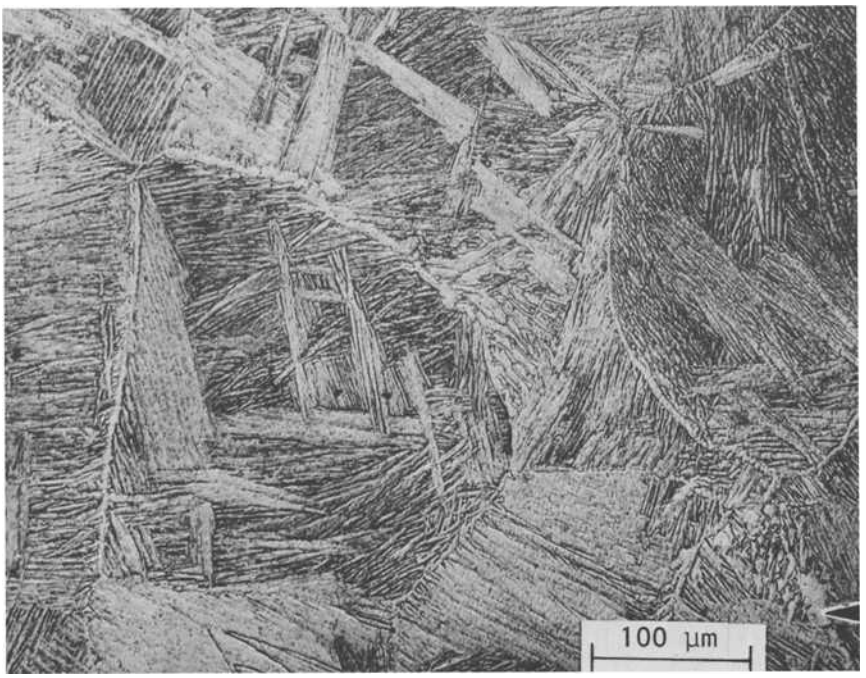

FIG. 4—*Optical micrograph of as-β-extruded Ti-6Al-2Sn. Structure consists of equiaxed prior β grains outlined by continuous layer of primary α. The normally acicular primary α within the prior β grains contains isolated areas where the primary α tends to be rounded, see arrow.*

Transmission electron microscopy of the as-extruded condition shows Widmanstätten α separated by the β matrix (Fig. 5). Dark field micrographs (Fig. 6), taken using the interface α reflection, showed that the α-β interface contained the interface phase recently reported by Rhodes and Williams [*22*]. The interface region contains a high dislocation density and a high density of α phase particles. Figure 6 clearly shows that the interface α phase is not continuous; it appears as discrete particles lying along the α-β interface. The interface phase was observed through all the microstructural conditions examined during this study and seemed to be relatively unaffected by subsequent heat treatment.

Finally, the primary α phase itself had a low dislocation density and the transformed β matrix contained some secondary α particles.

Duplex Annealed—Figure 7 shows the microstructure after each stage of the two-stage duplex-annealing heat treatment. A comparison with the as-extruded conditions (Fig. 4) suggests that some rounding of the acicular primary α phase has occurred during the annealing cycle. In addition, the quantitative measurements indicate that while the prior β grain size and volume fraction primary α have increased slightly to 248 μm and 0.52,

FIG. 5—*Transmission electron micrograph of as-β-extruded Ti-6Al-6V-2Sn showing Widmanstätten α separated by the β matrix.*

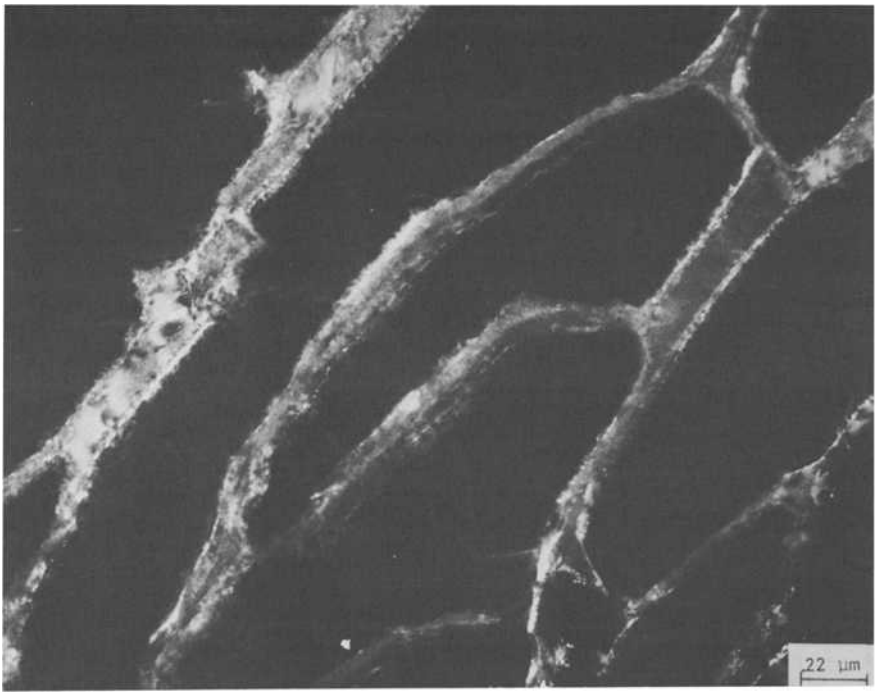

FIG. 6—*Dark field transmission electron micrograph of as-β-extruded Ti-6Al-6V-2Sn. Photo taken using the interface α reflection showing the high density of discrete alpha phase interface particles as well as the high dislocation density at the interface.*

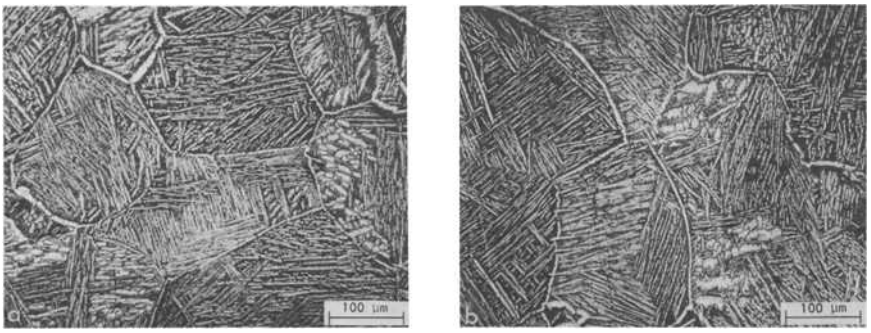

FIG. 7—*Optical micrographs of β-extruded Ti-6Al-6V-2Sn after each phase of duplex anneal:* (a) *after 2 h at 900°C and air cool, and* (b) *after an additional 2 h at 785°C and air cool. This heat treatment results in a rounding of the acicular primary α, an increase in prior β grain size and volume fraction primary α and a decrease in grain boundary α thickness compared to the as-β-extruded condition.*

FIG. 8—*Transmission electron micrograph of duplex-annealed Ti-6Al-6V-2Sn showing planar arrays of dislocations which result from this heat treatment.*

respectively, the grain boundary α thickness has decreased to 3.6 from 4.7 μm.

Transmission electron microscopy indicates that the primary α phase in the duplex-annealed condition again contained a low dislocation density which was generally arranged in planar arrays (Fig. 8). In addition, further evidence for increased formation of secondary α in the β matrix was obtained.

Solution Treated and Aged—Several solution-treated-and-aged conditions were examined. An optical micrograph following solution treatment at 850°C is presented in Fig. 9. Transmission electron microscopy showed that the structure consisted of primary α and a heavily dislocated martensitically transformed β matrix. Quantitative measurements indicate that the solution treatment at 850°C increased the amount of primary α to 75 volume percent without materially affecting either the prior β grain size or the grain boundary α thickness. A more detailed examination of the effect of the 900°C solution treatment on the prior β grain size, the volume fraction α, and the grain boundary α thickness is presently underway and will be reported at a later date.

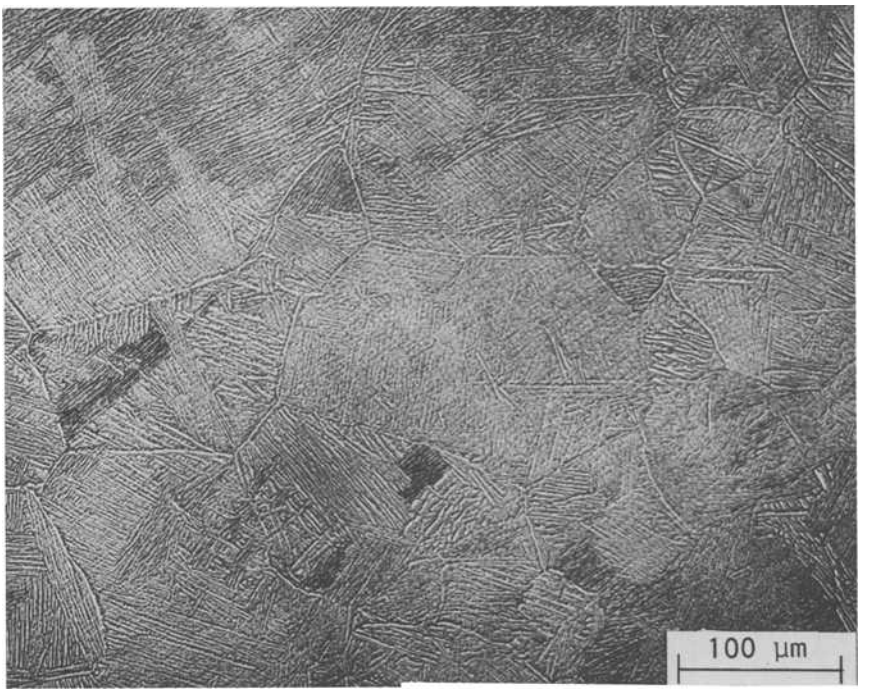

FIG. 9—*Optical micrograph of Ti-6Al-6V-2Sn solution treated 1 h at 850°C and water quenched.*

Probably the most significant feature observed in the examination of the various solution-treated-and-aged conditions was the presence of Ti_3Al in the primary α phase after the 900/650/8 treatment. Its appearance is best illustrated by the $(0002)_\alpha$ selected area diffraction pattern presented in Fig. 10 where the superlattice reflections correspond to the DO_{19} lattice of Ti_3Al.

Finally, aging of solution-treated Ti-6Al-6V-2Sn results in precipitation of α in the previously transformed β matrix.

To date no difference in α phase precipitation has been observed between material solutionized at 850°C and at 900°C prior to aging. A recent paper [*23*] does suggest that changing the solution temperature from 800 to 900°C should result in a morphological transition from needle or platelike α to lamellar α precipitates upon aging. This observation however was made after longer aging times than the maximum of 8 h used in this study. Consequently, it is not surprising that this transition was not observed in the present study.

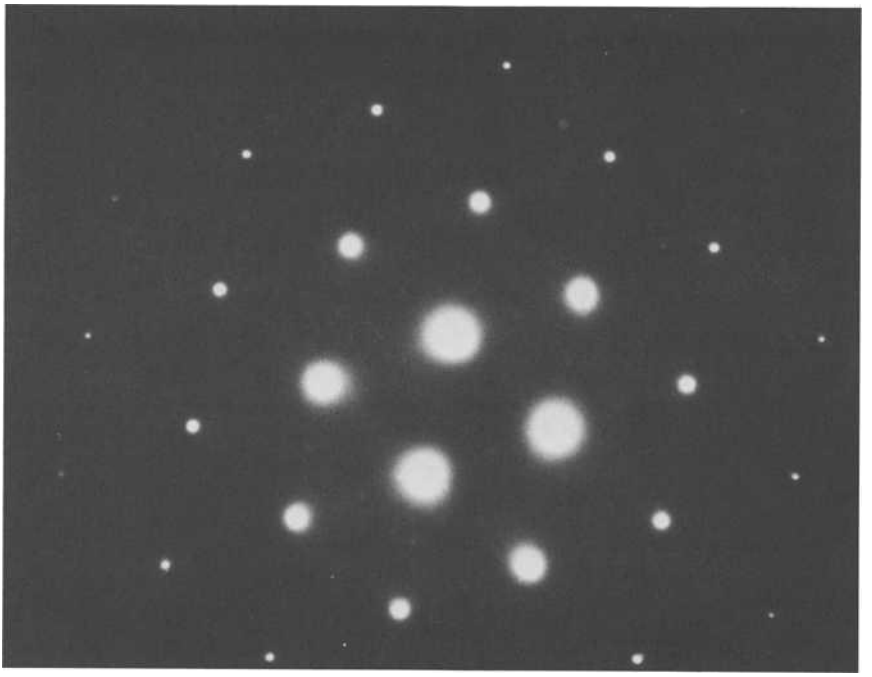

FIG. 10—*Selected area of diffraction of Ti-6Al-6V-2Sn which has been solutionized 1 h at 900°C, water quenched, aged 8 h at 650°C and air cooled. The zone axis is the* $(0002)_\alpha$ *and the superlattice reflections correspond to the* DO_{19} *lattice of* Ti_3Al.

Mechanical Properties

Tensile Behavior—Results of the yield and ultimate tensile strength tests for all heat treat conditions are given in Table 3. Percent elongation in 25.4 mm and percent reduction in area (RA) results are also presented in this table. Figure 11 shows the longitudinal yield strength versus aging

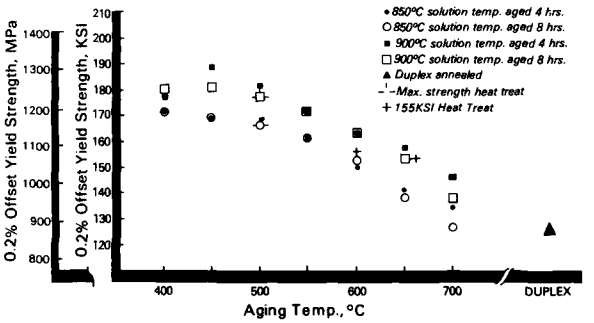

FIG. 11—*Yield strength versus aging temperature for all heat treat conditions studied. Data are the average of two tests*

TABLE 3—*Tension test results for solution-treated-and-aged longitudinal specimens.*

Aging Temperature, ° C	0.2% Offset Yield Strength, MPa (ksi)	Ultimate Tensile Strength, MPa (ksi)	Elongation in 25.4 mm, %	Reduction in Area, %
	Solutionized 1 h at 850° C, WQ, aged 4 h, AC			
400	1178 (171)	1316 (191)	1.3	1.1
450	1171 (170)	1357 (197)	1.1	1.7
500	1158 (168)	1295 (188)	7.3	6.1
550	1116 (162)	1213 (176)	9.3	12.3
600	1040 (151)	1137 (165)	10.9	19.6
650	978 (142)	1075 (156)	13.5	25.1
700	923 (134)	1027 (149)	15.2	22.4
	Solutionized 1 h at 850° C, WQ, aged 8 h, AC			
400	1178 (171)	1302 (189)	1.9	2.0
450	1171 (170)	1344 (195)	3.3	1.8
500	1151 (167)	1268 (184)	6.0	8.7
550	1123 (163)	1220 (177)	8.4	11.2
600	1047 (152)	1144 (166)	10.9	17.0
650	951 (138)	1054 (153)	15.4	27.4
700	882 (128)	1006 (146)	16.0	26.1
	Solutionized 1 h at 900° C, WQ, aged 4 h, AC			
400	1226 (178)	1137 (197)	1.7	2.8
450	1302 (189)	1371 (199)	2.1	3.3
500	1261 (183)	1364 (198)	2.1	4.6
550	1185 (172)	1288 (187)	4.0	6.7
600	1123 (163)	1199 (174)	7.5	10.7
650	1082 (157)	1192 (173)	10.1	13.7
700	1013 (147)	1116 (162)	11.1	19.8
	Solutionized 1 h at 900° C, WQ, aged 8 h, AC			
400	1240 (180)	1412 (205)	3.6	3.3
450	1247 (181)	1378 (200)	2.6	2.4
500	1233 (179)	1344 (195)	3.4	4.7
550	1192 (173)	1261 (183)	4.6	6.3
600	1130 (164)	1226 (178)	6.6	11.1
650	1054 (153)	1158 (168)	11.0	15.7
700	944 (137)	1047 (152)	14.6	25.4

NOTE—WQ=water quenched, and
AC=air cooled.
Values given are averages of two tests.

temperature for all heat treat conditions. The data show that solution-treated-and-aged Ti-6A1-6V-2Sn exhibits the characteristics of classical age hardening behavior. That is, the strength increases with aging temperature up to some peak and then decreases as aging temperature is increased further. Note that the material solutionized at 900°C appears to reach the peak strength condition when aged at 450°C. This is true for aging times of either 4 or 8 h. On the other hand, the material solutionized at 850°C exhibits overaging behavior even when aged at 400°C for 4 h.

Ultimate tensile strength as a function of aging temperature is plotted

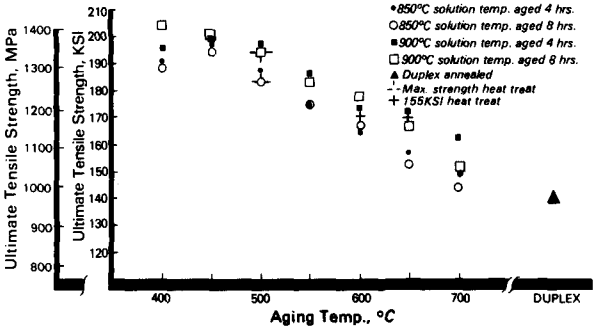

FIG. 12—*Ultimate tensile strength versus aging temperature for all heat treat conditions studied. Data are the average of two tests.*

in Fig. 12. The ultimate strength followed essentially the same trend as the 0.2 percent yield strength and showed expected peak aging and overaging behavior.

Beta processing of Ti-6A1-4V and Ti-6A1-6V-2Sn alloys has previously been shown to reduce noticeably the tensile elongation as compared to conventional α-β processing [*17*]. Figure 13 shows a plot of percent elongation in 25.4 mm as a function of yield strength. Note that the elongation appears to be dependent only upon the strength level and is not a function of the details of heat treatment, whether duplex annealed or solution treated and aged. These values of tensile elongation are about 4 to 8 percent lower than those for Ti-6A1-6V-2Sn heat treated to the same strength level but processed in α-β temperature range [*24*]. Percent reduction in area as a function of yield strength is shown in Fig. 14. Again, the details of the heat

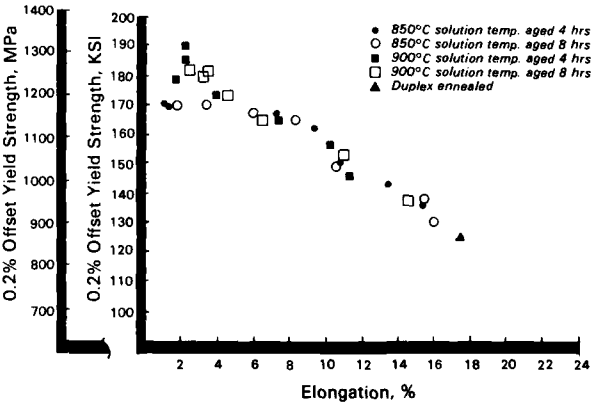

FIG. 13—*Percent elongation in 25.4 mm versus yield strength for all heat treat conditions studied. Data are the average of two tests.*

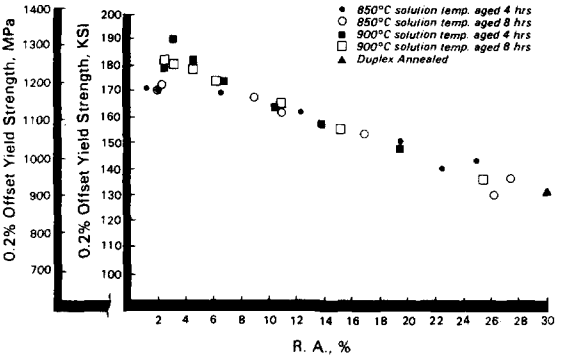

FIG. 14—*Reduction in area versus yield strength for all heat treat conditions studied. Data are the average of two tests.*

treatment do not appear to influence the percent reduction in area at a given strength level. The strength level appears to be the sole determining factor. Reduction in area of β processed Ti-6A1-6V-2Sn is only about half that for α-β processed material at the same strength level [*24*].

Although yield strength levels above 1240 MPa (180 ksi) can be achieved in β processed Ti-6A1-6V-2Sn (see, for example, heat treatments 900/400/8, 900/450/8, 900/450/4, and 900/500/4), these conditions result in tensile elongations of less than 4 percent. In order to achieve normally acceptable elongation of 10 percent, heat treatments such as 800/600/8 or 900/650/8 must be employed. These heat treatments produce yield strengths in the 1034 to 1066 MPa (150 to 155 ksi) range. These values can be compared to the α-β processed material reported by Lewis et al [*24*] which had a yield strength of 1160 MPa (167 ksi) and 14 percent elongation.

Dynamic Fracture Toughness—Figure 15 shows the dynamic fracture

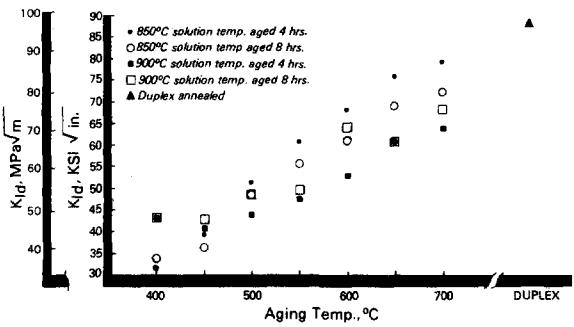

FIG. 15—*Dynamic fracture toughness versus aging temperature for all heat treat conditions studied. Data are the average of three tests.*

toughness, K_{Id}, determined from precracked Charpy impact tests, as a function of aging temperature. All K_{Id} values were calculated using linear elastic fracture mechanics since there was no evidence of general yielding before fracture. The values plotted in Fig. 15 were taken from Table 4. As expected, toughness increases by increasing aging temperature (that is, with decreasing tensile strength). However this figure does indicate, contrary to the tensile behavior, that the details of the heat treat procedure do have an effect on toughness. Solution treatment at 850°C generally lead to

TABLE 4—*Fracture toughness test results for LT orientation solution-treated-and-aged specimens.*

Aging Temperature, °C	Fracture Toughness, K_{Id}, MPa$\sqrt{m}$ (ksi$\sqrt{in.}$)	Fracture Toughness, K_{Ic}, MPa$\sqrt{m}$ (ksi$\sqrt{in.}$)
	Solutionized 1 h at 850°C, WQ, aged 4 h, AC	
400	35.1 (31.9)	
450	43.9 (39.9)	
500	56.9 (51.7)	
550	67.1 (61.0)	
600	74.8 (68.0)	
650	83.2 (75.6)	
700	87.2 (79.3)	
	Solutionized 1 h at 850°C, WQ aged 8 h, AC	
400	36.5 (33.2)	35.9 (32.6)
450	40.6 (36.9)	38.7 (35.2)
500	53.7 (48.8)	48.2 (43.8)
550	60.9 (55.4)	60.3 (54.8)
600	68.3 (62.1)	67.5 (61.4)
650	76.2 (69.3)	81.6 (74.2)
700	79.4 (72.2)	89.3 (81.2)
	Solutionized 1 h at 900°C, WQ, aged 4 h, AC	
400	48.2 (43.8)	
450	44.7 (40.6)	
500	48.5 (44.1)	
550	52.3 (47.5)	
600	58.1 (52.8)	
650	66.9 (60.8)	
700	70.6 (64.2)	
	Solutionized 1 h at 900°C, WQ, aged 8 h, AC	
400	48.2 (43.8)	
450	47.3 (43.0)	
500	53.4 (48.5)	39.8 (36.2)
550	54.9 (49.9)	
600	70.5 (64.1)	
650	66.9 (60.8)	65.5 (59.5)
700	74.5 (67.7)	

NOTE—WQ=water quenched, and
AC=air cooled.
Values given are averages of three tests.

higher fracture toughness at a given aging temperature above 450°C than did solutionizing at 900°C. In addition, aging for only 4 h following solutionizing at 850°C further enhanced toughness. The underlying causes for these differences are as yet undetermined and form the basis for on-going studies at our laboratories.

The interrelationship between yield strength and dynamic fracture toughness is represented in Fig. 16. This figure shows that an acceptable combination of yield strength and toughness can be realized from heat-treated, β-processed Ti-6A1-6V-2Sn. These results again indicate that, for yield strengths between 827 and 1034 MPa (120 and 150 ksi), maximum fracture toughness can be achieved by solutionizing at 850°C and aging for 4 h. It also suggests that at strength levels above 1170 MPa (170 ksi), solutionizing at 900°C results in maximum toughness levels.

Tensile and Fracture Toughness Behavior of Selected Heat Treatments—Based on the aforementioned results, two solution-treated-and-aged conditions were chosen to produce yield stresses of 1034 to 1068 MPa (150 to 155 ksi) and fracture toughness of approximately 55 MPa $\sqrt{m}$ (50 ksi $\sqrt{in.}$). Details of these heat treat cycles and the test results are given in Table 5. In addition to the preliminary tests already discussed for these heat treatments, the following tests were performed: tension tests in both the long and short transverse directions and fracture toughness tests according to ASTM Test E 399-74 in the three orientations shown in Fig. 2.

Table 5 shows that there is very little difference, with orientation or heat treatment, in the tension test results. The short transverse direction does show a lower ductility than the other test directions. The toughness produced by the 850/600/8 treatment is slightly but consistently higher than that produced by the 900/650/8 treatment. This difference is small for the

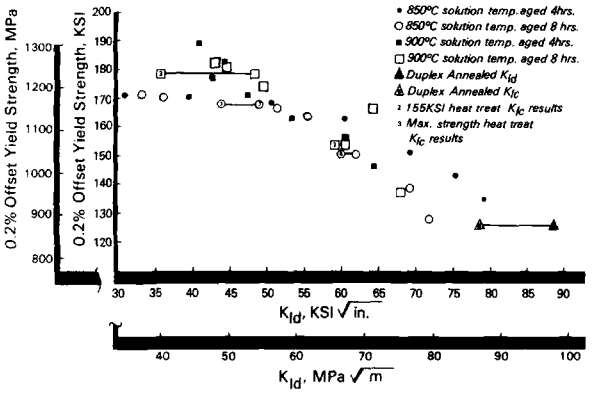

FIG. 16—*Yield strength versus dynamic fracture toughness for all heat treat conditions studied.*

LT orientation but amounts to about 10 percent in both the TL and SL orientations.

Fracture toughness measurements also were performed on LT orientation specimens that were given two different heat treatments which were selected to maximize the usable tensile strength of Ti-6A1-6V-2Sn. These treatments were chosen with attention to maintaining an acceptable level of tensile ductility and therefore do not represent a true maximum of tensile strength (see Fig. 11). Results from these two heat treatments, 850/500/8 and 900/500/8, are given in Table 6. A comparison of Tables 5 and 6 shows that there is a substantial loss in toughness (30 to 40 percent) in going from the 1034 MPa (150 ksi) to the 1170 to 1240 MPa (170 to 180 ksi) strength level. Note from Table 6 that the K_{Ic} and K_{Id} data show good agreement for the high strength heat treatment, but not as good as for the 1068 MPa (155 ksi) heat treatment (Table 5). This effect is shown

TABLE 5—*Results of additional tests of specimens heat treated to give 1068 MPa (155 ksi) yield strength.*

Specimen Orientation	0.2% Offset Yield Strength, MPa (ksi)	Ultimate Tensile Strength, MPa (ksi)	Elongation in 25.4 mm, %	Reduction in Area, %
	TENSION TEST RESULTS			
	Solutionized 1 h at 850°C, WQ, aged 8 h at 600°C, AC			
Longitudinal	1047 (152)	1144 (166)	10.9	17.0
Long transverse	1068 (155)	1158 (168)	8.8	14.2
Short transverse	1094 (159)	1164 (169)	6.0	12.2
	Solutionized 1 h at 900°C, WQ. aged 8 h at 650°C, AC			
Longitudinal	1054 (153)	1158 (168)	11.0	15.7
Long transverse	1068 (155)	1164 (169)	10.5	15.7
Short transverse	1068 (155)	1164 (169)	7.0	12.6

FRACTURE TOUGHNESS TEST RESULTS

Solutionized 1 h at 850°C, WQ, aged 8 h at 600°C, AC

Specimen Orientation	Fracture Toughness, K_{Id}, MPa$\sqrt{m}$ (ksi$\sqrt{in.}$)	Fracture Toughness, K_{Ic}, MPa$\sqrt{m}$ (ksi$\sqrt{in.}$)
LT	68.3 (62.1)	66.6 (60.5)
TL		66.2 (60.2)
SL		61.1 (55.5)
	Solutionized 1 h at 900°C, WQ, aged 8 h at 650°C, AC	
LT	66.9 (60.8)	65.5 (59.5)
TL		61.1 (55.5)
SL		57.6 (52.4)

NOTE—WQ=water quenched, and
AC=air cooled.
Tensile and K_{Ic} results are average of two tests.
K_{Id} results are average of three tests.

TABLE 6—*Results of additional tests of specimens heat treated to give maximum usable strength.*

Specimen Orientation	0.2% Offset Yield Strength, MPa (ksi)	Ultimate Tensile Strength, MPa (ksi)	Elongation in 25.4 mm, %	Reduction in Area, %
	TENSION TEST RESULTS			
	Solutionized 1 h at 850°C, WQ, aged 8 h at 500°C, AC			
Longitudinal	1151 (167)	1268 (184)	6.0	8.7
	Solutionized 1 h at 900°C, WQ, aged 8 h at 500°C, AC			
Longitudinal	1233 (179)	1344 (195)	3.4	4.7
Specimen Orientation	Fracture Toughness, K_{Id}, MPa$\sqrt{m}$ (ksi$\sqrt{in.}$)		Fracture Toughness, K_{Ic}, MPa$\sqrt{m}$ (ksi$\sqrt{in.}$)	
	FRACTURE TOUGHNESS TEST RESULTS			
	Solutionized 1 h at 850°C, WQ, aged 8 h at 500°C, AC			
LT	53.7 (48.8)		48.3 (43.9)	
	Solutionized 1 h at 900°C, WQ, aged 8 h at 500°C, AC			
LT	53.4 (48.5)		39.8 (36.2)	

NOTE—WQ=water quenched, and
AC=air cooled.
Tensile and K_{Ic} results are average of two tests.
K_{Id} results are average of three tests.

graphically in Fig. 16 for those heat treatments selected for further study and for the duplex-annealed material, where the symbols with the numbers inside show K_{Ic} values from LT orientation compact tension specimens.

The fairly good agreement between K_{Ic} and K_{Id} values has been noted but should not be given undue weight at this time. This relationship is being examined in more detail.

Mechanical Testing of Duplex-Annealed Material—Witness pieces from three duplex-annealed extrusions were tested for longitudinal, and long and short transverse tensile properties, LT orientation precracked Charpy impact properties, and LT orientation fracture toughness. The specimens were prepared from 57-mm (2¼-in.) thick sections. The results given in Table 7 show that there is little difference in tensile properties with test direction. The duplex-anneal condition resulted in the lowest strength, highest toughness material evaluated in this study.

Fractography

Duplex-Annealed Condition—Scanning electron microscopy showed that failure in duplex-annealed Ti-6A1-6V-2Sn was characterized by transgranular ductile, dimple formation (Fig. 17). Further examination of specimens that had been nickel-plated, mounted, and polished such that the

TABLE 7—*Results for duplex-annealed specimens.*

Specimen Orientation	0.2% Offset Yield Strength, MPa (ksi)	Ultimate Tensile Strength, MPa (ksi)	Elongation in 25.4 mm, %	Reduction in Area, %
	TENSION TEST RESULTS			
Longitudinal	861 (125)	971 (141)	17.9	28.9
Long transverse	875 (127)	971 (141)	17.0	28.9
Short transverse	868 (126)	971 (141)	20.5	25.7
Specimen Orientation	Fracture Toughness, K_{Id}, MPa$\sqrt{m}$ (ksi$\sqrt{in.}$)		Fracture Toughness, K_{Ic}, MPa$\sqrt{m}$ (ksi$\sqrt{in.}$)	
	FRACTURE TOUGHNESS TEST RESULTS			
LT	98.5 (89.5)		90.9 (82.6)	

NOTE—Values given are averages of two tests.

subsequent examination plane was perpendicular to the original fracture surface suggest that propagating cracks deflect locally at the boundaries of Widmanstätten $\alpha+\beta$ colonies (Fig. 18). The absence of any intergranular fracture is consistent with the findings of Froes et al [*25*] who showed that subtransus annealing tends to suppress the intergranular fracture mode that is normally observed in β processed α-β titanium alloys. It is suggested that this may be due to the recrystallization of the transformed β matrix which

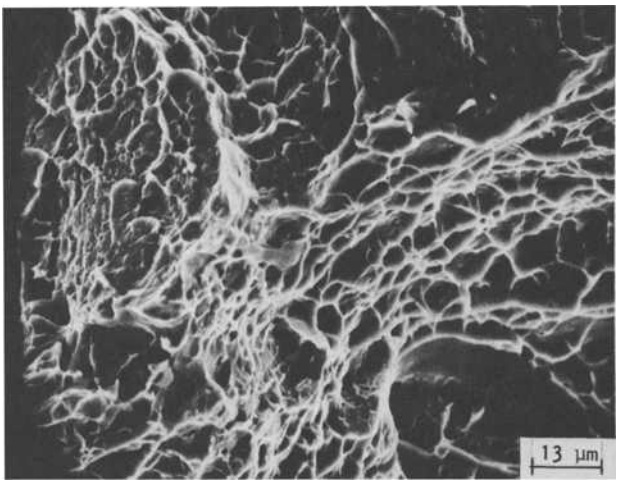

FIG. 17—*Scanning electron micrograph taken normal to fracture surface of duplex-annealed Ti-6Al-6V-2Sn tension test specimen. Fracture is characterized by transgranular ductile fracture with large areas of dimple formation.*

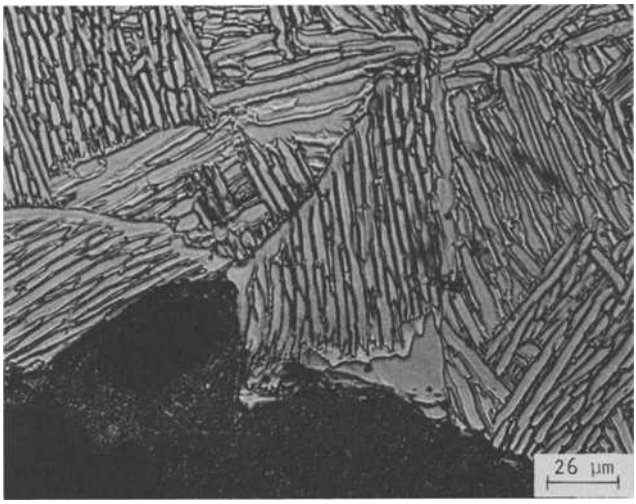

FIG. 18—*Optical micrograph of plane normal to fracture plane of duplex-annealed Ti-6Al-6V-2Sn tension specimen showing crack growth occurs by local crack deflection at boundaries of Widmanstätten α–β colonies.*

occurs during the subtransus anneal. Indeed, this phenomena has its parallel in the increase in fracture toughness observed in Ti-6A1-4V when the latter is given a recrystallization annealing treatment.

Solution-Treated-and-Aged Condition

The decrease in tensile ductility and fracture toughness which accompanies increased strength in Ti-6A1-6V-2Sn can be associated with an increase in the amount of intergranular and flat fracture. The intergranular regions are generally observed only after aging at low temperatures (that is, less than about 500°C), Fig. 19. When viewed perpendicular to the principal fracture surface, cracks appear to follow the interface between the primary α particles lying both along the prior β grain boundaries and within the β matrix (Fig. 20). This observation suggests that the interface phase, which has previously been shown to exist in the β-extruded Ti-6A1-6V-2Sn alloy presently under investigation, may play an important, although as yet undetermined, role in controlling the fracture toughness of α-β titanium alloys.

The change in the appearance of the fracture surface as a function of aging temperature after solution treating at 900°C is shown in Fig. 19. This figure shows the change from intergranular, flat fracture at the lower

aging temperatures to transgranular ductile, dimple-type fracture at the higher aging temperatures. Finally, it should be noted that the flat fracture regions observed in Ti-6A1-6V-2Sn which was aged at less than 500°C contain rather small equiaxed dimples.

Summary and Conclusions

This investigation has shown that when β-extruded Ti-6A1-6V-2Sn is given a subsequent subtransus heat treatment, attractive combinations of strength and fracture toughness can result. Indeed, the fracture toughness was found to be more sensitive to the subtransus treatment than was the yield strength. Three essential levels of strength and toughness were achieved in β-extruded Ti-6A1-6V-2Sn.

1. At low strength levels, 895-MPa (130-ksi) yield stress, duplex-annealed Ti-6Al-6V-2Sn has a fracture toughness of 82.5 MPa $\sqrt{m}$ (75 ksi $\sqrt{in.}$).

2. At intermediate strength levels, 1034-MPa (150-ksi) yield stress, Ti-6A1-6V-2Sn solution treated at 850°C and aged 4 h at 600°C has a fracture toughness of 74.8 MPa $\sqrt{m}$ (68 ksi $\sqrt{in.}$).

3. At high strength levels, 1200-MPa (175-ksi) yield stress, Ti-6A1-6V-2Sn solution treated at 900°C and aged 8 h at 550°C has a fracture toughness of 54.9 MPa $\sqrt{m}$ (49.9 ksi $\sqrt{in.}$).

It appears that the fracture toughness increase associated with beta processing is due to local crack rotation which occurs when the crack encounters the boundary between adjacent Widmanstätten α-β colonies. Although transmission electron microscopy has shown that at the highest aging temperature examined some ordering takes place in the primary α, this does not appear to be the principal strengthening mechanism in Ti-6A1-6V-2Sn; indeed, precipitation of α in the previously transformed β matrix appears to be more important. Finally, some evidence is presented which suggests that as the strength level increases, the interface phase may play an increasingly important role in limiting the fracture toughness of α-β titanium alloys.

Acknowledgments

We wish to thank the following individuals whose technical assistance greatly aided us in this program: M. C. Collins, D. L. Stoltz, and C. E. Watterson, at Bendix, and G. V. Bartin, S. Duliere, F. Greulich, and J. Smith at Sandia.

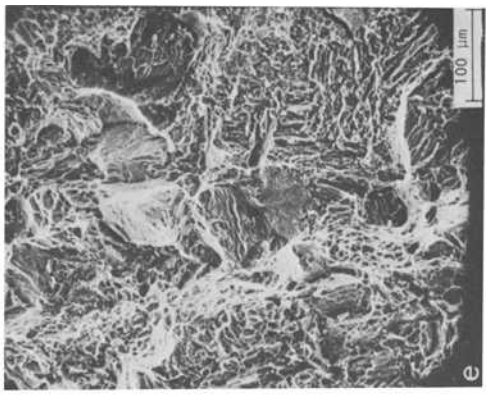
100 µm
e

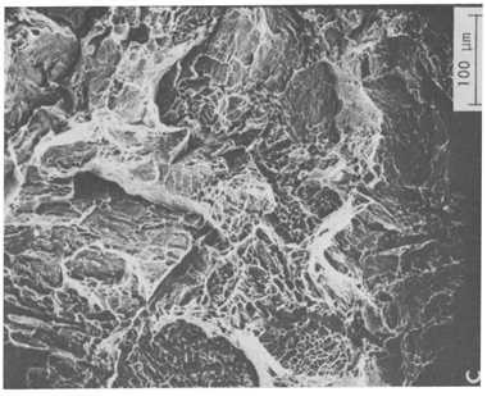
100 µm
d


100 µm

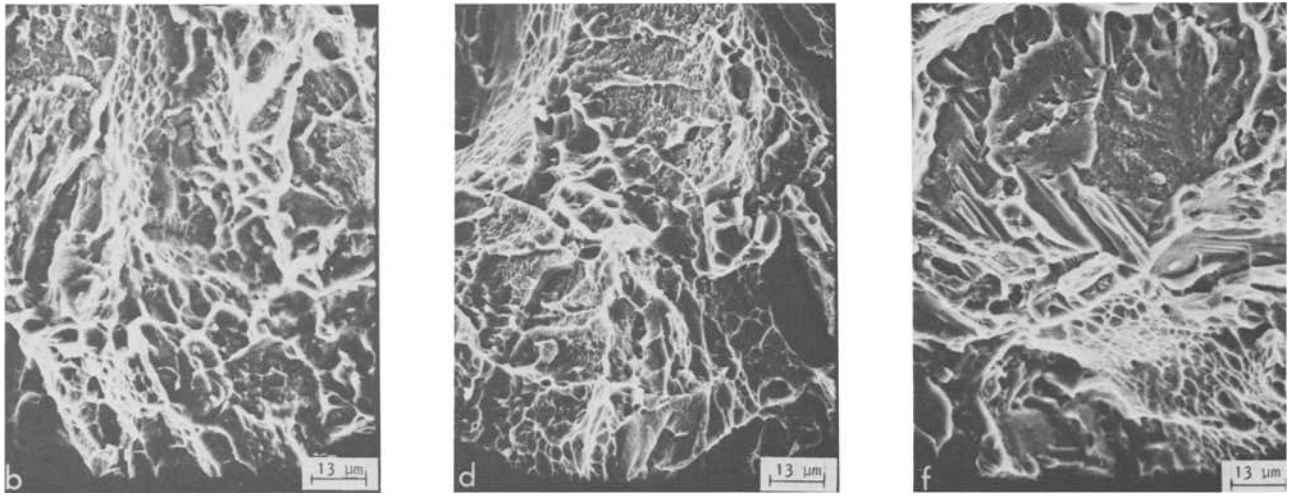

FIG. 19—*Scanning electron micrographs of fracture surfaces at high and low magnification for various solution-treated-and-aged tension specimens of Ti-6Al-6V-2Sn:* (a) *and* (b) *given 900/400/8 treatment,* (c) *and* (d) *given 900/450/4 treatment,* (e) *and* (f) *given 900/500/8 treatment,* (g) *and* (h) *given 900/550/8 treatment,* (i) *and* (j) *given 900/650/8 treatment. Note in* (a) *and* (b) *and* (c) *and* (d) *that the areas of flat fracture contain small areas of equiaxed dimples.*

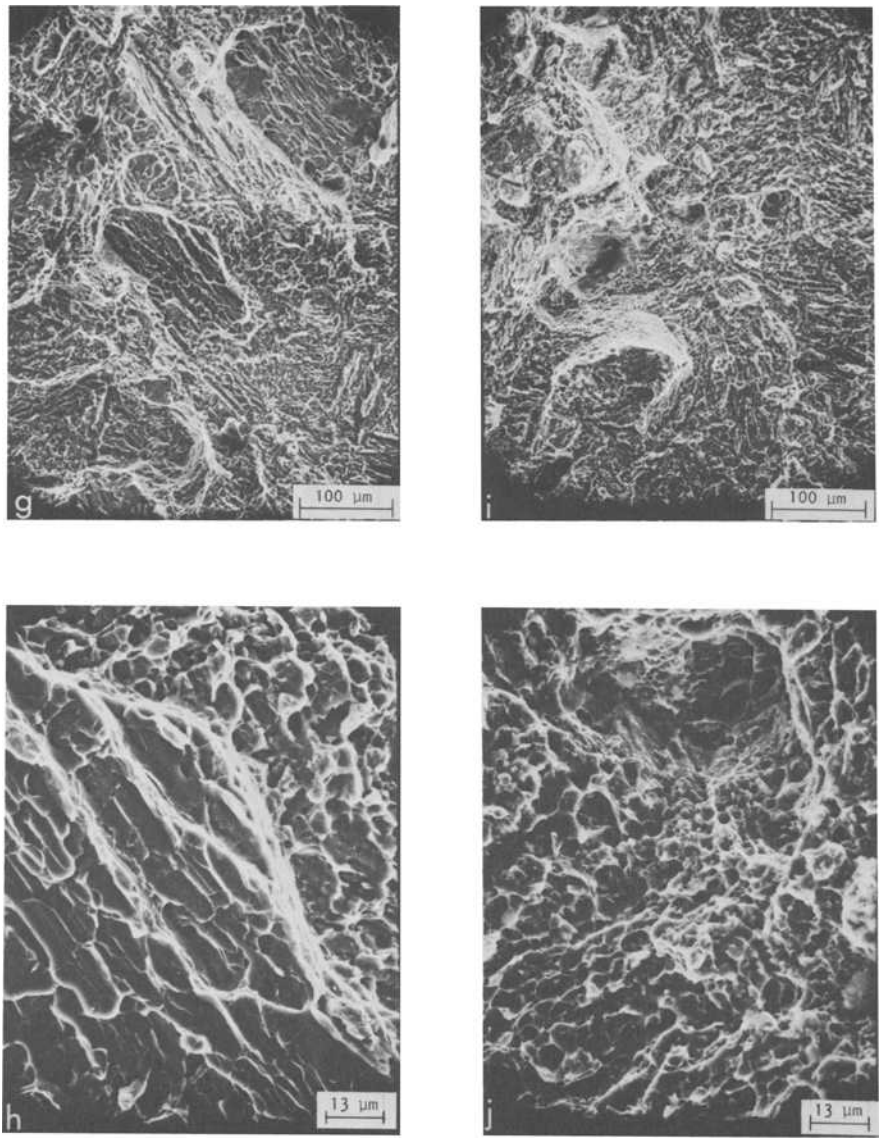

FIG. 19—*Continued.*

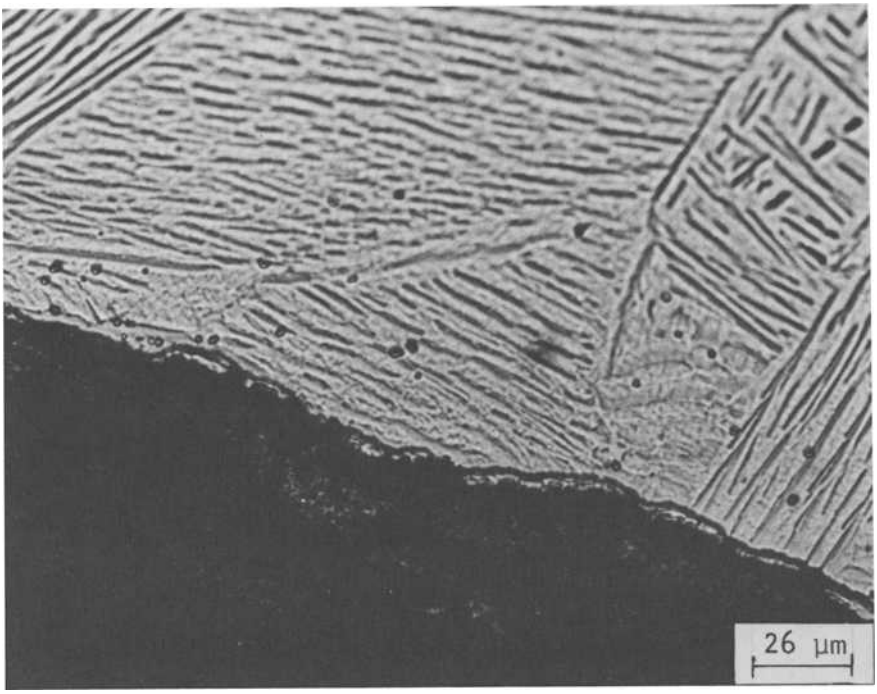

FIG. 20—*Optical micrograph of plane normal to fracture plane of Ti-6Al-6V-2Sn tension specimen solutionized at 900°C, water quenched, aged 8 h at 500°C, and air cooled showing how the crack follows the interface between the primary α particles along the prior β grain boundaries and the β matrix.*

References

[1] *Aerospace Structural Materials Handbook,* Mechanical Properties Data Center, Balfour Stulen, Inc., 1974.

[2] *Damage Tolerant Design Handbook,* Metals and Ceramics Information Center, MCIC-HB-01, Columbus, Ohio, 1972, Supplement 1973.

[3] Parkinson, F. L. and Spurr, W. F., "Mechanical and Metallurgical Characteristics of Titanium Alloy 6A1-4V," Report No. FAA-SS-72-13, The Boeing Co., July 1977.

[4] Parkinson, F. L., "Beta Processed Titanium Alloy 6A1-4V Plate," Report No. FAA-SS-72-10, The Boeing Co., July 1972.

[5] Chesnutt, J. C., Rhodes, C. G., and Williams, J. C. in *Fractagraphy—Microscopic Cracking Processes, ASTM STP 600,* C. D. Beachem and W. R. Warke, Eds., American Society for Testing and Materials, 1976, p. 99.

[6] "Properties of Ti-6A1-4V," Titanium Engineering Bulletin No. 1, Titanium Metals Corporation of America, Feb. 1965.

[7] "Facts About RMI 6A1-4V," Reactive Metals, Inc., 1967.

[8] Ferguson, R., B-1 Division, Rockwell International, Private Communication.

[9] "Properties of Ti-6A1-6V-2Sn," Titanium Engineering Bulletin No. 10, Titanium Metals Corporation of America, Sept. 1976.

[10] Hall, J. A. and Pierce, C. M., "Improved Properties of Ti-6A1-6V-2Sn Through Microstructure Modification," AFML-TR-70-312, Air Force Materials Laboratory, Dayton, Ohio, Feb. 1971.

[11] Coyne, J. E., Heitman, G. H., McClain, J., and Sparks, R. B., *Metals Engineering Quarterly*, Aug. 1968, p. 10.
[12] Heitman, G. H., Coyne, J. E., and Galipeau, R. P., *Metals Engineering Quarterly*, Aug. 1968, p. 15.
[13] Henning, H. J., "Beta Forging of Titanium Alloys," DMIC Report No. S-24, Defense Materials Information Center, Columbus, Ohio, 1 Aug. 1968.
[14] Chesnutt, J. C., Fransden, J. D., Thompson, A. W., and Williams, J. C., "Influence of Metallurgical Factors on the Fatigue Crack Growth Rate in Alpha-Beta Titanium Alloys," Interim Reports on Contract No. F33615-74-C-5067, Science Center, Rockwell International, 1974-1975.
[15] Curtis, R. E. and Spurr, W. F., *Transactions*, American Society for Metals, Vol. 61, 1968, p. 115.
[16] Fager, D. N. and Spurr, W. F., *Transactions*, American Society for Metals, Vol. 61, 1968, p. 283.
[17] Dawson, D. B., "Comparison of 9Ni-4Co-0.20C Steel and Titanium Alloy Properties for Weight-Critical Structural Applications," SAND 75-8301, Sandia Laboratories, Livermore, Calif., Jan. 1976.
[18] Rack, H. J. and Newman, R. W., *Physical Metallurgy*, R. W. Cahn, Ed., North Holland Press, Amsterdam, 1970, Chapter 12.
[19] Rack, H. J. and Kalish, D., *Metallurgical Transactions*, Vol. 5, 1974, p. 685-694.
[20] Rack, H. J., Kalish, D., and Fike, K. D., *Material Science Engineering*, Vol. 6, 1970, pp. 181-198.
[21] Zarkades, A. and Larson, F. R. in *Titanium Science and Technology*, R. I. Jaffee and H. M. Burte, Eds., Plenum Press, New York, 1973, Vol. 2, pp. 1321-1339.
[22] Rhodes, C. G. and Williams, J. C., *Metallurgical Transactions*, Vol. 6A, 1975, pp. 1670-71.
[23] Majdic, M., Welsch, G., and Ziegler, G., *Proceedings*, Third International Conference on Titanium, Moscow, May 1976, in press.
[24] Lewis, R. E. and Corssley, F. A., "Correlation of Microstructure with Fracture Toughness Properties in Metals," Report LMSC-D454884, National Technical Information Center, Jan. 1975.
[25] Froes, F. H., Berryman, R. G., Williams, J. C., Chesnutt, J. C., Malone, R. F., and Highberger, W. T., "Development of a New Moderate Strength, High Fracture Toughness Titanium Alloy: Ti-4.5Al-5Mo-1.5Cr (Corona 5)," presented at the American Institute of Mining, Metallurgical, and Petroleum Engineers' Spring Meeting, Las Vegas, Feb. 1976.

H. J. Rack [1]

Fracture Toughness Behavior of Unaged Beta-III Titanium

REFERENCE: Rack, H. J., **"Fracture Toughness Behavior of Unaged Beta-III Titanium,"** *Toughness and Fracture Behavior of Titanium, ASTM STP 651,* American Society for Testing and Materials, 1978, pp. 43–63.

ABSTRACT: The dynamic fracture toughness behavior of unaged Beta-III (Ti-10.2 Mo-6Zr-4.5Mo) titanium has been investigated. Both solution treatment practice and subsequent test temperature have been found to affect the fracture toughness. Decreasing the solution treatment temperature from 1255 to 1005 K generally led to a decrease in the fracture toughness over the entire range of test temperatures investigated. In addition, decreasing the test temperature from 473 to 77 K also resulted in lower fracture toughness. These reductions in fracture toughness have been shown to be related to the introduction of increasing amounts of a localized shear fracture mode with both decreasing solution and test temperature. Based on these observations, a model has been proposed which describes the stress/strain conditions at the tip of a propagating crack that appear to enhance shear fracture. Finally, it has been suggested that the principal metallurgical variable controlling the choice of fracture mode transition from either dimple to cleavage or dimple to shear dimple in unaged metastable β titanium alloys is the primary deformation mechanism. Twinning tends to promote shear instability while slip may be associated with low temperature cleavage crack propagation.

KEY WORDS: titanium, fracture (materials), mechanical properties, crack propagation, impact, low temperature tests, titanium alloys

Previous examinations [*1-4*] [2] of the tensile and fracture toughness behavior of unaged, metastable β titanium alloys have shown that they, in concert with other body-centered-cubic (bcc) metals, undergo a macroscopic ductile-brittle transition with decreasing temperature. Microscopically, this transition has been associated with a change in fracture mode from dimple rupture to cleavage crack propagation. Recently, the present

[1] Member of technical staff, Sandia Laboratories, Albuquerque, N. Mex. 87115.

[2] The italic numbers in brackets refer to the list of references appended to this paper.

Copyright© 1978 by ASTM International www.astm.org

author [5] has observed a similar decrease in tensile ductility with decreasing test temperature in another metastable β titanium alloy, namely, Beta-III (Ti-11.5Mo-6Zr-4.5Sn). This alloy, when compared with previous systems investigated, is unusual in that its primary deformation process involves multiple-order twinning [6-9] rather than slip [10]. Furthermore, the tensile ductility decrease was found to be due to the introduction of a low energy "shear" fracture mode rather than to cleavage crack propagation. Some question remains however as to the relevency of these observations to the low temperature fracture toughness behavior of Beta-III. The investigation reported herein was intended to examine this concern by considering the influence of test temperature on crack propagation in this alloy system.

Experimental Procedures

The chemical composition of the 1.9-cm plate used in this study was 10.2Mo, 5.8Zr, 4.7Sn, 0.03Fe, 0.014N, 0.02C, 0.13O, and balance titanium. It was received in the hot rolled and solution treated condition, the latter having been performed below the α-β transus.[3] The influence of the solution treatment condition was examined by resolution treating full thickness sections of the as-received plate for 1 h at 1005, 1060, 1144, or 1255 K, followed by water quenching.

Fracture toughness measurements were performed utilizing specimens prepared after completion of all heat treatments. The toughness tests were carried out over a temperature range of 77 to 473 K and made use of full-size fatigue precracked Charpy V-notch specimens taken from the L-S grain orientation [11]. Fatigue precracking was accomplished using the method described by Krafft [12] where K_f, the final stress intensity factor, was always less than 15 $MNm^{-3/2}$. Except as noted, all toughness tests were performed on an instrumented 325-N/m capacity impact machine with an initial impact velocity of 3.3 m/s [13,14]. In those instances where fracture occurred following general yield, that is, at elevated temperatures, the dynamic fracture toughness, K_d, was determined utilizing the "equivalent energy" criteria [15,16].[4]

Following failure, selected fracture surfaces were examined on a scanning electron microscope operated at 25 kV. Additional specimens were also mounted and polished for optical examination, the subsequent examination plane lying normal to the original fracture surface. These were etched with either 1.5-ml hydrofluoric acid (HF), 3.5-ml nitric acid (HNO_3), and 95-ml water (H_2O) or 30-ml glycerine, 20-ml HNO_3, and 20-ml HF; the choice of etchant depending upon the solution treatment being considered.

[3] The α–β transus for this alloy was approximately 1028 K [6].

[4] It should be noted that there is as yet no standardized test for dynamic fracture toughness and therefore the measurements reported herein form only a comparative index of the toughness for the conditions investigated.

Experimental Results

Microstructures

Figure 1 illustrates the microstructural conditions that were produced by the solution treatments considered in the present investigation. Solution treatment at 1005 K, below the α-β transus, yielded a three-phase ($\alpha+\beta+\omega$) alloy [*17*], the α phase being situated either on prior β grain boundaries or within the ($\beta+\omega$) matrix, Fig. 1(*a*).[5] The α phase distribution however appeared to be nonuniform when viewed over a number of grains, some alignment or banding having occurred relative to the prior rolling direction. This banding phenomena has previously [*19*] been shown to be a common occurrence in Beta-III and has been associated with microsegregation of certain alloying elements contained within this alloy, that is, molybdenum and tin.

Solution treating above the transus, at 1060, 1144, or 1255 K, resulted in a ($\beta+\omega$) microstructure, Fig. 1(*b*) through (*d*). The microsegregation observed after solution treatment at 1005 K was also evidenced after the 1060 and 1144 K treatment. In this instance its principal manifestation was the highly elongated and generally nonuniform β grain structure observed after these treatments. The degree of nonuniformity did however decrease with increasing solution temperature, until at the highest temperature considered, namely, 1255 K, the β grain structure was essentially equiaxed with only isolated instances of nonuniformity being noted.[6]

Fracture Toughness

The results of the fracture toughness measurements are summarized in Fig. 2. In all instances, decreasing the exposure temperature decreased the fracture toughness of unaged Beta-III, albeit the specifics of this reduction depended upon the solution treatment procedure being considered. The subtransus treatment, at 1005 K, exhibited an essentially linear relationship between fracture toughness and test temperature. In addition, this solution treatment condition resulted, at any given test temperature, in the minimum observed fracture toughness.

The fracture toughness of specimens solution treated above the transus, tended to be superior to those treated below the transus. Furthermore,

[5] ω is an hcp transitional structure which is not resolvable by optical microscopy and develops during either cooling from the elevated temperature solution treatment or as a consequence of low temperature aging [*18*].

[6] Although the microstructures produced by solution treatment at 1005, 1060, and 1144 K are not uniform, this does not appear to influence either the fracture toughness or tensile properties of unaged Beta-III titanium (see present results and Ref *5*).

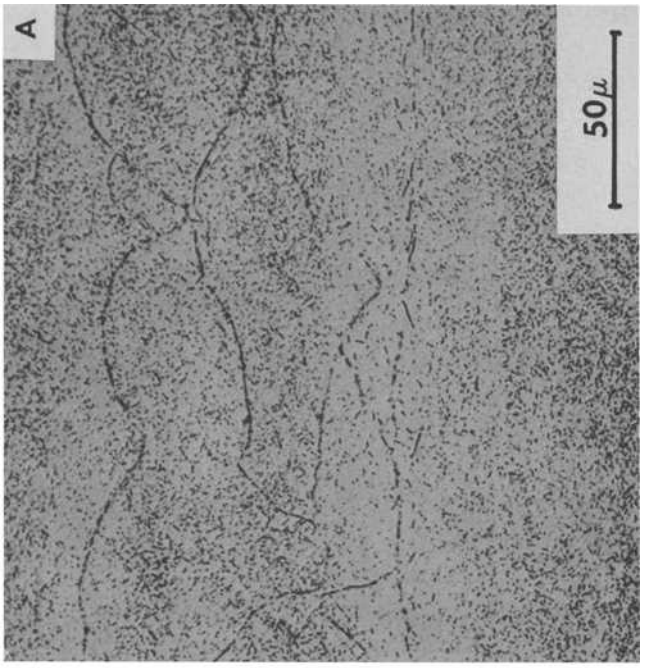
A
50μ

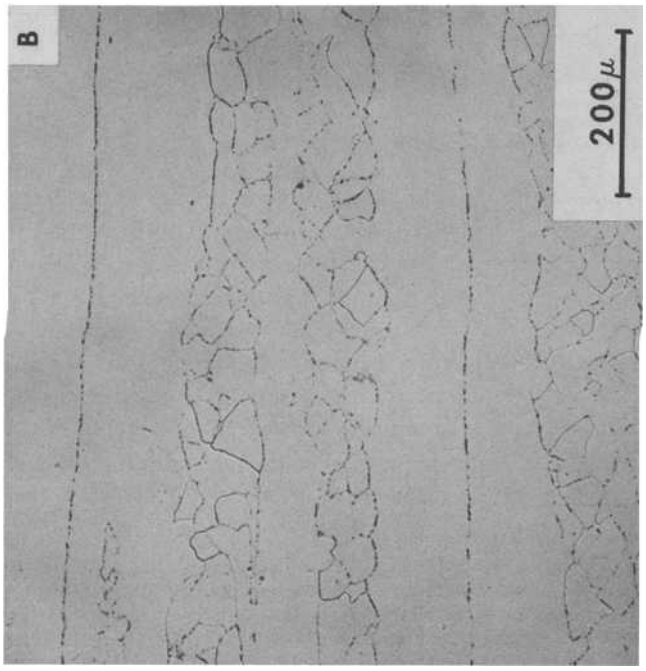
B
200μ

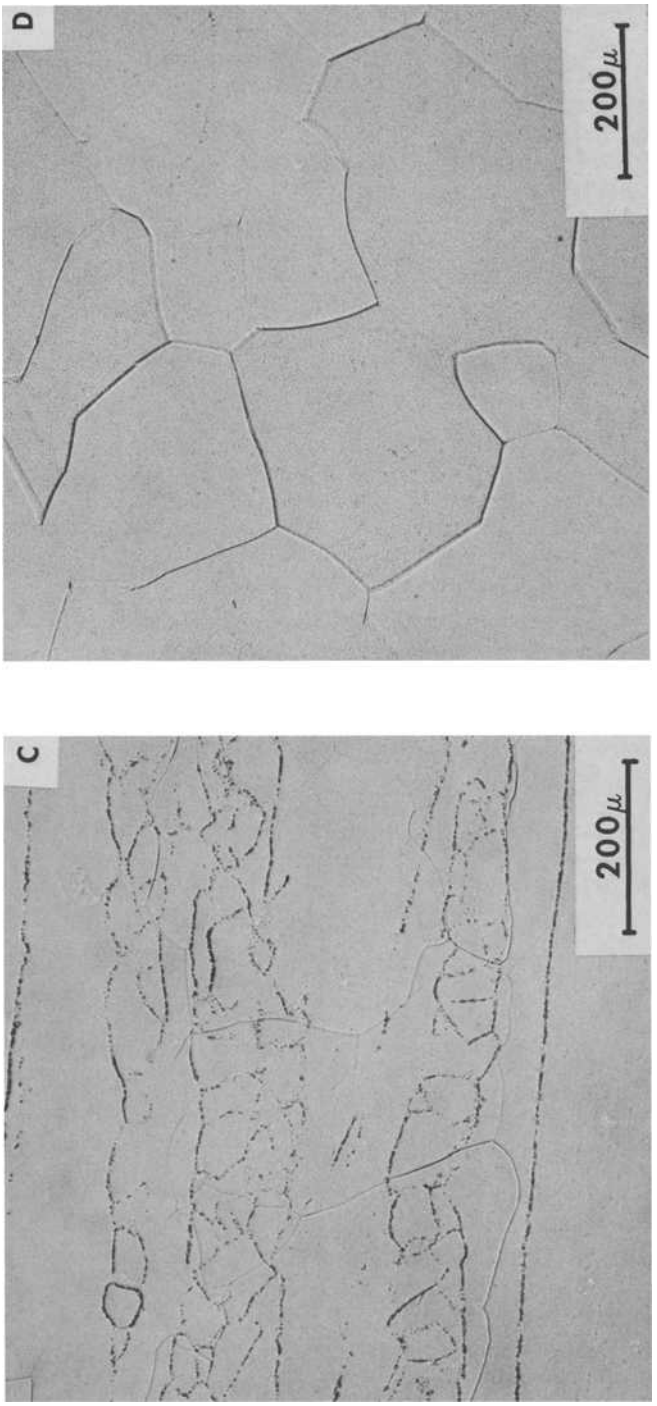

FIG. 1—*Typical optical micrographs of Beta-III titanium solution treated at* (a) *1005*, (b) *1060*, (c) *1144*, *and* (d) *1255 K for 1 h and water quenched.*

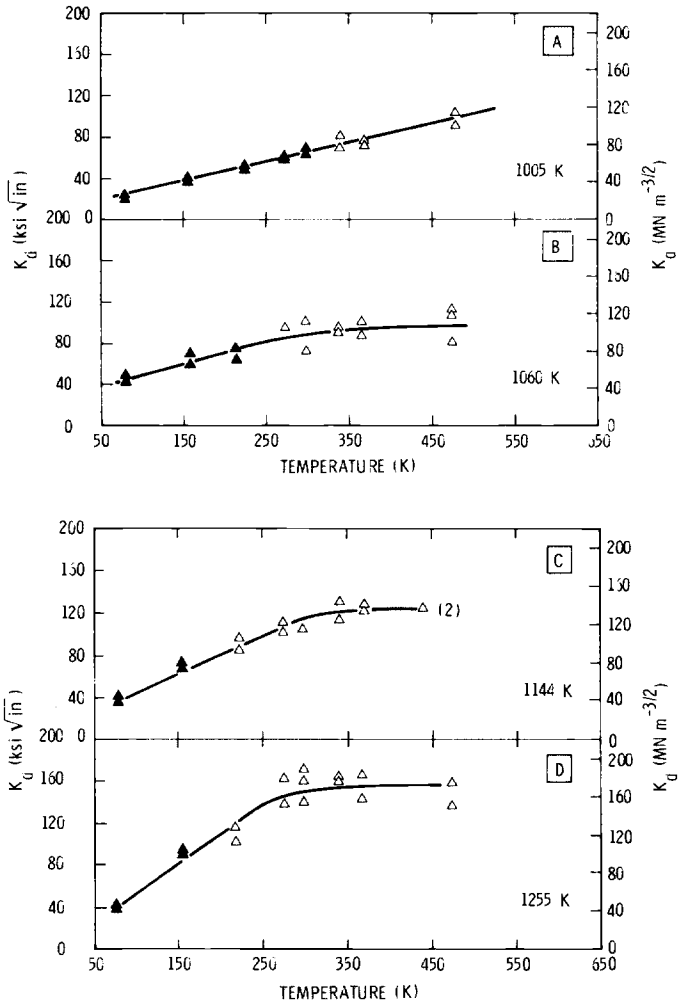

FIG. 2—*Dynamic fracture toughness-temperature behavior of Beta-III solution treated at* (a) *1005,* (b) *1060,* (c) *1144, and* (d) *1255 K. Open symbols represent toughness determined using equivalent energy criteria.*

Fig. 2 gives some indication that increasing the β solution temperature resulted in a further increase in elevated test temperature toughness above that associated with specimens treated at 1060 K. Ultimately, however, the toughness of β solution treated specimens also decreased with decreasing test temperature. The manner in which this decrease occurred was quite similar to that of specimens solution treated below the α-β transus; there was a linear decrease in toughness with decreasing temperature. However,

the temperature at which the initial decrease was observed decreased and the rate of decrease increased with increasing prior β solution temperature. This latter rate dependence eventually resulted in the fracture toughness at 77 K, the lowest temperature examined in the present investigation, being independent of the β solution temperature, that is, $K_d \cong 44$ MNm$^{-3/2}$.

Fractography

Scanning electron microscope observations of specimens tested between 77 and 473 K indicated that the aforementioned decrease in fracture toughness with decreasing test temperature was not due to the occurrence of a classical ductile-brittle, dimple-cleavage transition but rather was due to the introduction of increasing amounts of "shear" failure with decreasing temperature. Figures 3 through 7 are illustrative micrographs prepared from specimens solution treated either below or above the α-β transus and tested at the indicated temperatures. Crack propagation in the former involved substantial amounts of localized shear dimple failure over the entire temperature range investigated, Fig. 3. The regions of shear fracture were localized in the sense that they were separated by ridges which seemed to have failed in a more classical manner, namely, involving dimple formation, Fig. 4. Quite interestingly the distance between these ridges also tended to decrease with decreasing test temperature, compare Fig. 3(*a*) and (*c*).

Similar indications of localized shear failure and dimple ridge formation were observed in specimens solution treated above the α-β transus, Figs. 5 through 7. Increasing the beta solution treatment tended to decrease the test temperature at which this shear failure mode first became a major fracture mechanism. Indeed for specimens solution treated at 1255 K and tested in the temperature regime where the fracture toughness had previously been found to be essentially independent of temperature, no localized shear failure was observed, only transgranular ductile, dimple formation, see for example Fig. 7(*a*).

Deformation Mechanisms

Microscopic examinations of both failed fracture toughness specimens and ones that had been tested to a point just beyond maximum load (discussed next) confirmed the previously reported observations [*5-9*] that the primary deformation mode in unaged Beta-III, when deformed within the temperature range presently considered, is twinning, Fig. 8. Furthermore, deformation twinning was not confined to regions immediately adjacent to the fracture surface, twinning was found to have occurred far in advance of the initial crack propagation, Fig. 9. The latter indicates that twin formation occurred prior to rather than as a consequence of crack propagation.

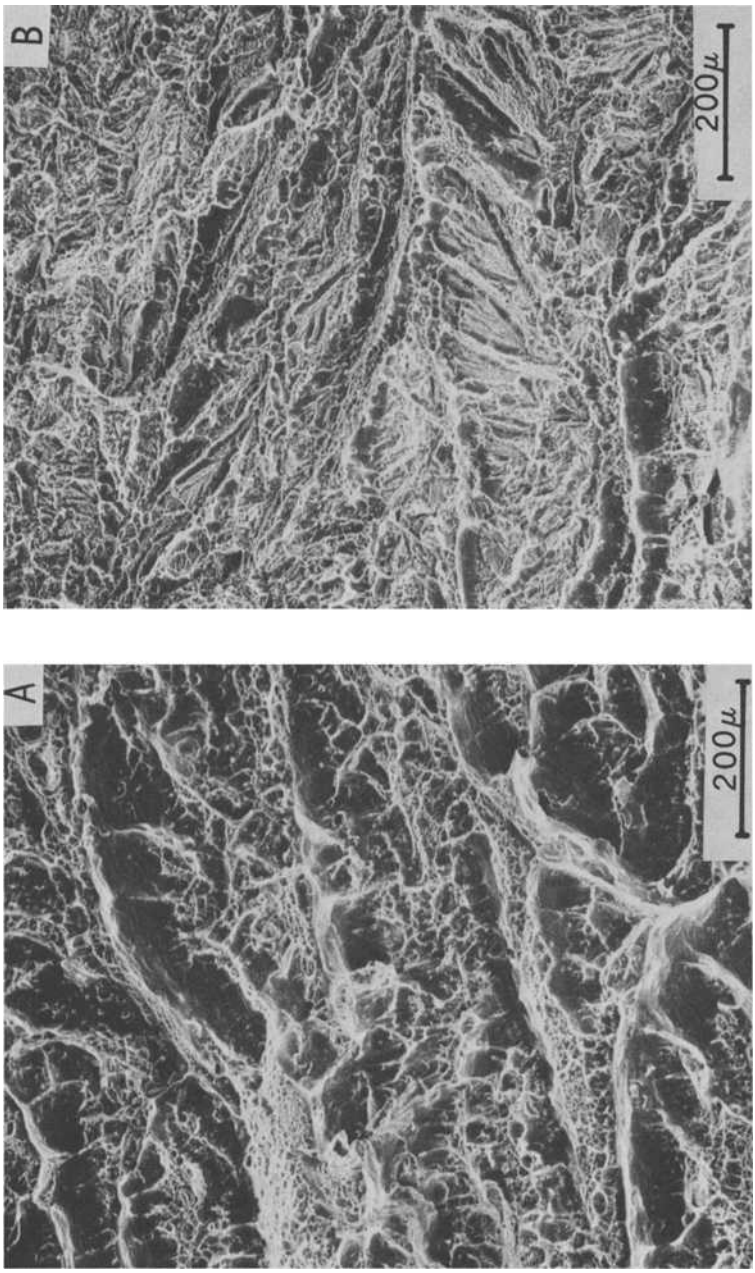

FIG. 3—*Scanning electron fractographs of Beta-III solution treated at 1005 K and tested at* (a) *333,* (b) *223 and* (c) *77 K.*

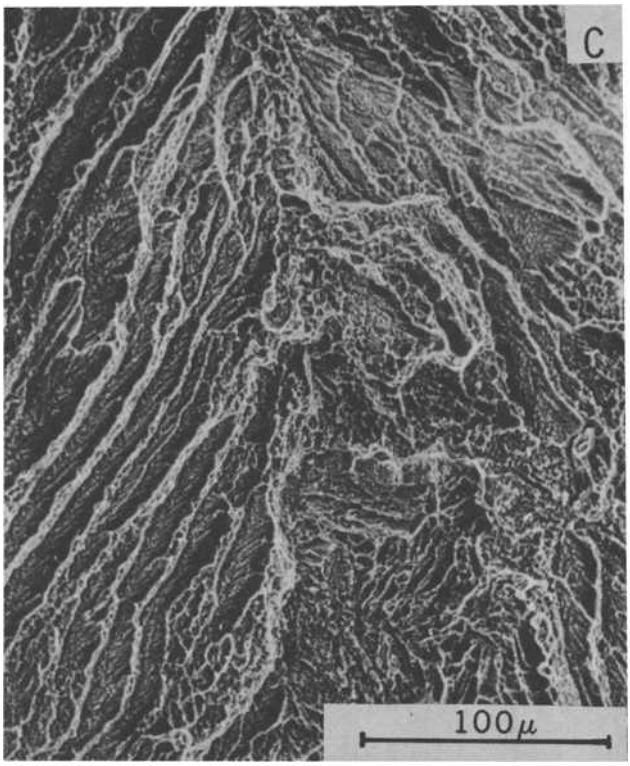

FIG. 3—*Continued.*

Discussion

The previous section has shown that the fracture toughness behavior of unaged Beta-III titanium is a function of both solution treatment temperature and subsequent test temperature. Minimum fracture toughness was associated with specimens that were solution treated below the α-β transus and tested at low temperatures, for example, 77 K. Microscopic observations also indicated that the observed decrease in toughness with either decreasing solution treatment or test temperature was due to the introduction of increasing amounts of localized shear dimple failure.

Spretnak [*20*] has postulated that there are three basic requirements for the activation of such a shear instability: (*a*) a free surface, (*b*) a stress gradient, and (*c*) a material which simulates a perfectly plastic body. A number of previous investigations [*21-24*] have shown that the aforementioned conditions for plastic shear instability can be met below a notch root or at the tip of a blunt crack. Figure 10(*a*) shows the slip-line field solution for a sharp crack tip in plane strain considering only small

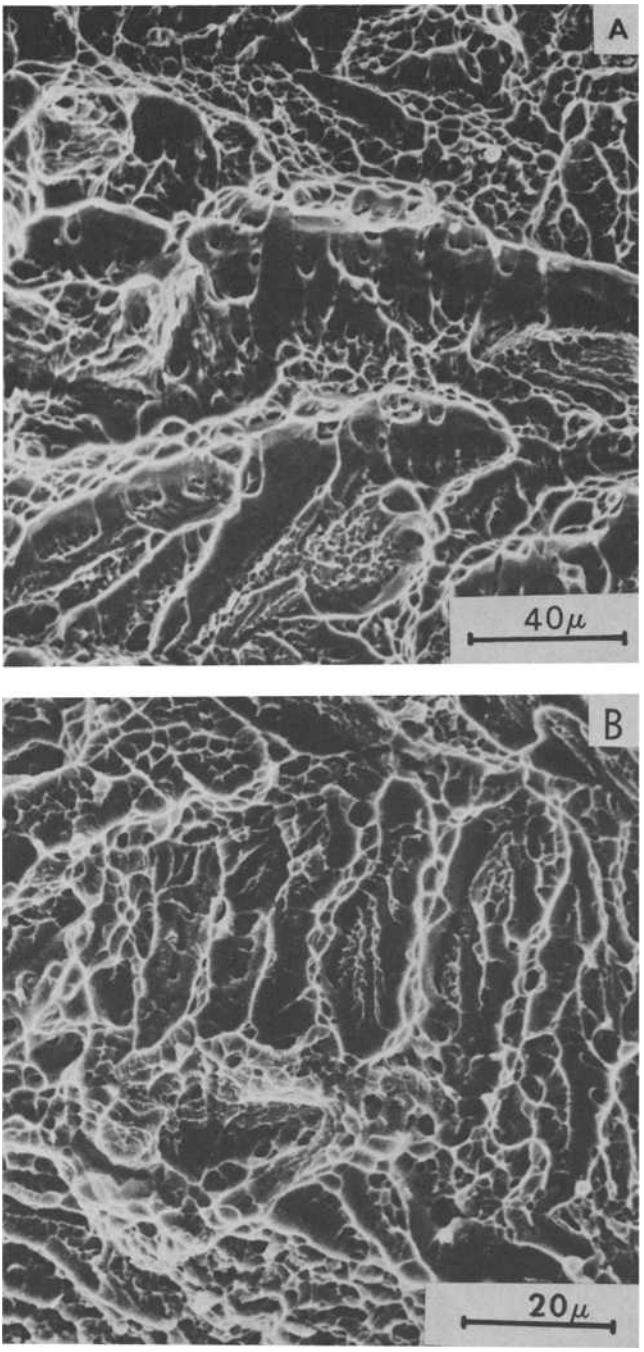

FIG. 4—*Scanning electron fractographs illustrating ductile ridge formation in Beta-III solution treated at 1005 K and tested at* (a) *223 and* (b) *77 K.*

geometry changes. Note that in Regions A and B the fans are centered and the lines, straight. This construction indicates that there will be no strain concentration immediately ahead of the crack tip, but intense shear concentrations will be formed both above and below the crack tip (Region C). Rice and Johnson [*25*] have shown however that continuity of displacement at the crack tip requires progressive crack blunting, Fig. 10(*b*). In this case, the fan region at the crack tip becomes noncentered, and intense strains are focused into a Region D directly ahead of the blunted crack tip. Knott and his coworkers [*23,24*] have shown that void initiation at inclussions in mild steel will indeed occur in this region when the logarithmic spirals, which are a pictorial description of the highly localized deformation slip-lines occurring ahead of the crack tip, first envelope an inclusion. However, inclusions need not be required *per se;* any material discontinuity may serve as an initiation site. Indeed, twin-twin, twin-grain boundary, and possibly twin-α particle interfaces have all been found to be crack initiation sites in unaged Beta-III titanium [*5*]. These observations suggest that the dimple ridges observed in Beta-III may be formed as a consequence of repeated void initiation taking place ahead of the crack tip. It may also be possible that the observed decrease in the ridge spacing with decreasing test temperature is due to an increase in the probability that the stress concentrations, which arise at twin-twin, twin-grain boundary, and twin-α particle interfaces, are relieved, as the test temperature is reduced, by cracking rather than by secondary deformation processes. Again the previous examination of the tensile behavior of unaged Beta-III [*5*] tends to support this conclusion, that is, reductions in temperature minimize the degree of multiple-order twinning and secondary slip in the alloy. It is also probable that it is this variation in the ability of Beta-III to relieve highly localized internal strains by secondary deformation processes which are ultimately responsible for the decrease in fracture toughness with decreasing test temperature.

Once a void or crack has been initiated at any of the aforementioned initiation sites, deformation will be concentrated along slip-line directions which are coincident with the directions of both maximum shear stress and pure shear. Eventually a critical displacement will be reached at the blunted crack tip, and final separation will then occur along these slip-line field characteristics.

During the course of this investigation, an attempt was made to examine the validity of the proposed shear linkage model. Fatigue precracked specimens were prepared as previously described and tested in three-point bending. These specimens were stressed to just beyond maximum load, unloaded, and examined using standard metallographic procedures. Figure 11 shows an example of a section through a crack tip in unaged Beta-III titanium solution treated at 1144 K and tested in bending at 183 K. The

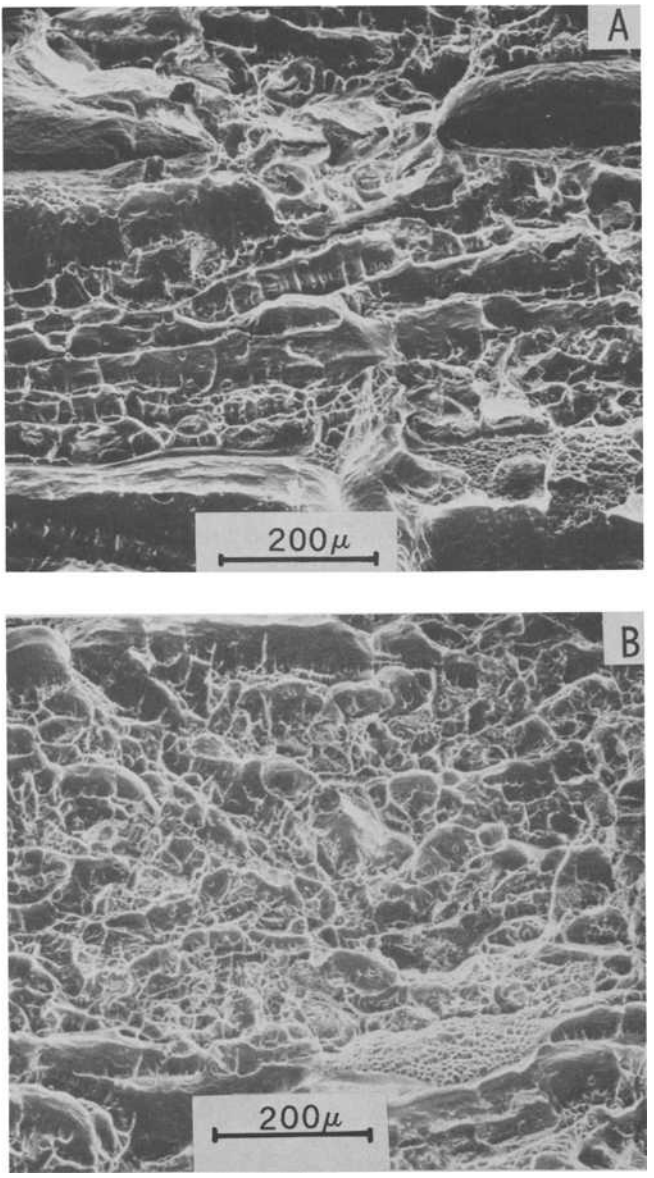

FIG. 5—*Scanning electron fractographs of Beta-III solution treated at 1060 K and tested at* (a) *298,* (b) *223, and* (c) *77 K.*

linkages between the main fatigue precrack and the two observable stable microcracks are clearly visible (see arrows). It should be noted that when similar specimens were tested in the regime where the fracture toughness is

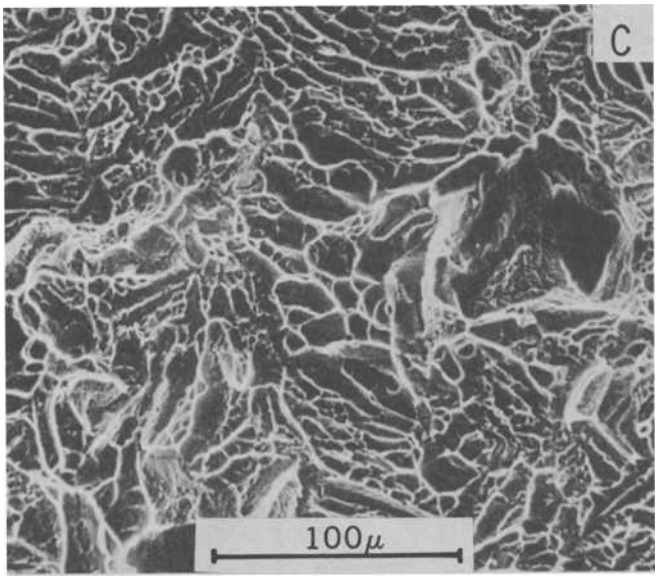

FIG. 5—*Continued.*

essentially independent of test temperature shear linkage was not observed, ductile dimple failure at the crack tip predominated.

Although the localized shear failure mode observed in the present investigation appears to be promoted in materials with low strain hardening capacity [*21-24*] the question still remains as to why this same fracture mode transition is not observed in other unaged metastable β titanium alloys, for example, RMI 38644, even though they, as well as Beta-III, have low strain hardening exponents, that is, $n \sim 0.05$. This apparent discrepancy is not unique to unaged metastable β titanium alloys, previous investigators having reported similar results in mild steel [*26*] and tantalum [*27*]. The behavior of metastable β titanium alloys may be rationalized if the metallurgical variables that affect the associated plastic shear instability are considered. Rosenfield and Owen [*27*] have presented an expression for this instability

$$k_y d^{-1/2} > K n^n - \sigma_i \tag{1}$$

where

$2d$ = the average grain diameter,
n = strain hardening exponent,
K = a material constant,
σ_i = friction stress, and
k_y = pinning parameter.

The latter constants are derived by considering the influence of grain size

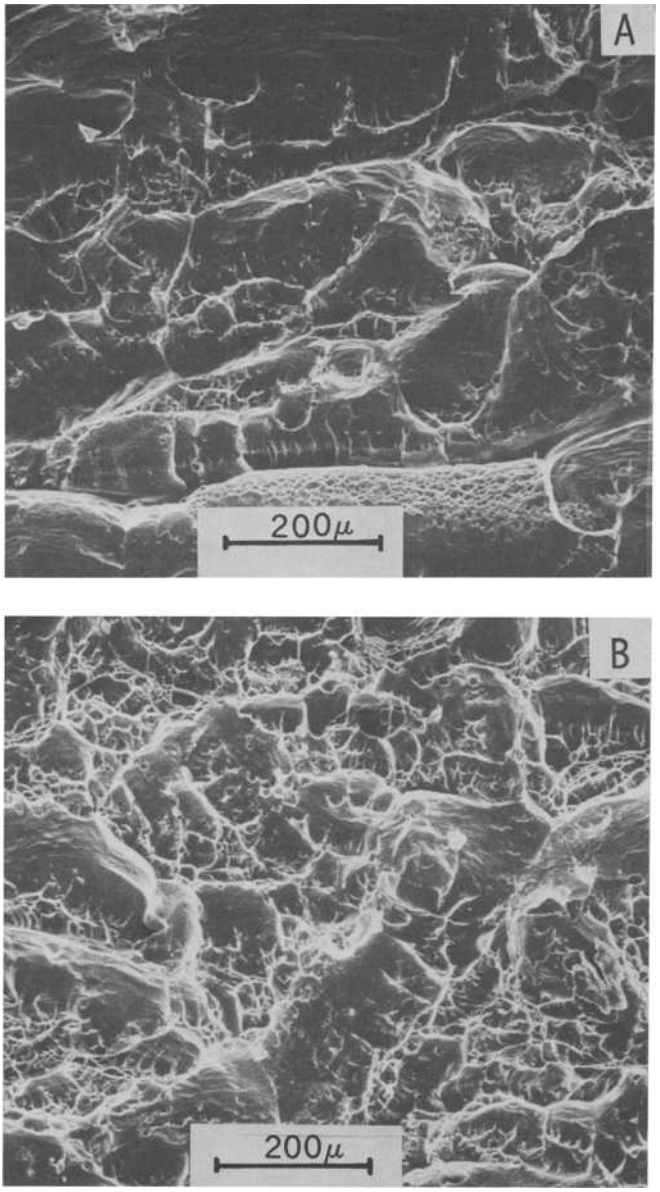

FIG. 6—*Scanning electron fractographs of Beta-III solution treated at 1144 K and tested at* (a) *298,* (b) *223, and* (c) *77 K.*

on the yield strength [*28*], while K and n are determined by assuming that the work hardening, stress (σ)-strain (ϵ), behavior of the material under investigation can be approximated by the relationship, $\sigma = K\epsilon^n$. Equation 1

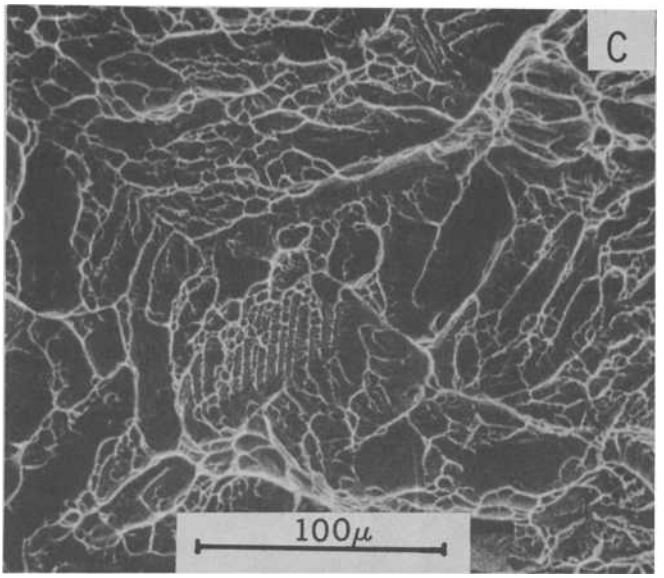

FIG. 6—*Continued.*

indicates that plastic shear instability may be promoted by (*a*) decreasing the strain hardening exponent, (*b*) decreasing the grain size, (*c*) increasing the friction stress, and (*d*) increasing the dependence of yield strength on grain size, k_y.

Since, as noted previously, the strain hardening exponents of unaged metastable β alloys are all generally low, this factor cannot be the predominant one controlling the fracture transition behavior of these alloys. Although decreased grain size does appear to be a contributing factor, at least in extending the temperature range over which shear fracture is observed, it also cannot be the primary factor, since Beta-III, solution treated at 1255 K, has a comparable grain size to that reported for RMI 38644, an alloy known to undergo a ductile, dimple to brittle, cleavage transition [*3*], and yet the former still undergoes a ductile, dimple to shear, dimple fracture transition.

This discussion suggests that the primary factors which control the appearance of the plastic shear instability in unaged metastable β titanium alloys are k_y and σ_i, that is, those parameters derived from measurements of the effect of grain size on yield strength. Unfortunately a direct measure of their effect is presently limited by a lack of experimental evidence and is complicated further by the differing deformation modes that have been observed in these titanium alloys. Indeed, it appears that it may again be this latter variation which ultimately controls the selection of the type of fracture mode transition observed. Some support for this proposal is given

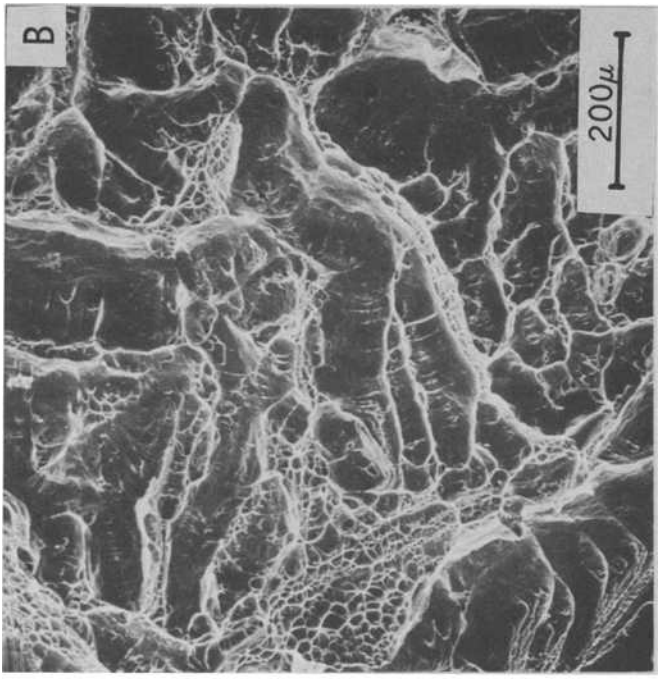
B
200μ

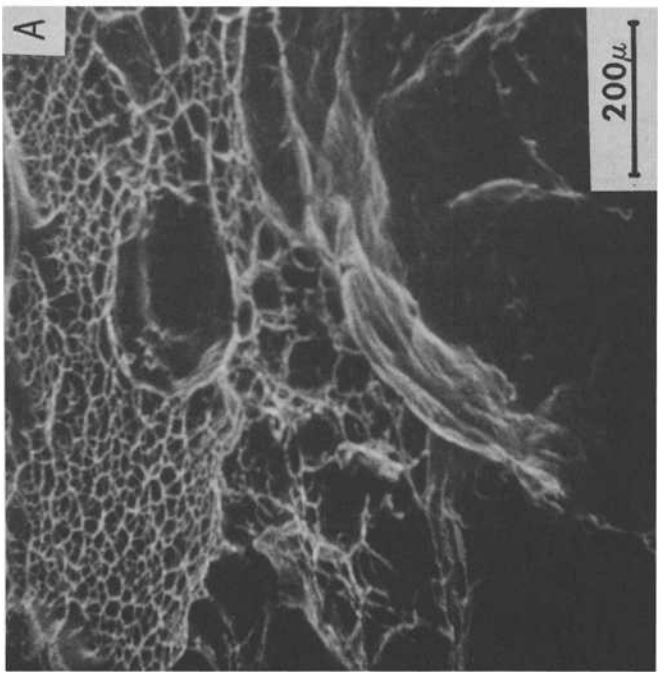
A
200μ

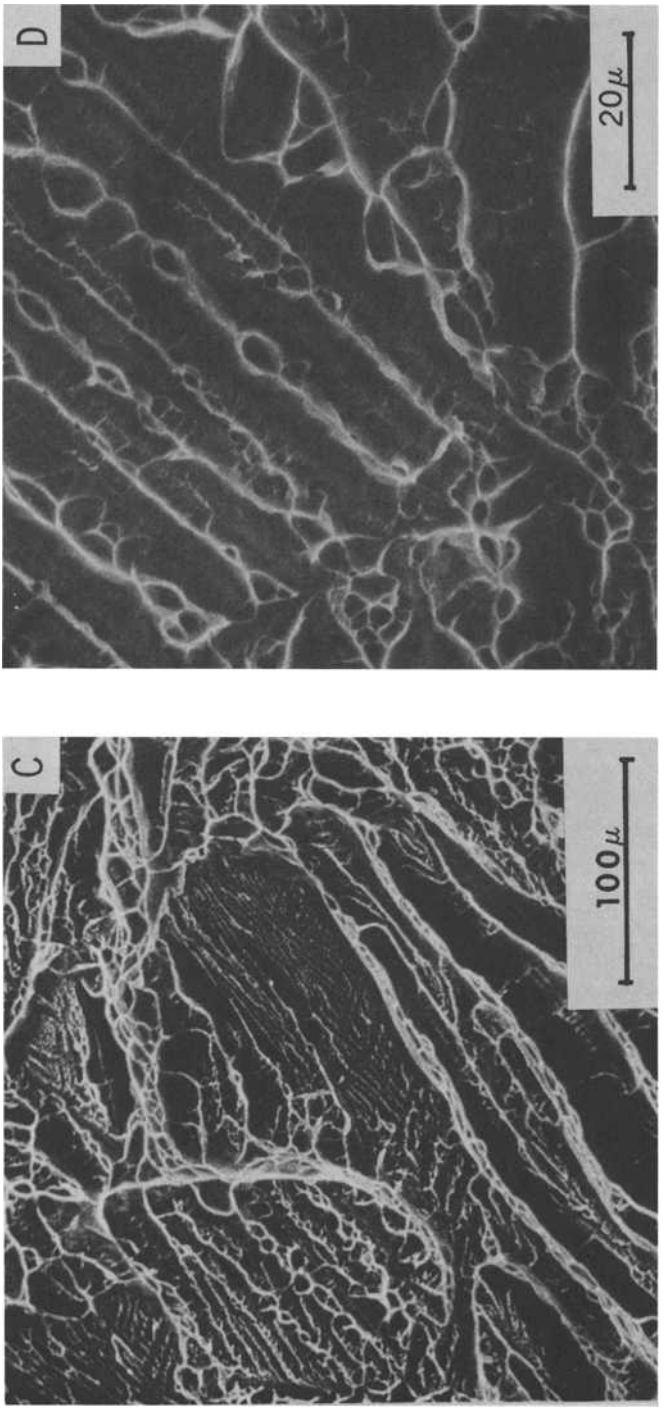

FIG. 7—*Scanning electron fractographs of Beta-III solution treated at 1255 K and tested at* (a) *298,* (b) *223 and* (c), (d) *77 K.*

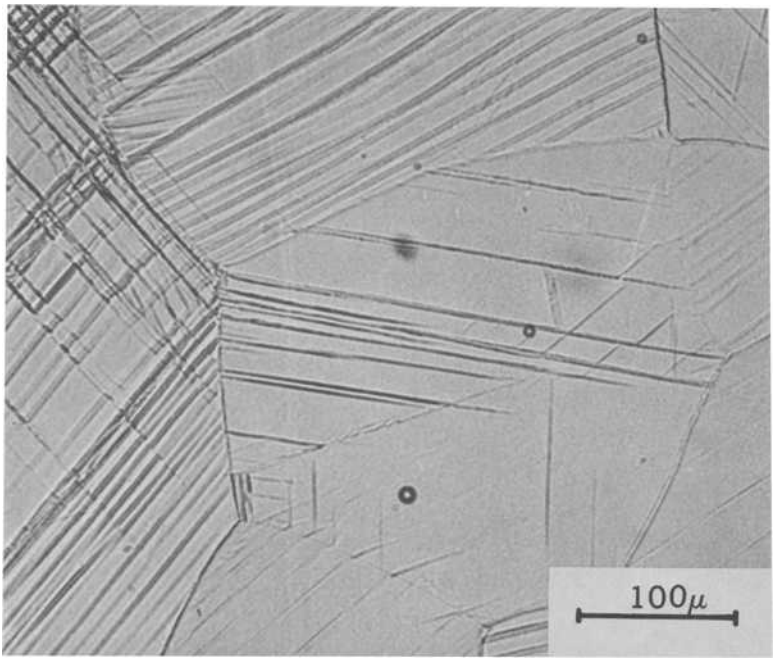

FIG. 8—*Optical micrograph of deformation twinning in Beta-III solution treated at 1255 K and tested at 223 K.*

by an investigation of the effect of varying deformation mechanism on the grain size-yield strength relationship in chromium [*29*]. These authors have shown that although σ_i^{twin} is somewhat smaller than σ_i^{slip}, k_y^{twin} is much larger and more temperature sensitive than k_y^{slip}. This observation, if translatable to the alloy systems presently being considered, would tend to promote the formation of early plastic shear instabilities. More direction confirmation on the proposed role of deformation mode on the fracture transition selection criteria awaits further experimental evidence.

Conclusions

This investigation has shown that the fracture toughness behavior of unaged Beta-III (Ti-11.5Mo-6Zr-4.5Sn) titanium is sensitive to both the solution treatment practice and the subsequent test temperature. A decrease in either the solution treatment temperature or the test temperature will result in a decrease in the dynamic fracture toughness of Beta-III titanium. The decrease has been shown to be due to the introduction of a localized shear, dimple fracture mode at the expense of more ductile, dimple failure. It has been proposed that the introduction of the low energy fracture mode

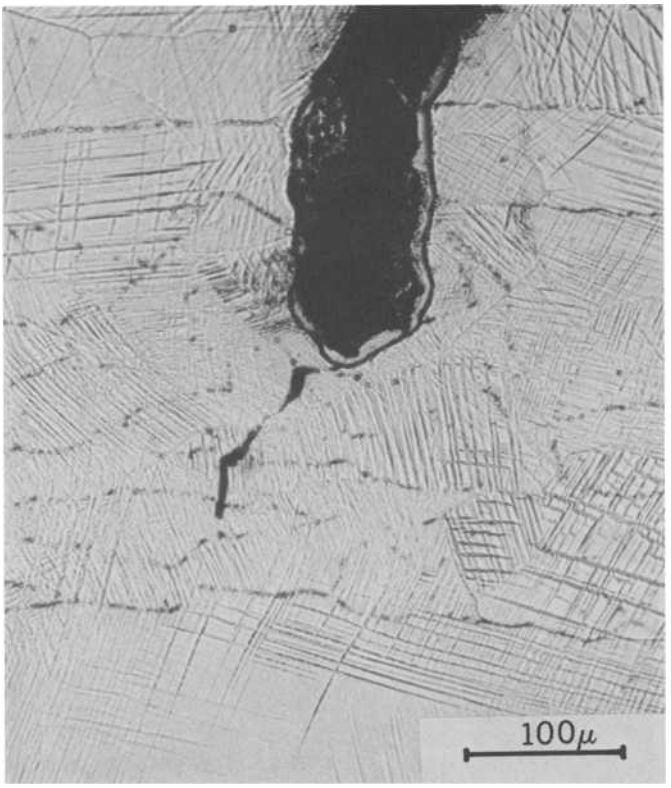

FIG. 9—*Optical micrograph of slow bend specimen of Beta-III solution treated at 1144 K and tested to just beyond maximum load at 183 K.*

is due to severe strain localization at the tip of a propagating crack, the latter being enhanced at low temperatures by the inability of this alloy to relieve locally high stress concentrations.

Finally, it appears that the primary deformation mode plays an important role in controlling the fracture mode transition behavior of unaged

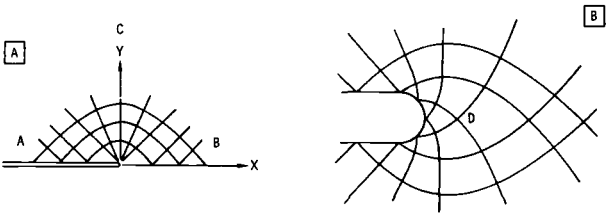

FIG. 10—*Slip line field for* (a) *sharp crack and* (b) *blunted crack tip in plane strain* [25].

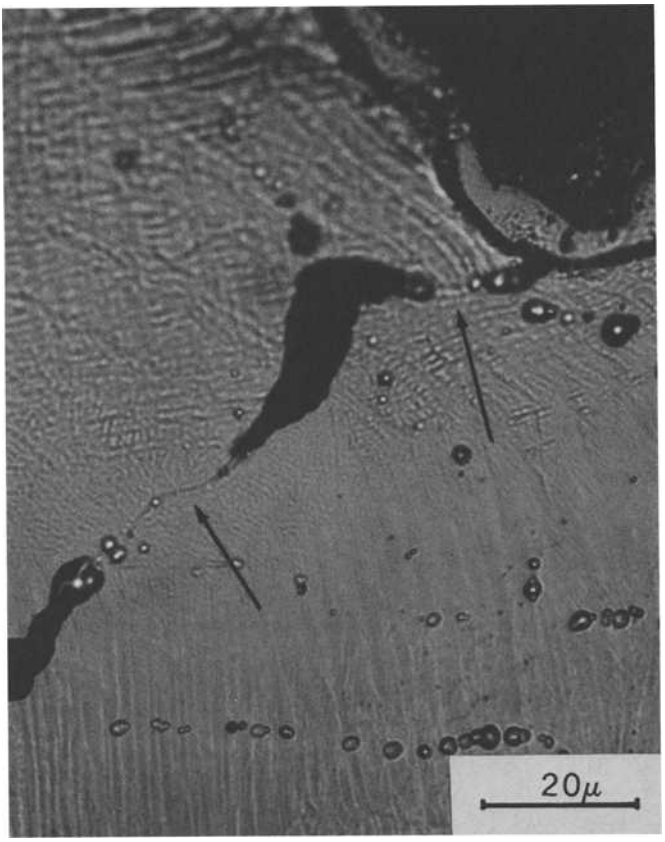

FIG. 11—*Optical micrograph showing cross-section through crack tip in Beta-III solution treated at 1444 K and tested in three-point bending at 183 K.*

metastable β titanium alloys. Twinning seems to promote shear instabilities while slip is associated with cleavage crack propagation at low temperatures.

Acknowledgments

The author wishes to acknowledge the assistance of J. Smith and S. Duliere during the various phases of this investigation.

This work was supported by the U.S. Energy Research and Development Administration.

References

[*1*] Gorynin, I. V., Ushkov, S. S., and Belova, O. S. in *Titanium Science and Technology*, R. I. Jaffee and H. M. Burte, Eds., Plenum Press, New York, 1973, Vol. 2, pp. 1109-1118.

[2] Bogatchev, I. N. and Dyakova, M. A. in *Titanium Science and Technology*, R. I. Jaffee and H. M. Burte, Eds., Plenum Press, New York, 1973, Vol. 2, pp. 1119-1130.
[3] Rack, H. J., *Journal of Engineering Materials and Technology*, Vol. 97, 1975, pp. 330-337.
[4] Rack, H. J., *Proceedings*, 2nd International Conference on Mechanical Behavior of Metals, American Society for Metals, 1976, pp. 1196-1200.
[5] Rack, H. J., *Proceedings*, 4th Internnational Conference on Fracture, D. M. R. Taplin, Ed., University of Waterloo Press, Waterloo, Canada, 1977, Vol. 2, pp. 203-214.
[6] Rack, H. J., Kalish, D. and Fike, K. D., *Materials Science and Engineering*, Vol. 6, 1970, pp. 181-198.
[7] Blackburn, M. J. and Feeney, J. A., *Journal of the Institute for Metals*, Vol. 99, 1971, pp. 132-134.
[8] Roberson, J. A., Fujishiro, S., Arunachalan, V. S., and Sargent, C. M., *Metallurgical Transactions*, Vol. 5, 1974, pp. 2317-2322.
[9] Feeney, J. A. and Blackburn, M. J., *Metallurgical Transactions*, Vol. 1, 1970, pp. 3309-3323.
[10] Rack, H. J., *Scripta Metallurgica*, Vol. 10, 1976, pp. 739-740.
[11] Goode, R. J., *Materials Research and Standards*, Vol. 12, No. 9, 1972, pp. 31-32.
[12] Krafft, J. M. and Gray, R. A. in *Practical Applications of Fracture Mechanics to Pressure Vessel Technology*, Institution of Mechanical Engineers, London, 1971, pp. 93-102.
[13] Wullaert, R. A. in *Impact Testing of Metals, ASTM STP 466*, American Society for Testing and Materials, 1970, pp. 148-164.
[14] Rack, H. J., *Journal of Testing and Evaluation*, Vol. 4, 1976, pp. 176-180.
[15] Witt, F. J., "Equivalent Energy Procedures for Predicting Gross Plastic Fracture," USAEC Technical Report ORNL-TM-3172, Oak Ridge National Laboratory, Oak Ridge, Tenn., 1972.
[16] Rack, H. J., *Metallurgical Transactions*, Vol. 6A, 1975, pp. 947-949.
[17] Froes, F. H., Malone, R. F., Fujishiro, S., Gersendorfer, R. F., and Hall, J. A., "Effect of Omega Phase on Selected Properties of Beta-III Titanium," Technical Report AFML-TR-75-30, Air Force Materials Laboratory, Dayton, Ohio, 1975.
[18] Williams, J. C. in *Titanium Science and Technology*, R. I. Jaffee and H. M. Burte, Eds., Plenum Press, New York, 1973, pp. 1433-1494.
[19] Rack, H. J., "An Investigation of Chemical Segregation in Beta Titanium Alloys," Report ER-10224, Lockheed-Georgia, Marietta, Ga., July 1969.
[20] Spretnak, J. W., "A Basis for Design on Allowable Plastic Strain," EUR-4820, Vol. 6, Part L, 20-24 Sept. 1971, pp. 615-635.
[21] Griffis, C. A. and Spretnak, J. W., *Transactions*, Iron and Steel Institute of Japan, Vol. 9, 1969, pp. 372-380.
[22] Griffis, C. A. and Spretnak, J. W., *Metallurgical Transactions*, Vol. 1, 1970, pp. 550-551.
[23] Green, G. and Knott, J. F., *Journal of Engineering Materials and Technology*, Vol. 98, 1976, pp. 37-46.
[24] Knott, J. F. in *The Mechanics and Physics of Fracture*, Metals Society/Institute of Physics, 1975, pp. 86-94.
[25] Rice, J. R. and Johnson, M. A. in *Inelastic Behavior of Solids*, M. F. Kanninen, W. F. Adler, A. R. Rosenfield, and R. I. Jaffee, Eds., McGraw-Hill, New York, 1970, pp. 641-670.
[26] Holzman, M., *Journal of the Iron and Steel Institute*, Vol. 204, 1966, pp. 739-741.
[27] Rosenfield, A. R. and Owen, W. S., *Journal of the Institute for Metals*, Vol. 91, 1962-63, pp. 117-119.
[28] Armstrong, R. W., *Metallurgical Transactions*, Vol. 1, 1970, pp. 1169-1176.
[29] Marcinkowski, M. J. and Lipsitt, H. A., *Acta Metallurgica*, Vol. 10, 1962, pp. 95-111.

J. C. Williams,[1] *F. H. Froes,*[2] *J. C. Chesnutt,*[3] *C. G. Rhodes,*[3] *and R. G. Berryman* [4]

Development of High Fracture Toughness Titanium Alloys

REFERENCE: Williams, J. C., Froes, F. H., Chesnutt, J. C., Rhodes, C. G., and Berryman, R. G., **"Development of High Fracture Toughness Titanium Alloys,"** *Toughness and Fracture Behavior of Titanium, ASTM STP 651,* American Society for Testing and Materials, 1978, pp. 64–114.

ABSTRACT: This paper describes the relationship between composition, processing history, and microstructure of a series of $\alpha + \beta$ and metastable β titanium alloys. The relation between a wide range of microstructures and the resulting properties of these alloys has been investigated by making extensive use of electron fractography and metallographic fracture path determinations. These results were obtained in connection with an alloy development program in which two alloy compositions ultimately were selected: Ti-5Mo-4.5Al-1.5Cr and Ti-8Mo-2.5Al-4.5Cr. These alloys were processed according to various schedules in order to achieve microstructures which produce good strength-toughness combinations. In the $\alpha + \beta$ alloy (Ti-5Mo-4.5Al-1.5Cr), the optimum property combinations were achieved in β-processed material which has an acicular microstructure and α-phase at prior β-grain boundaries, although excellent properties also were obtained in equiaxed $\alpha + \beta$ processed material. In the metastable β-alloy (Ti-8Mo-2.5Al-4.5Cr), significantly better strength-toughness combinations were achieved in $\alpha + \beta$ processed material which contains globular primary α, compared to β-processed material which contains grain boundary α. The metastable β-alloy exhibits a significant degree of directionality of properties in all microstructural conditions. It is suggested that such directionality is due to the elongated β-grain structure which causes more crack branching when the crack is propagating in the transverse direction compared to the longitudinal direction. Finally, a model is presented to account for the effect of grain boundary α on fracture toughness of $\alpha + \beta$ and metastable β alloy.

[1] Associate professor, Department of Metallurgy and Materials Science, Carnegie-Mellon University, Pittsburgh, Pa. 15213.

[2] Manager, Titanium Research and Development, Colt Industries, Crucible Materials Research Center, Pittsburgh, Pa. 15230.

[3] Members of technical staff, Science Center, Rockwell International, Thousand Oaks, Calif. 91360.

[4] Member of technical staff, Rockwell International, Los Angeles Aircraft Division, Los Angeles, Calif. 90009.

Copyright© 1978 by ASTM International www.astm.org

KEY WORDS: titanium, titanium alloys, electron fractography, microstructure, fracture toughness, thermomechanical processing

In recent years, the increased emphasis on reliability of aircraft structures has brought about a greater concern for maintainability and inspectability. Attendant to such emphasis is the requirement for larger critical flaw sizes in fracture critical components. This can only be accomplished by increasing the fracture toughness of the materials used for these components. In current state-of-the art alloys, improvements in fracture toughness have been achieved through reductions and control of oxygen content or by "dead-annealing," but these methods have some attendant reductions in strength with resultant weight penalties. Such weight penalties are becoming less acceptable because of the increasing economic significance of specific fuel consumption. Accordingly, more efficient designs which utilize higher strength materials are attractive to minimize fuel consumption and maximize payload. At the same time, the increased emphasis on reliability just mentioned has introduced the minimum flaw size concept. This places a further limitation on the utilization of higher strength materials because increases in strength alone are unsatisfactory unless parallel increases in toughness can be achieved to retain a constant critical flaw size and therefore a constant degree of inspectability and reliability.

This paper describes the results of an alloy development program designed to provide new titanium alloys with superior strength-fracture toughness combinations by comparison to those of currently available commercial alloys. Two strength-toughness property combinations were set as goals for this program. These goals, together with properties representative of those currently attainable in commercial alloys, are listed here.

	Typical Values	
	Ultimate Tensile Strength, MPa	K_{Ic}, MPa $\sqrt{m}$
Contract Goal A	930 (135 ksi)	110 (100 ksi $\sqrt{in.}$)
Present Ti-6A1-4V (RA condition)[5]	896 (130 ksi)	83 (75 ksi $\sqrt{in.}$)
Contract Goal B	1171 (170 ksi)	88 (80 ksi $\sqrt{in.}$)
Present deep hardenable alloys [*1*][6]	1171 (170 ksi)	66 (60 ksi $\sqrt{in.}$)

[5] RA condition=925°C (~1700°F)/4 h/cool at 55°C (100°F)/h to 760°C (1400°F) and air cool.

[6] The italic numbers in brackets refer to the list of references appended to this paper.

The explicit purpose of this program was to identify one or two alloy compositions together with an appropriate processing sequence which would permit attainment of the two sets of goal properties. However, the implicit purpose of the program was to utilize existing microstructure-property information together with the information generated during this program to accelerate the convergence process required to arrive at the desired composition and processing sequence. To do this, a number of alloy compositions were screened and the two most promising ones were selected. Processing studies were then conducted on these two alloys to enable microstructural manipulation and optimization of properties. This paper summarizes the results of these studies. A detailed account of the entire program is contained elsewhere [*2*].

Experimental Procedure

The program was conducted in two stages: a preliminary phase in which alloy composition was optimized and a later stage in which thermomechanical processing of the selected compositions was optimized. For the preliminary stage ~ 10-kg (22-lb) 110-mm (4.25-in.) ingots were melted and converted to ~ 12-mm (½-in.) plate by a processing sequence in which the final 60 percent reduction was subtransus [*2*]. In the later scale-up stage, 225-kg (500-lb) 380-mm (15-in.) ingots were processed to ~ 250-mm (~ 10-in.) bloom from 1040°C (1900°F) by a multidirection upset and draw-out cycle. These blooms were then forged to 100-mm (4-in.) slabs from 980°C (1800°F) for the higher β transus Goal A alloy and 900°C (1650°F) for the more heavily alloyed Goal B alloy. The Goal A alloy was then rolled to 45-mm (1.75-in.) plate and the Goal B alloy, to 25-mm (1.00-in.) plate. Details of this final processing step is given in a following section of this paper.

Mechanical property evaluation consisted of tension testing and fracture toughness determinations. The latter was predominantly by slow bend precracked Charpy specimens (K_v) with valid compact tension fracture toughness testing (K_{Ic}) of selected specimens. The usefulness of the K_v test as a screening tool in alloy development programs is discussed in another paper in this publication [*1*]. Also given in this referenced paper are details of the orientation nomenclature used.

The basic procedure was to process the material according to several different schedules in order to achieve a wide range of microstructures. Properties corresponding to these microstructures were then determined and correlations with microstructure established. Details of the techniques used for microstructure characterization are contained in Refs *3* and *4*.

Results and Discussion

Microstructure Development and Control

In the later sections of this paper, the emphasis will be placed on relating properties to microstructure. Therefore it is appropriate to describe briefly the microstructures and the factors which influence microstructural development. Such factors include the temperature and extent of hot and warm [7] working and subsequent annealing or heat treatment, or both. The degree of β-stabilization selected for alloys intended to meet Goal A and B are quite different. Thus the microstructures are significantly different and will be discussed separately.

Goal A—The modest strength requirements for this goal can be met by utilizing the combined contributions of solid solution strengthening and microstructural scale strengthening (microduplex) strengthening. Such strengthening contributions have been discussed elsewhere [*5*]. Thus the microstructures which correspond to the required strength levels can be achieved by various combinations of warm working and annealing. The interplay between these processing variables and the resultant microstructures is complex; this will be discussed next.

The alloy compositions selected to meet Goal A and which were evaluated in this program were all more highly β-stabilized than Ti-6A1-4V.[8] These compositions are listed in Table 1. Such compositions were selected to ensure that goal strengths would be achievable. Accordingly, some preliminary postworking annealing studies were required to permit the attainment of the desired $\alpha + \beta$ worked microstructures. This is illustrated by the following results obtained for hot rolled plate of a Ti-5Mo-4.5A1 alloy. This material was hot rolled under conditions of continuously decreasing temperatures starting at 968°C (1775°F) (8°C (15°F) above the β-transus) and finishing at 690°C (1275°F) with the last 30 percent reduction performed between 746°C (1375°F) and 690°C (1275°F). The as hot-rolled microstructure consists of elongated α-particles in a β-matrix as shown in Fig. 1(*a*). Subsequent annealing of this material at 871°C (1600°F) for increasing times results in a coarsening of the α-particles with a simultaneous decrease in aspect ratio as shown in Fig. 1(*b*) and (*c*). In all cases, however, the microstructure was very fine compared to that of commercial Ti-6A1-4V in the recrystallization annealed condition [*3*]. One possible reason for this is that the β-phase matrix recovers and polygonzies rather than recrystallizes during postwork annealing. At the same time, the α-phase which also has been deformed during working recrystallizes and

[7] As used here, hot and warm working refer to working above and below the recrystallization temperature, respectively.

[8] All alloy compositions are given in weight percent.

TABLE 1—*Alloy compositions.*[a]

Mo	Al	Zr	Cr	V	Ti	Goal Properties
5	4.5	...	...	...	bal	A
3	4.5	...	1.5	...	bal	A
8	4.5	...	...	...	bal	A
8	4.5	4	...	...	bal	A
5	4.5	...	1.5	...	bal	A
8	5.5	...	...	...	bal	A
3	5.5	...	1.5	...	bal	A
4	4.5	...	1.5	...	bal	A
11	4.5	...	...	...	bal	A and/or B
11	4.5	4	...	...	bal	A and/or B
8	4.5	...	1.5	...	bal	A and/or B
8	2.5	...	...	4	bal	B
11	2.5	...	...	...	bal	B
11	2.5	4	...	...	bal	B
8	2.5	...	1.5	...	bal	B
8	2.5	...	4.5	...	bal	B
8	2.5	4	4.5	...	bal	B
8	2.5	...	3.0	4	bal	B
11	2.5	...	6.0	4	bal	B
8	2.5	4	4.5	...	bal	B

[a] In weight percent.

becomes nearly equiaxed. This equiaxed primary α pins the subgrain boundaries which contributes to the fine scale of the microstructure. This is illustrated in Fig. 2.

In more heavily β-stabilized alloys, such as Ti-8Mo-4.5Al-4Zr, the optimum working temperature range is closer to or above the β-transus because the elevated temperature flow stress has a different composition dependence than does the β-transus temperature. In fact, increasing molybdenum may increase the flow stress in the 700 to 900°C (1300 to 1650°F) range. The optimum working temperature is defined as that temperature which leads to both a minimal flow stress and sufficiently slow recrystallization kinetics that α-phase nucleation sites remain after working. Using this definition, it is clear that optimum working temperature for a range of alloy compositions is not simply related to the β-transus temperature. As a result, empirical working studies are required to determine a processing temperature which will lead to the desired microstructure.

In addition to the $\alpha + \beta$ worked and recrystallized microstructures just described, an alternate microstructural condition of the Goal A alloys was achieved by β-annealing. This was accomplished by heating approximately 28°C (50°F) above the β-transus for 15 min and then air cooling. The alloys were then given a 4 h stabilization anneal at 704°C (1300°F). A typical β-annealed microstructure is shown in Fig. 3. From this it can be

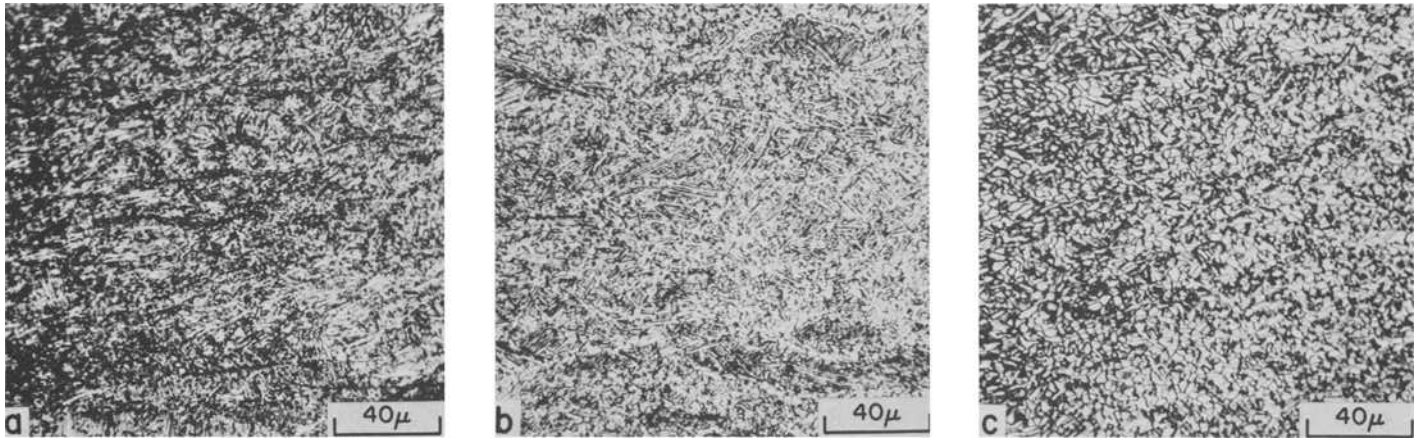

FIG. 1—*Light micrographs illustrating the effect of hot rolling and annealing on the microstructure of Ti-5Mo-4.5Al. Note especially the change in α-phase aspect ratio and the size of the α-phase particles.* (a) *As hot rolled from 10°C above and finished at 275°C below the β-transus.* (b) *Hot rolled and annealed for 30 min at 870°C.* (c) *Hot rolled and annealed for 8 h at 870°C.*

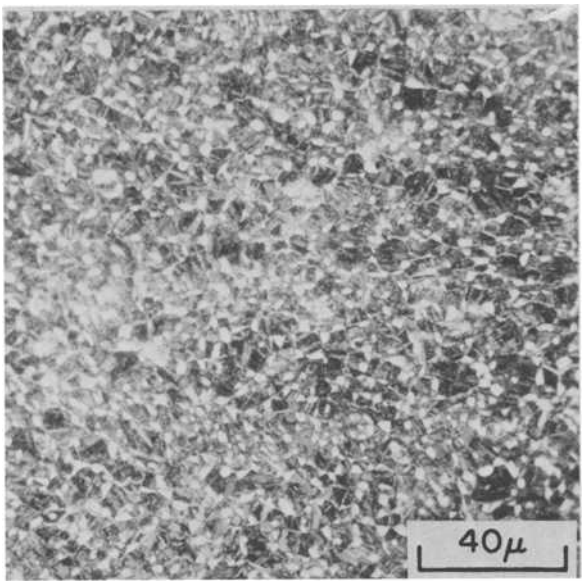

FIG. 2—*Light micrograph of Ti-5Mo-4.5Al hot rolled as described in Fig. 1*(a) *and annealed for 15 min at 927°C* (T_β *—34°C) showing equiaxed primary* α *and* α*-phase precipitates along subboundaries in the* β*-matrix.*

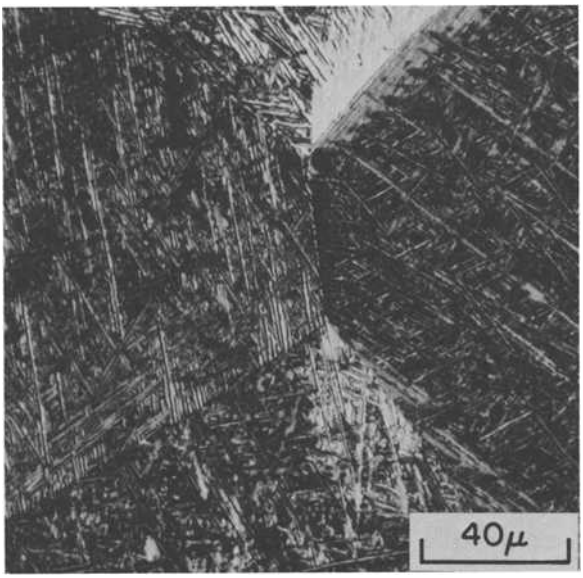

FIG. 3—*Light micrograph of Ti-5Mo-4.5Al-1.5Cr in* β*-annealed and stabilized condition (968°C/15 min/air cool + 704°C/4 h/air cool).*

seen that the microstructure consists of Widmanstätten α-plates in a β-phase matrix. The prior β-grain boundaries also contain heterogeneously nucleated α-phase. Because of the higher β-stabilizer content in the alloys studied here, the Widmanstätten α-phase occurs as randomly oriented individual plates rather than as colonies as is frequently the case in Ti-6A1-4V [*3,6*]. Such a structure affords numerous interfaces for crack branching but does not have the long slip length typical of the colony structure in Ti-6A1-4V [*3*].

Goal B—The strengths required to meet this goal can only be met by solution treating and aging (STA). In this context, STA means cooling from the solution treatment temperature to room temperature rapidly enough to avoid α-phase precipitation during cooling and then subsequently aging for a time-temperature combination which will precipitate α-phase with the volume fraction and particle size necessary to achieve the goal strength. It is well-known that metastable β-alloys have the potential to achieve strengths well in excess of goal properties [*1,7*]. However, it is also well known that the fracture toughness of lean β-alloys depends strongly on the amount and distribution of primary α-phase and that this is controlled by processing history or thermomechanical treatment (TMT) [*1,7-9*]. The alloy compositions which were evaluated for achieving Goal B properties are shown in Table 1. These alloys were continuously hot rolled using a starting temperature above the β-transus and a finishing temperature below the β-transus. Earlier studies have suggested that refinement of the β-grain size is beneficial to toughness and a few alloys were subsequently cold rolled and recrystallized to achieve this [*10*]. However, cracking was frequently encountered during cold rolling and, even when it was not, mill forces were prohibitively high. As a result, cold rolling was eliminated as a means of achieving fine β-grain size. Thus the primary α-phase in the Goal B alloy microstructures was controlled by the amount of warm work, the final working temperature and the subsequent annealing treatment. Typical microstructures are shown in Fig. 4. These micrographs show that the alloys all have elongated β-grains, extensive networks of grain boundary α, and some equiaxed primary α. In addition to the primary α which occurs on a micron scale, the matrix contains a high volume fraction of very small ($\lesssim 0.25$ μm) α-phase precipitates. These can be resolved only by electron microscopy techniques. Figure 5 shows surface replica and thin foil micrographs of this fine α-phase. It is this fine α-phase that controls the strength of the alloy whereas the primary α (also shown in Fig. 5) has a much greater influence on fracture behavior. Thus the amount and distribution of primary α is controlled by hot rolling and annealing schedules whereas the size and volume fraction of the fine matrix α is controlled by aging time and temperature. On the basis of the foregoing, it is possible to vary the primary α and precipitated α-distributions independently. To a degree this is true,

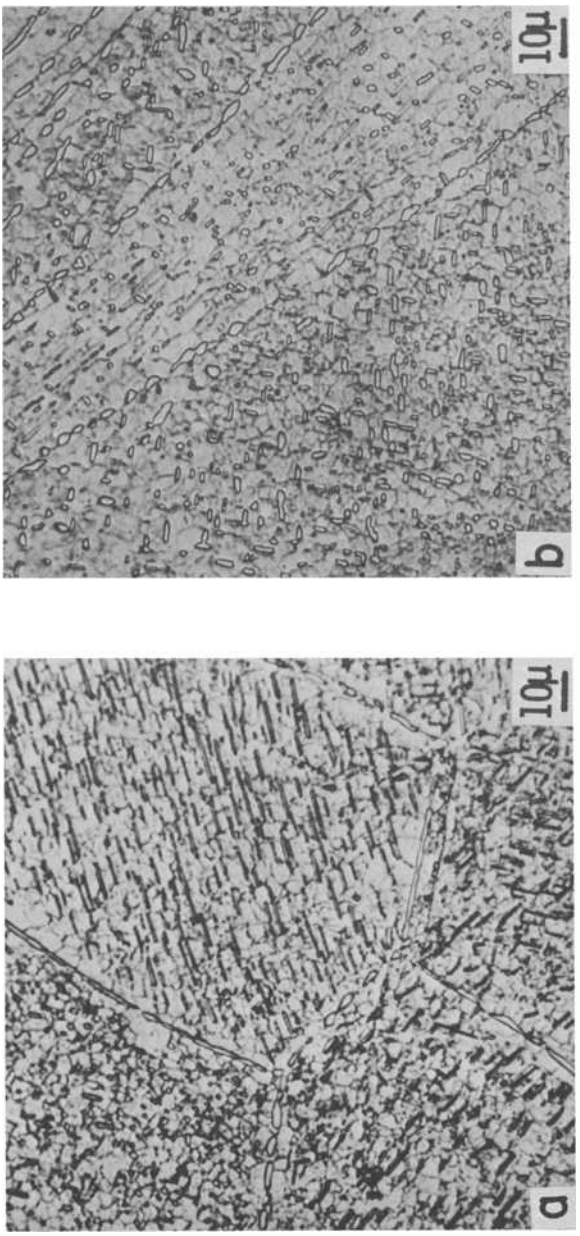

FIG. 4—*Light micrographs of two metastable β-alloys showing effect of working and heat treatment on microstructure.* (a) *Ti-1Mo-2.5Al hot rolled from above the β-transus and finished at 175°C below the β-transus. Annealed at 829°C for 72 h. Note semicontinuous grain boundary α, slightly elongated primary α particles and subgrain boundaries in β-matrix.* (b) *Ti-8Mo-2.5Al-1.5Cr hot rolled from above the β-transus and finished at 90°C below the β-transus. Annealed at 829°C* (T_β—*48°C*) *for 72 h. Note semicontinuous grain boundary α, nearly equiaxed primary α and subgrain boundaries in β-matrix.*

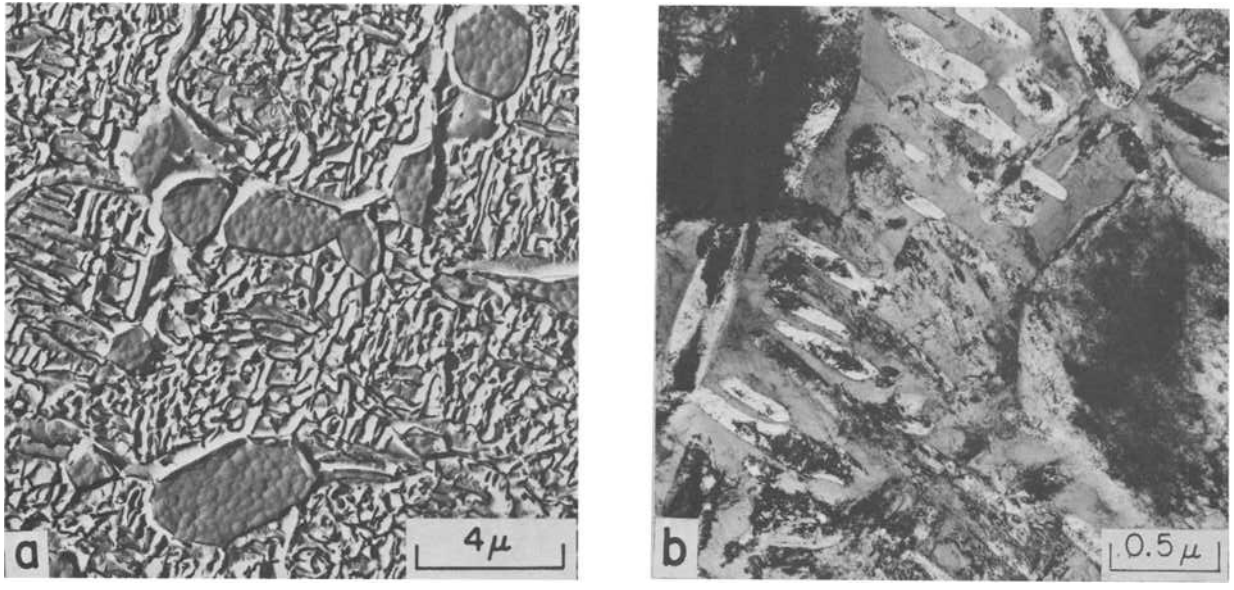

FIG. 5—*Replica and thin foil electron micrographs showing the fine α-phase precipitates in the β-matrix of the aged metastable β-alloy Ti-8Mo-2.5Al-4.5Cr.* (a) *Replica micrograph of alloy aged 8 h at 607°C.* (b) *Thin foil micrograph of alloy after same aging treatment as* (a).

however, there is a significant interaction between the two because solute partitioning to the β-phase during primary α-formation affects the nucleation and growth of α-phase precipitates during aging.

Additional studies of processing and annealing temperatures were conducted on a particularly promising alloy, Ti-8Mo-2.5Al-4.5Cr. The effects of these variables on primary α-distribution are shown in Fig. 6(*a*) through (*c*). The rolling and annealing temperatures used to produce these microstructures are shown in Table 2. Figure 6(*a*) through (*c*) shows that two of the three conditions illustrated exhibit extensive grain boundary α. From Table 2 it can be seen that one of these was rolled at 915°C (1679°F) and the other at 800°C (1472°F). Further, the primary α is very uniformly distributed and equiaxed in the specimen which contains no grain boundary α. Comparison of the heat treatment and processing histories of these three conditions leads to the conclusion that the equiaxed α is formed during annealing at 760°C (1400°F), the lower of the two temperatures. It is also apparent that the two different processing histories (Table 2) did not significantly affect the primary α-distribution. This result is in contrast to other studies which have shown the primary α-distribution depends critically on processing history. Thus it is possible that other processing schemes may affect the primary α-distribution in Ti-8Mo-2.5Al-4.5Cr [*1,11*].

Effect of Microstructure on Properties

The range of microstructures described in the previous sections have a significant effect on properties, especially fracture toughness. Because of the diversity of microstructures of Goal A and Goal B alloys, the role of microstructure on strength and toughness will be discussed separately for these two classes of alloys.

TABLE 2—*Hot rolling and heat treatment schedules for Ti-8Mo-2.5Al-4.5Cr alloy.*

Initial Roll Temperature, °C	Microstructure	Annealing Temperature, °C, 8 h	Aging Temperature, °C, 8 h
915[a]	Fig. 6(*a*)	790	605
915[a]	not shown	790	550
915[a]	not shown	760	605
915[a]	not shown	760	550
800[b]	Fig. 6(*b*)	790	605
800[b]	not shown	790	550
800[b]	Fig. 6(*c*)	760	605
800[b]	not shown	760	550

[a] Reheats at 802°C.
[b] Reheats at 690°C.

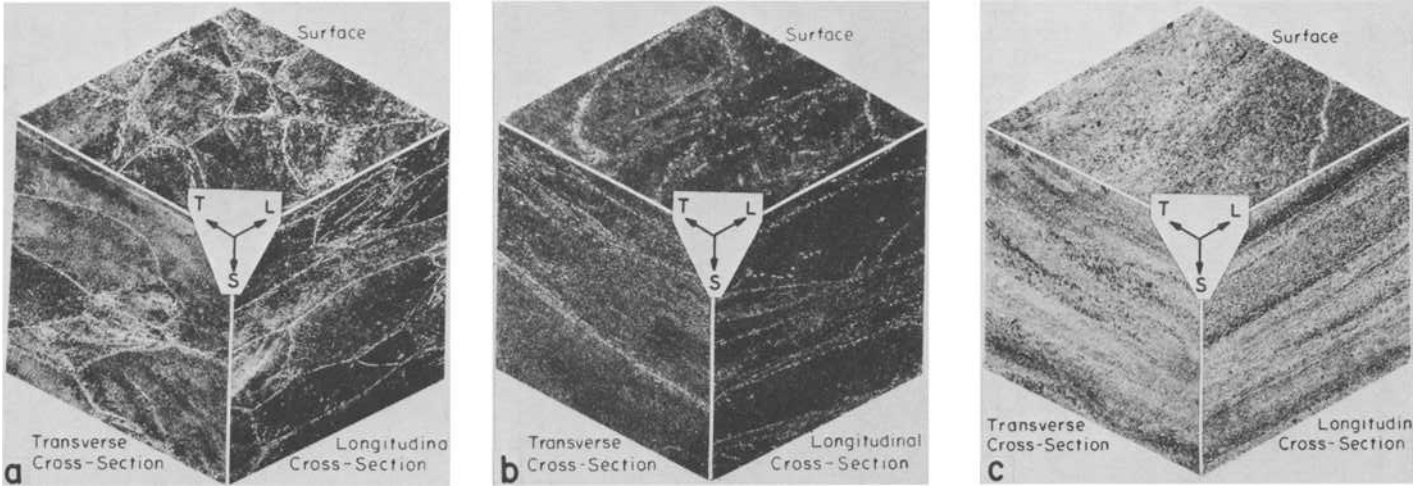

FIG. 6—*Light metallographic isometric cubes showing effect of processing and heat treatment history on extent of grain boundary α in Ti-8Mo-2.5Al-4.5Cr.*

Goal A—The strength and toughness values obtained from several Goal A alloys are shown in Table 3. From this table it can be seen that both the strength and toughness vary with microstructure, making direct comparison difficult. To permit direct comparison of these data for the various alloys and microstructures, the data for each alloy and microstructure have been plotted as a strength-toughness trend line. Several of these are shown in Figs. 7 through 10. These plots greatly facilitate evaluation of the potential of an alloy to meet the goal properties which also are shown on the plots. From these data it is apparent that three of the four alloys represented by Figs. 7 through 10 have the potential to meet or exceed Goal A properties. Of these the most promising is the alloy Ti-5Mo-4.5A1-1.5Cr. The basis for this judgment is twofold. First, the slope of the K_v versus ultimate tensile strength (UTS) plot is reasonably small; this indicates a smaller toughness penalty in higher strength conditions. Second, both the $\alpha + \beta$ processed and recrystallization annealed material and the β-processed material appear to meet Goal A properties. This permits the alloy to be processed or heat treated so as to optimize a variety of other requirements such as stress corrosion resistance, fatigue crack growth rate, or creep resistance without sacrificing the Goal A strength-toughness combination. In view of this, a substantial amount of additional work has been performed on optimizing the processing of the Ti-5Mo-4.5A1-1.5Cr alloy. The balance of this discussion will describe these results.

In order to guide the further processing studies, an analysis was made of the failed specimens from which the data of Fig. 9 were obtained. In the $\alpha + \beta$ worked and recrystallization annealed conditions, there was a

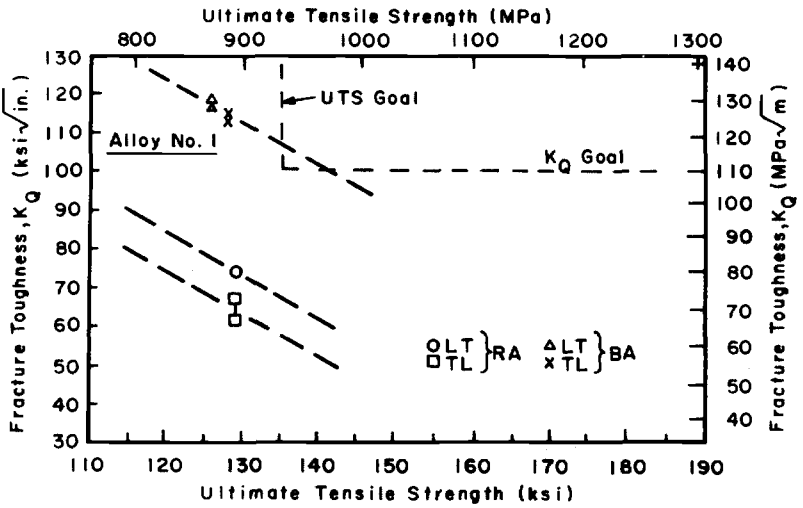

FIG. 7—*Strength-toughness trend for Ti-5Mo-4.5Al.*

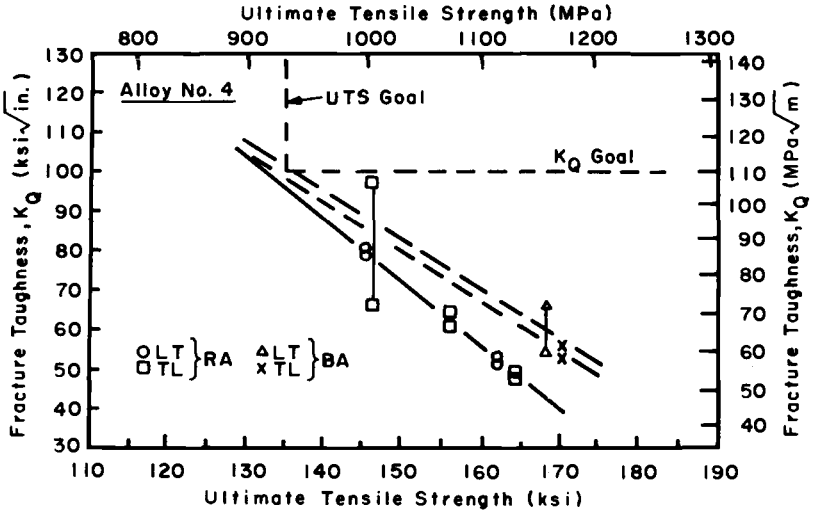

FIG. 8—*Strength-toughness trend for Ti-8Mo-4.5Al-4Zr.*

reasonable correlation between fracture appearance and toughness. Two $\alpha + \beta$ annealed microstructures, together with crack profile micrographs and scanning electron microscope (SEM) fractographs are shown in Figs. 11 through 16. These two microstructures correspond to different annealing temperatures with attendant variations in primary α-morphology and extent of prior β-grain boundary α. These figures show that the fracture path is

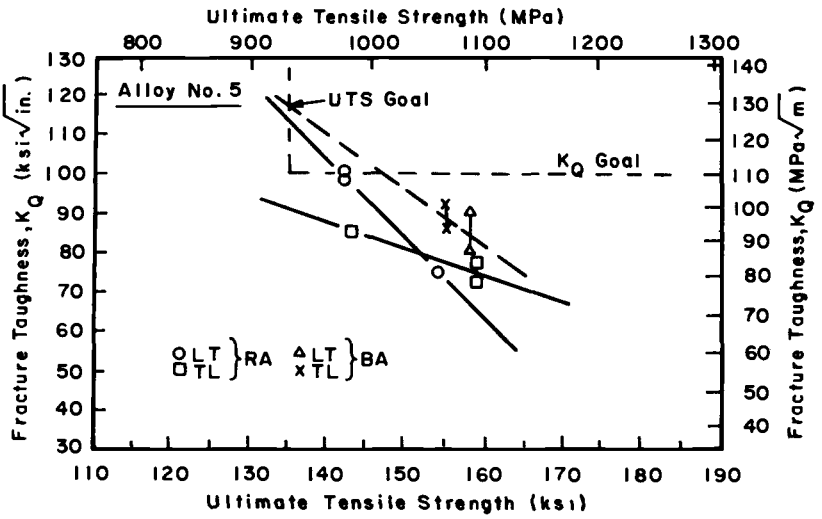

FIG. 9—*Strength-toughness tend for Ti-5Mo-4.5Al-1.5Cr.*

TABLE 3—*Mechanical properties of several Goal A alloys.*

Composition (bal Ti)	Heat Treatment [a]			Tensile Properties								Fracture Properties, MPa$\sqrt{m}$ (ksi$\sqrt{in.}$)	
					Ultimate Tensile Strength		Yield Strength				E	K_Q [b]	
	Type [c]	Temperature, °C	Time, h	Direction	MPa	(ksi)	MPa	(ksi)	Elongation, %	Reduction in Area, %	$\times 10^3$ MPa	($\times 10^6$ psi)	RW	WR
Goal	...	...	...		930	(135.0)							110 (100.0)	110 (100.0)
5Mo-4.5A1	ReX	870	4.0	L	889	(129.1)	820	(119.4)	20.5	59.6	118	(17.1)	81 (73.5)	...
				T	882	(128.7)	827	(120.5)	19.0	52.4	121	(17.6)	...	74 (66.9)
														67 (60.6)
	BA	995 plus	0.25											
		705	4.0	L	868	(126.3)	765	(111.5)	18.0	31.3	122	(17.7)	130 (118.0)	...
													128 (116.5)	...
				T	881	(127.8)	854	(124.2)	13.0	25.3	119	(17.2)	...	125 (113.5)
													...	127 (115.2)
8Mo-4.5A1-4Zr	ReX	815	72.0	L	956	(138.8)	911	(132.2)	12.5	19.2	101	(14.7)	92 (84.0)	...
													89 (80.8)	...
				T	1008	(146.3)	969	(140.7)	14.0	30.7	107	(15.5)	...	73 (66.2)
													...	106 (96.8)
		840	4.0	L	1115	(161.9)	940	(136.5)	3.5	5.1	110	(16.0)	57 (52.2)	...
													58 (52.9)	...
				T	1129	(163.8)	1086	(157.6)	5.5	24.1	114	(16.5)	...	54 (48.8)
													...	53 (48.6)
		800	4.0	L	1000	(145.2)	937	(136.4)	9.0	13.8	115	(16.7)	88 (79.9)	...
													87 (79.4)	...
				T	1074	(155.9)	1039	(150.0)	14.5	25.0	119	(17.2)	...	67 (61.3)
													...	70 (63.7)
	BA	940 plus	0.25											
		705	4.0	L	1158	(168.1)	1046	(151.8)	10.0	22.0	124	(18.0)	73 (66.0)	...
													59 (53.7)	...
				T	1169	(169.7)	1081	(156.9)	9.5	19.4	126	(18.3)	...	60 (54.8)
													...	60 (54.2)

5Mo-4.5Al-1.5Cr	ReX	855	4.0	L	1062	(154.2)	943	(166.8)	14.0	36.6	114	(16.6)	82	(74.9)	...
				T	1093	(158.6)	1002	(145.4)	14.0	35.7	112	(16.3)	...		85 (77.3)
													...		80 (72.8)
		800	48.0	L	880	(127.7)	832	(120.8)	19.0	46.1	97	(14.1)	100	(91.0)	...
													106	(96.8)	...
				T	932	(135.3)	912	(132.3)	17.5	43.2	105	(15.2)	...		55 (49.6)
													...		59 (53.9)
	ReX	855	4FC[d]	L	974	(141.4)	898	(130.3)	3.0	26.0	123	(17.8)	109	(99.3)	...
													109	(99.4)	...
				T	985	(142.9)	918	(133.3)	18.0	28.0	125	(18.1)	...		93 (84.5)
	BA	970 plus	0.25												
		705	4.0	L	1087	(157.8)	1007	(146.2)	10.0	18.8	128	(18.6)	98	(89.4)	...
													88	(79.9)	...
				T	1067	(154.8)	994	(144.3)	10.0	17.4	131	(19.0)	...		95 (86.1)
													...		100 (91.3)
11Mo-4.5Al-4Zr	ReX	815	4.0	L	994	(144.3)	974	(141.3)	10.5	20.6	102	(14.8)	68	(62.0)	...
													78	(71.3)	...
				T	1070	(155.3)	1047	(152.0)	12.5	25.0	96	(14.0)	...		(43.5)
		815 plus	4.0												
		760	24.0	L	949	(137.8)	916	(133.1)	11.0	22.2	103	(15.0)	95	(86.7)	...
													104	(94.6)	...
				T	1029	(149.4)	978	(141.9)	16.0	31.6	114	(16.5)	...		74 (67.5)
													...		82 (74.8)
	ReX	815 plus	4.0												
		885	4FC[d]	L	978	(141.9)	929	(134.8)	4.0	20.2	124	(18.0)	107	(97.5)	...
													103	(93.7)	...
				T				no test					...		...
	BA	925 plus	0.25												
		705	4.0	L	1253	(181.9)	1209	(175.4)	3.0	5.8	125	(18.1)	53	(48.2)	...
				T				no test					...		...

[a] Heat treatment followed by air cooling.

[b] From slow bend precracked Charpy specimens. Calculated using $K_Q^2 = \frac{W}{A} \times \frac{E}{2(1-\nu^2)}$

[c] ReX = recrystallization treated, and
BA = beta annealed.

[d] Furnace cooled at 37.8°C/h to 537.8°C (100°F/h to 1000°F), then air cooled.

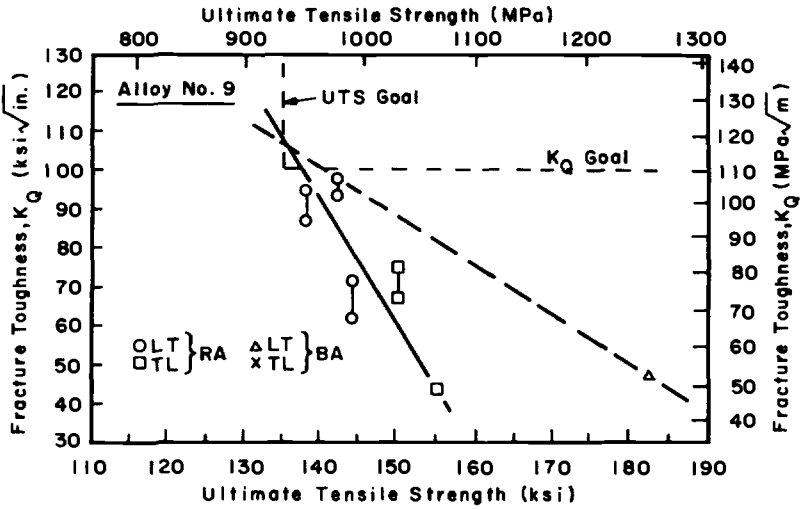

FIG. 10—*Strength-toughness trend for Ti-11Mo-4.5Al-4Zr.*

more undulating and that the fracture surface is rougher and more irregular in the tougher orientation of each condition. Further, the undulations are large with regard to the individual microstructural constituents. There is also an extensive amount of secondary cracking in the toughest condition (K_Q=109 MPa$\sqrt{m}$ (99 ksi$\sqrt{in.}$)) as can be seen in the LT [9] specimen (Fig. 13). This secondary cracking apparently occurs at prior β-grain boundaries which contain α-phase as shown in Fig. 11. In the long time annealed material shown in Fig. 14, the toughness is much more directional (57.2 MPa$\sqrt{m}$ (52 ksi$\sqrt{in.}$)) in TL specimens compared to (102 MPa $\sqrt{m}$ (93 ksi $\sqrt{in.}$)) in LT specimens. These specimens also show a good correlation between fracture path undulations and toughness as can be seen in Fig. 15. The fractography also shows that the LT specimens have larger dimples which appear to be associated with the primary α:β interfaces. The light metallography, Fig. 14, shows that the primary α-particles are somewhat more elongated in the fracture direction in a TL specimen and equiaxed in an LT specimen. The increased flatness of the fracture surface in the TL specimen also is probably influenced by this microstructural factor. Finally, the general coarsening of the microstructure due to long term annealing leads to an increased slip length and thus tends to exacerbate any tendency for strain localization which the alloy may exhibit. Simultaneously, the coarsening also results in lower strength. Thus the finer micro-

[9] LT specimens are loaded in the L direction and crack propagation occurs along the T direction. TL specimens are the inverse of this.

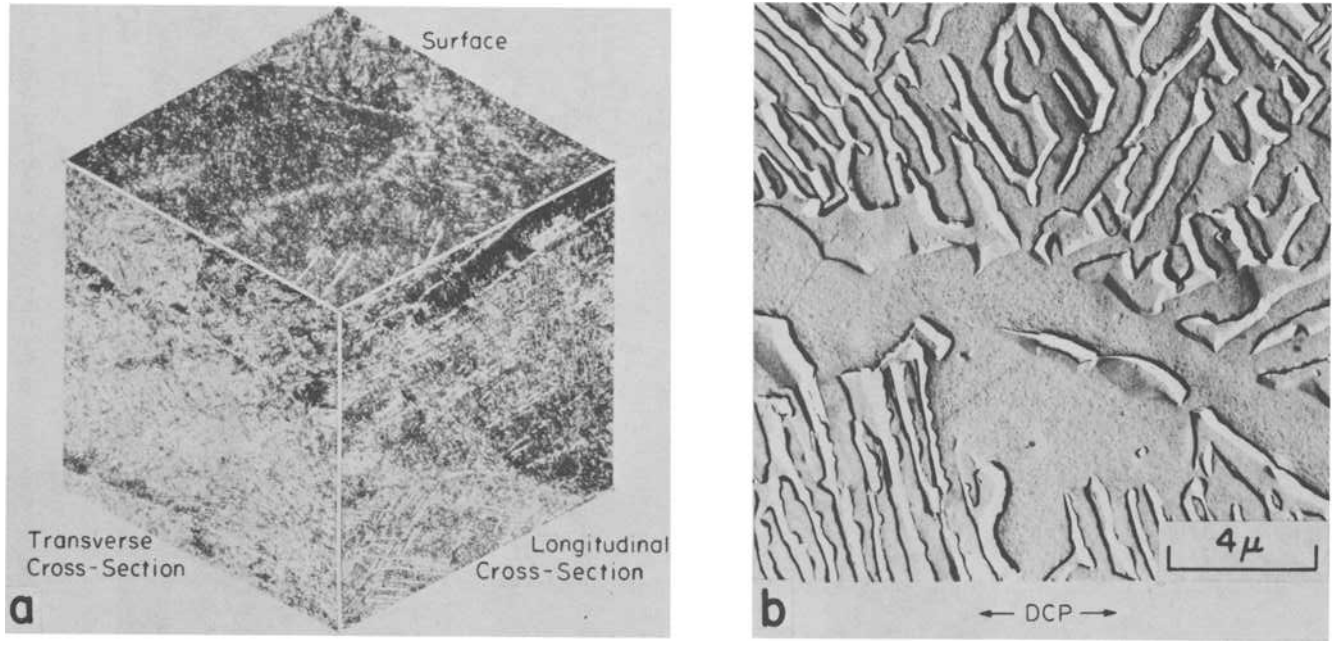

FIG. 11—*Light and electron micrographs showing elongated and grain boundary α in Ti-5Mo-4.5Al-1.5Cr anneal at 857°C for 4 h.* (a) *Light micrographs in isometric cube.* (b) *Surface replica electron micrograph.*

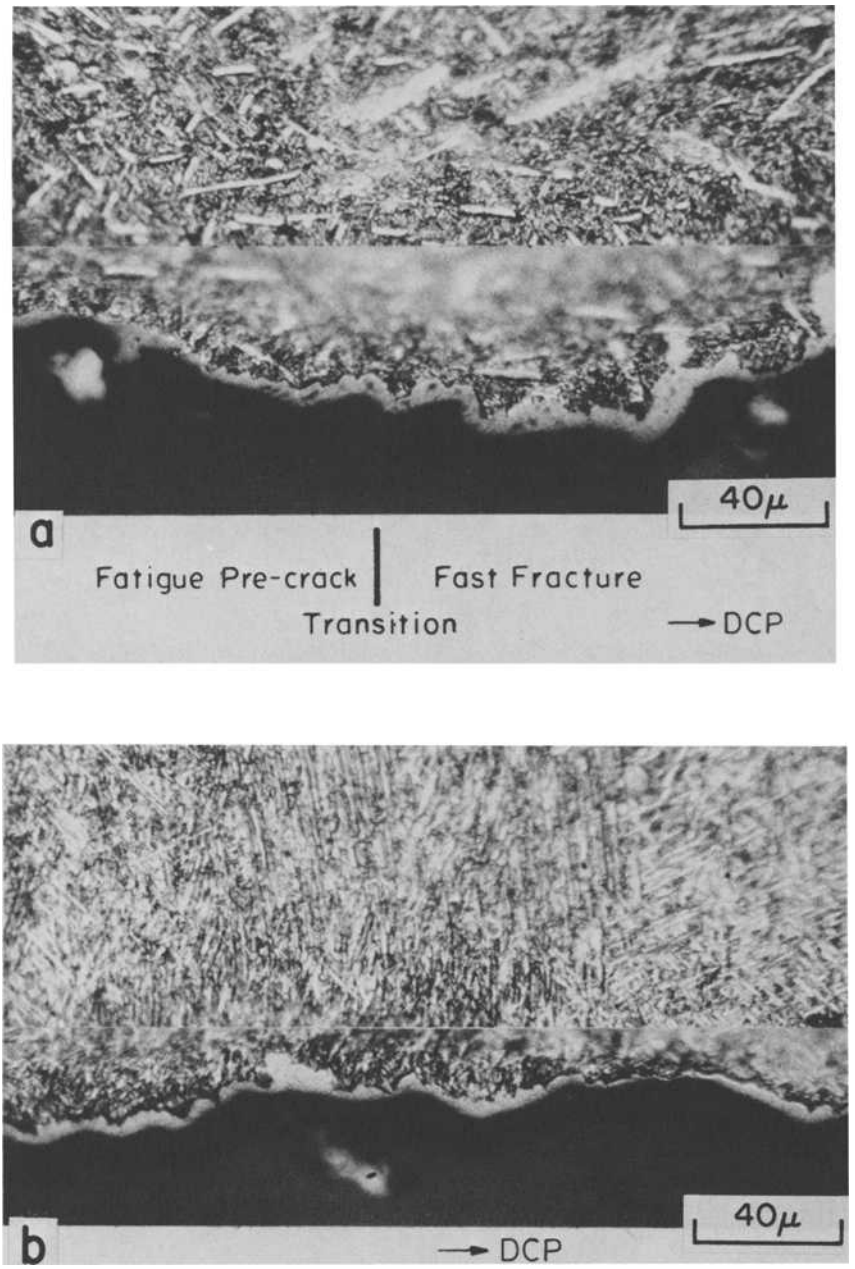

FIG. 12—*Light micrographs showing fracture path in material shown in Fig. 11.* (a) *TL specimen,* $K_v = 94\ MPa\sqrt{m}$. (b) *LT specimen,* $K_v = 109\ MPa\sqrt{m}$.

structural scale, such as that associated with shorter annealing times, is a very useful way of improving both toughness and strength. This comment, of course, only pertains when the morphology of constituents is constant.

In the β-annealed material, the fracture toughness is much more isotropic and is relatively good as shown in Table 3. The microstructure of this material is shown in Fig. 17; this figure shows that the material contains an extensive network of prior β-grain boundary α-phase. Fracture profiles (Fig. 18) show that the crack generally follows prior β-grain boundaries. This is consistent with the fracture topography which has a faceted, largely intergranular appearance as shown in Fig. 19. In this microstructural condition, where the cracks follow the prior β-grain boundaries, the distribution of preferred fracture paths is very similar in the LT and TL specimens, thus the extent of directionality in toughness would be expected to be minimum, as is the case (Table 3). Further, the fracture topography is irregular and there is extensive secondary cracking both of which contribute to the relatively high toughness. If the high strength level (999 MPa (145 ksi) TYS, 1067 MPa (155 ksi) UTS) of the β-annealed material is taken into account, this microstructural condition appears to be especially attractive.

The aforementioned observations suggest that fine equiaxed or β-annealed microstructures have attractive strength-toughness combinations. Further, the most attractive strength-toughness combinations correspond to β-annealed microstructures, which have lenticular α-phase. On this basis, a second, larger ingot of Ti-5Mo-4.5A1-1.5Cr was melted and processed into plate using two processing sequences followed by several postprocessing heat treatments. These are summarized in Fig. 20. The resultant properties for the 8 heat treatment-processing combinations are shown in Table 4. Based on these data, three heat treatment-processing conditions were selected for additional study. These are marked with a (+) in Table 4. The microstructures of these three conditions are shown in Figs. 21 through 23. From these and from Fig. 20, it can be seen that all three conditions have lenticular primary α-microstructures but that the aspect ratio of the primary α is different in each one.

From the property data shown in Table 4, it can be seen that 829°C (1525°F) recrystallization annealed material has the most attractive K_{Ic}-strength combinations, although the properties of this material are somewhat more direction dependent. Fractographic and fracture path examination showed that the β-annealed material exhibited extensive prior β-grain boundary fracture whereas the two recrystallization annealing treatments led to more limited grain boundary α, even though the prior β-boundaries are still identifiable in Figs. 22 and 23. The fracture path profiles are shown in Fig. 24(a) through (c). The 855°C (1575°F) recrystallization annealed material showed the least tortuous fracture path

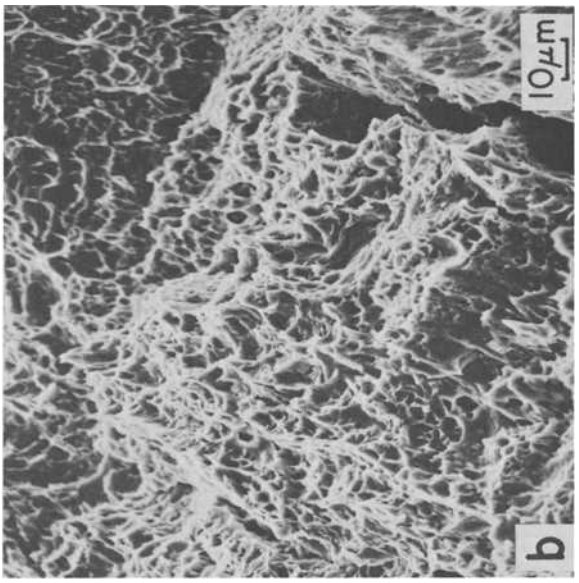
b
10μm

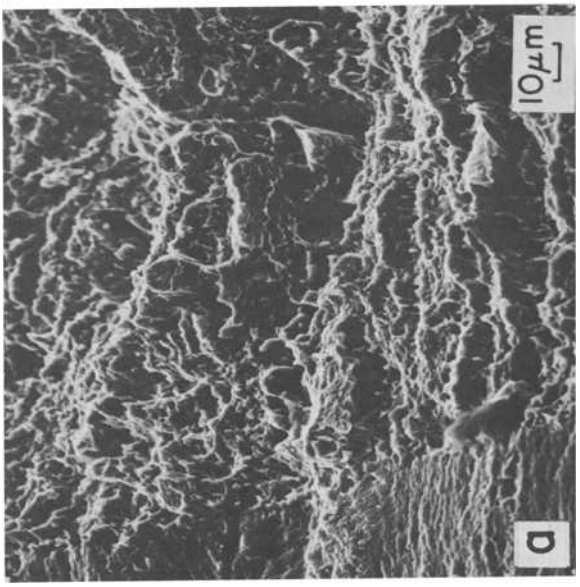
a
10μm

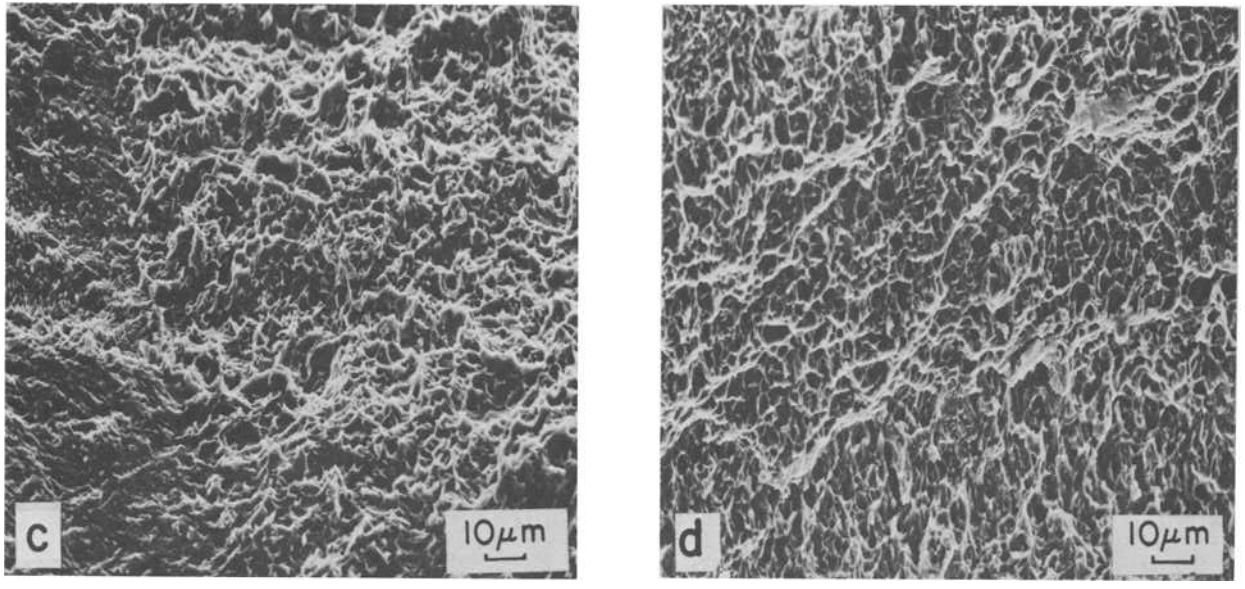

FIG. 13—*Scanning electron fractography of specimens shown in profile in Fig. 12.* (a) *LT specimen, fatigue precrack —fast fracture transition region* ($K_v = 109\ MPa\sqrt{m}$). (b) *LT specimen showing extensive secondary cracking.* (c) *TL specimen, fatigue precrack-fast fracture transition region* ($K_v = 94\ MPa\sqrt{m}$). (d) *TL specimen showing lack of secondary cracking.*

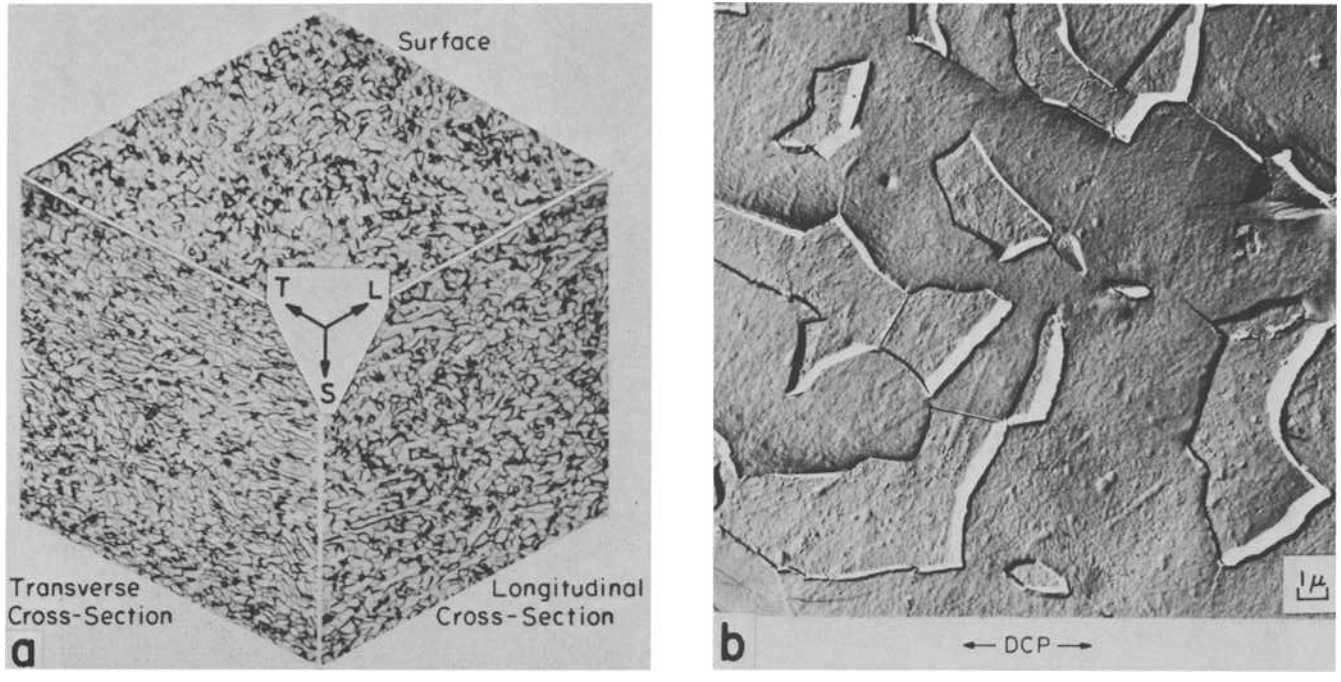

FIG. 14—*Light and electron micrographs showing equiaxed α in Ti-5Mo-4.5Al-1.5Cr annealed at 802°C for 48 h.* (a) *Light micrographs in isometric cube.* (b) *Surfact replica electron micrograph.*

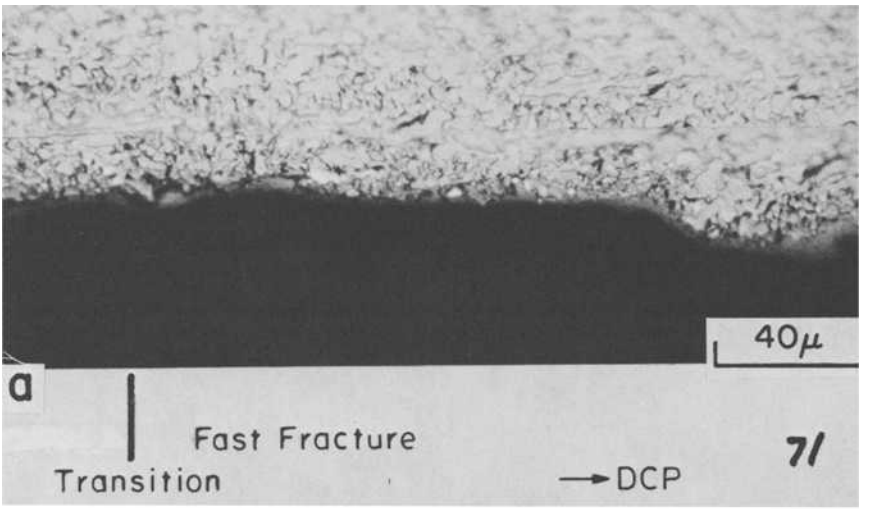

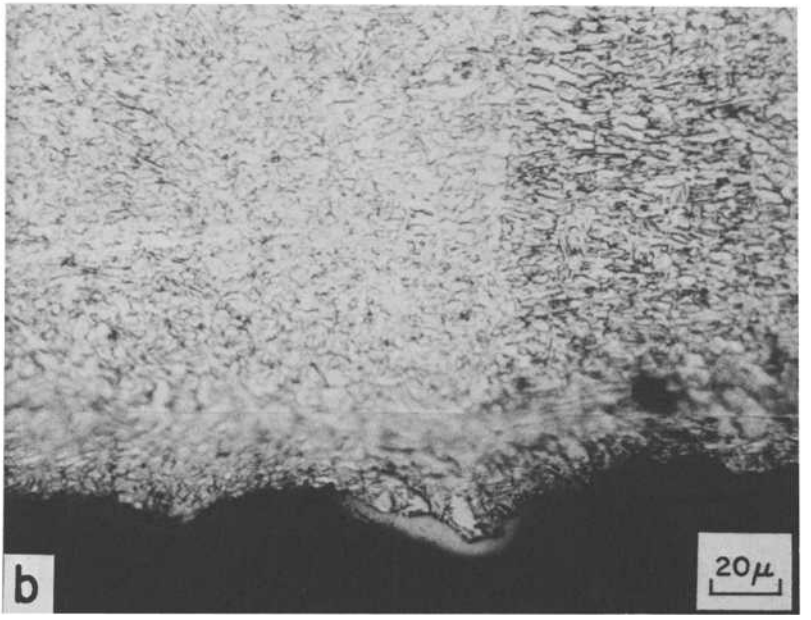

FIG. 15—*Light micrographs showing fracture path in material shown in Fig. 14.* (a) *TL specimen,* $K_v = 57\ MPa\sqrt{m}$. (b) *LT specimen,* $K_v = 102\ MPa\sqrt{m}$.

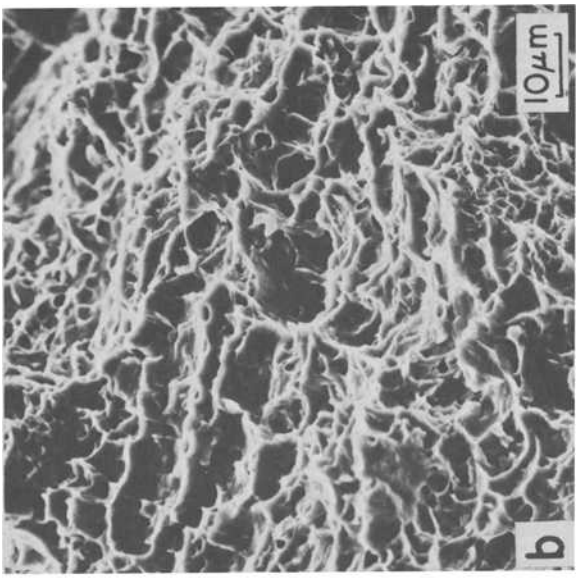
10μm
b

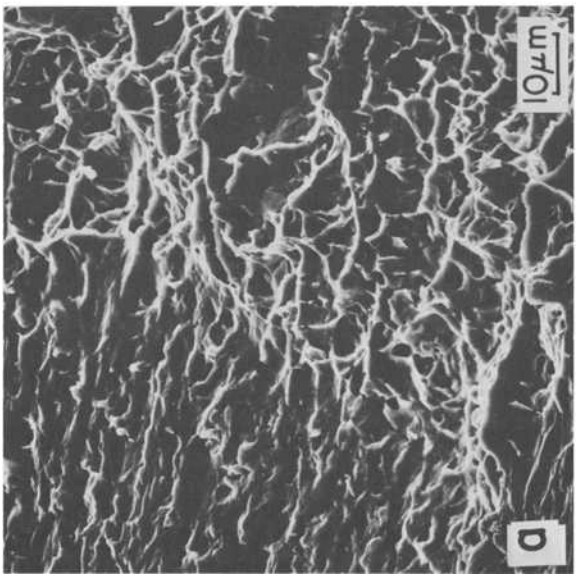
10μm
a

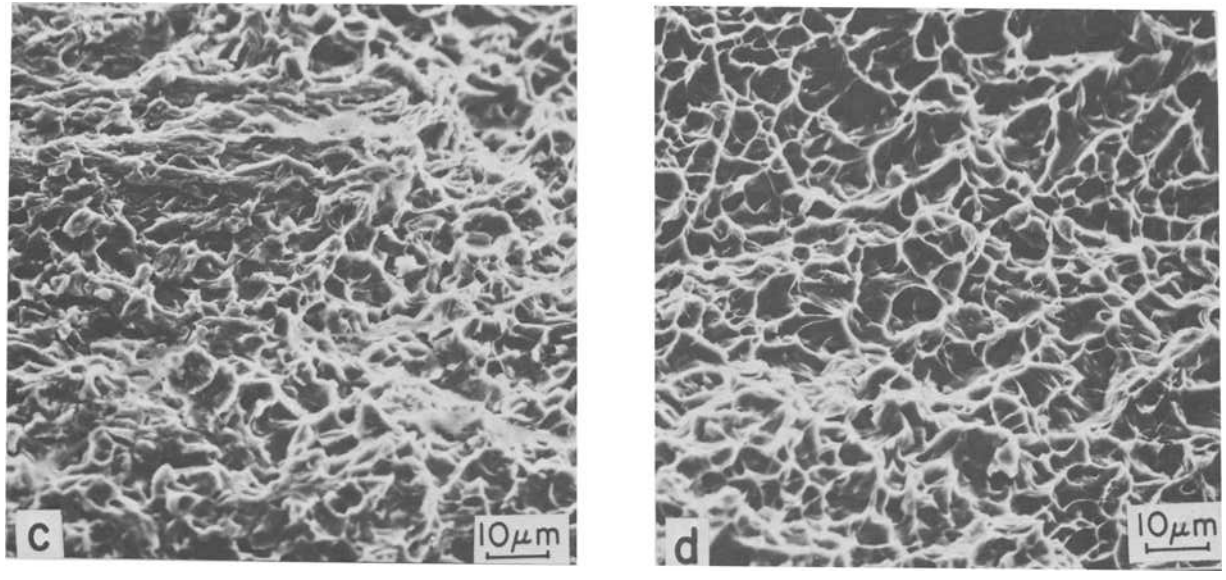

FIG. 16—*Scanning electron fractography of specimens shown in profile in Fig. 15.* (a) *LT specimen, fatigue precrack-fast fracture transition* (K_v=*57 MPa*$\sqrt{m}$). (*b*) *LT specimen showing large dimples and tearing.* (c) *TL specimen, fatigue precrack-fast fracture transition* (K_v=*102 MPa*$\sqrt{m}$). (d) *TL specimen showing smaller dimples than in* (b) *and very little tearing.*

TABLE 4—*Mechanical property data for Ti-5Mo-4.5Al-1.5Cr alloy.*

Processing Route [a]	Annealing Treatment: Temperature, °C	Annealing Treatment: Time, h	Direction [b]	Properties: Tensile Properties: Ultimate Tensile Strength, MPa	Ultimate Tensile Strength, (ksi)	Yield Strength, MPa	Yield Strength, (ksi)	Elongation, %	Reduction in Area, %	E, $\times 10^3$ MPa	E, ($\times 10^6$ psi)	Toughness (MPa$\sqrt{m}$): K_Q, TL	K_Q, LT	K_{Ic} [d], TL
H	970+	0.25 [e]	L	865	(125.6)	777	(112.7)	16.0	30.4	103	(15.0)	125 [a] 120	... ...	129
			T	898	(130.3)	811	(117.7)	14.0	30.1	110	(16.0)	... ...	145 [a] 201	
	855+	4.0 [f]	L	800	(116.1)	719	(104.3)	21.5	62.3	109	(15.8)	195 [g] 176	... ...	139
			T	822	(119.3)	756	(109.7)	18.5	39.7	113	(16.4)	... ...	201 [g] 193	
	830+	4.0 [f]	L	854	(124.0)	761	(110.4)	19.5	53.5	111	(16.1)	186 [g] 175	... ...	145
			T	861	(125.0)	812	(117.9)	19.0	55.2	111	(16.1)	... ...	205 [g] 197	
	830	16.0 [f]	L	803	(116.6)	695	(100.8)	20.5	67.7	99	(14.4)	170 172	... ...	
			T	830	(120.5)	765	(111.0)	19.0	49.5	107	(15.5)	... ...	207 193	
L	970	0.25 [e]	L	794	(115.3)	722	(104.8)	16.0	34.2	105	(15.2)	180 179	... ...	
			T	814	(118.1)	738	(107.1)	19.0	35.9	103	(15.0)	... ...	170 169	

855	4.0[f]	L	773	(112.2)	741	(107.5)	24.0	64.9	99	(14.3)	158	...
											201	...
		T	835	(121.2)	810	(117.5)	22.5	60.1	101	(14.7)	...	147
											...	173
	4.0[f]	L	785	(114.0)	760	(110.3)	22.5	69.7	103	(15.0)	191	...
											151	...
		T	830	(120.5)	801	(116.2)	20.0	59.1	110	(16.0)	...	130
											...	178
830	16.0[f]	L	777	(112.8)	727	(105.5)	24.0	61.0	114	(16.6)	162	...
											181	...
		T	828	(120.2)	798	(115.8)	20.5	60.6	113	(16.4)	...	173
											...	162

[a] H=high processing route, see Fig. 20, and
L=low processing route, see Fig. 20.
[b] L=longitudinal, and
T=transverse.
[c] Calculated from slow bend precracked Charpy specimens using
$K_Q^2=\frac{WE}{2A(1-\nu^2)}$ where
W=energy,
E=Young's modulus,
A=area of specimen, and
ν=Poisson's ratio.
[d] Failed minimum thickness requirement of ASTM Test for Plane-Strain Fracture Toughness of Metallic Materials (E 399).
[e] Air cooled and stabilize annealed 4 h, 704.4°C (1300°F), air cooled.
[f] Furnace cooled 37.8°C (100°F)/h to 537.8°C (1000°F), air cooled.
[g] Used for microstructural and fractographic analysis.

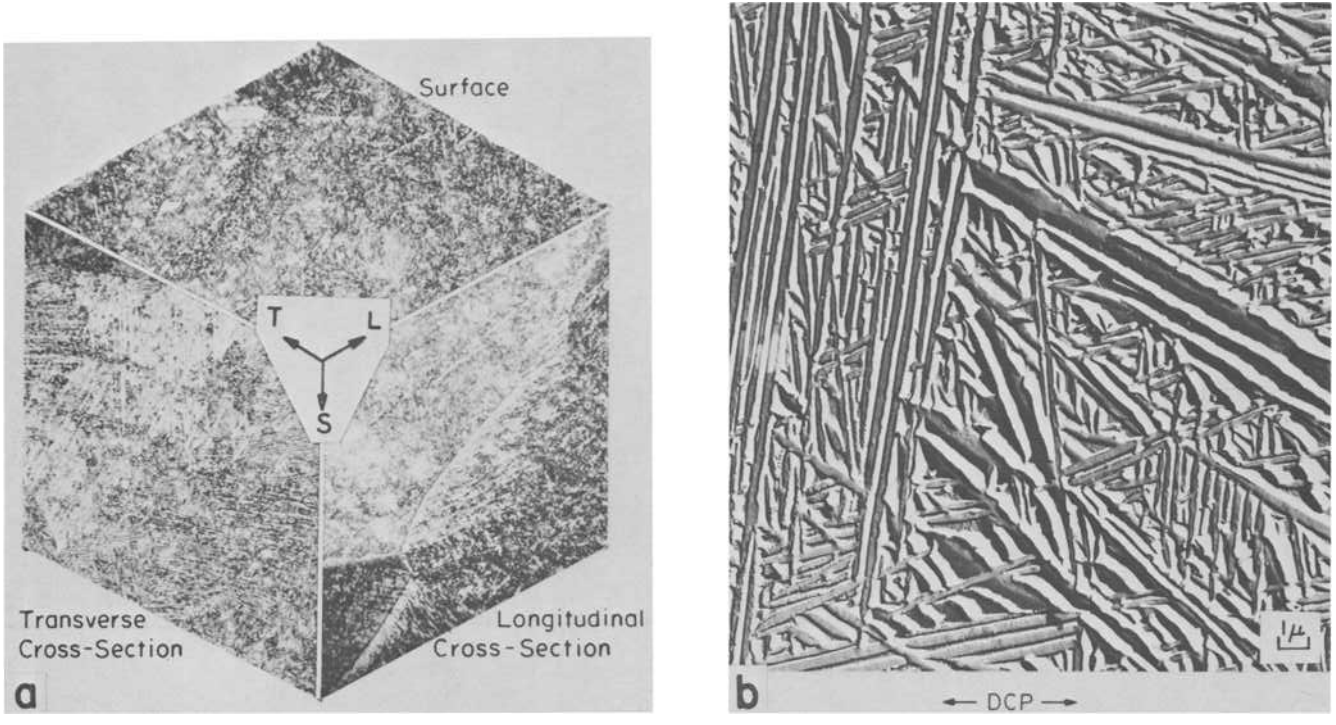

FIG. 17—*Light and electron micrographs showing grain boundary and acicular α in Ti-5Mo-4.5Al-1.5Cr β-annealed at 968°C for 15 min and air cooled.* (a) *Light micrographs in isometric cube.* (b) *Surface replica electron micrograph.*

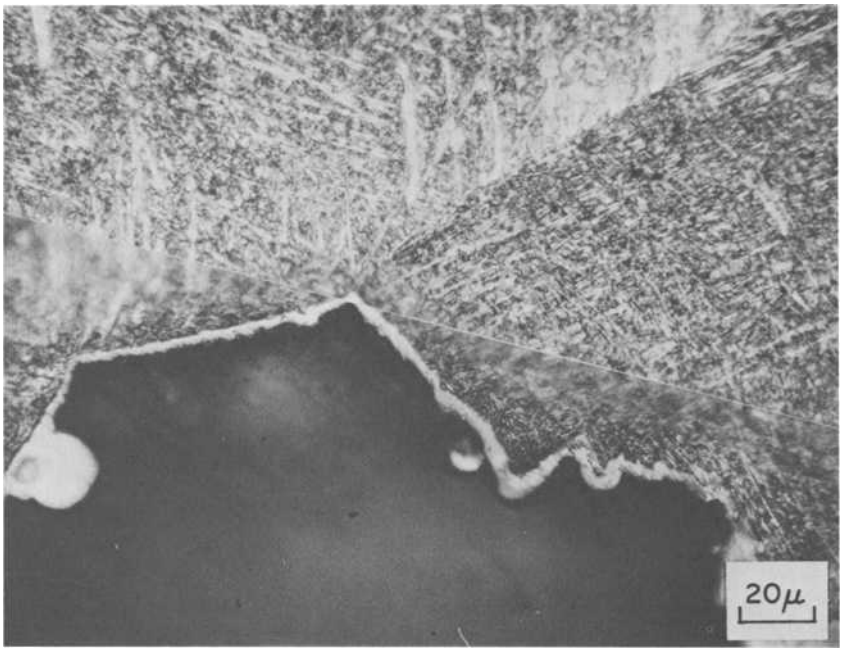

FIG. 18—*Light micrographs showing fracture path in material shown in Fig. 17.*

but the fracture surface still exhibits extensive secondary cracking as seen by comparing Fig. 25(*b*) to Fig. 25(*a*) or (*c*). All fractures occurred by microvoid formation, growth, and coalescence and thus are highly ductile in nature. Examples of these fractures are shown in Fig. 25(*a* through *c*) and at higher magnification in Fig. 25(*d*). The principal difference in the three conditions is the extent to which the fracture path is deviated by the prior β-grain boundaries and by the equiaxed primary α-particles. These differences are the result of decreasing continuity of grain boundary α-phase in the two recrystallization annealed conditions and in decreasing α-phase aspect ratio. As the primary α-phase aspect ratio decreases during subtransus working and recrystallization, the propensity for cracking at α/β interfaces decreases, resulting in less crack branching and a decreased tortuosity of crack path as the crack crosses these interfaces. In the present case, the lowest aspect ratio corresponds to the 855°C (1575°F) recrystallization annealed material which also has the least-attractive strength-toughness combinations. Finally, the reduction in primary α-aspect ratio also is accompanied by an increase in microstructural scale. This results in a strength reduction as can be seen by comparing the properties of the β-annealed and recrystallization annealed conditions (Tables 3 and 4) with the surface replica microstructure photos shown in Figs. 22 and 23.

TABLE 5—*Mechanical properties of several Goal B alloys.*

Composition (bal Ti)	Heat Treatment: Recrystallize, °C	(°F)	Age, °C	(°F)	Tensile Properties: Direction	Ultimate Tensile Strength, MPa	(ksi)	Yield Strength, MPa	(ksi)	Elongation, %	Reduction in Area, %	E $\times 10^3$ MPa	E ($\times 10^6$ psi)	Fracture Properties, MPa$\sqrt{m}$ (ksi$\sqrt{in.}$): LT	K_Q	TL
Ti-11Mo-2.5Al	829	(1525)	510	(950)	L	1396	(202.6)	1292	(187.7)	3.5	2.4	116	(16.8)	0[a]		...
														0[a]		...
					T	1523	(221.0)	1393	(202.2)	5.0	3.6	120	(17.4)	...	40 (36.0)	
														...	37 (34.0)	
			552	(1025)	L	1348	(195.7)	1258	(182.6)	3.0	3.6	114	(16.6)	38 (34.6)		...
														50 (45.8)		...
					T	1391	(201.9)	1277	(185.4)	4.5	6.7	127	(18.5)	...	48 (44.0)	
														...		
			593	(1100)	L	1206	(175.0[b])		no test					59 (53.2)		...
																...
					T				no test					...		
Ti-8Mo-2.5Al-1.5Cr	829	(1525)	538	(1000)	L				invalid test					7 (6.5[c])		...
														35 (32.0)		...
					T	1517	(220.2)	1461	(212.1)	5.0	5.6	115	(16.7)	...	25 (22.4)	
														...	31 (28.1)	
			593	(1100)	L	1240	(180.0[b])		no test					52 (47.0)		...
														72 (65.0)		...
					T				no test					...		
Ti-8Mo-2.5Al-4.5Cr	802	(1475)	496	(925)	L	1435	(208.3)	1432	(207.8)	1.0	1.6	118	(17.1[c])	38 (34.8)		...
					T	1633	(237.0)	1465	(212.6)	2.0	3.2	114	(16.5[c])	...	40 (36.1)	
														...	39 (35.4)	
			538	(1000)	L	1229	(178.4)	1229	(178.4)	1.0	1.6	119	(17.2[c])	41 (37.1)		...
														38 (34.4)		
					T	1737	(252.1)	1655	(240.2)	1.0	2.8	112	(16.3)	...	35 (32.0)	
														...	24 (26.4)	
			593	(1100)	L	1254	(182.0)	1179	(171.1)	3.5	2.8	119	(17.3)	64 (58.4)		...
														64 (57.9)		...
					T				no test						65 (59.2)	
															61 (55.8)	

[a] Precrack very deep.
[b] Estimated from hardness (VPN) value using regression analysis from deep hardenable contract F33615-71-C-1525[*12*].
[c] Estimated value.

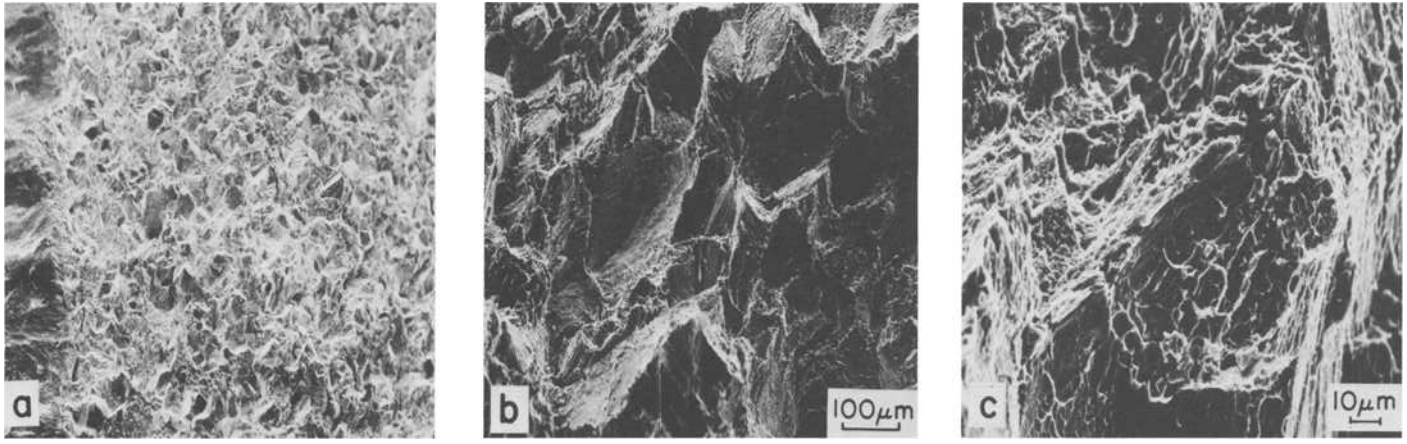

FIG. 19—*Scanning electron fractography of specimen shown in profile in Fig. 18.* (a) *Low magnification of fatigue precrack-fast fracture transition showing blocky, intergranular appearing fracture.* (b) *Higher magnification showing grain boundary facets.* (c) *Still higher magnification showing that fracture mode is microvoid formation and tearing.*

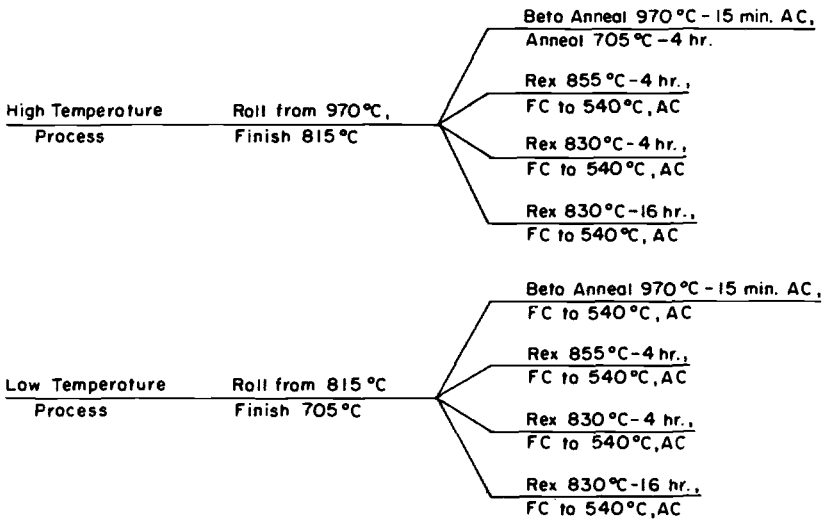

FIG. 20—*Schematic of processing and heat treatment schedule for further studies of Ti-5Mo-4.5Al-1.5Cr.*

Goal B—The properties of some of the various Goal B alloys are shown in Table 5. These also were plotted as UTS versus K_Q in order to assess each alloy's potential for meeting goal properties. Several of the resulting strength-toughness trend lines are shown in Figs. 26 through 28. These trends were used to select the alloy Ti-8Mo-2.5Al-4.5Cr for further study. Table 6 shows additional property data for this alloy processed and subsequently heat treated to a total of eight different conditions as described in Table 2. These properties and the trends in Figs. 26 through 28 also show that the metastable β-alloys which are intended to meet Goal B properties have somewhat more severe toughness-strength limitations than were originally considered. Also, it is apparent that a significant degree of directionality of properties exists, probably due to $\alpha + \beta$ working, that is, the toughness of TL specimens is consistently less than that of LT specimens. The origin of the directionality of toughness appears to be partly connected with the presence of elongated β-grains which contain grain boundary α and with elongated primary α. However, examination of Fig. 6 and the data in Table 6 shows that even in the low temperature ((760°C) (1400°F)) annealed material (Fig. 6(*c*)), which contains more nearly equiaxed primary α and very little grain boundary α, that a distinct directionality in properties exists. In the materials which contain extensive grain boundary α (Fig. 6(*a*) and (*b*)), the studies of the fracture paths and fracture topographies showed that the elongated β-grain structure causes significant differences in fracture topography and path for TL and LT

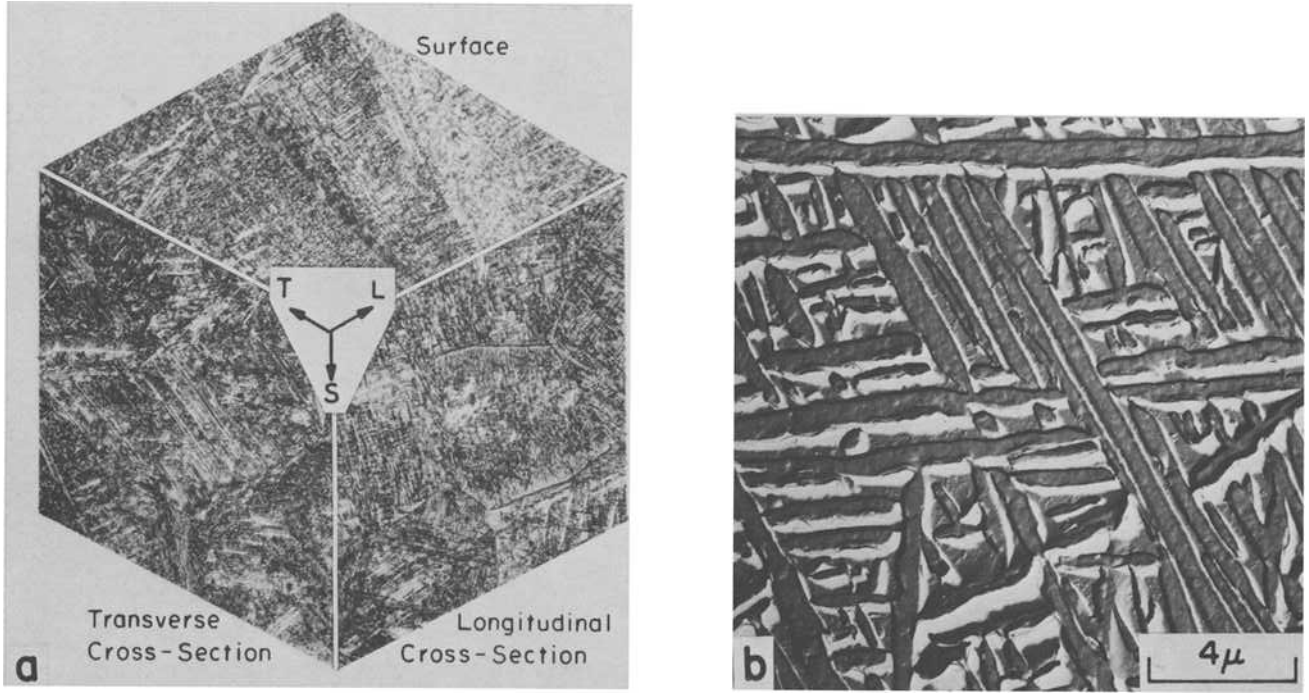

FIG. 21—*Light and electron micrographs showing very acicular and grain boundary α in β-annealed Ti-5Mo-4.5Al-1.5Cr.* (a) *Light micrographs in isometric cube.* (b) *Surface replica electron micrograph.*

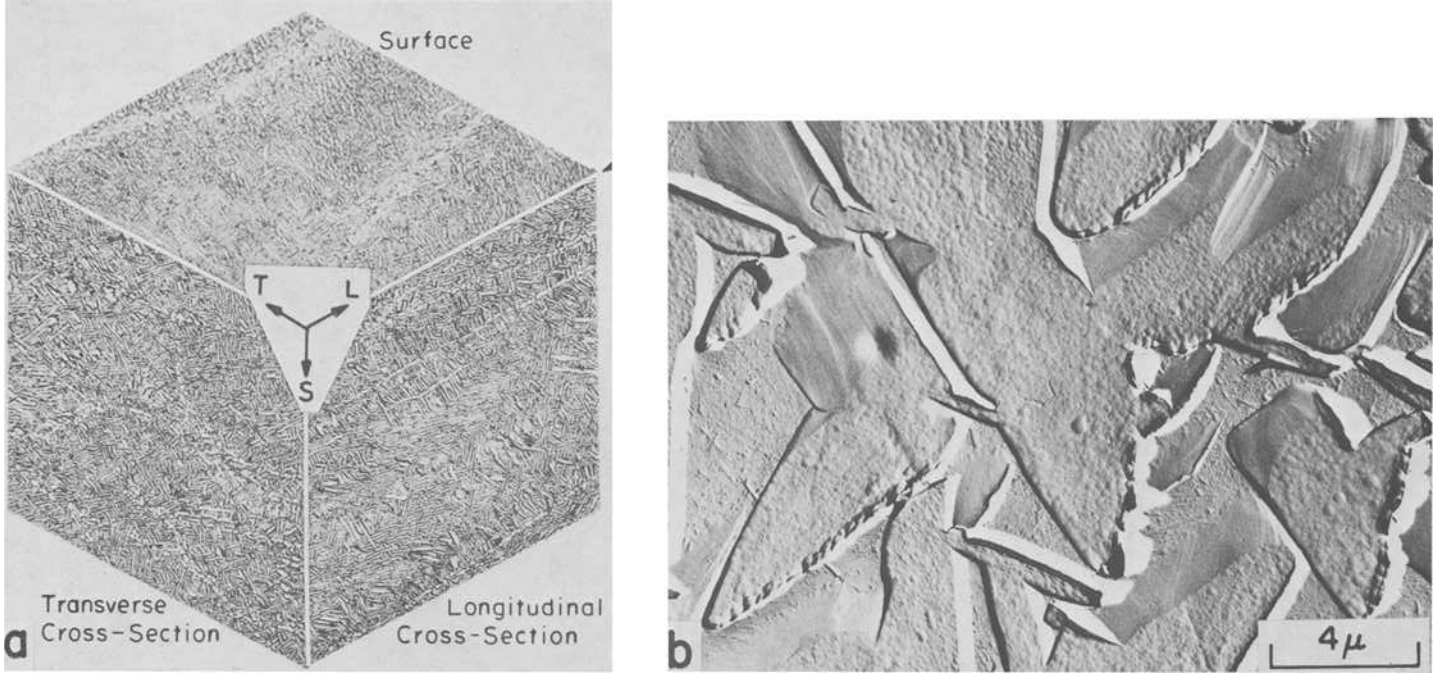

FIG. 22—*Light and electron micrographs showing lower aspect ratio acicular α and less pronounced grain boundary α in Ti-5Mo-4.5Al-1.5Cr annealed 4 h at 855°C.* (a) *Light micrographs in isometric cube.* (b) *Surface replica electron micrograph.*

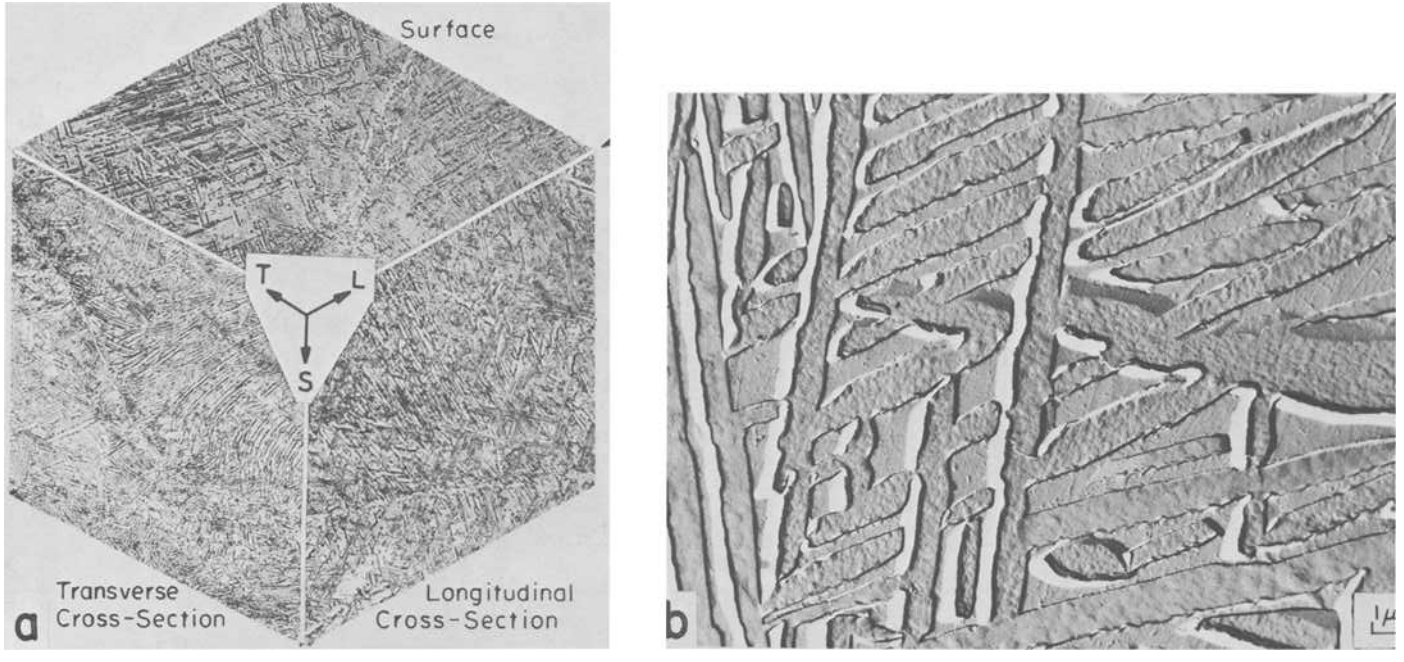

FIG. 23—*Light and electron micrographs showing acicular α in Ti-5Mo-4.5Al-1.5Cr annealed 4 h at 830°C.* (a) *Light micrographs in isometric cube.* (b) *Surface replica electron micrograph.*

TABLE 6—*Additional mechanical property data for Ti-8Mo-2.5Al-4.5Cr alloy.*

Processing Route [a]	Annealing Treatment [b]	Aging Treatment [c]	Direction	Mechanical Properties: Tensile Properties: Ultimate Tensile Strength MPa	(ksi)	Yield Strength MPa	(ksi)	Elongation, %	Reduction in Area, %	E $\times 10^3$ MPa	($\times 10^6$ psi)	Toughness, K_v [d]: MPa$\sqrt{m}$ LT	(ksi$\sqrt{in.}$) TL
H	H	H	L	1103	(160.1)	1064	(154.4)	10.5	16.8	105	(15.3)	85 (77.7)	...
												84 (76.7)	...
			T	1209	(175.4)	1160	(168.3)	3.0	5.9	119	(17.3)	...	72 (65.4)*
												...	65 (58.8)
		L	L	1319	(191.5)	1256	(182.3)	4.0	10.0	107	(15.5)	55 (50.0)	...
												49 (44.5)	...
			T	1454	(211.1)	1387	(201.3)	2.0	3.8	109	(15.8)	...	40 (36.5)
												...	49 (44.7)
	L	H	L	1055	(153.1)	1014	(147.2)	14.0	34.5	103	(14.9)	97 (88.2)	...
												105 (95.7)	...
			T	1109	(160.9)	1071	(155.4)	12.0	21.2	108	(15.7)	...	90 (82.0)
												...	75 (68.4)
		L	L	1178	(170.9)	1096	(159.1)	8.5	16.8	101	(14.7)	75 (68.3)	...
												59 (53.5)	...
			T	1288	(186.9)	1216	(176.5)	4.5	10.6	108	(15.7)	...	45 (41.1)
												...	44 (39.9)

L	H	H	L	1109	(161.0)	1079	(156.6)	15.0	36.2	104	(15.1)	81 (72.8) 81 (73.8)	... ...	
			T	1206	(175.0)	1160	(168.4)	5.0	9.5	107	(15.5)	... ...		74 (66.9)* 66 (60.2)
		L	L	1361	(197.5)	1305	(190.9)	5.5	8.0	101	(14.6)	40 (36.1) 44 (40.3)	... ...	
			T	1437	(208.6)	1377	(199.8)	2.5	5.3	115	(16.7)	... ...		44 (39.7) 41 (37.0)
	L	H	L	1038	(150.7)	1027	(149.1)	18.0	61.3	96	(14.0)	90 (82.2)* 89 (80.5)	... ...	
			T	1151	(167.0)	1119	(162.4)	12.5	20.4	110	(15.9)	... ...		80 (72.7)* 74 (67.0)
		L	L	1187	(172.3)	1168	(169.5)	12.5	31.7	106	(15.4)	62 (56.6) 64 (58.1)	... ...	
			T	1290	(187.2)	1233	(178.9)	9.0	19.8	109	(15.8	... ...		62 (56.8) 60 (54.9)

[a] H=high processing route (roll from 913°C (1675°F) with reheats at 802°C (1475°F)), and
L=low processing route (roll from 802°C (1475°F) with reheats at 691°C (1275°F)).
[b] H=high annealing treatment (8 h ReX at 788°C (1450°F), and
L=low annealing treatment (8 h ReX at 760°C (1400°F).
[c] H=high age (8 h at 607°C (1125°F), and
L=low age (8 h at 552°C (1025°F).
[d] Calculated from slow bend precracked Charpy specimens using

$$K^2 = \frac{W}{A} \times \frac{E}{2(1-\nu^2)}$$

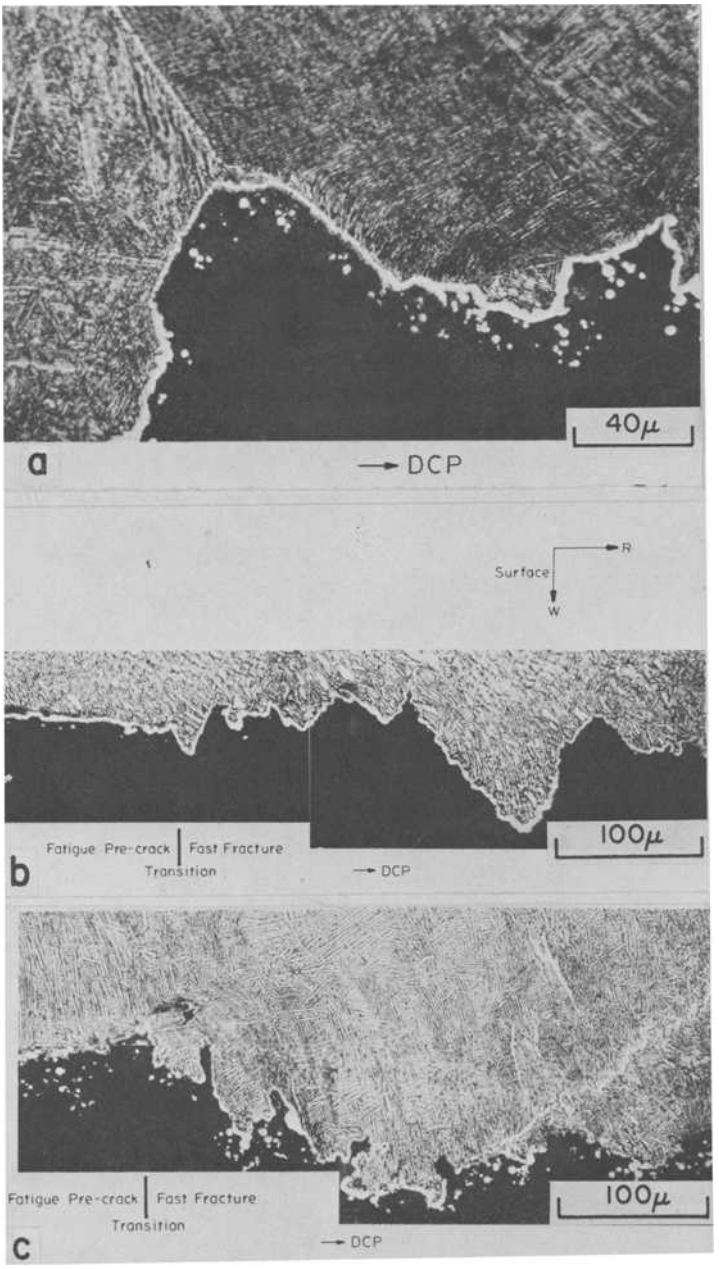

FIG. 24—*Light micrographs showing fracture paths in materials shown in Figs. 21, 22, and 23:* (a) *Fig. 21,* (b) *Fig. 22,* and (c) *Fig. 23.*

toughness specimens. In contrast to the 760°C (1400°F) annealed material, these differences are more apparent on a microscopic than on a macroscopic scale. This is shown in Fig. 29 for the higher temperature ((788°C) (1450°F)) annealed material (see Table 6). In the LT specimens, the crack front encounters a larger number of β-grain boundaries which cause the crack to deviate, usually with attendant secondary cracking. These factors have been suggested to lead to higher toughness values since more energy is expended in crack propagation [*3*]. In all cases, when both grain boundary fracture and transgranular fracture are observed, the mechanism of fracture is microvoid formation, growth, and coalescence. This is illustrated in Figs. 29 through 31. Similar features are observed in the other microstructural condition in which grain boundary α is present (Fig. 6(*b*)). In the low temperature annealed material (Table 6) which contains mostly intragranular primary α, the fracture is largely transgranular as shown in Fig. 31. However, even in this case, there is significant directionality of fracture toughness. The microstructural basis for this is less clear in this case, but the macroscopic fracture appearance (Fig. 32) shows that the LT specimen has a more irregular fracture surface than the TL specimen and hence there is probably more energy dissipated during crack propagation. The origin of this roughness may be an elongated β-grain structure which is less obvious because it is not decorated with grain boundary α. Since this condition exhibits the highest toughness, some additional understanding of this point would be helpful. It is interesting to note the contrast between the micro- and macrofracture appearances in this microstructural condition and that which contains grain boundary α (Fig. 6(*a*)) mentioned earlier. In the latter case, the microscopic appearances of LT and TL specimens were very different whereas the maroscopic appearances were not. In the former case (Fig. 6(*c*)), the opposite is true.

Comparison of the Effect of Microstructure on Fracture Toughness of Metastable β and $\alpha + \beta$ Titanium Alloys

The foregoing makes it clear that one microstructural feature important to the understanding of fracture toughness in titanium alloys is grain boundary α. Further, in high strength $\alpha + \beta$ alloys such as β-forged Ti-6A1-2Sn-4Zr-6Mo (Ti-6-2-4-6) the presence of grain boundary α leads to a preferred fracture along prior β-grain boundaries with extensive secondary or branch cracking [*3*]. In β-alloys, grain boundary α leads to a similar fracture behavior [*1,2*]. However, there is a paradox when the effect of grain boundary α on properties is considered. In high strength $\alpha + \beta$ alloys such as Ti-6-2-4-6, the K_{Ic} values associated with the fracture mode just described are significantly higher (as much as 50 percent) than those associated with transgranular fractures when globular primary α is pres-

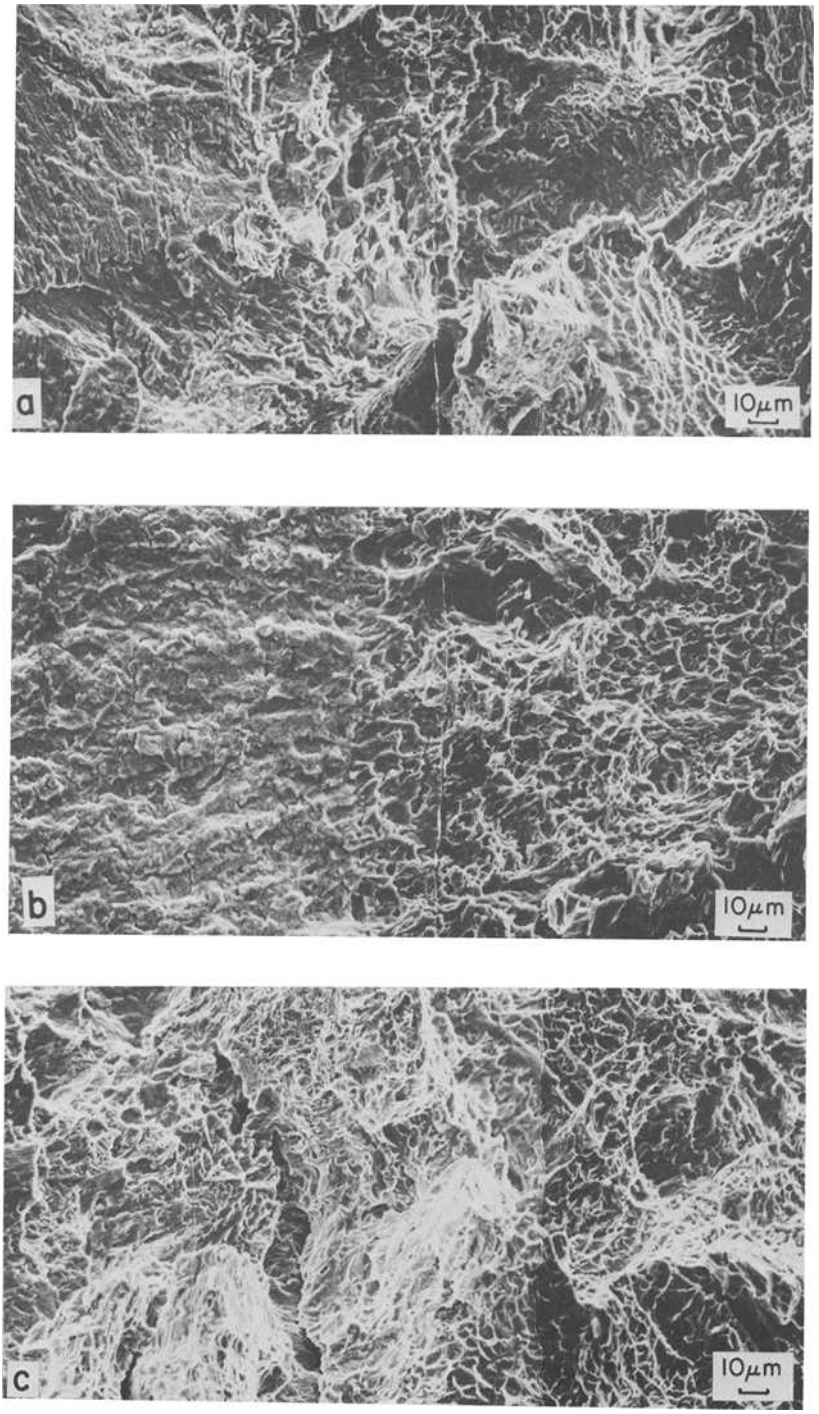
a
10μm
b
10μm
c
10μm

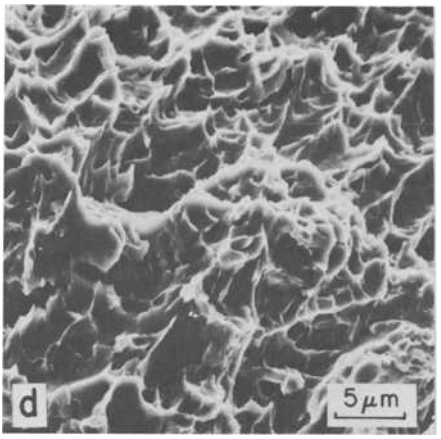

FIG. 25—*Scanning fractographs showing effect of microstructure on fracture topography in the fatigue precrack-fast fracture regions of Ti-5Mo-4.5Al-1.5Cr.* (a) *For microstructure and fracture path shown in Figs. 21 and 24*(a). (b) *For microstructure and fracture path shown in Figs. 23 and 24*(b). (c) *High magnification fractograph showing microvoid coalescence and tearing typical of all three fractures above when examined at higher magnifications.*

ent [*3*]. On the other hand, the toughness drops (as much as 20 percent) in β-alloys when grain boundary α is present [*1,2,11*]. This effect can be rationalized if the relative strengths of the grain boundary α and the precipitation strengthened matrix are considered. In $\alpha + \beta$ alloys, the strength of the $\alpha + \beta$ matrix typically is less than in metastable β-alloys because the dispersion of α-phase precipitates is coarser and the precipitates are larger.

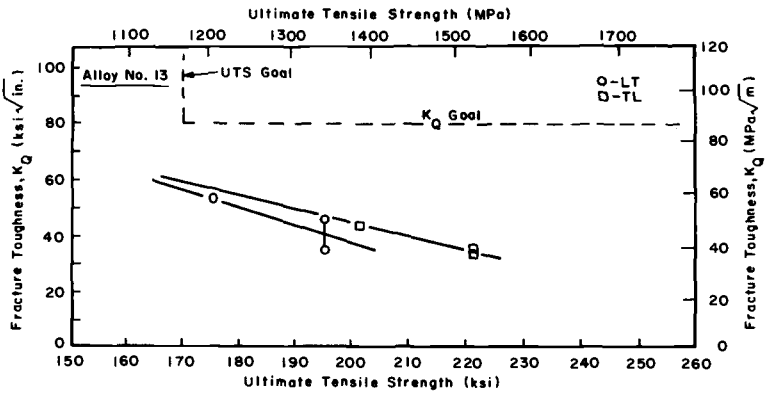

FIG. 26—*Strength-toughness trend for Ti-11Mo-2.5Al.*

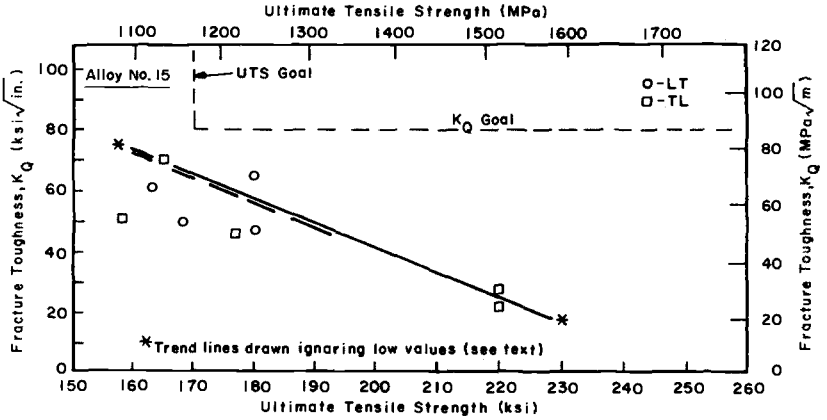

FIG. 27—*Strength-toughness trend for Ti-8Mo-2.5Al-1.5Cr.*

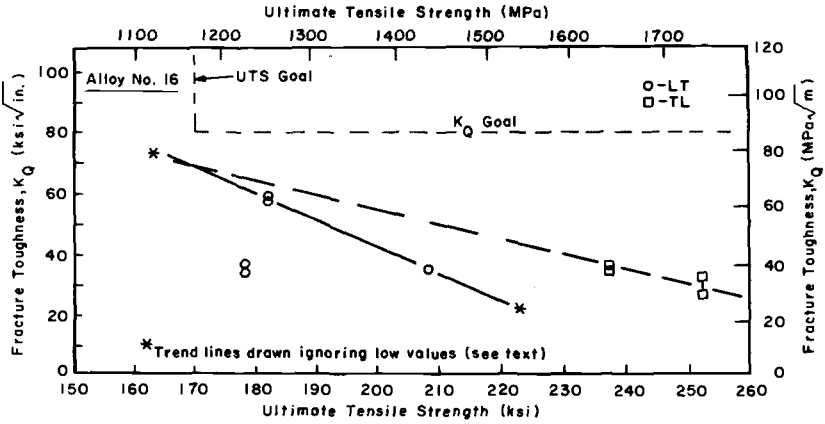

FIG. 28—*Strength-toughness trend for Ti-8Mo-2.5Al-4.5Cr.*

Also, because aluminum partitions to and solid solution strengthens the grain boundary α-phase, the grain boundary α-phase is stronger in $\alpha + \beta$ alloys than in metastable β-alloys which have lower aluminum contents. These two factors work in unison to create a much larger strength difference between the grain boundary α and the matrix in the metastable β-alloys than in $\alpha + \beta$ alloys. As a result, the plastic zone is largely, if not exclusively, confined to the grain boundary α in the metastable β-alloys, whereas it can spread into the matrix in the $\alpha + \beta$ alloys. This is shown schematically in Fig. 32(*a*) and (*b*). As a result of this localized plastic inhomogeneity, the effective plastic zone size is much smaller in the metastable β-alloys, even though at comparable yield strengths continuum theory would predict comparable plastic zones [*13*]. This factor tends to lower the toughness of the metastable β-alloys in the presence of grain

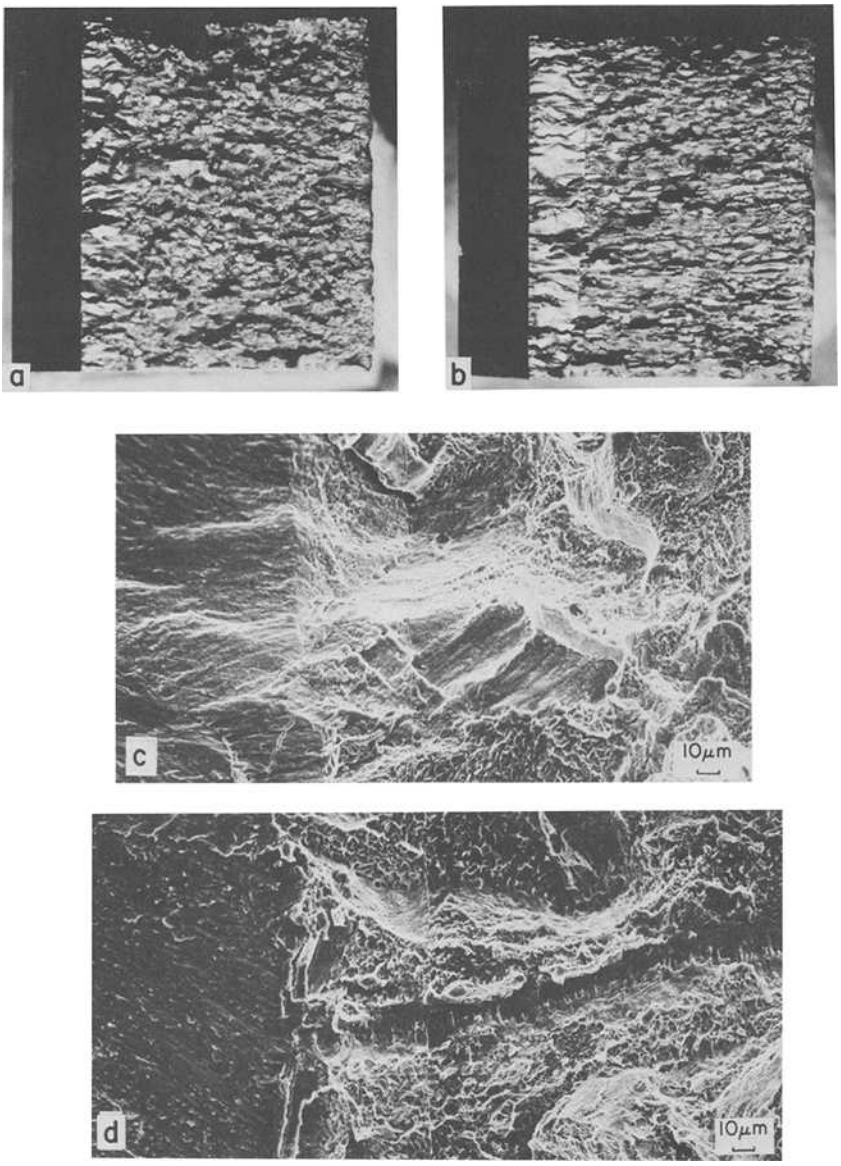

FIG. 29—*Illustrating the effect of specimen orientation on fracture topography of Ti-8Mo-2.5Al-4.5Cr in microstructural condition shown in Fig. 6*(a). (a) *LT specimen at ~X4.8 magnification.* $K_v = 72\ MPa\sqrt{m}$. (b) *TL specimen also at X4.8.* $K_v = 85\ MPa\sqrt{m}$. (c) *Electron fractograph of fatigue precrack-fast fracture transition. Showing tortuous fracture path in LT specimen,* $K_{Ic} = 83\ MPa\sqrt{m}$. (d) *Similar to* (c) *but showing less tortuous fracture path in TL specimen,* $K_{Ic} = 72\ MPa\sqrt{m}$.

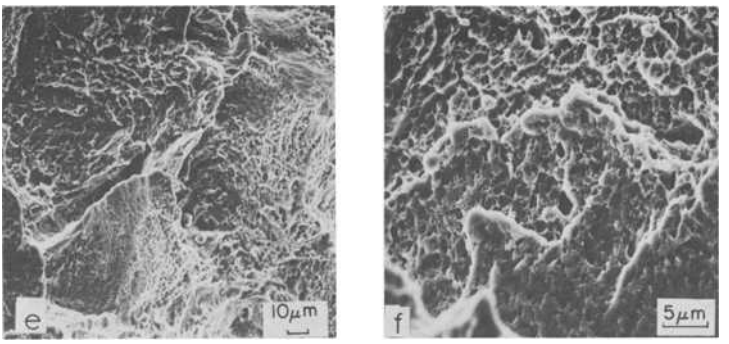

FIG. 29—*Continued* (e) *Electron fractograph showing secondary cracking in TL specimen.* (f) *Higher magnification fractograph showing microvoid coalescence fracture typical of both LT and TL specimens when examined at high magnification.*

boundary α. On the other hand, grain boundary α promotes prior β-grain boundary cracking and extensive secondary cracking at grain boundary triple points. In the α + β alloys, where the plastic zone is not as extensively constricted by the microstructure, this factor adds to the energy dissipated in the fracture process and leads to an increased toughness [*3*]. In metastable β-alloys, the constriction of the plastic zone by the weaker grain boundary α overrides this effect with the net result of lowering the toughness.

Summary and Conclusions

In this paper we have described the effect of alloy composition, heat treatment, and processing history on the microstructure of a series of titanium alloys ranging from α + β to the metastable β-type. The properties of these alloys have also been determined, and electron fractography has been used extensively to relate properties to microstructure. Among the α + β alloys studied, one composition was selected as particularly promising: Ti-5Mo-4.5A1-1.5Cr. This alloy exhibits attractive strength-toughness combinations in several microstructural conditions, but the β-processed condition, in which acicular α-phase is present together with α-phase at prior β-grain boundaries, had the best strength-toughness combinations. Fractographic and metallographic crack profile studies showed that the fracture path in the β-processed material largely follows the prior β-grain boundaries and that extensive crack branching accompanies the fracture. This has been suggested to contribute strongly to the high toughness associated with this microstructural condition.

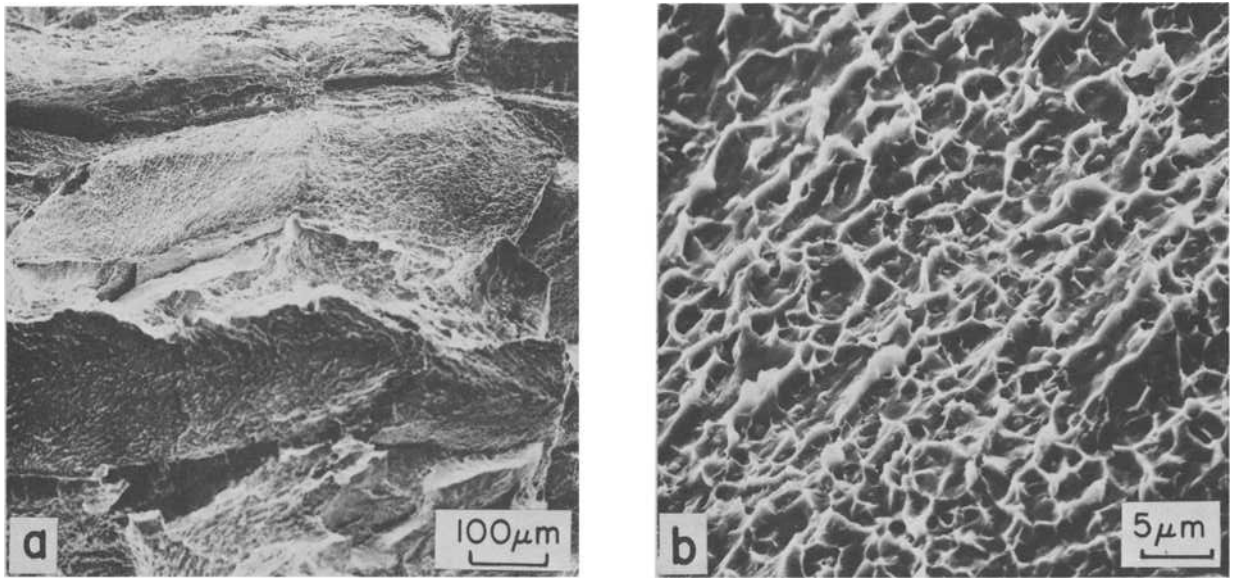

FIG. 30—*Electron fractographs showing details of prior β-grain boundary fracture in microstructures which exhibit extensive grain boundary α (see, for example, Fig. 6*(a)*.*(a) *Low magnification fractograph showing intergranular character of fracture.* (b) *Higher magnification fractograph showing microvoid formation mode on grain boundary facets.*

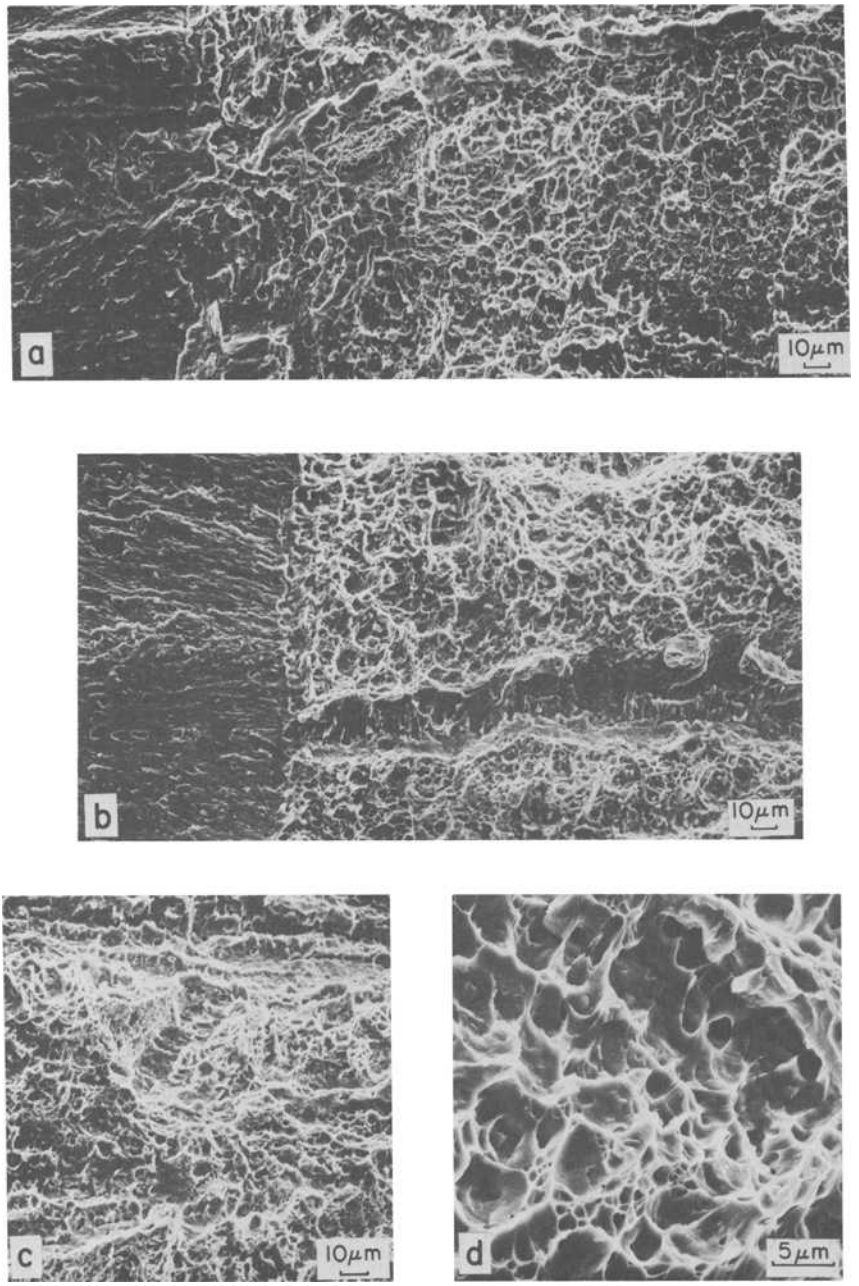

FIG. 31—*Electron fractographs and fracture path profiles in Ti-8Mo-2.5Al-4.5Cr which does not contain grain boundary α Fig. 6*(c). (a) *Fatigue precrack-fast fracture transition showing decreased crack path tortuosity in LT specimen* (K_v=*90 MPa*$\sqrt{m}$). (b) *Same as* (a) *but in a TL specimen* (K_v=*80 MPa*$\sqrt{m}$). (c), (d) *Fractographs showing details of microvoid coalescence fracture typical of* (a) *and* (b) *above.* (e) *Crack path profile in LT specimen.* (f) *Crack path profile in TL specimen.*

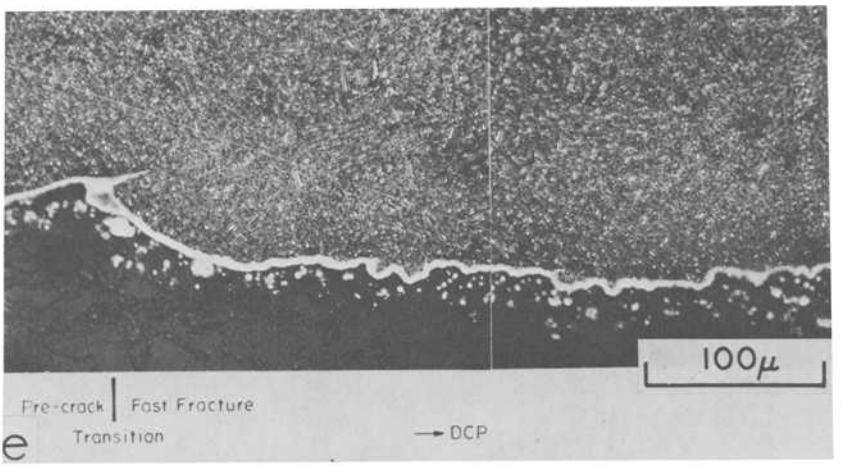

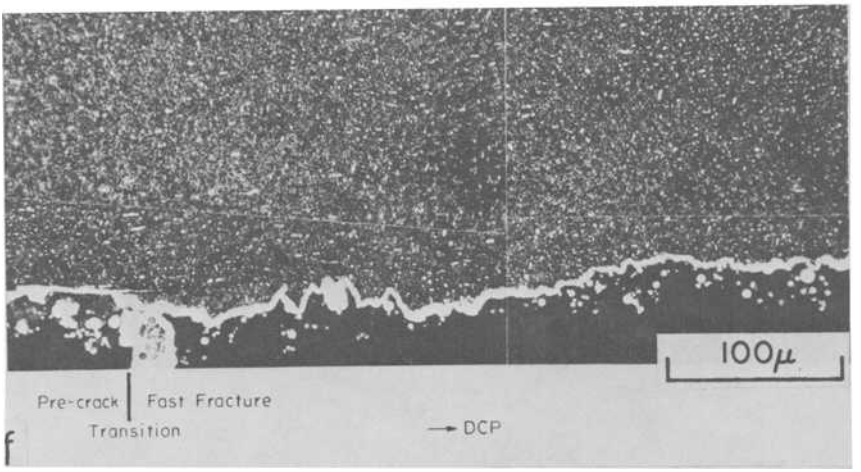

FIG. 31—*Continued*

Among the metastable β-alloys studies, one composition also was selected for further study: Ti-8Mo-2.5Al-4.5Cr. This alloy can be heat treated to much higher strengths than the $\alpha + \beta$ alloy but also exhibits lower toughness. Further, in contrast to the $\alpha + \beta$ alloy, the best strength-toughness combinations correspond to equiaxed primary α-microstructures rather than a microstructure which exhibits grain boundary α. Fractographic and metallographic crack path studies show that the fracture

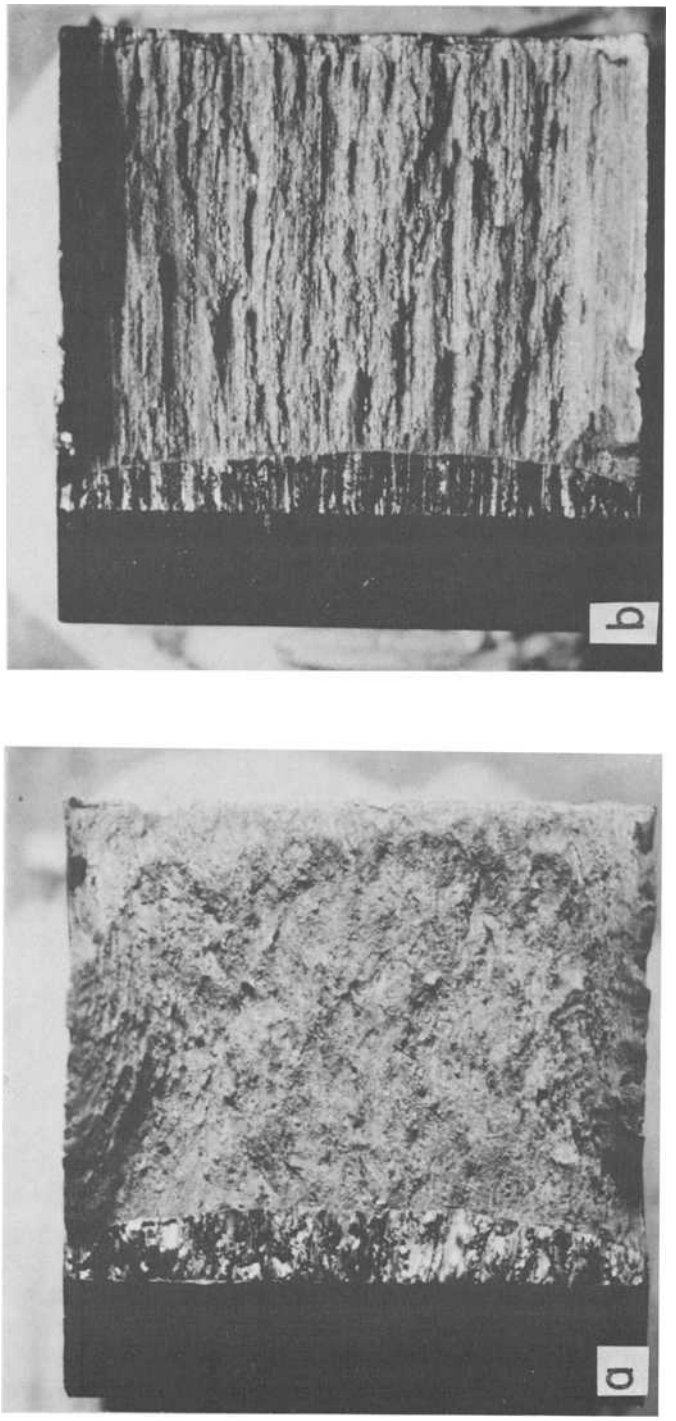

FIG. 32—*Low magnification photos (X8) showing the effect of specimen orientation on fracture topography in Ti-8Mo-2.5Al-4.5Cr in microstructural condition shown in Fig. 6*(c). (a) *TL specimen* $K_v = 77\ MPa\sqrt{m}$. (b) *LT specimen* $K_v = 89\ MPa\sqrt{m}$.

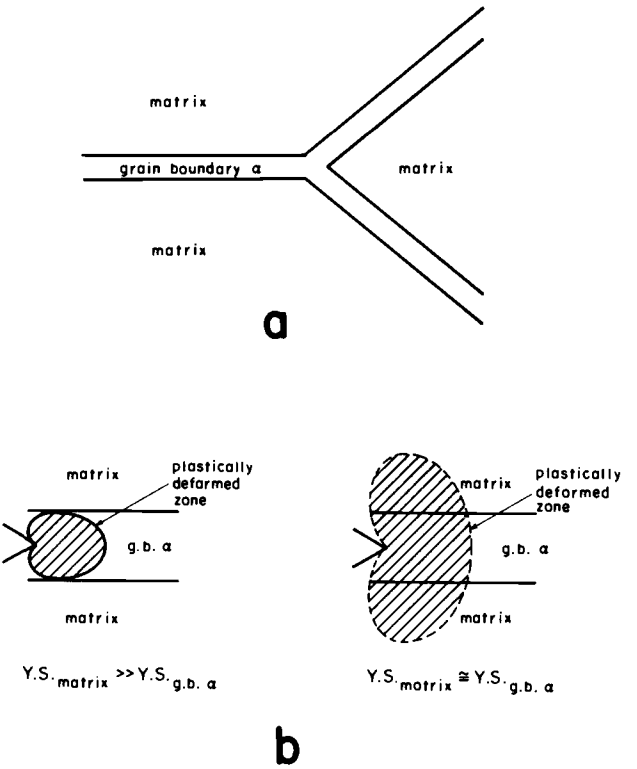

FIG. 33—*Schematic drawings showing the effects of the relative strengths of the grain boundary α and the α + β matrix on the plastic zone size during fracture.* (a) *YS matrix >> YS grain boundary α.* (b) *YS matrix ≅ YS grain boundary α.*

modes associated with these two microstructures are transgranular and largely intergranular, respectively. Thus the dependence of toughness on fracture mode is reversed between the α + β and metastable β-alloys studied. A qualitative model based on relative matrix and grain boundary α-strengths is suggested to account for this effect. The model incorporates the concept of restricted plastic zone size in the situation where the grain boundary α is decidedly weaker than the matrix. Such a restriction in plasticity is consistent with a reduced toughness.

Acknowledgments

The work reported here was performed under the sponsorship of the Naval Air Systems Command (Contract No. N00019-73-C-0335). The

authors gratefully acknowledge the experimental assistance of R. A. Hokowski, J. M. Capenos, C. F. Yolton, P. Q. Sauers, E. G. Wright, and R. A. Spurling. Helpful discussions with A. W. Thompson, J. P. Hirth, and A. G. Evans are also gratefully acknowledged.

References

[1] Froes, F. H., Chesnutt, J. C., Rhodes, C. G., and Williams, J. C.; "Relationship of Fracture Toughness and Ductility to Microstructure and Fractographic Features in Advanced Deep Hardenable Titanium Alloys," this volume, p. 115.

[2] Berryman, R. G., Froes, F. H., Chesnutt, J. C., Rhodes, C. G., Williams, J. C., and Malone, R. F.; "High Toughness Titanium Alloy Development," Technical Report TFD-74-65F, Naval Sir Systems Command, Washington, D. C., 1974.

[3] Chesnutt, J. C., Rhodes, C. G., and Williams, J. C. in *Fractography-Microscopic Cracking Processes, ASTM STP 600*, American Society for Testing and Materials, 1976, pp. 99-138.

[4] Spurling, R. A., *Metallurgical Transactions*, Vol. 6A, 1975, pp. 1660-1661.

[5] Copley, S. M. and Williams, J. C. in *Alloy Design*, Academic Press.

[6] Paton, N. E., Williams, J. C., Chesnutt, J. C., and Thompson, A. W., "The Effects of Microstructure on the Fatigue and Fracture of Commercial Titanium Alloys," Advisory Group for Aerospace Research and Development (NATO), Conference Proceedings #185, (1976), p. 4-1.

[7] Rosales, L. A., "Strengthening of Beta Titanium Alloys," Ph.D. thesis, U.C.L.A., 1973.

[8] Chesnutt, J. C. and Froes, F. H.; "Effect of α-Phase Morphology and Distribution on the Tensile Ductility of a Metastable β-Ti Alloy," *Metallurgical Transactions*, Vol. 8A, 1977, pp. 1013-1017.

[9] Williams, J. C., Thompson, A. W., Chesnutt, J. C., and Rhodes, C. G.; "Strengthening and Fracture of Titanium Alloys," A Review, Proceedings of 3rd International Titanium Conference, Moscow, 1975, in press.

[10] Ono, K., Rosales, L. A., Motokura, S., and Sommers, A. W.; "Mechanical Behavior of High Strength Beta-Titanium Alloys," Report NA-71-754, North American Rockwell Corporation, Aug. 1971.

[11] Froes, F. H., Malone, R. F., Petersen, V. C., Rhodes, C. G., Chesnutt, J. C., and Williams, J. C.; "Research on Deep Hardening Titanium Alloy for Large Airframe Structural Members," Technical Report AFML-TR-75-41, Vols. I and II, Air Force Materials Laboratory, Wright-Patterson, Ohio, 1975.

[12] Froes, F. H., Capenos, J. M., and Wells, M. G. H. in *Titanium Science and Technology*, R. I. Jaffee and H. M. Burte, Eds., Plenum Press, 1973, p. 1621.

[13] Knott, J. F., *Fundamentals of Fracture Mechanics*, Halstead Press, Wiley, New York, 1973.

F. H. Froes,[1] *J. C. Chesnutt,*[2] *C. G. Rhodes,*[2] *and J. C. Williams* [3]

Relationship of Fracture Toughness and Ductility to Microstructure and Fractographic Features in Advanced Deep Hardenable Titanium Alloys

REFERENCE: Froes, F. H., Chesnutt, J. C., Rhodes, C. G., and Williams, J. C., **"Relationship of Fracture Toughness and Ductility to Microstructure and Fractographic Features in Advanced Deep Hardenable Titanium Alloys,"** *Toughness and Fracture Behavior of Titanium, ASTM STP 651,* American Society for Testing and Materials, 1978, pp. 115–153.

ABSTRACT: This paper describes the results of a program conducted to develop a metastable β titanium alloy with deep hardening characteristics and with a yield strength of 1165 MPa (170 ksi), a fracture toughness of 66 MPa$\sqrt{m}$ (60 ksi$\sqrt{in}$), and tensile ductility of 12 percent elongation and 18 percent reduction of area. After a screening study, three compositions were chosen: Ti-10Mo-6Cr-2.5Al (Alloy 334), Ti-7Mo-4Cr-2.5Al (Alloy 227), and Ti-10Mo-8V-2.5Al (Alloy 253). Both β-working and β followed by α-β working were investigated as means of controlling the primary α distribution. Three distinct microstructures were subjected to extensive testing together with microstructural and fractographic analysis. It was found that grain boundary α was detrimental to properties in most cases. Stringered α, resulting from β-working, caused a directionality in mechanical properties with longitudinal values being higher than those in the transverse direction. Lenticular primary α was generally beneficial to toughness, whereas equiaxed or globular primary α was beneficial to tensile ductility. The predominant role of secondary (aged) α was in influencing strength level. The causes for these property variations with α phase morphology were analyzed using metallographic fracture face profiling and scanning electron fractography. It was found that the α-β interfaces initiate fracture and thus have a large influence on fracture related properties. Finally, the properties of the three metastable β alloys were compared to those of high strength, deep hardening α/β alloys.

[1] Manager, Titanium Research and Development, Colt Industries, Crucible Materials Research Center, Pittsburgh, Pa. 15230.

[2] Members of technical staff, Science Center, Rockwell International, Thousand Oaks, Calif. 91360.

[3] Associate professor, Carnegie-Mellon University, Pittsburgh, Pa. 15213.

Copyright© 1978 by ASTM International www.astm.org

More attractive strength-toughness combinations are achievable in the metastable β alloys. The tensile ductilities of the α-β alloys were somewhat higher than those of the metastable β alloys. However, ductilities of the latter class of alloys were acceptable.

KEY WORDS: titanium, crack propagation, fractures (materials), deep hardenable, titanium alloys, mechanical properties, fractography, microscopy, microstructure

Nomenclature

YS	Yield strength
K_{Ic}	Fracture toughness obtained in accordance with ASTM Test for Plane-Strain Fracture Toughness of Metallic Materials (E 399-72)
K_r	Toughness value obtained from slow bend precracked Charpy specimens [*1*] [4]
d	Interparticle spacing of fine (secondary) α
L, R, C	Major directions in billet (Fig. 1)
L, T, S	Major directions in plate (Fig. 1)
DCP	Direction of crack propagation, from left to right

Titanium alloys were initially attractive for airframe applications primarily because of their high strength-to-density ratio. Early optimization studies focused on improving this ratio by utilizing age hardening to achieve even higher strength conditions. More recently it has been recognized that strength increases in isolation are not useful and, accordingly, improvements in fracture toughness have been sought in optimization studies. The traditional α/β titanium alloys, the most common of which is Ti-6Al-4V, have other attractive characteristics such as a relatively high modulus-to-density ratio and good ductility. However, they suffer from the deficiencies of (*a*) exhibiting low fracture toughness in the high strength condition, and (*b*) not being deep hardenable [*2*]. In this context, the term "deep hardenable" refers to the ability to achieve acceptable mechanical property levels in heavy sections with a minimum variation in these properties through the thickness. In contrast, the heat treatable β-alloys are inherently deep hardenable because of their high alloy content, and they exhibit superior fracture toughness when compared to α-β alloys heat treated to comparable high strength levels. Shortcomings of the metastable β alloys which inhibit use

[4] The italic numbers in brackets refer to the list of references appended to this paper.

in heavy sections are tensile ductility, particularly in the transverse direction when the alloys are in the aged condition, and a low elastic modulus:density ratio.

In view of these shortcomings, a program was initiated to develop alloys which have deep hardenability, good fracture toughness, and good tensile ductility. In this program, alloy compositions were selected which potentially combine the deep hardenability, high strength capability, and high fracture toughness of the heat treatable β alloys wtih the tensile ductility and elastic modulus of the α/β alloys [*3*]. This was achieved by choosing a compositional range based on a lean heat treatable β alloy composition. Specific program goals were then to maintain a strength level of approximately 1165-MPa (170-ksi) yield strength and a fracture toughness of 66 MPa$\sqrt{m}$ (60 ksi$\sqrt{in.}$), typical of advanced β titanium alloys [*2*] in all directions throughout a wrought 150-mm (6-in.) bar. At the same time, ductilities characteristic of the α/β alloys at this strength level, 12 percent elongation and 18 percent reduction in area, were required. By solution treating below the β-transus temperature, primary α was produced which is directly beneficial to both tensile ductility and elastic modulus. In addition, this primary α results in an enrichment of the remaining β-matrix in β-stabilizing elements with an attendant improvement in deep hardenability at modest total alloy content. This effect is particularly pronounced when alloy additions which partition strongly to the β-phase are chosen. Examples of such additions are molybdenum, vanadium, and chromium. The enriched β-matrix was then sufficiently stable to exhibit relatively slow decomposition during cooling, allowing subsequent aging. Alloy density was lower than conventional β-alloys because of the reduced addition of heavy alloying elements. Concurrently, addition of aluminum, an α-stabilizing element, strengthened the α-phase and raised its modulus. Complete details of alloy design and heat treatment cycles are given elsewhere [*3-5*].

The present paper will discuss the relationship between processing history/heat treatment and microstructures and, in turn, mechanical properties of three metastable β-alloys. The properties of these alloys, developed under the present investigation, are compared with current state-of-the-art deep hardenable alloys in the final section. A complete account of the full program, which was conducted in three phases, can be found elsewhere [*3*].

Experimental Procedure

The starting stock for both the 150-mm (6-in.) billet and 12-mm (½-in.) plate studied in this program was 270-mm (10.5-in.) round-corner-square (RCS) bloom. This bloom was produced from a 240-kg (500-lb), 380-mm (15-in.) diameter ingot by a tridirectional upset and drawout operation which imparted a large amount of work into the material.

Complete details of this operation are given elsewhere [*3*]. Average chemistry for the three alloys is given in Table 1 and shows good agreement with nominal (formulated) compositions. Details of the final processing to the two product forms and postprocessing heat treatments are given in Table 2. Thermomechanical processing of Alloy 253 was identical to that used for Alloy 334 [*3*].

Specimens were cut such that the loading axis of the tension specimens was parallel to the loading axis of the fracture toughness specimens (K_{Ic} and K_v [*1*]). The nomenclature used to define specimen orientation in plate and billet is that defined in ASTM Test E 399-72 and is shown in Fig. 1. Posttest analysis of specimens consisted of light, surface replica and thin foil microscopy and examination of fractographic features by crack path analysis and scanning electron microscopy.

Standard light metallographic examination was conducted on specimens representing the three principal planes of the product forms. Isometric projections of these microstructures were constructed for the conditions studied. Surface replicas were prepared from metallographically polished and lightly etched samples. Metal shadowed plastic replicas were then prepared and examined using a transmission electron microscope. A uniform magnification of $\times 5200$ was used for the surface replica photomicrographs shown throughout this report. Thin foils were prepared by techniques described in detail elsewhere [*6*] and examined using a transmission electron microscope.

Crack path analysis was carried out using fractured specimens (mainly slow-bend precracked Charpy specimens) which were first coated with a protective lacquer and then a transverse section approximately 6 mm (0.25 in.) thick containing the fracture face was cut off. The lacquer was removed, the specimen was cleaned, and an edge preservative was applied as directed by the manufacturer. The coated specimen was then mounted so that a plane orthogonal to the fracture surface, with the direction of crack propagation contained in this plane, could be examined. This examination was carried out at locations approximately halfway across the fracture face in the direction at right angles to the crack propagation direction. In the majority of cases, the transition from the relatively flat fatigue crack to the

TABLE 1—*Alloy chemistry.*[a]

Alloy	Mo	Cr	V	Al	O_2	H_2	N_2	C	Fe	Ti
334	9.7	6.1	...	2.7	0.13	0.0029	0.008	0.020	0.06	bal
227	6.6	4.1	...	2.5	0.13	0.0015	0.010	0.021	0.09	bal
253	9.9	...	8.1	2.5	0.17	0.0007	0.013	0.016	0.09	bal

[a] Average values.

TABLE 2—*Processing and heat treatment summary.*[a]

Alloy Condition	Alloy	Product Form	Primary Breakdown	Finish	Anneal,[b] °C(°F) First	Anneal,[b] °C(°F) Second	Age, °C(°F)
A	334	150-mm billet	Tridirectional β breakdown to 250-mm RCS in all alloys	low β-process to 150-mm	700 (1300) 4 h	...	480 (900) 96 h
	227	150-mm billet		low β + high α-β process to 150-mm	800 (1475) 2 h	...	550 (1025) 8 h
B	334	150-mm billet		low β-process to 150-mm	830 (1525) 1 h	700 (1300) 4 h	480 (900) 96 h
	227	150-mm billet		low β + high α-β process to 150-mm	860 (1575) 0.5 h	800 (1475) 2 h	550 (1025) 8 h
C	334	12-mm plate		β-process α-β finish to 12-mm	730 (1350) 8 h	...	550 (1025) 96 h
	227	12-mm plate		β-process low α-β finish to 12-mm	790 (1450) 8 h	...	550 (1025) 8 h
D	334	150-mm billet		low β-process to 150-mm	730 (1350) 4 h	670 (1225) 2 h	...
	227	150-mm billet		low β + high α-β process to 150-mm	790 (1450) 2 h	730 (1350) 8 h	...

[a] Alloy 334, β-transus, 775°C (1425°F) and Alloy 227, β-transus, 830°C (1525°F).
[b] Followed by water quench.

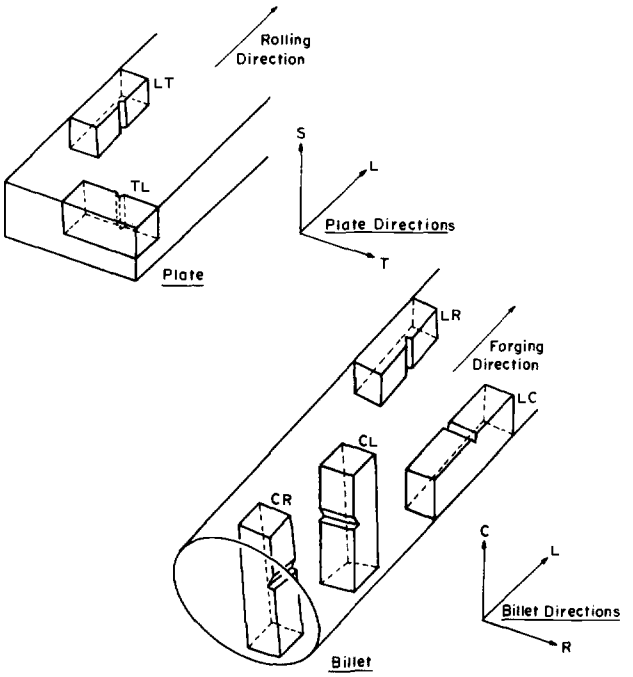

FIG. 1—*Orientation nomenclature for plate and billet, in accordance with ASTM Test E 399-72.*

fast fracture region was easily discernible. Examination of the fracture face was carried out both optically and by using a scanning electron microscope (SEM) capable of 100Å resolution. Specimens were examined at 20 kV and 30-deg tilt. In all figures, fracture surfaces are shown with the direction of crack propagation (DCP) from left to right. In view of the strong directionality which can occur in alloys of the type studied, the direction of maximum working and other major directions were identified where possible.

In addition to these microstructure and fractographic characterization techniques, pole figures were used to determine the β-matrix texture. The method used was the one quadrant reflection technique described in detail by Olsen [7].

The majority of the toughness values reported in this paper were obtained using the slow-bend precracked Charpy method (K_v), a method which allows a relatively inexpensive and quick screening of fracture toughness [1]. A good one-to-one relationship existed between these values and valid K_{Ic} values (derived in accordance with ASTM Test E 399-72) at least to the 130-MPa$\sqrt{\text{m}}$ (120-ksi$\sqrt{\text{in.}}$) level. This is shown in Fig. 2 where

each point is the average of at least two values for each parameter. Thus it was felt that the K_r values presented herein are adequate to rank the toughness of the various alloys and microstructural conditions.

Results

Microstructural Development

As with other classes of titanium alloys such as the α/β alloys [*8*], the microstructure of metastable β-titanium alloys depends on both the thermal and mechanical processing sequences which have been imposed on it. A detailed description of the microstructural behavior of the metastable β-class of titanium alloys has recently been given [*2*] so that only a brief summary will be presented here. Above a critical temperature, commonly referred to as the β-transus temperature, the alloy is single-phase β and the microstructure consists only of β-phase grains. Below this critical temperature, at least four β-phase decomposition products can be formed, depending on β-phase composition and temperature. These are α-phase, ω-phase, martensite (α'', of the orthorhombic type) and β', the product of the phase separation reaction. The latter three phases are considered in the work referenced previously [*3*] and will receive only minor attention here. It may be noted in passing that the phase separation reaction was used to reduce aging times of some of the more highly alloyed compositions; details are given in the original work [*3*]. Also, it was shown that α'', present after rapid cooling from the solution treatment temperature, generally resulted in undesirably rapid hardening during aging. In contrast, alloys containing primary α (see following text) and metastable β in the as-quenched condition exhibited a desirable, relatively slow hardening response [*3-5*]. In all of the heat treatments described in this paper, precipitation of the α-phase ultimately was responsible for the microstructural changes which affected the strength and fracture properties. The α-phase which occurs may be divided into two basic types: primary α and secondary α. The primary α forms during working or on annealing just below the β-transus temperature. It is relatively coarse and thus produces little strengthening. As will be shown, however, it can strongly influence fracture related properties. Secondary α forms at lower temperatures, is relatively fine, and thus has the primary effect on strength. In the present work, two types of the secondary α were noted: Burgers and non-Burgers (also called Type 1 and Type 2) [*9,10*]. The former type occurred first as a fine precipitate at subboundaries, followed later by general matrix precipitation which was found not to obey the Burgers orientation relationship [*3*].

During the early stages of the study, no attempt was made to quantify the effect of the fine secondary α on properties. However, a number of

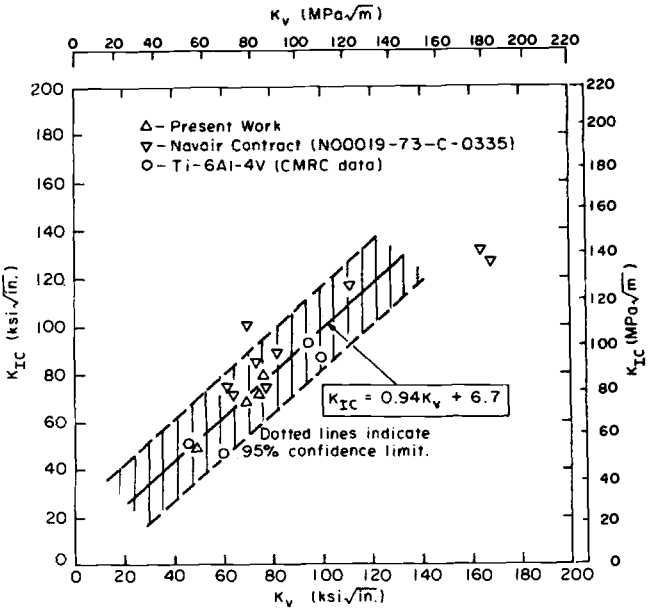

FIG. 2—*Relationship of* K_{Ic} *to* K_v. K_{Ic} *determined from valid test,* K_v *from slow bend precracked Charpy specimens* [*1*].

important effects of the primary α phase were noted in a semi-quantitative manner. The fracture path in both tensile and fracture toughness specimens was almost always transgranular, was frequently associated with the α/β interfaces, was characterized by a microvoid coalescence mode, and was strongly influenced by the shape of the primary α-phase [*3,11*]. The role of coarse α in influencing the fracture path is shown in Fig. 3 for a fracture toughness specimen. A similar effect was observed in tension specimens, and in both cases deformation and voids could be seen ahead of a propagating crack (Fig. 4). Primary α with a high aspect ratio (lenticular) promoted high toughness-low ductility while a low aspect ratio (globular) primary α resulted in low toughness-high ductility (Fig. 5).

Microstructure, Fractographic Features, and Mechanical Properties

To illustrate the major microstructural features, fractographic characteristics, and consequent mechanical properties observed in the alloys studied, three conditions were chosen, two from billet stock, one from plate. Other conditions are presented in similar detail in the original program final report [*3*]. In addition, material in the unaged condition was evaluated to permit a better understanding of directionality effects. Mechanical properties of this latter material are summarized in this section, while micro-

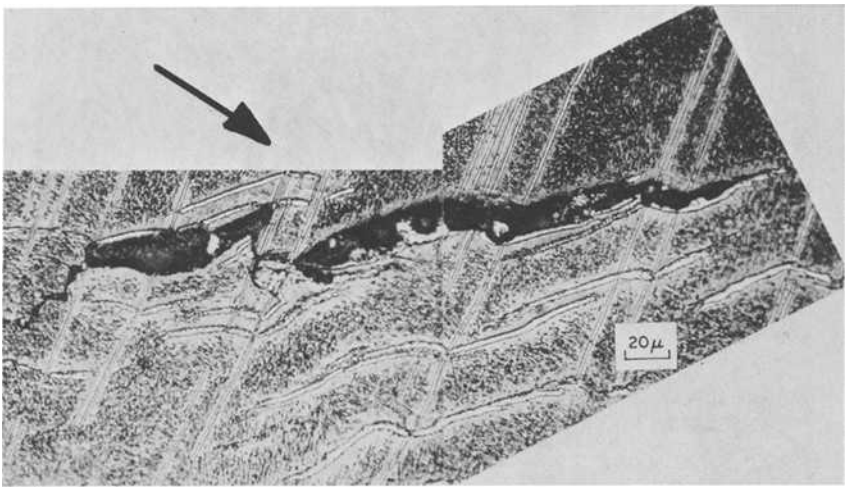

FIG. 3—*Influence of coarse α on fracture path in a fracture toughness specimen. The original crack direction (arrow) has been changed by the coarse α phase.*

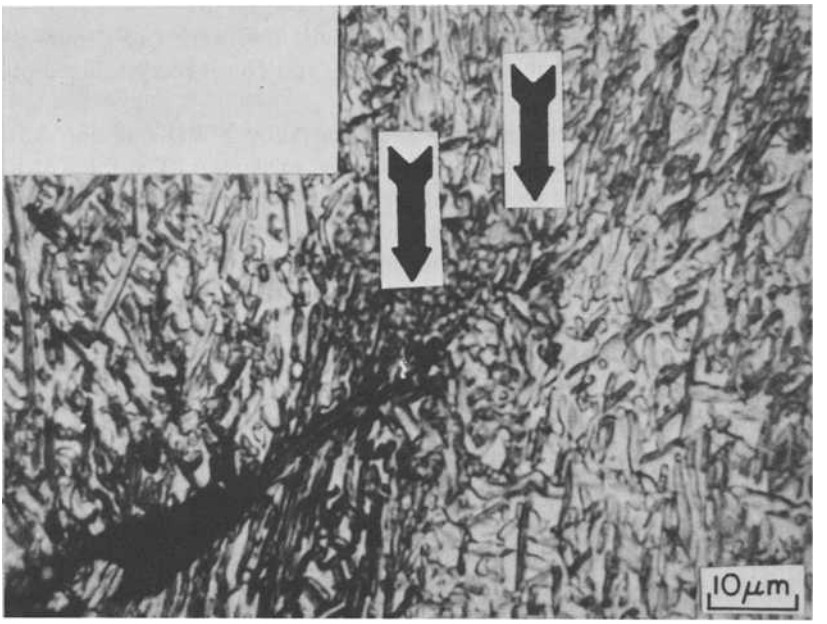

FIG. 4—*Deformation and voids (arrowed) ahead of a crack in a tension specimen.*

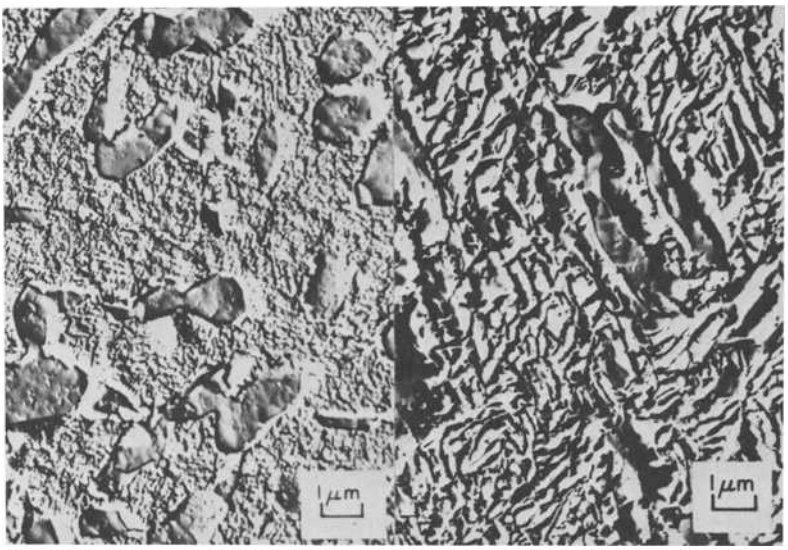

FIG. 5—*Primary α with a low aspect ratio (left) promotes low toughness-high ductility (<22 MPa$\sqrt{m}$ [<20 ksi$\sqrt{in.}$], 40 percent reduction in area) while a high aspect ratio (right) leads to high toughness-low ductility (77 MPa$\sqrt{m}$ [70 ksi$\sqrt{in.}$], 7 percent reduction in area.) Strength level ~1170MPa (170 ksi) yield strength.*

structure and fractographic features are presented in the section on directionality.

The two conditions selected from the billet stock were (*a*) β plus α-β worked followed by α-β annealing and aging, and (*b*) β recrystallized plus α-β annealing and aging.

The first of these conditions is illustrated for Alloy 227 (Condition A) in Fig. 6 which includes observations of Charpy specimens. The microstructure consists of stringered α resulting from working through the β-transus, primary α from the annealing cycle and fine secondary α from the aging treatment (Fig. 6(*a*)). At higher magnification, a subgrain structure can be seen decorated with α-phase between the primary α-particles (Figs. 6(*b* and *c*)). Fractographically, there appears to be more intergranular fracture in the CR specimen than in the LR orientation. However, a study of the crack path indicated that in both orientations fracture was predominantly intergranular with more tendency for the crack to follow certain crystallographic planes in the CR specimen, hence giving it a faceted appearance similar to that observed after mixed intergranular-transgranular fraction (see next section).

The β-recrystallized condition (Condition B) is shown in Fig. 7 for Alloy 334 and is characterized by continuous grain boundary α and fine Widmanstätten α. The strong influence of the continuous grain boundary α, formed both during cooling from the supratransus treatment and during the

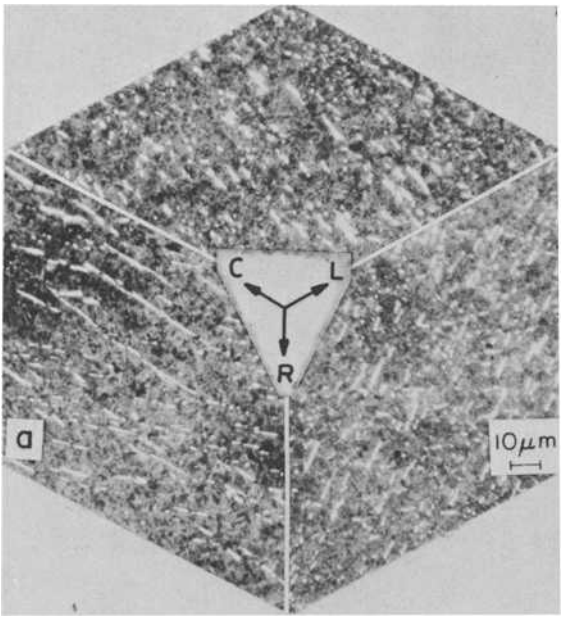

FIG. 6—(a) *Condition A, Alloy 227. Isometric optical.*

subtransus anneal is manifested in the fracture model which is mixed transgranular-intergranular (Fig. 7(*f*)). This causes the fracture surface to appear faceted (Fig. 7 (*c* and *d*)).

The microstructural and fractographic features exhibited by β plus α-β processed plate (Condition C) is shown for Alloy 227 in Fig. 8. This microstructure is characterized by globular primary α and a decomposed β-matrix containing fine secondary α. The primary α-particles are connected by a subgrain substructure decorated with α-particles. The optical micrograph of the fracture surface indicates a directionality with flow patterns in the rolling direction. As in billet, the primary α has a strong influence on the crack path.

Microstructural features and mechanical properties for Conditions A, B, and C are summarized in Table 3. Fracture toughness and tensile ductility for both alloys in Condition A are substantially better in the direction of major working (L) than at right angles to this direction for a similar strength level. Condition B is also characterized by a superior property combination in the longitudinal direction, although strengths are a little higher in the transverse direction. In addition, the continuous grain boundary α-phase present in Condition B appears to lead to a degradation in ductility in both alloys when compared with Condition A in agreement with the results of other work [*12*]. The fracture toughness in Alloy 334 (Condition

TABLE 3—*Mechanical properties and corresponding microstructural features.*

Alloy Condition [a]	Alloy	Direction	Fracture Toughness (K_v), MPa$\sqrt{m}$(ksi$\sqrt{in.}$)	Ultimate Tensile Strength, MPa (ksi)	Yield Strength, MPa (ksi)	Elongation %	Reduction of Area, %	Stringered α [b]	Grain Boundary α [c]	Primary α		Dimple Size, μm
										Aspect Ratio	Spacing, pm	
A	334	L	(LR) 92 (84)	1330 (193)	1260 (183)	7	15	P	SC	~6	2 to 5	10 to 15
		T	(CR) 63 (57)	1340 (194)	1275 (185)	2	4					
	227	L	(LR) 65 (59)	1240 (180)	1200 (174)	8	24	P	NP	~6	5 to 10	10 to 15
		T	(CR) 56 (51)	1230 (178)	1180 (171)	4	12					
B	334	L	(LR) 64 (58)	1185 (172)	1150 (167)	4	14	NP	C	~6	2 to 5	5 to 10
		T	(CL) 50 (45)	1260 (183)	1225 (178)	2	6					
	227	L	(LR) 63 (57)	1305 (189)	1240 (180)	1	5	NP	C	~6	~10	5 to 10
		T	(CL) 45 (41)	1360 (197)	1295 (188)	1	6					
C	334	L	(LT) 71 (65)	1105 (160)	1095 (159)	13	36	P	SC	~3	5 to 10	10 to 15
		T	(TL) 66 (60)	1235 (179)	1180 (171)	5	9					
	227	L	(LT) 53 (48)	1180 (171)	1130 (164)	13	47	NP	SC	~2	5 to 10	10 to 15
		T	(TL) 47 (43)	1275 (185)	1225 (178)	11	32					
D	334	L	...	940 (136)	890 (129)	23	52	P	SC	~3	~2	10 to 15
		T	...	930 (135)	905 (131)	15	44					
	227	L	...	860 (125)	840 (122)	20	57	P	SC	~5	2 to 5	5 to 10
		T	...	885 (128)	855 (124)	15	48					

[a] See Table 2.
[b] P=present and NP=not present.
[c] C=continuous, SC=semicontinuous, and NP=not present.

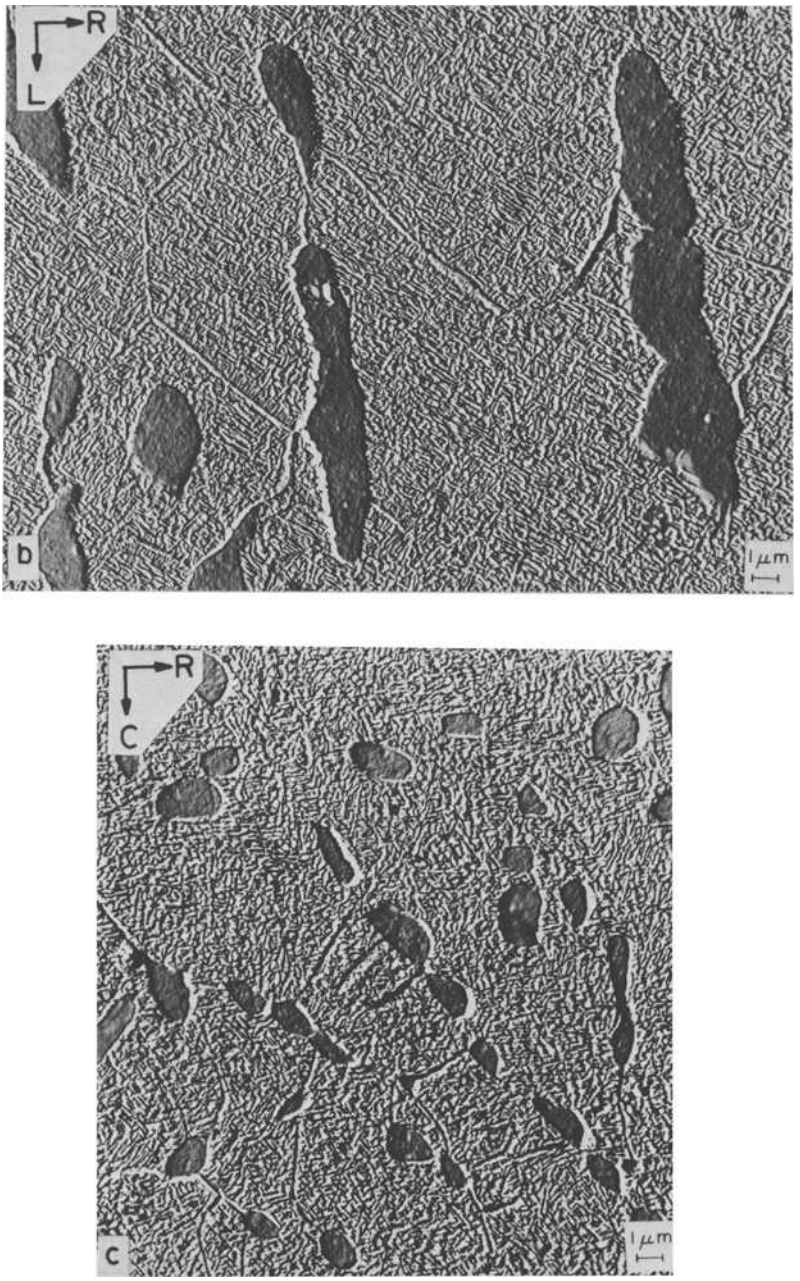

FIG. 6—(*continued*) *Condition A, Alloy 227.* (b) *Surface replica, LR plane, and* (c) *surface replica, CR plane.*

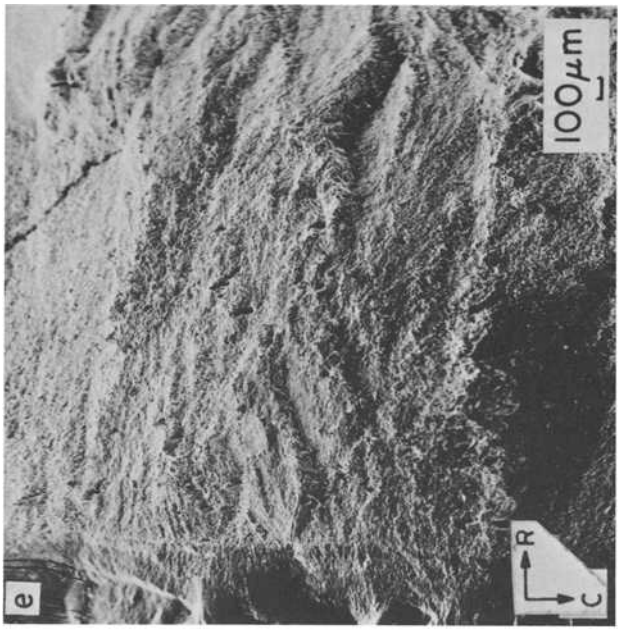
e
100μm
R
C


d
1000μm
R
C

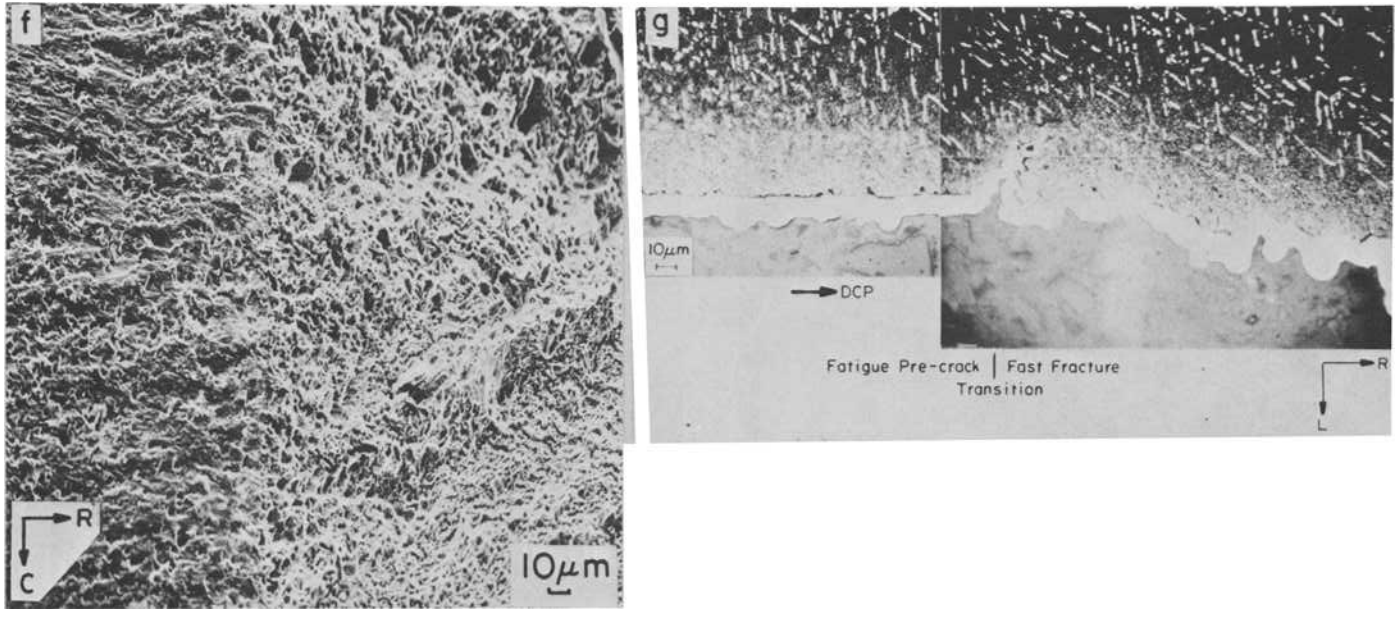

FIG. 6—(*Continued*) *Condition A, Alloy 227.* (d) *Optical of CR fracture face,* (e) *SEM of CR fracture face,* (f) *SEM of CR fracture face, and* (g) *optical of crack path, LR plane.*

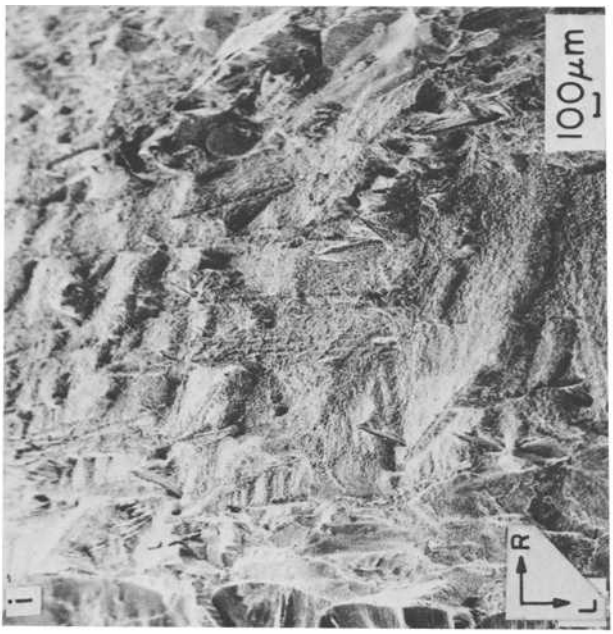
i
100μm
R
L

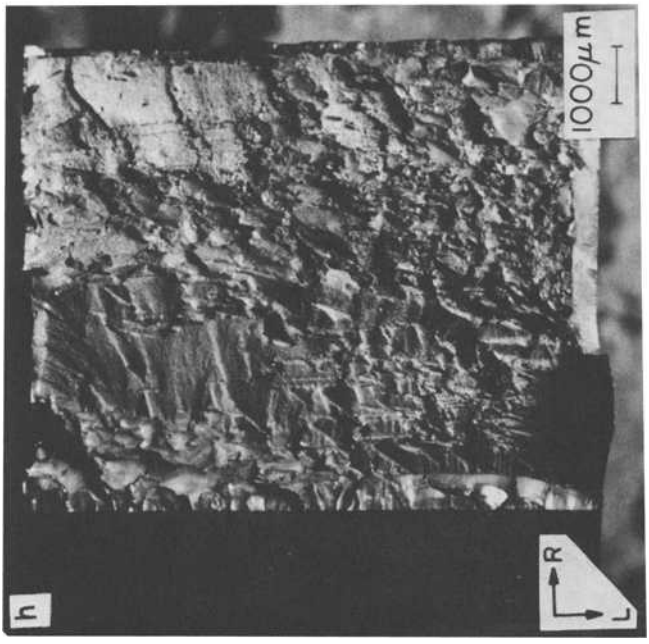
h
1000μm
R
L

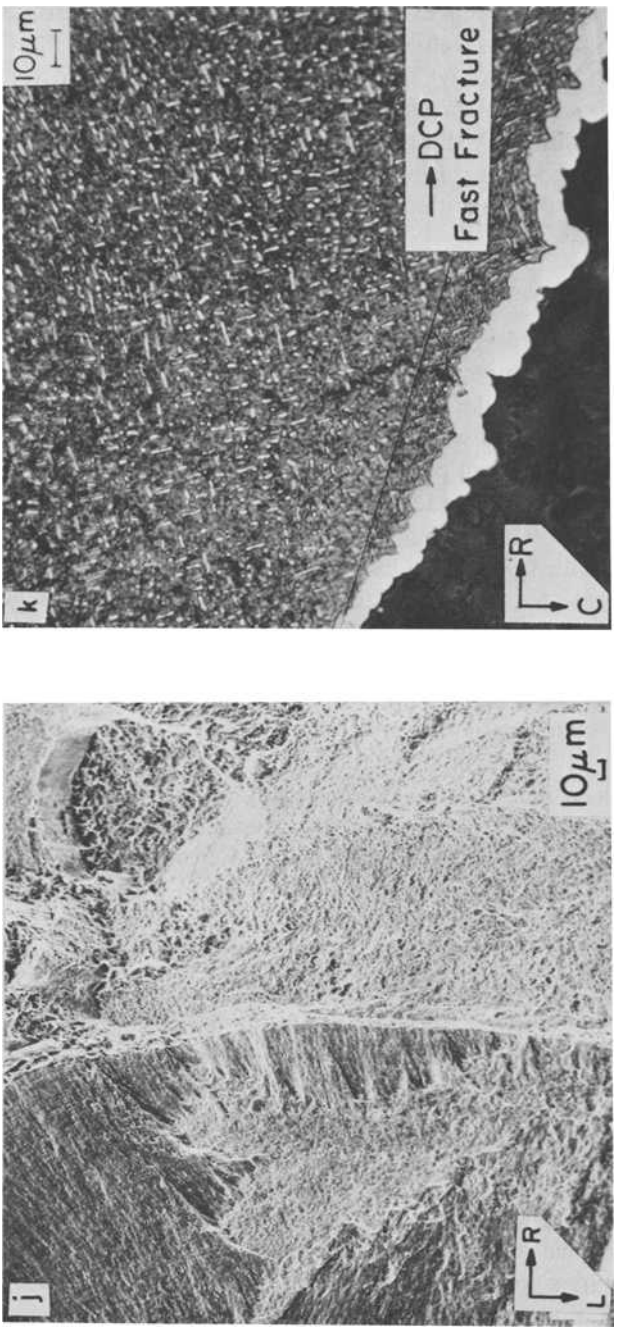

FIG. 6—(*Continued*) *Condition A, Alloy 227.* (h) *Optical of LR fracture face,* (i) *SEM of LR fracture face,* (j) *SEM of LR fracture face, and* (k) *optical of crack path, CR plane.*

B) is also reduced compared to Condition A. This is not the case for Alloy 227 where the higher strength levels exhibited by Condition B compensate for the higher fracture toughness values recorded for Condition A. Plate properties (Condition C) for Alloy 227 are characterized by improved ductility and reduced fracture toughness when compared with billet properties for this alloy (Conditions A and B). Alloy 334 plate properties show a similar trend, although comparison with Condition A is complicated by the higher strength level of this condition (A).

Fracture of Tension Specimens

All of the fractographic work presented in the immediately preceding section pertains to slow bend precracked Charpy specimens. Earlier work [*13*] had indicated that the predominant fracture mode in both fracture toughness and tension specimens was microvoid coalescence. To illustrate that this was the case in the present program—a point of significant importance in attempting to relate fracture toughness to tensile properties [*11*]—tension specimens were also studied fractographically. Conditions A and B were chosen to examine this point. Figure 9 shows the fractographic features of a transverse specimen from Condition A. Both the fracture topography and crack path are similar to those observed in corresponding fracture toughness specimens. The fractographic features of a transverse tension specimen from the β-recrystallized condition (Condition B) are shown in Fig. 10. Again the fractographic features are extremely similar to those characteristics of the corresponding fracture toughness specimens. An example of a crack close to the actual fracture surface is shown in Fig. 10(*d*). The crack has propagated by the mixed transgranular-intergranular mode previously presented for fracture toughness specimens.

Directionality

The results presented in the two previous sections indicate that longitudinal property combinations are superior to those obtained in the transverse direction. This directionality is larger in billet (Conditions A and B) than in plate (Condition C). This directionality could arise from preferred orientation of either the β-matrix (β-texture) or β-grains ("cigar" shaped grains), or from preferred orientation of α-phase, or a combination of the β and α effects (obviously, the latter effect must depend on the former). An understanding of the reason for this directionality may then lead to the design of thermomechanical treatments to circumvent the effect. Some preliminary attempts at achieving such an understanding are presented in this section.

Beta Texture—Solution treated billet and plate material from Alloys 334

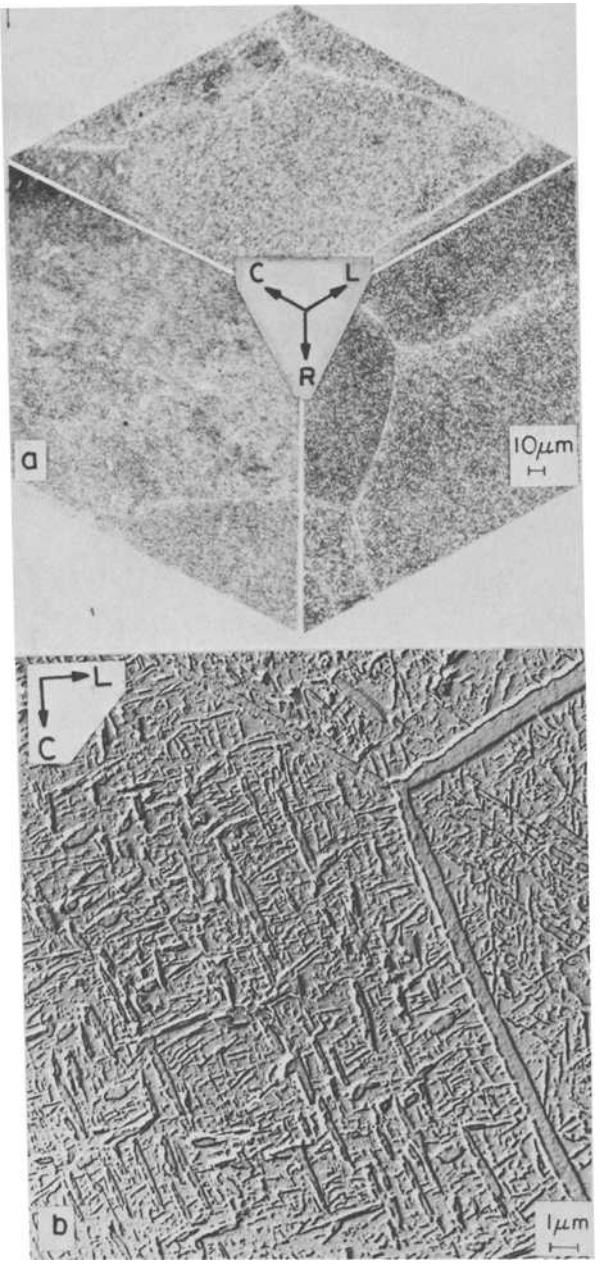

FIG. 7—*Condition B, Alloy 334.* (a) *Isometric optical, and* (b) *surface replica CL plane.*

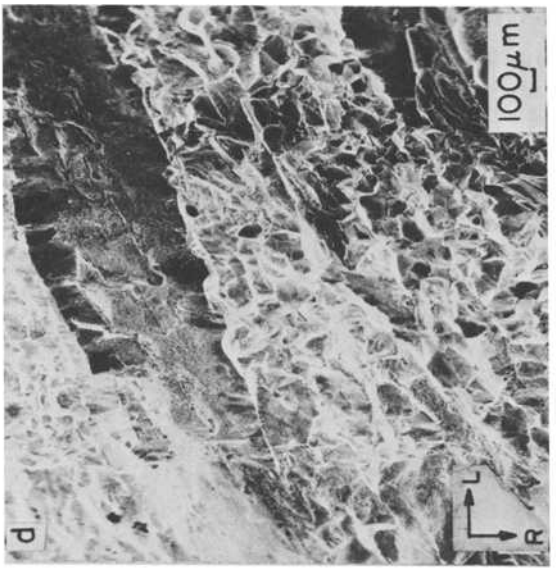
d
100μm
L
R

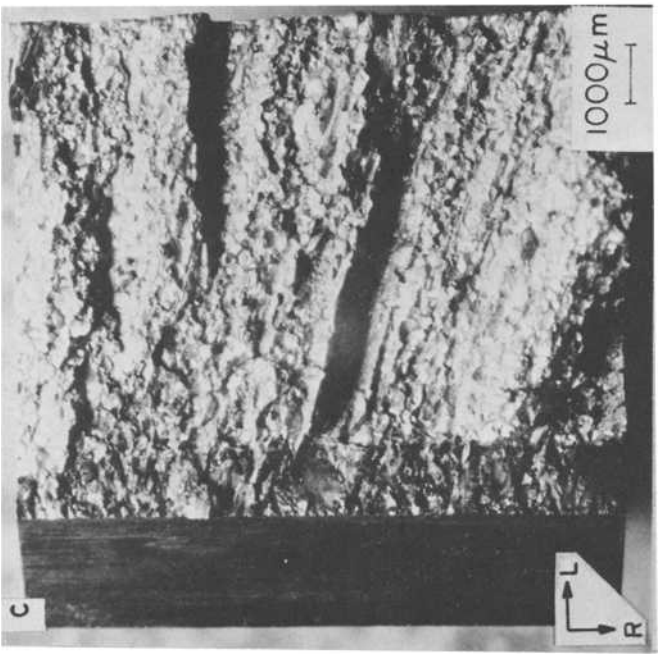
c
1000μm
L
R

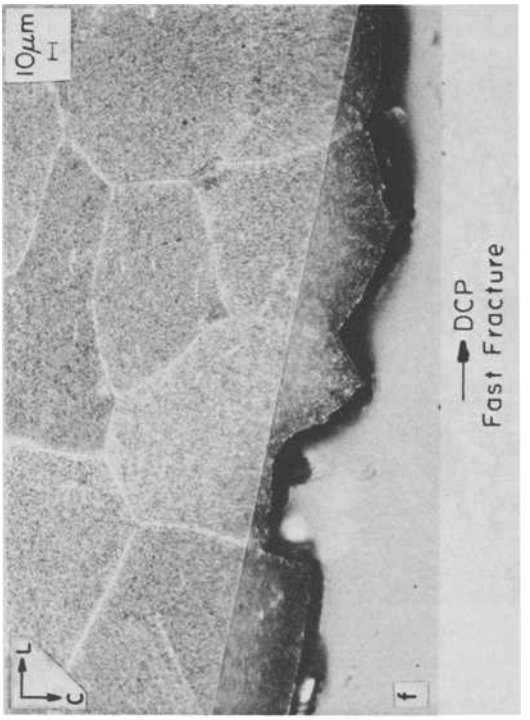

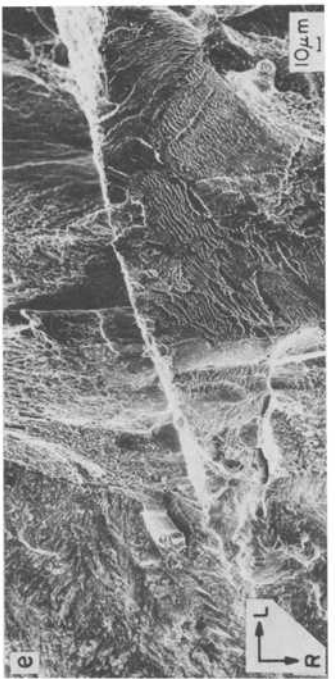

FIG. 7—*(Continued) Condition B, Alloy 334.* (c) *Optical of RL fracture face,* (d) *SEM of RL fracture face,* (e) *SEM of RL fracture face, and* (f) *optical of crack path, CL plane.*

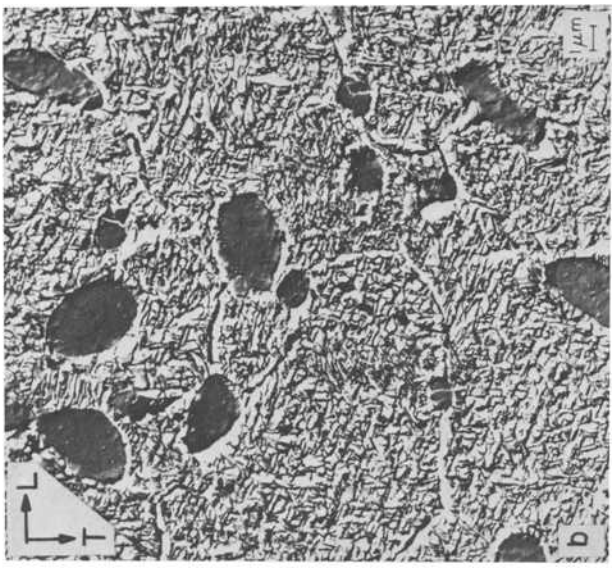
1 μm
L
T
a

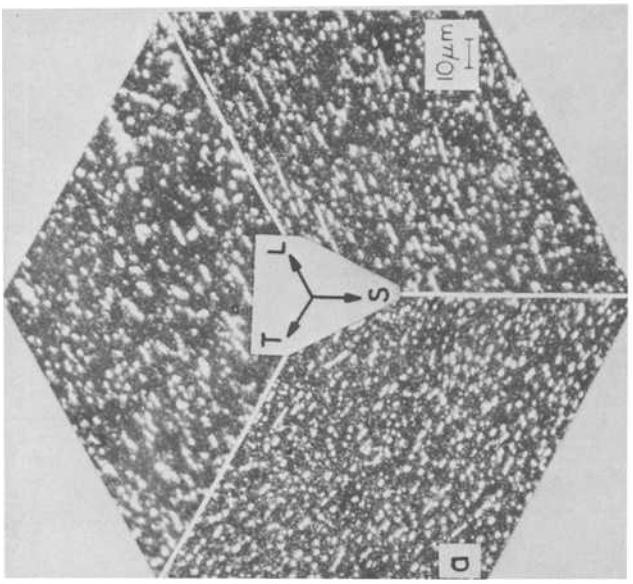
10 μm
L
S
T
b

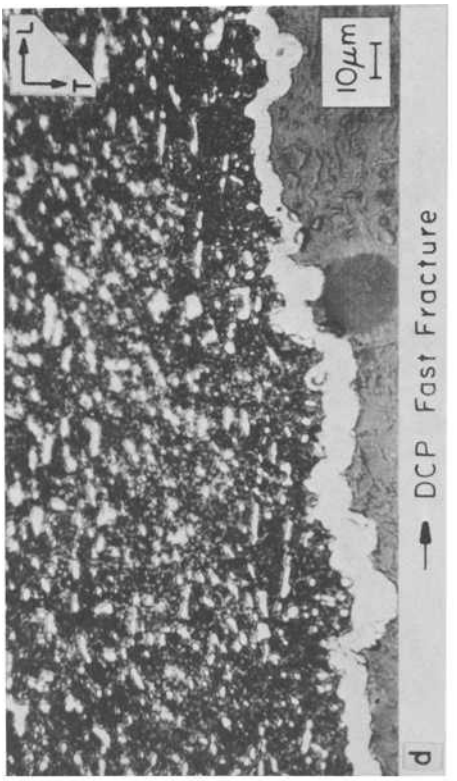

FIG. 8—*Condition C, Alloy 227.* (a) *Isometric optical,* (b) *surface replica TL plane,* (c) *optical of SL fracture face, and* (d) *optical of crack path, TL plane.*

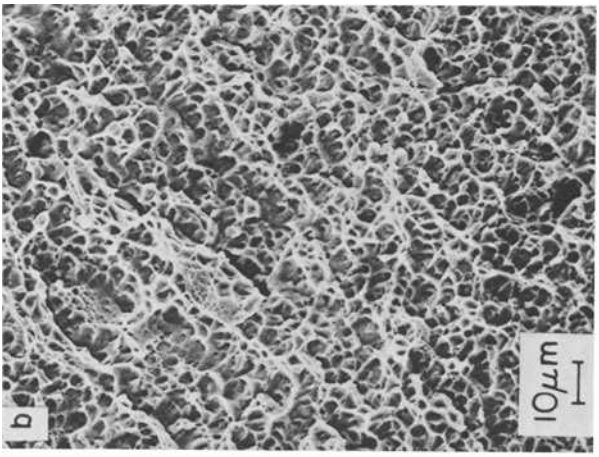
b
10μm

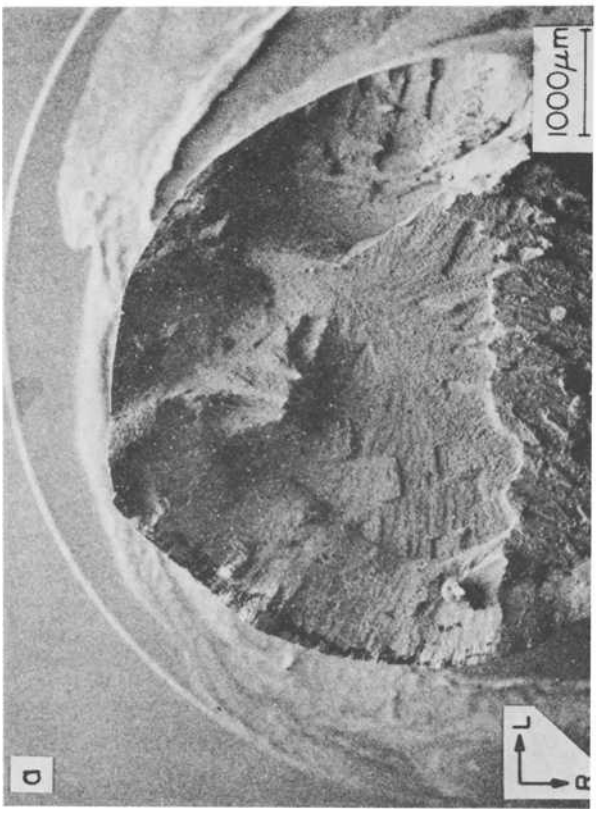
a
1000μm
L
R

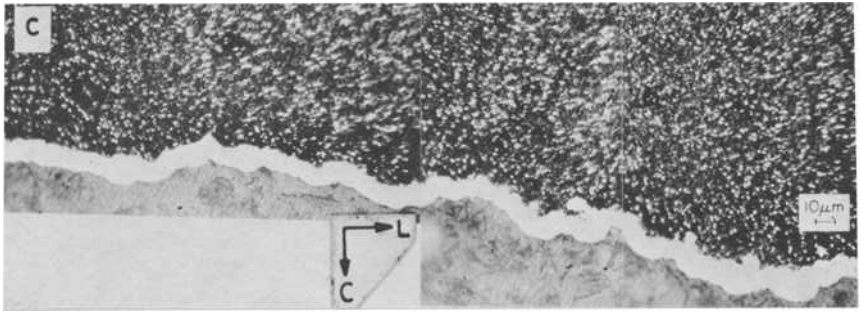

FIG. 9—*Condition A, Alloy 227.* (a) *Fractured tension specimen LR plane,* (b) *SEM of LR fracture face, and* (c) *optical of crack path, CL plane.*

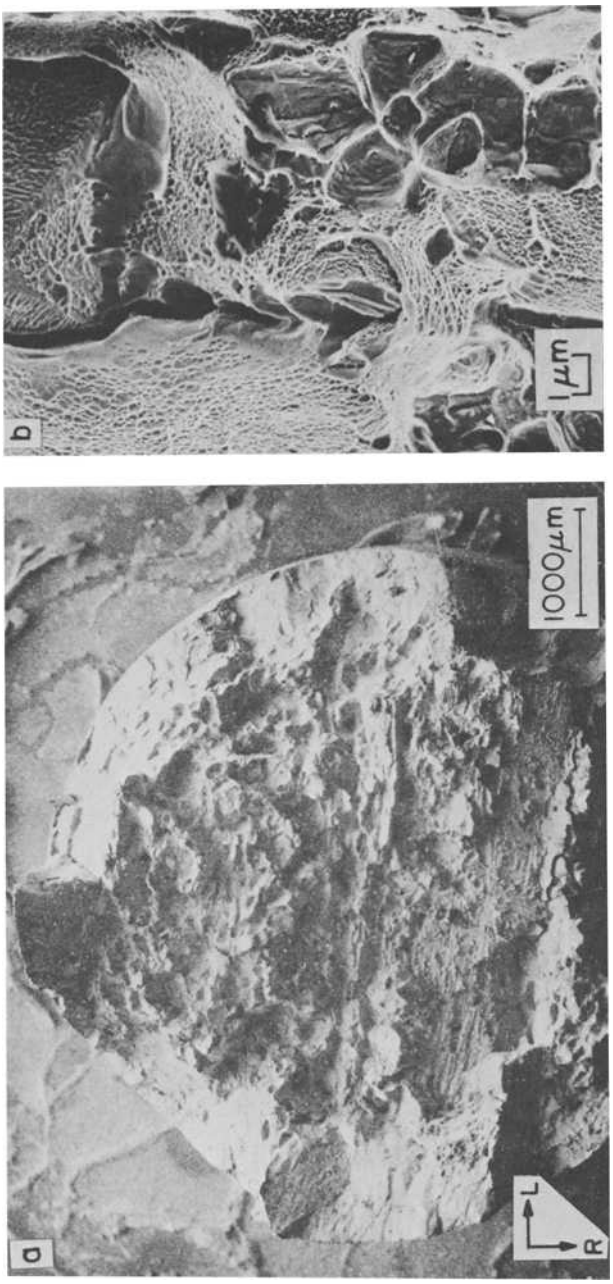
a
L
R
1000μm
b
1μm

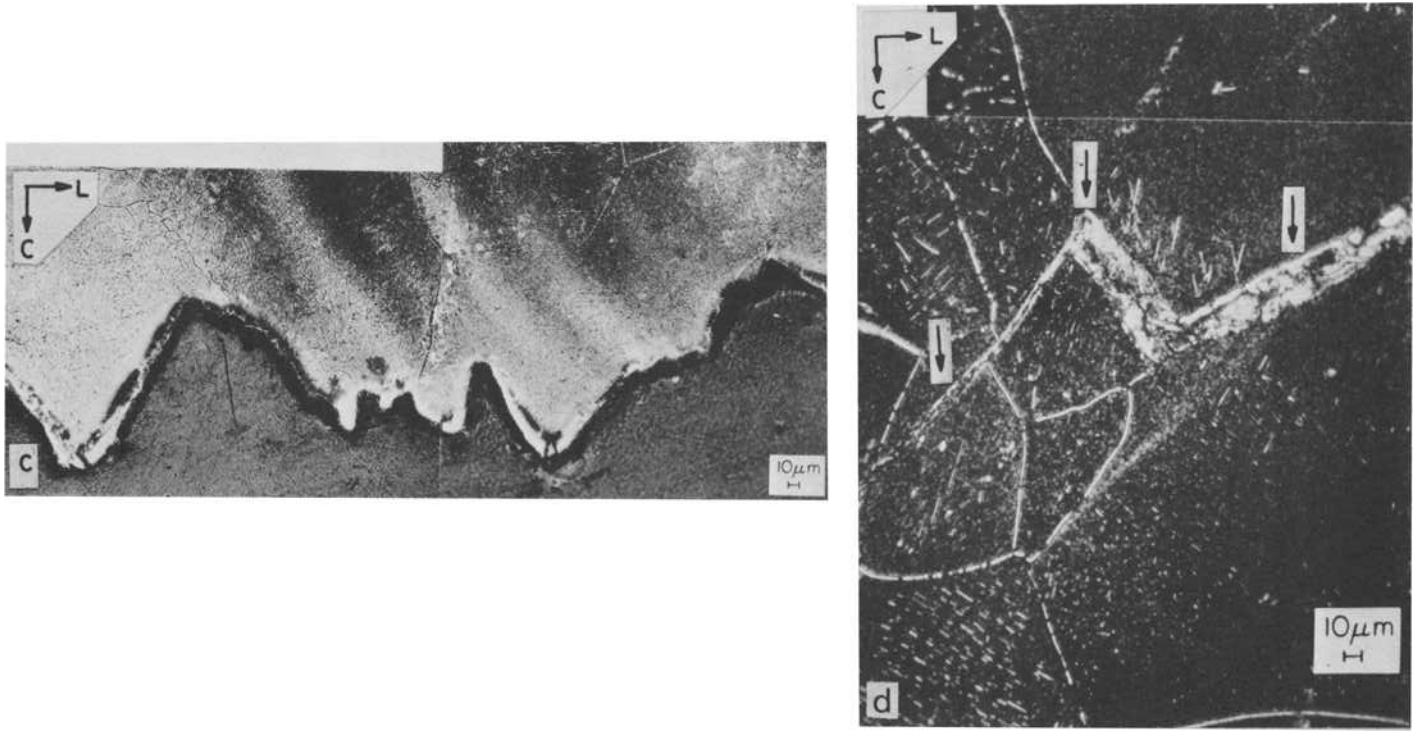

FIG. 10—*Condition B, Alloy 227.* (a) *Fractured tension specimen, LR plane,* (b) *SEM of LR fracture face,* (c) *optical of crack path, CL plane, and* (d) *sectioned tension specimen with side crack (arrowed) exhibiting mixed intergranular-transgranular fracture mode, CL plane.*

and 227 were analyzed for texture using a reflection technique described elsewhere [7]. By using an angle-cut specimen, determination of an entire quadrant of the pole figure by reflection is possible. Examples of the resulting pole figures are shown in Fig. 11(*a* and *b*). These show that in billet, the maximum <100> pole density is aligned along the major working direction; in plate, the <100> pole density distribution exhibits cubic symmetry, resulting in an approximately equal density of <100> poles in each of the principal plate directions.

Alpha-Phase Orientation—Tensile properties and ductility directionality of Alloys 334 and 227 billet in the duplex (high-low) solution annealed condition are listed in Table 4. The reduction in diameter occurring during these tests in the major mutually perpendicular directions is also recorded in this table. Directionality here is a result of β-matrix effects, stringered α (transgranular and at α-grain boundaries), and primary α; that is, the influence of secondary (precipitated during aging) α has been removed by studying unaged material. It can be seen that in longitudinal specimens the cross section of the tension specimens at the point of fracture is almost circular. In contrast, transverse specimens exhibit an oval cross section at the point of fracture, with the reduction in diameter being substantially greater in the longitudinal direction than in the (other) transverse direc-

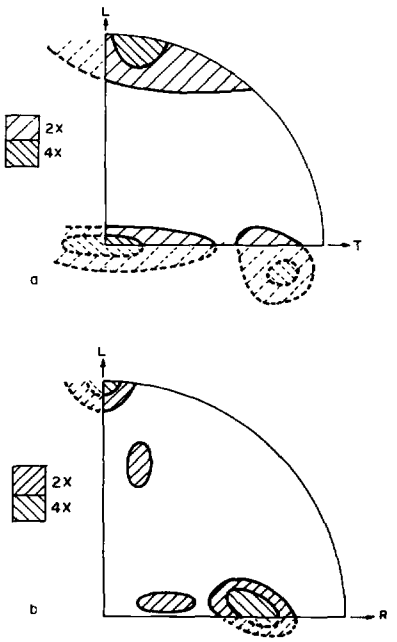

FIG. 11—*Pole figures, {200} planes, Alloy 334,* (a) *plate and* (b) *billet. Key indicates intensity times random.*

TABLE 4—*Billet ductility directionality as duplex annealed.*[a]

Alloy	Direction	Average Reduction in Area, %	Reduction in Diameter, %			Significance Test [b]
			L	R	C	
334	L	53±4	...	30±3	29±2	S
	C	44±4	29±3	23±2	...	D
227	L	59±3	...	36±4	34±5	S
	C	49±2	31±3	22±3	...	D

[a] Alloy 334: 730°C (1350°F), 4 h water quench plus 665°C (1225°F), 2 h water quench. Alloy 227: 790°C (1450°F), 2 h water quench plus 730°C (1350°F), 8 h water quench.

[b] A significance test was performed on the two sets of reduction in diameter data to determine whether the two sets of data were significantly different. (S indicates that the two sets of data were from the same population, and D, that they were from different populations.) *[21]*.

tion. Fracture mode was similar to that in specimens given this annealing treatment plus an age. An example of the crack path in annealed material is shown in Fig. 12.

Discussion

Microstructure, Fractographic Features, and Mechanical Properties

The results presented have shown that crack propagation in both tension and toughness tests occurs by microvoid coalescence. Further, there is a bimodal distribution of microvoids or dimples on the fracture surface as

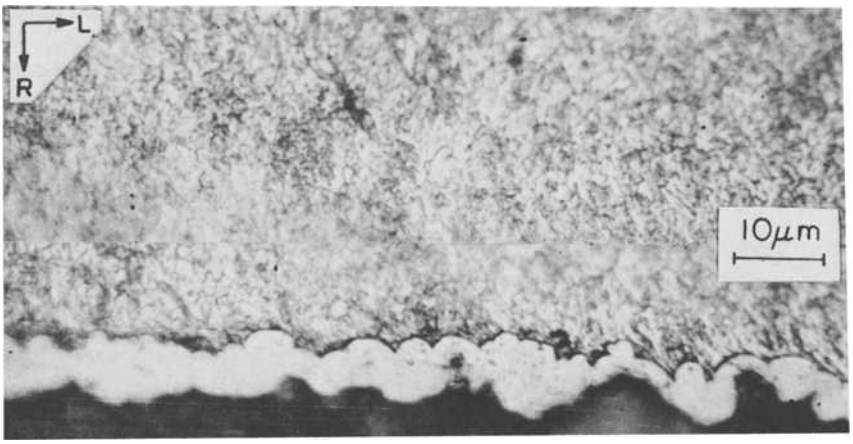

FIG. 12—*Condition D, Alloy 334. Optical of crack path tension specimen, RL plane.*

has been discussed for other titanium alloys [8]. The larger of these "dimples" are similar in size for both fracture modes and show a reasonable correspondence to the primary α-particle spacing (Table 3), thus suggesting that the primary α particles are involved in the void nucleation process. In order to understand the influence of microstructure on the fractographic features and hence mechanical properties, the role of the following variables must be elucidated: stringered α, grain boundary α, primary α distribution and morphology, secondary α-dispersion, and the texture of the β-matrix.

The stringered α is elongated in the direction of maximum working. The fracture path tends to follow this feature, leading to a more tortuous crack path for longitudinal specimens. The influence of this stringered α can be seen by comparing the mechanical properties for Condition A (Fig. 6) where stringered α is present and Condition C (Fig. 8) where it is not. Higher toughness is noted for Condition A in the longitudinal direction (LR) and less directionality is noted for Condition C. The result of the directionality of this α and the effect of the increased tortuosity will be considered further in subsequent sections of the discussions.

Grain boundary α appears to be an easy crack path in both fracture toughness and tension specimens (Condition B, Fig. 7). This results in generally lower mechanical properties. Even when grain boundary α is only semicontinuous a drop in mechanical properties is noted. This will be discussed in the directionality section.

During transgranular fracture, the primary α affects fracture toughness and ductility in opposite ways. High fracture toughness is favored by lenticular primary α (in a similar manner to that in which the stringered α contributes to higher toughness in the LR orientation), while high ductility is promoted by globular primary α. This effect may be explained by considering Figs. 13 and 14. Figure 13 shows a schematic representation of

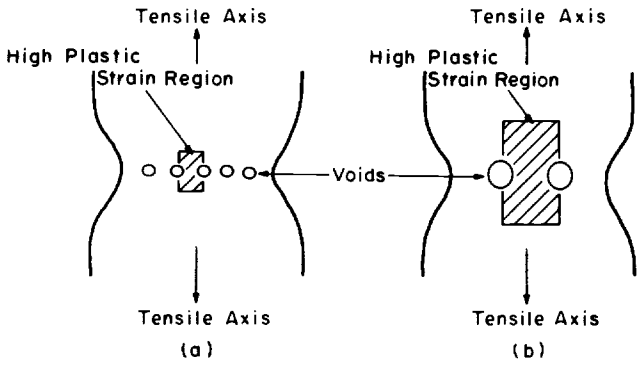

FIG. 13—*Schematic representation of void formation and high plastic strain region as a result of applied tensile stress.*

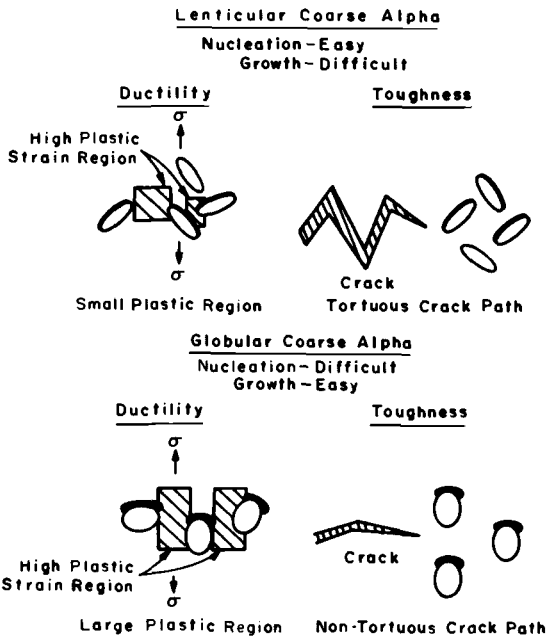

FIG. 14—*Schematic representation of effect of coarse α shape on ductility and toughness.*

void formation and the associated highly deformed regions as a result of applied tensile stress [*11*]. The total plastic deformation with many closely spaced voids is less than that with a few widely spaced voids, resulting in greater macroscopic ductility in the latter case. This model may be expanded to explain the effect of primary α-phase by considering Fig. 14. For a given volume fraction of primary α, the high plastic strain region is larger for a globular morphology. In contrast, for a propagating crack, the tortuosity of the crack path for lenticular α is significantly higher than for globular α. Thus the increased tortuosity of crack path has the same effect as enlarging the plastic zone. This leads to higher fracture toughness for lenticular-shaped primary α. This concept will be used in a subsequent section to interpret the directionality observed. This effect of primary α morphology on K_v tended to be more pronounced at lower strength levels. This may be due to the decreased plastic zone size at high strength levels which leads to sampling of fewer α/β interfaces during the onset of unstable crack propagation.

The secondary α does not appear to affect directly the void nucleation stage of fracture. Rather, this fine α influences strength directly and influences fracture toughness and ductility only by changing the local strength level and hence the extent of local plasticity. The influence of the secondary

α on strength was quantified using linear regression analysis to establish the relationship between the fine α spacing, d (in μm) and the yield strength, YS (in MPa)

$$YS = 850 + 70d^{-1}$$

which is a relationship similar to the Orowan particle spacing relationship.

The influence of β-texture on fracture-properties will be considered along with other directionality effects in a following section.

The present work has shown that the fracture mode for crack propagation during fracture toughness testing and tension testing is essentially the same. Consequently, it was possible to relate the critical stress intensity factor for fracture with tensile properties; this is considered in detail elsewhere [*11*].

Directionality

The results presented indicate that longitudinal mechanical property combinations are generally better than those in the transverse direction; this effect appears to be larger in billet than in plate (Table 3). Comparing the reduction of area values presented in Table 4, it can be seen that tensile ductility is essentially the same in the two transverse directions (longitudinal specimen directions R and C) but is substantially higher in the longitudinal direction than the transverse direction (transverse specimen directions L and R, respectively). In this section, an explanation is proposed for this directionality.

The observed directionality is unlikely to result from precipitation of α-phase in preferred directions because the orientation relationship between α and β has enough variants that it permits a nearly spherically symmetric distribution of α-orientations. Such a distribution obviously would not lead to directionality.

Considering now β-texture effects: the directions in body-centered-cubic (bcc) materials which tend to give rapid sliding and plastic instability are near $<111>$ and near $<100>$ [*14*]. Orientations near $<110>$ give stable flow and normal "plastic" necks. Thus the directionality in ductility cannot be related to this effect since the $<100>$ direction tends towards the longitudinal axis.

Thus we are left with stringered α which occurs both transgranularly and at grain boundaries. Observation of the voids nucleated adjacent to the final crack path indicates that there are fewer in L specimens than in R or C specimens. This is consistent with the discussion in the last section which showed that void nucleation occurs mainly in conjunction with the larger α-particles, since the stringer α and grain boundary α (cigar-shaped grains) are oriented towards the L direction. Using the model illustrated in Fig. 13, loading normal to a plane where many voids are nucleated will result in a

lower ductility than for loading normal to a plane where a smaller number of voids are formed. Thus the ductility directionality noted in Table 4 can qualitatively be related to variations in both planar void density and void shape anisotropy in the billet as shown in Fig. 15(*a*). The case in which the crack path extends along the long void axis is expected to result in slightly lower ductility than when extension is normal to the void axis since final void agglomeration is likely to be easier in the former case (less propagation through α-particles).

The model can be further extended to cover plate, where voids will assume a disk-like shape following large α- particles (Fig. 15(*b*)). Again, overall ductility directionality will be controlled by (*a*) the planar density of voids and (*b*) shape anisotropy of voids. In this case, the directionality is predicted to be less than in billet, in agreement with experimental results both in this program and in another similar investigation [*15*]. In addition, work in this latter investigation confirmed that the ductility directionality exhibited in solution annealed material (Table 4) also existed in aged material (that is, difference in L and R ductility in a transverse tension specimen)

A summary of the ductility directionality based on the model just presented is given in Table 5. It is anticipated that the model will be applicable to other product forms and other alloy systems.

Microstructural Requirements for Optimum Mechanical Properties

The results just discussed suggest that the major factor affecting fracture and hence properties is the α-phase, with the β-phase texture playing a

TABLE 5—*Predicted ductility directionality based on the anticipated crack characteristics in plate and billet.*

Product Form	Direction		Crack Characteristics		Predicted Ductility
	Tensile Axis	Crack Propagation	Nucleation [a]	Growth [b]	
Billet	L	R or C	D	L	high
	C	L	E	L	moderate
	C	R	D	S	low
Plate	L	T	E/D	L	moderate high
	L	S	D	L	high
	T	L	E	L	moderate
	T	S	D	S	low

[a] *D*=difficult nucleation, and E=easy nucleation. See Summary and Conclusions in text.

[b] L=large amount of plastic work during deformation, and S=small amount of plastic work during deformation.

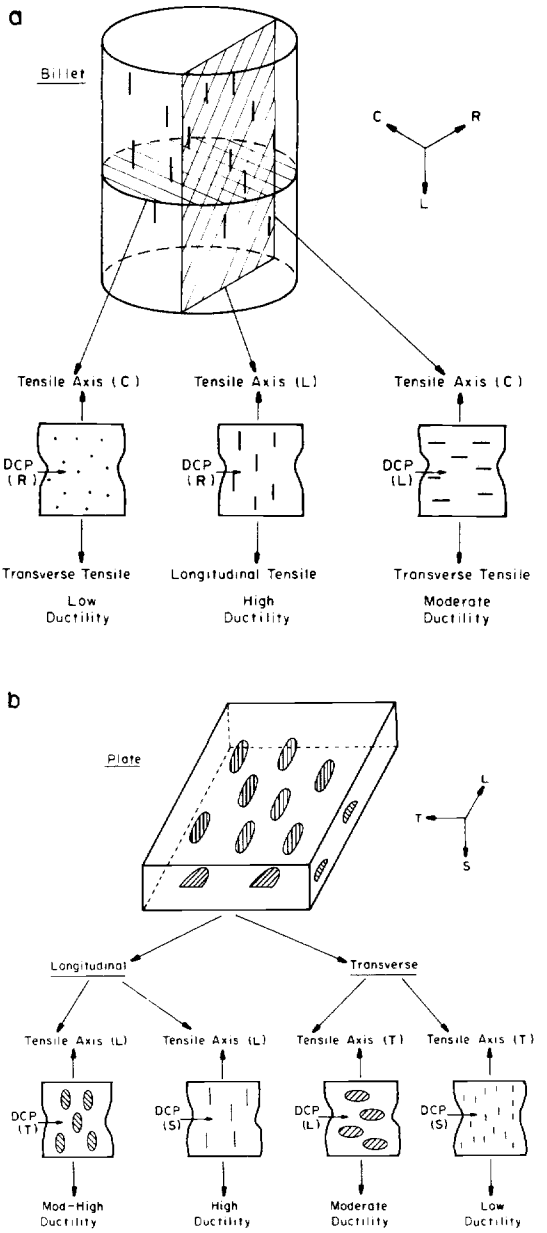

FIG. 15—*Schematic representation of relationship of ductility directionality to voids formed as a result of tensile stress.* (a) *Cigar-shaped voids formed in billet and* (b) *disk-shaped voids formed in plate.*

relatively insignificant role. In general, primary α affects mechanical properties by acting as a nucleation site for voids, with lenticular primary α favoring high toughness-low ductility and globular primary α promoting low toughness-high ductility, the effect being greatest at lower strength levels. The secondary α influences fracture only insofar as it controls the local strength level. Thus both nucleation and growth of voids are influenced only in a secondary manner by this fine dispersion of α. The other two forms of α present in these alloys—stringered α and grain boundary α (either continuous or semicontinuous)—influence fracture and are particularly significant in determining directionality effects. Stringered α should be avoided in order to increase transverse mechanical properties, with a concurrent reduction in the longitudinal property level. However, generally it is important to have isotropic mechanical properties rather than a combination of high and low levels. Stringered α can be eliminated either by annealing above the transus—in which case recrystallization and subsequent undesirable grain boundary α results—or by working a substantial amount below the transus, followed by a subtransus anneal [*16*]. This latter treatment did not prove practical in the present program but represents an obvious way to improve transverse mechanical properties in the future. In fact, a recently initiated program [5] for isothermal forging of the alloys developed in this program will examine this processing technique.

Continuous grain boundary α generally results in a degradation in properties and thus should be avoided. This can be done by completing the processing sequence with worked material rather than recrystallized material. Even when grain boundary α is semicontinuous, it can lead to undesirable properties. Deformed grains are elongated in the longitudinal direction (cigar-shaped grains). This results in more semicontinuous grain boundary α oriented in the longitudinal direction and hence in accordance with Fig. 15(*a*) (billet) and (*b*) (plate), a lower property combination in the transverse direction. Although an attempt was made in the present program to control this microstructural feature, it did not succeed to the extent to be anticipated from a process which allows more control of the microstructure, such as isothermal forging.

Assessment of the State of the Art in Deep Hardenable Alloys

In most of the conditions of the three alloys studied, the fracture toughness levels and tensile ductility in the longitudinal direction generally exceeded the goals. However, microstructural control following the guidelines presented in the last section was required to upgrade transverse properties, especially tensile ductility. Once the optimum microstructures according to these guidelines were achieved, good combinations of strength, fracture

[5] "Isothermal Forging Beta Titanium Alloys," Contract F33615-76-C-5386, Air Force Materials Laboratory, Wright-Patterson Air Force Base, Ohio.

toughness, and tensile ductility were obtained in addition to attractive values of other mechanical properties, such as elevated temperature strength, fatigue strength, fatigue crack growth rate and stress corrosion cracking resistance (K_{Iscc}) [*3*].

Three alloys, Ti-10Mo-6Cr-2.5Al (Alloy 334), Ti-7Mo-4Cr-2.5Al (Alloy 227), and Ti-10Mo-8V-2.5Al (Alloy 253) were studied in detail. It is appropriate to compare the strength-toughness combinations achievable in these alloys to other titanium alloys capable of similar strengths. To accomplish this, strength-toughness trend lines for the three metastable β-alloys studied here are compared with commercial and semicommercial deep hardenable, α-β alloys [*17-20*] in Fig. 16(*a*) and (*b*). Trend lines compiled from both longitudinal and transverse values have been used for the metastable β-alloys as well as for the comparison alloys. From these plots it can be seen that, in terms of strength-toughness, the metastable β-alloys compare very favorably to the high strength α-β alloys. In terms of strength-ductility, the α-β alloys are slightly better but all alloys shown in Fig. 16(*b*) are acceptable for most applications.

In addition to comparing the strength-toughness and strength-ductility of the three metastable β-alloys with the α-β deep hardenable alloys, the edge to center strength differences inherent in large sections of α-β alloys must also be considered. The metastable β-alloys have much smaller edge-to-center variations because their more slugglish transformation kinetics permit controlled hardening during aging. For example, typical edge-to-center yield strength variations for the metastable β-alloys are as follows: ~90 MPa (~13 ksi) for Alloy 227, ~14 MPa (~2 ksi) for the richer Alloy 334, and ~21 MPa (~3 ksi) for the intermediate Alloy 253. For comparison, the deep hardening characteristics of the commercial alloy Ti-6Al-2Sn-4Zr-6Mo and the semicommercial alloy Ti-6Al-2Sn-2Zr-2Mo-2Cr-0.25Si also were evaluated. For the Ti-6-2-4-6 alloy, good strength and ductility were obtained for the center of a 150-mm (6-in.) section with a 91-MPa (14-ksi) edge to center strength differential, while for the Ti-6-2-2-2-2-0.25 alloy, differences of 170 to 205 MPa (25 to 30 ksi) were observed. Alternate heat treatments can be used to reduce these variations in the α-β alloys, but in these instances the resulting microstructures lead to reduced fracture toughness [*17*]. Thus it would appear that the metastable β-alloys have superior deep hardening potential compared to high strength α-β alloys. It also appears that the three alloy compositions described herein are attractive examples of metastable β alloys.

Summary and Conclusions

The effect of composition, processing history and heat treatment on the strength, fracture toughness, and tensile ductility of a number of metastable

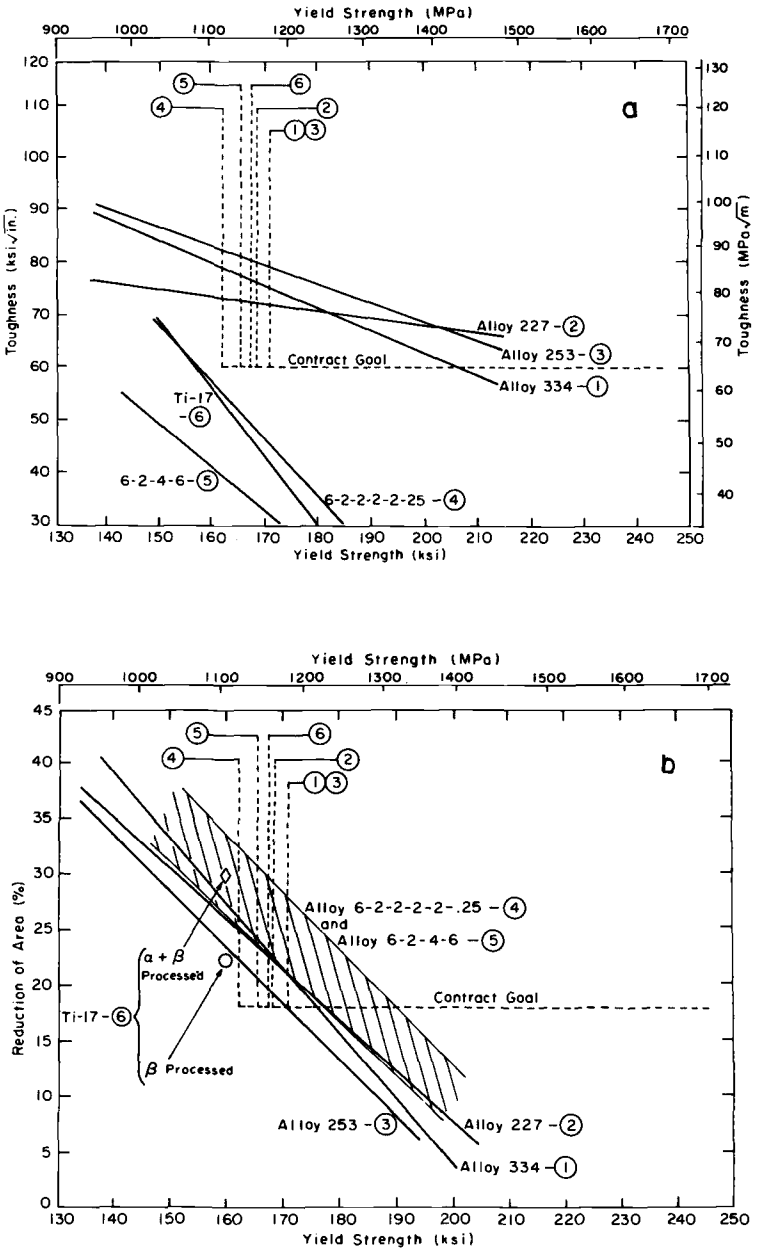

FIG. 16—*Alloy trend lines for present alloys and experimental and semicommercial deep hardenable alloys.* (a) *Toughness-yield strength and* (b) *ductility (reduction of area)-yield strength. Goal properties for each alloy are density normalized (number code).*

β-alloys has been studied. The goals of the study were to identify one or more compositions, processing sequences, and heat treatments which would permit attainment of 1165-MPa (179-ksi) yield strength, 66 MPa$\sqrt{m}$ (60 ksi$\sqrt{in.}$) fracture toughness, 12 percent elongation, and 18 percent reduction of area at all locations in a 150-mm (6-in.) section. Three compositions capable of meeting these goals were identified: Ti-10Mo-6Cr-2.5Al (Alloy 334), Ti-7Mo-4Cr-2.5Al (Alloy 227), and Ti-10Mo-8V-2.5Al (Alloy 253). These alloys were fabricated into 12-mm (½-in.) plate and 150-mm (6-in.) billet. Both of these product forms were either β and α-β worked, α-β annealed and aged, or β annealed and aged. Three distinct microstructures were selected for detailed testing and analysis. These were characterized by: (*a*) stringered or elongated α, primary α, and fine secondary α, (*b*) continuous grain boundary α and secondary α, and (*c*) globular α and secondary α. In all of these microstructures the properties in the principal working direction were generally superior to those in the transverse direction(s). The effect of β-matrix texture, primary α-morphology, stringered α (a result of working above or through the β-transus), and grain boundary α were studied in an attempt to account for the directional dependence of properties. These studies lead to the conclusions that β-matrix texture is not responsible for the directionality, that grain boundary α is deleterious to properties in both directions, and that primary α-morphology strongly influences fracture-related properties. Lenticular primary α favors high fracture toughness-low tensile ductility, while globular primary α leads to high tensile ductility-low fracture toughness. Because they are strung out or elongated in the primary working direction, α-particles in grain boundaries act in a manner similar to stringered α and degrade transverse mechanical properties. This can be explained using the observation that α-β interfaces act as preferred fracture initiation sites. Finally, a comparison between the deep hardening characteristics of the metastable β-alloys studied here and two α-β alloys shows that the metastable β-alloys have better deep hardening characteristics in terms of edge to center strength and toughness variations but that the α-β alloys are slightly better in terms of tensile ductility.

Acknowledgments

The authors gratefully acknowledge the experimental assistance of E. W. Campbell, J. M. Capenos, R. A. Hohowski, P. Q. Sauers, F. R. Shuss, R. A. Spurling, and E. H. Wright and helpful discussions with J. P. Hirth, R. F. Malone, V. C. Petersen, M. G. H. Wells, and C. F. Yolton. This work was supported in part by Air Force Contract F33615-71-C-1525 with J. A. Hall and M. A. Greenfield as program monitors.

References

[1] Ronald, T. M. F., Hall, J. A., and Pierce, C. M., *Metallurgical Transactions*, Vol. 3, 1972, pp. 813-818.

[2] Froes, F. H., Malone, R. F., Williams, J. C., Greenfield, M. A., and Hirth, J. P., "Alloy Design and Property Interrelations of Metastable Beta Titanium Alloys," to be published in *Proceedings of Joint Conference on Forging and Properties of Aerospace Materials*, University of Leeds, England, 5-7 Jan. 1977.

[3] Froes, F. H., Malone, R. F., Petersen, V. C., Rhodes, C. G., Chesnutt, J. C., and Williams, J. C., "Research on Deep Hardenable Titanium Alloys for Large Airframe Structural Members," Technical Report AFML-TR-75-4 Vols. I and II, Air Force Materials Laboratory, Dayton, Ohio, 1975.

[4] Froes, F. H., Malone, R. F., Petersen, V. C., Rhodes, C. G., Chesnutt, J. C., Williams, J. C., and Hall, J. A., "The Metallurgical Synthesis of a New Generation of Deep Hardenable Titanium Alloys. The Metastable Beta Ti-Mo-V-Cr-Al System—Design and Properties," Presented at the Third International Titanium Conference, Moscow, Russia, May 1976, proceedings to be published.

[5] Froes, F. H., Petersen, V. C., Malone, R. F., Berryman, R. G., Chesnutt, J. C., Rhodes, C. G., and Williams, J. C. in *Proceedings of the Second International Conference on Mechanical Behavior of Materials*, American Society for Metals 1976, pp. 2009-2013.

[6] Spurling, R. A., *Metallurgical Transactions*, Vol. 6A, 1975, pp. 1660-1661.

[7] Olsen, R. H., Boeing Document D6-25265, 1970.

[8] Chesnutt, J. C., Rhodes, C. G., and Williams, J. C. in *Fractography-Microscopic Cracking Processes, ASTM STP 600*, American Society for Testing Materials, 1976, pp. 99-138.

[9] Williams, J. C. in *Titanium Science and Technology*, R. I. Jaffee and H. M. Burke, Eds., Plenum Press, Vol. II, 1973, p. 1433.

[10] Rhodes, C. G. and Williams, J. C., *Metallurgical Transactions*, Vol. 6A, 1975, p. 2103.

[11] Hirth, J. P. and Froes, F. H., *Metallurgical Transactions*, Vol. 8A, 1977, pp. 1165-1176.

[12] Chesnutt, J. C. and Froes, F. H., *Metallurgical Transactions*, Vol. 8A, 1977, pp. 1013-1017.

[13] Froes, F. H., Malone, R. F., Petersen, V. C., Rhodes, C. G., and Williams, J. C., "Research on Deep Hardenable Titanium Alloys for Large Airframe Structural Members," Technical Report AFML-IR-7351(V), Air Force Materials Laboratory, Dayton, Ohio 1973.

[14] Clauer, A. H., Ph.D. thesis, Ohio State University, 1968.

[15] Berryman, R. G., Froes, F. H., Chesnutt, J. C., Rhodes, C. G., Williams, J. C., and Malone, R. F., "High Toughness Titanium Alloy Development," Technical Report TFD-74-657, Naval Air Systems Command, Washington, D.C., 1974.

[16] Froes, F. H., Chesnutt, J. C., Rhodes, C. G., and Berryman, R. G., "Effect of Processing Variables on Structure-Property Relationships in Ti-4.5Al-5Mo-1.5Cr (Corona 5)," to be submitted to *Metallurgical Transactions*.

[17] Bartlo, L. J., Bomberger, H. B. and Seagle, S. R., "Deep Hardenable Titanium Alloy," Technical Report AFML-TR-73-122, Air Force Materials Laboratory, Dayton, Ohio, 1973.

[18] "The Ti-17 Alloy—Processing and Properties," Report by General Electric Company, Cincinnati, Ohio, 1973.

[19] Sparks, R. B. and Rossow, J. A., "Improved Manufacturing Methods for Producing High Integrity, More Reliable Titanium Forgings," Technical Report IR-226-(II), Air Force Materials Laboratory, Dayton, Ohio, 1972.

[20] Sparks, R. B. and Long, J. R., "Improved Manufacturing Methods for Producing High Integrity, More Reliable Titanium Forgings," Technical Report IR-226-I(V), Air Force Materials Laboratory, Dayton, Ohio, 1972.

[21] Duckworth, W. E. in *Statistical Techniques in Technological Research*, Methuen and Co., Ltd., London, 1968, p. 14.

R. H. Van Stone,[1] J. L. Shannon, Jr.,[2] W. S. Pierce,[2] and J. R. Low, Jr.[3]

Influence of Composition, Annealing Treatment, and Texture on the Fracture Toughness of Ti-5Al-2.5Sn Plate at Cryogenic Temperatures

REFERENCE: Van Stone, R. H., Shannon, J. L., Jr., Pierce, W. S., and Low, J. R., Jr., **"Influence of Composition, Annealing Treatment, and Texture on the Fracture Toughness of Ti-5Al-2.5Sn Plate at Cryogenic Temperatures,"** *Toughness and Fracture Behavior of Titanium, ASTM STP 651,* American Society for Testing and Materials, 1978, pp. 154–179.

ABSTRACT: The plane strain fracture toughness (K_{Ic}) and conventional tensile properties of two commercially produced 25.4-mm (1-in.) thick Ti-5Al-2.5Sn plates were determined at cryogenic temperatures. One plate was extra-low interstitial (ELI) grade, the other, normal interstitial. Portions of each plate were mill annealed at 1088 K (1500°F) followed by either air or furnace cooling. The tensile properties, flow curves, and K_{Ic} of these plates were determined at 295 K (room temperature), 77 K (liquid nitrogen temperature), and 20 K (liquid hydrogen temperature).

The air-cooled ELI plate was the toughest material evaluated. The K_{Ic} of the furnace-cooled ELI plate was about 25 percent below that of the air-cooled ELI material. Cooling rate from the annealing temperature had no influence on the toughness of the normal interstitial plates, both of which had a K_{Ic} approximately half that of the air cooled ELI plate. The 20 K fracture toughness of the normal interstitial plates varied only slightly with specimen orientation. The LS toughness of both ELI plates was approximately 20 percent greater than the LT toughness.

Based on these results and a study of the microstructural fracture mechanism, it is recommended that Ti-5A1-2.5Sn, which is to be used in applications requiring high fracture toughness, should have the lowest possible in-

[1] Graduate student, Department of Metallurgy and Materials Science, Carnegie-Mellon University, Pittsburgh, Pa.; presently metallurgist, General Electric Corporate Research and Development Center, Schenectady, N. Y. 12301.

[2] Head and engineer, respectively, Strength of Materials Section, NASA-Lewis Research Center, Cleveland, Ohio 44135.

[3] Professor, Department of Metallurgy and Materials Science, Carnegie-Mellon University, Pittsburgh, Pa. 15213.

Copyright© 1978 by ASTM International www.astm.org

terstitial level and be air-cooled from the annealing treatment so as to prevent ordering.

KEY WORDS: titanium, titanium alloys, cryogenics, plane strain fracture toughness (K_{Ic}), microstructure, crystallographic texture, fracture properties

Nomenclature

d_0= Initial diameter of smooth tension specimen

d= Instantaneous diameter of smooth tension specimen

A_0= Original cross-sectional area of smooth tension specimen

A= Instantaneous cross-sectional area of smooth tension specimen

a= Instantaneous half-diameter of smooth tension specimen necked region = $d/2$

R= Radius of curvature of smooth tension specimen necked region

e= Conventional linear strain

P= Load

σ_t= True stress

σ= Bridgman corrected flow stress

ϵ= True strain

P_{max}= Maximum load in plane strain fracture toughness test

P_Q= Secant offset load as defined in ASTM Test for Plane-Strain Fracture Toughness of Metallic Materials (E 399-74)

K_Q= Provisional value of plane strain fracture toughness as defined in ASTM Test E 399-74

K_{Ic}= Plane strain fracture toughness as defined by ASTM Test E 399-74

The embrittling effects of increased levels of the interstitial elements (carbon, oxygen, nitrogen, and hydrogen) and substitutional iron, increased thickness, low test temperature, and slow cooling from the annealing treatment were first demonstrated for Ti-5Al-2.5Sn sheet in the early 1960s. Christian et al [*1*] [4] observed decreases in mild-notch strength in liquid hydrogen (20 K) (−423°F) as alloy oxygen levels exceeded 0.1 weight percent and iron exceeded 0.25 weight percent. Broadwell and Wood [*2*] showed similar effects for sheet with 0.12 weight percent oxygen when the iron content exceeded 0.2 weight percent. These and similar studies resulted in the development of the extra low interstitial (ELI)

[4] The italic numbers in brackets refer to the list of references appended to this paper.

grades of titanium alloys used today in applications where toughness is the limiting design consideration.

In 1963 Shannon and Brown [*3*] studied the effects of several alloy production and fabrication variables on sheet gages up to 6.4 mm (0.25 in.) at temperatures down to 20 K (−423°F) using sharp-notch tension specimens. Notch strength was reduced as temperature decreased, the effect being more pronounced the heavier the sheet gage. At 20 K (−423°F) the sharp-notch strength of normal interstitial sheet was half that of ELI grade. The so-called plane-stress nominal fracture toughness, K_c, from the sharp-notched specimens of the air-cooled ELI sheet was 50 percent greater than furnace-cooled material, with no difference in smooth tensile strength. It was speculated that the precipitation of the ordered α_2 phase during slow furnace cooling was responsible for the lower toughness. These results are consistent with more recent work of Curtis et al [*4*] which show reduced apparent toughness at room temperature for Ti-5Al-2.5Sn plate step cooled from the annealing temperature when compared to air-cooled plate. Attempts to detect α_2 precipitation using thin foil transmission electron microscopy (TEM) in the lower toughness material were unsuccessful [*4*].

It has not been demonstrated that the effects observed for relatively thin gages of stock using sharp-notch strength or "plane-stress" fracture toughness are indicative of the behavior of heavy-section plane-strain fracture toughness. The present investigation therefore was designed to examine the effects of interstitial level, annealing treatment cooling rate, and test temperature on the conventional smooth tensile properties and plane strain fracture toughness of heavy plate at temperatures down to 20 K (−423°F). In a companion study [*5*] the microstructure and fracture mechanism have been studied using fractographic and metallographic techniques. Those results are summarized here in an attempt to explain the observed trends in fracture toughness.

Material

Commercially available 25.4-mm (1-in.) thick plate of Ti-5Al-2.5Sn alloy was investigated in four combinations of interstitial content and heat treatment: ELI and normal interstitial, either air cooled or furnace cooled from a 1088 K (1500°F) mill anneal. A single plate of each interstitial grade was subdivided for each of the two heat treatments. Chemical analyses of the as-received plates are given in Table 1 along with the specified compositions. It should be noted that in both the specified and analyzed compositions, higher iron contents accompanied increased interstitial levels. In this paper, the two investigated plate compositions are distinguished solely by the interstitial element level differences (ELI and

TABLE 1—*Chemical analyses of Ti-5Al-2.5Sn plates (weight percent).*

	Al	Sn	Fe	Mn	O	C	N	H
ELI specification	4.7/5.6	2.0/3.0	0.1/0.2	...	0.12 max	0.08 max	0.05 max	0.0125 max
ELI, AC [a]	5.09	2.44	0.140	0.002	0.054	0.0057	0.0098	0.0056
ELI, FC [b]	5.10	2.47	0.145	0.002	0.052	0.0041	0.0098	0.0050
Normal interstitial specification	4.0/6.0	2.0/3.0	0.50 max	0.30 max	0.20 max	0.15 max	0.07 max	0.003/0.020
Normal interstitial AC [a]	5.22	2.47	0.300	0.002	0.164	0.0140	0.0163	0.0072
Normal interstitial FC [b]	5.24	2.47	0.270	0.002	0.169	0.0120	0.0172	0.0042

[a] Air cooled.
[b] Furnace cooled.

normal) as is customarily done by the titanium industry, notwithstanding the fact that some observed effects may be due to variations in iron content rather than interstitial content differences. The furnace cooling rate was essentially linear at approximately 15 K (27°F)/h; air cooling rate was initially 4500 K (8100°F)/h, with total cooling time to room temperature of about 1 h.

Microstructures were examined with optical metallography, thin foil TEM, microprobe analysis, and texture pole figure determinations. The results are presented elsewhere [*5*] and are summarized in Table 2. The α-grain size of the furnace-cooled ELI plates was only slightly larger than the other plates. The iron-stabilized β-phase particle size and volume fraction was greater for the normal interstitial plate due to its higher iron content. The ELI plates had an annealed α-deformation texture; the normal interstitial plates had a β-deformation texture. Figure 1 shows a computer plotted pole figure of the basal (0002) and prism ($10\bar{1}0$) planes for the air-cooled ELI plate using the technique described by Olsen [*6*]. This texture is a typical annealed α-deformation texture [*7*], with the basal planes parallel to the plate surface and split slightly toward the transverse direction. Figure 2 shows pole figures for the air-cooled normal interstitial plate. This is a β-processing texture [*7*], with the basal planes perpendicular to the longitudinal and transverse directions. Figures 1 and 2 show that the prism planes are distributed in an almost random intensity. Although both plates were to have been identical except for interstitial and iron content, the differences in texture are most likely due to variations in processing [*6*]. Regardless of its source, the observed texture was quite mild for α-titanium. Variations in cooling rate did not greatly alter the texture; however, they did affect the ordering characteristics of the α-matrix. Figure 3 shows electron diffraction patterns of the α matrix of the air-

TABLE 2—*Summary of microstructure of Ti-5Al-2.5Sn plates.*

	ELI		Normal Interstitial	
Microstructural Feature	AC [a]	FC [b]	AC [a]	FC [b]
α-grain size (μm)	46.2	58.1	41.6	41.4
Estimated size of iron-stabilized β-particles (μm)	2	2	5	5
Ordering	no	yes	no	yes
Type of texture	α	α	β	β

[a] AC=air-cooled from mill anneal.
[b] FC=furnace-cooled from mill anneal.

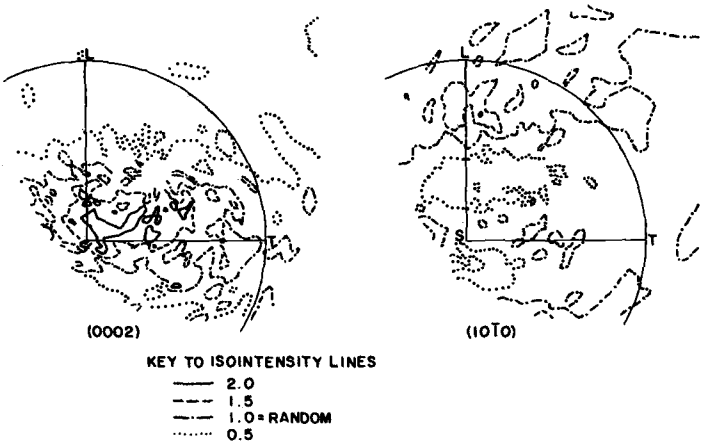

FIG. 1—*Texture pole figure of air-cooled ELI Ti-5Al-2.5Sn plate. L, T, and S indicate longitudinal, transverse, and short transverse directions, respectively.*

cooled and furnace-cooled ELI plates with zone axes close to $(4\bar{5}15)$. The extra spots on the furnace-cooled pattern can be indexed as the ordered α_2 phase [*8*]. Similar patterns were obtained for the normal interstitial plates. Thus, the furnace-cooled plates were more ordered than the air-cooled plates.

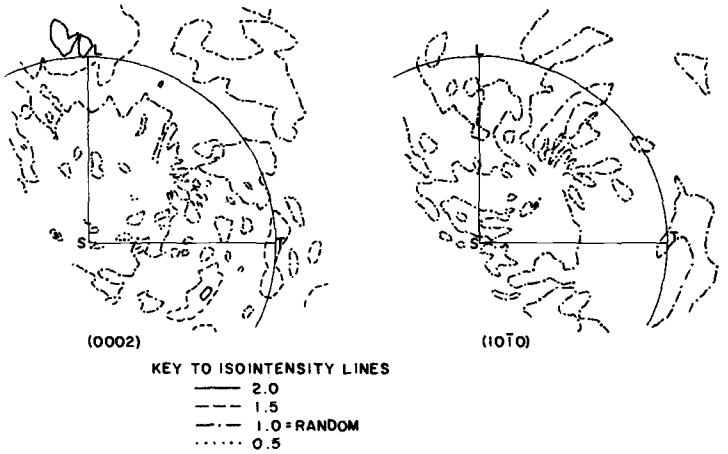

FIG. 2—*Texture pole figure of air-cooled normal interstitial Ti-5Al-2.5Sn plate. L, T, and S indicate longitudinal, transverse, and short transverse directions, respectively.*

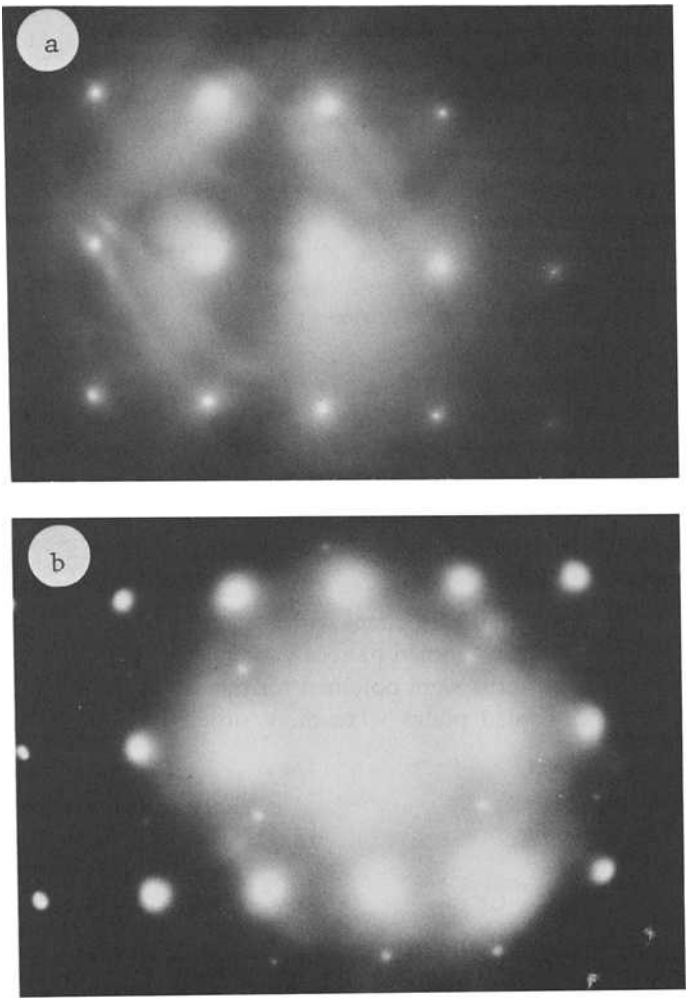

FIG. 3—*Electron diffraction patterns of* (a) *air-cooled and* (b) *furnace-cooled ELI Ti-5Al-2.5Sn plates having a* $(4\bar{5}15)$ *zone axis.*

Procedure

The conventional tensile properties and plane-strain fracture toughness (K_{Ic}) were determined for all plates at room temperature (295 K) (72°F), liquid nitrogen temperature (77 K) (−320°F), and liquid hydrogen temperature (20 K) (−423°F). All cryogenic tests involved total immersion of the specimen in cryogen.

All conventional tensile properties were determined for the longitudinal plate direction. Cylindrical specimens with 11.4-mm (0.45-in.) diameter

by 101.6-mm (4-in.) long test sections were used at 20 K (−423°F); test sections 6.4 mm (0.25 in.) diameter by 25.4 mm (1 in.) long were used at the other test temperatures. Load versus extension was autographically recorded up to maximum load for all smooth specimen tests at room temperature and 77 K (−320°F) using an linear variable differential transformer (LVDT)-type extensometer. After maximum load, diametral strain was measured periodically by unloading and measuring specimen diameter at room temperature with a point micrometer. At 20 K (−423°F), strain was measured from two foil gages mounted 180 deg apart at specimen mid-length, and was recorded to just slightly beyond yield. Maximum and final loads were noted. From these measurements, Bridgman-corrected flow curves were constructed for all test temperatures by the procedure described in Appendix I.

Plane strain fracture toughness determinations were made for the LT orientation (ASTM Test E 399-74) at all three test temperatures, with additional LS orientation tests (ASTM Test E 399-74) at 20 K (−423°F). Standard compact specimens 25 mm (1 in.) thick were used at room temperature and 77 K. For these specimens, crack mouth opening displacement was measured using an LVDT clip gage developed by Shannon and Pierce [9]. The 20 K (−423°F) tests employed 25-mm (1-in.)-thick three-point bend specimens. The LT specimens were 25 mm (1 in.) and 50 mm (2 in.) wide and will be referred to as 1 by 1 and 1 by 2 bend specimens, respectively. The LS specimens were 1 by 1 bend specimens. Crack mouth opening displacement for the bend specimens was measured with a clip-in gage of the type described in ASTM Test (E 399-74). Special application of this gage to liquid hydrogen testing is described by Shannon et al [*10,11*].

Results

Strength and Toughness

The conventional strength and plane strain fracture toughness results are summarized in Table 3. Each value of mean and standard deviation is the result of triplicate tests at cryogenic temperatures and duplicate tests at room temperature except as noted. All tests except those of the ELI plate at room temperature met the thickness and test record P_{max}/P_Q requirements of ASTM Test E 399-74. Tests of the ELI plate at room temperature failed to meet the specimen thickness and test record P_{max}/P_Q requirements of ASTM Test E 399-74 and are properly noted as invalid in Table 3.

Strength and LT toughness are displayed as a function of test temperature in Fig. 4: 1 by 2 bend specimen results at 20 K (−423°F) and

TABLE 3—*Mechanical properties of Ti-5Al-2.5Sn plates.*
(Data indicates the mean ± one standard deviation.)

Alloy	Test Temperature, K	(°F)	σ_y 0.2% Yield Strength, ksi [a]	Ultimate Tensile Strength, ksi [a]	Tensile Fracture Strain	K_{Ic}, ksi$\sqrt{in.}$ [b]	K_{Ic} Specimen Orientation [c] and Type
Ti-5A1-2.5Sn	295	(72)	102.1±0.8	110.2±1.1	0.528±0.012	107.9 [c, d]	LT-compact
ELI	77	(−320)	171.4±2.0	181.9±0.6	0.407±0.041	101.1±4.4	LT-compact
Air-cooled	20	(−423)	189.0±1.0	203.5±0.8	0.254±0.028	81.5±4.5	LT-1 by 2 bend
						82.7±1.8	LT-1 by 1 bend
						96.9±4.5	LS-1 by 1 bend
Ti-5A1-2.5Sn	295	(72)	98.9±0.7	108.4±0.4	0.512±0.025	104.9 [c]	LT-compact
ELI	77	(−320)	170.6±0.5	180.5±1.0	0.402±0.024	75.1±0.4	LT-compact
Furnace-cooled	20	(−423)	189.4±0.3	204.7±1.6	0.207±0.043	64.0±1.1	LT-1 by 2 bend
						61.8±2.2	LT-1 by 1 bend
						73.4±5.1	LS-1 by 1 bend
Ti-5A1-2.5Sn	295	(72)	126.9±0.5	133.8±0.4	0.435±0.040	65.4±4.4	LT-compact
Normal interstitial	77	(−320)	194.5±1.0	207.3±1.1	0.317±0.015	48.6±1.3	LT-compact
Air-cooled	20	(−423)	215.4±2.3	228.9±0.1	0.209±0.029	46.8±1.0	LT-1 by 2 bend
						46.0±1.0	LT-1 by 1 bend
						45.7±0.4	LS-1 by 1 bend
Ti-5A1-2.5Sn	295	(72)	127.9±0.6	132.6±0.6	0.328±0.055	60.0±1.3	LT-compact
Normal interstitial	77	(−320)	200.0±0.5	209.9±0.3	0.327±0.034	52.5±1.8	LT-compact
Furnace-cooled	20	(−423)	220.3±1.2	228.7±0.4	0.124±0.051	46.2±0.2	LT-1 by 2 bend
						42.7±0.3	LT-1 by 1 bend
						47.8±3.3	LS-1 by 1 bend

[a] 1 ksi = 6.9 MN/m^2.
[b] 1 ksi$\sqrt{in.}$ = 1.1 MN/m$^{3/2}$.
[c] This result is invalid because specimen thickness is less than 2.5 $(K_{Ic}/\sigma_y)^2$. Only one test was conducted.
[d] This result is invalid because P_{max}/P_Q exceeds 1.1.
[e] Orientation notation is that of ASTM Test E 399-74.

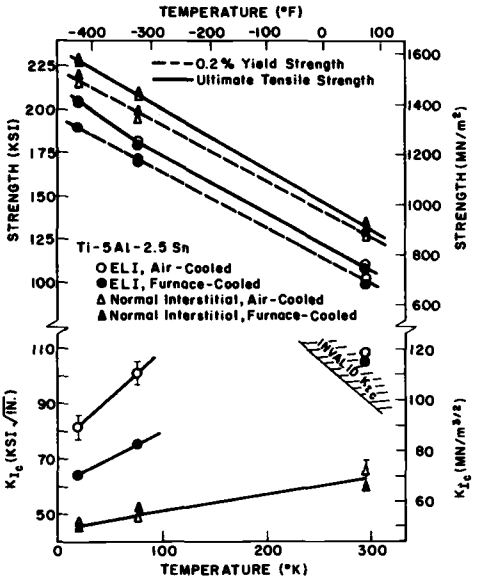

FIG. 4—*The variation of longitudinal tensile properties and LT fracture toughness of Ti-5Al-2.5Sn with test temperature. The error bars indicate the range of plus and minus one standard deviation.*

compact specimen results at the higher temperatures. The error bars indicate the range of plus or minus one standard deviation. If they are not shown, the scatter falls within the datum point. As noted by Shannon and Brown [*3*], strength is essentially doubled as temperature is reduced from 295 K (room temperature) to 20 K (−423°F). The normal interstitial stock is 172 to 207 MN/m² (25 to 30 ksi) stronger than the ELI material at all test temperatures, and no influence of cooling rate from the annealing treatment is observed on the strength of either grade.

As expected, the ELI grade is substantially tougher than the normal interstitial grade. Cooling rate from the annealing treatment has no effect on the normal interstitial toughness, but at cryogenic temperatures the air-cooled ELI grade toughness was 25 to 35 percent greater than that of the furnace-cooled ELI plate. Valid toughness of the ELI plate could not be measured at room temperature, but P_{max}/P_Q ratios from the test records suggest a similar effect at room temperature.

The 20 K toughness data are presented as bar graphs in Fig. 5. Both the 1 by 1 and 1 by 2 LT bend specimens gave essentially the same results. This is not unexpected since 20 K fracture always occurred abruptly at maximum load before the 5 percent secant intersection.

Comparison of the LS and LT orientation fracture toughness specimens for the various alloy conditions reveals some plate directionality. The LS

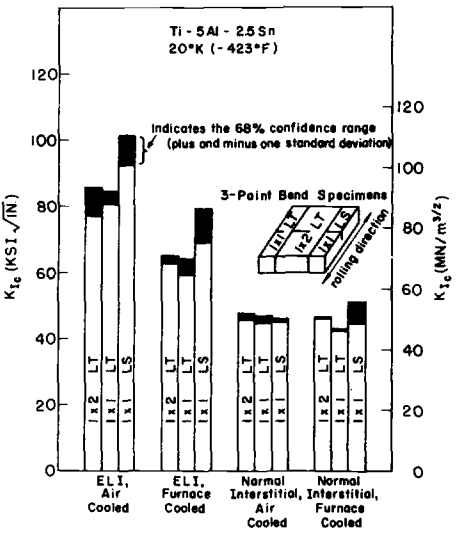

FIG. 5—*Directionality of plates investigated as indicated by 20K plane strain fracture toughness.*

toughness of the ELI grade is about 20 percent higher than the LT toughness. The toughness of the normal interstitial plates show little if any directionality.

Flow Curves

Tensile flow curves are shown in Fig. 6. The data points shown in that figure are the Bridgman-corrected [*12*] flow stress and the plastic strains as described in Appendix I. These data were fit using a least square regression analysis to the form

$$\sigma = \sigma_0 + A\epsilon^m \tag{1}$$

where σ_0, A, and m are constants determined by a linear least square regression analysis with iteration on m to minimize the squared error. This form was chosen on the basis of its successful application to unalloyed titanium [*13*]. Table 4 gives the values determined for the equation's constants. The fit of these curves is quite good; no experimental datum point was different from the regression stress by more than 3 percent.

Considerable license was taken in constructing the 20 K (−423°F) curves in Fig. 6 which were based only on the yield and fracture events, and this should be kept in mind when using those curves. The 20 K load-extension records were serrated and the specimens contained multiple necks, probably due to localized adiabatic heating during plastic deforma-

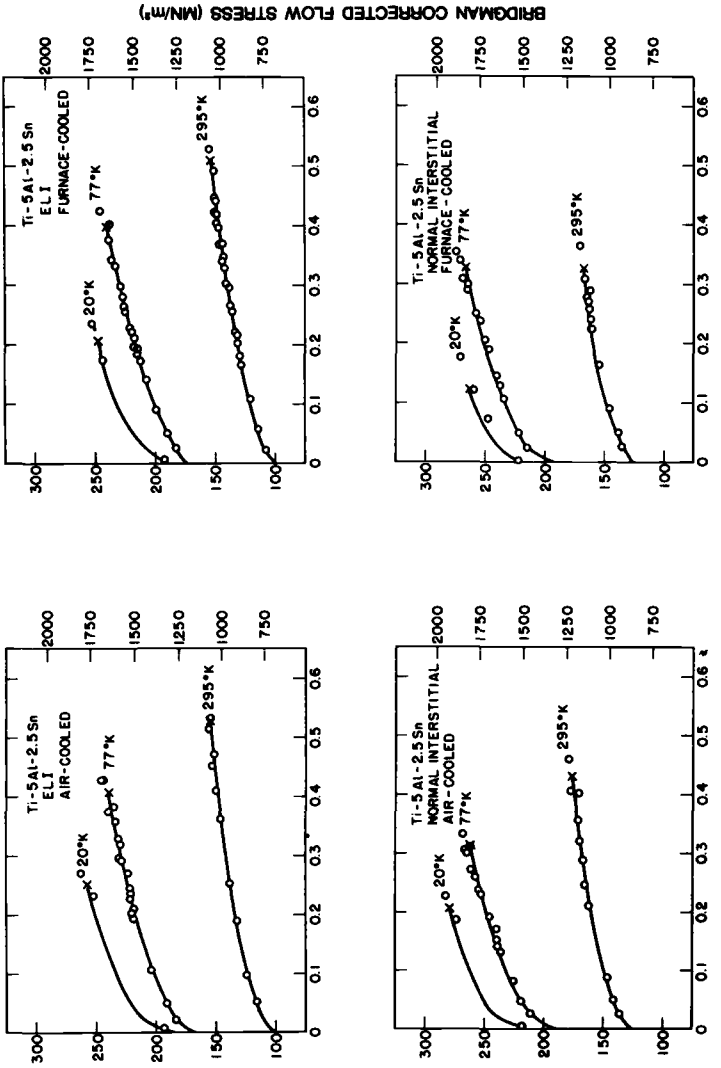

FIG. 6—*Tensile flow curves for Ti-5Al-2.5Sn.*

TABLE 4—*Flow curves of Ti-5Al-2.5Sn plate fit to the form* $\sigma = \sigma_o + A\epsilon^m$.

Alloy	Test Temperature, K	(°F)	σ_o, ksi [a]	A, ksi [a]	m
Ti-5Al-2.5Sn	295	(72)	98.0	77.5	0.50
ELI	77	(−320)	166.3	115.8	0.52
Air-cooled	20	(−423)	172.5	135.6	0.35
Ti-5Al-2.5Sn	295	(72)	96.4	81.5	0.54
ELI	77	(−320)	165.9	121.3	0.55
Furnace-cooled	20	(−423)	171.2	132.4	0.35
Ti-5Al-2.5Sn	295	(72)	120.5	82.9	0.47
Normal interstitial	77	(−320)	180.3	129.2	0.40
Air-cooled	20	(−423)	185.8	140.1	0.26
Ti-5Al-2.5Sn	295	(72)	123.4	81.2	0.55
Normal interstitial	77	(−320)	189.9	127.5	0.46
Furnace-cooled	20	(−423)	185.8	116.7	0.21

[a] 1 ksi = 6.9 MN/m^2.

tion as described by Basinski [*14*]. The behavior is consistent with the observations of Kula and DeSisto [*15*] for unalloyed titanium at 4 K (−453°F) and of Carman and Katlin [*16*] for Ti-5Al-2.5Sn at 20 K (−423°F). Serrated yielding would not be expected to influence the flow curves developed for this test temperature because it occurred outside the range where data were taken. Serrated yielding and multiple necking were not observed at the higher test temperatures, also consistent with Kula and DeSisto's [*15*] work.

Strain hardening rate as obtained by differentiating Eq 1

$$\frac{d\sigma}{d\epsilon} = m A\epsilon^{m-1} \tag{2}$$

is independent of σ_0. As shown in Fig. 7, $d\sigma/d\epsilon$ also appears independent of purity and cooling rate from the annealing treatment and is influenced only by test temperature.

Due to the uncertainty in the 20 K (−423°F) flow curves at intermediate strains, the corresponding work hardening curves are not shown in Fig. 7. Differences between the flow curves shown in Fig. 6 for the two interstitial compositions result primarily from an increase in the apparent elastic limit (σ_0) with decreasing alloy purity. Similar observations have been made by Conrad et al [*17*] for unalloyed titanium.

Elastic Modulus

Young's modulus was determined for the longitudinal plate direction from the load-extension records of triplicate tension specimens tested at

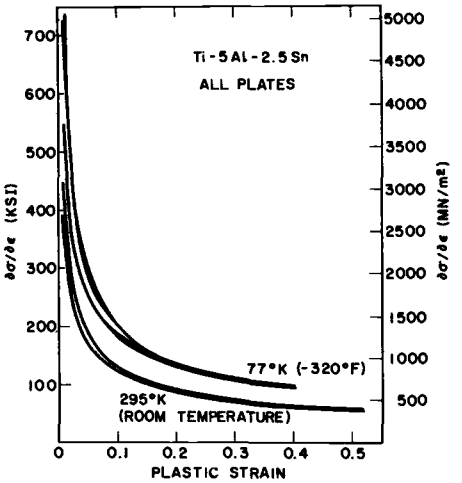

FIG. 7—*Variation of the work-hardening rate* (dσ/dε) *of Ti-5Al-2.5Sn with plastic strain and test temperature.*

20 K (−423°F) and from ultrasonic measurements on single specimens at room temperature. These results are tabulated in Table 5.

Crystallographic texture is known to influence the elastic properties of titanium. In unalloyed titanium, the elastic modulus normal to the basal plane is 45 percent greater than that in the basal plane [7]. Texture in-

TABLE 5—*Longitudinal Young's modulus* (E) *of Ti-5Al-2.5Sn plates.*

	E at 20 K (−423°F)[a] (10^6 psi)[d]	*E* at 295 K (Room Temperature) (10^6 psi)	Predicted[c] *E* at 295 K (Room Temperature) (10^6 psi)
ELI, air-cooled	18.1±0.1	16.8	15.3
ELI, furnace-cooled	18.4±0.1	16.9	15.2
Normal interstitial, air-cooled	19.2±0.1	18.0	16.1
Normal interstitial, furnace-cooled	19.4±0.1	18.0	19.1

[a] Determined from tension specimen loud-extension records. Error limits represent range of 68 percent confidence limits.
[b] Determined using ultrasonic techniques.
[c] Predicted by computer program of Olsen and Moreen [18].
[d] 10^6 psi=6900 MN/m².

formation (input to Figs. 1 and 2) was combined with single crystal elastic constants to compute the room temperature elastic modulus of the Ti-5Al-2.5Sn plates using the computer program of Olsen and Moreen [*18*]. The predicted moduli trends mirror the measured values extremely well. The experimental data are approximately 10 percent high in every case, probably due to the stiffening influence of the alloying additions in the Ti-5Al-2.5Sn plates [*19*]. Agreement between the predicted and measured values suggests that the observed variations are due principally to crystallographic texture, rather than alloy purity or anneal cooling rate differences.

The computer-predicted room temperature moduli are shown as a function of in-plane orientation in Fig. 8. The ELI plate had an annealed α-deformation texture: very few basal planes were perpendicular to the longitudinal direction, and some split toward the transverse directions. Increasing the number of grains with basal planes perpendicular to the tensile axis increases the modulus, as shown in Fig. 8. The normal interstitial plates had a β-processed texture. Basal planes were perpendicular to both the longitudinal and transverse plate directions, explaining the absence of a strong effect in Fig. 8.

Discussion

Strength and toughness variations with test temperature, alloy purity, and cooling rate from the annealing temperature observed in this study of

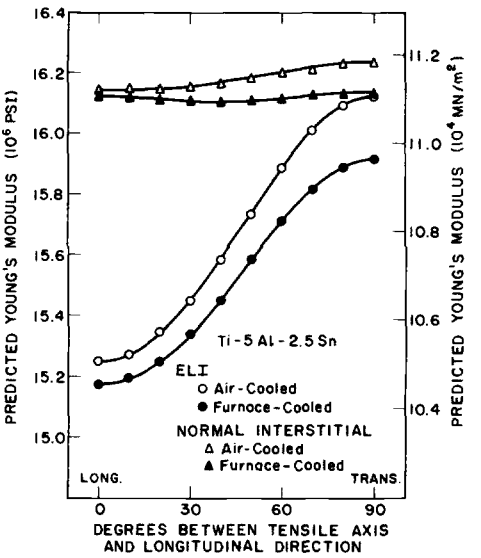

FIG. 8—*Predicted room temperature Young's modulus of the Ti-5Al-2.5Sn plates as a function of orientation.*

25.4-mm (1-in.) plate have confirmed earlier results by Shannon and Brown [3] for Ti-5Al-2.5Sn sheet. Decreasing test temperature and increasing interstitial and iron contents raise the strength and lower the toughness. Slow cooling from the annealing treatment reduces the toughness without affecting the strength of the ELI grade stock, but does not affect the normal interstitial material. The influence of cooling rate for plate was as great as observed previously for sheet. Plate texture differences resulting from what were purported by the vendor to be identical processing and annealing schedules for the plate were perplexing, but their apparent effect on the elastic modulus and toughness directionality provided an interesting highlight to the study.

Fracture Mechanism

Fractographic and metallographic sectioning studies have been conducted and the results reported separately [5]. Those results are drawn upon in this discussion to explain the observed trends in fracture toughness.

The in-depth metallurgical investigation was performed on specimens failed at 77 K (−320°F). Fractographic examination showed the fracture modes at 77 K (−320°F) and 20 K (−423°F) were identical, so it is assumed that metallurgical findings concerning fracture at 77 K (−320°F) apply equally to fracture at 20 K (−423°F). The fracture mode is dimpled rupture with a mixture of elongated and equiaxed dimples. Figure 9 shows a scanning electron microscope (SEM) fractograph of a furnace-cooled ELI K_{Ic} specimen. The area shown is just ahead of the fatigue precrack. Crack propagation is from left to right. The elongated dimples form from cigar-shaped voids which nucleate at the intersections of localized shear deformation (slip bands or deformation twins) with grain boundaries or deformation twin boundaries. Figure 10 shows an optical micrograph of a region 45 μm below the fracture surface of an air-cooled ELI smooth tension specimen tested at 77 K (−320°F). The fracture strain was 0.348. Two sets of parallel etched bands believed to be coarse slip bands intersect twin and grain boundaries to form offsets. The two voids indicated by arrows were observed at the offsets in a primary twin boundary. There is no void at the severe offset, A, indicating voids nucleate after offsets are formed.

The fracture process by nucleation, growth, and coalescence of cigar-shaped voids which produce elongated dimples on the fracture surface is schematically illustrated in Fig. 11. The process begins by the intersection of planar slip bands or deformation twins with twin or grain boundaries, as in Fig. 11(*a*). With increasing strain, offsets form in the boundaries at the end of the blocked shear bands, as in Fig. 11(*b*). The void nucleation event is characterized in Fig. 11(*c*) by decohesion at the offset. The voids grow

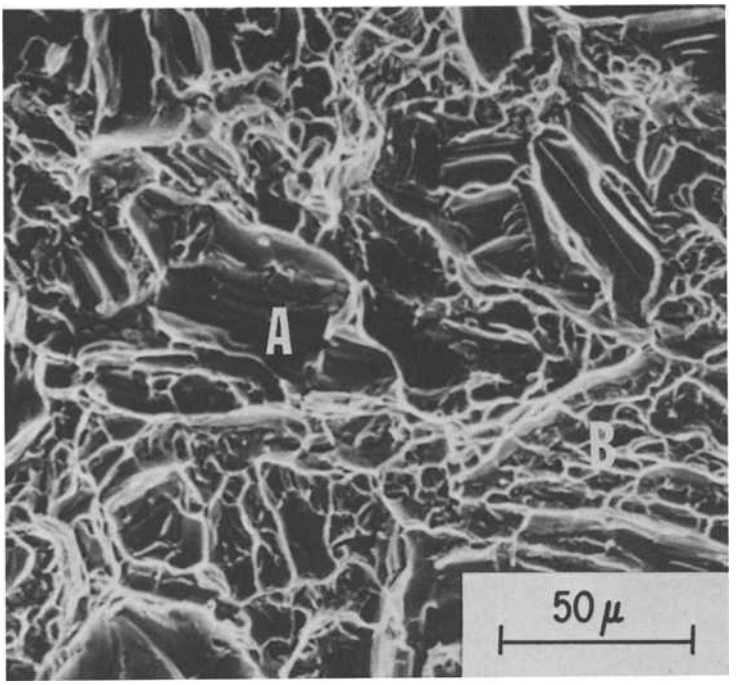

FIG. 9—*SEM fractograph of a furnace-cooled ELI Ti-5Al-2.5Sn fracture toughness specimen tested at 77K. The direction of crack propagation is from left to right. Regions A and B contain elongated and equiaxed dimples respectively.*

along the boundaries as in Fig. 11(*d*) and (*e*), and fracture occurs by void impingement and coalescence as in Fig. 11(*f*).

Some voids were observed to nucleate by decohesion at the interface of iron-stabilized β-particles and the α-matrix. This was observed frequently in the normal interstitial plates, but seldom in the ELI plates, most likely due to the smaller β-particle size [*20-22*] of the low-iron ELI plates. This suggests that iron contents below 0.15 weight percent (level of the ELI plates in this investigation) will not produce further improvement in toughness.

Relation of Fracture Mechanism to Toughness

Factors influencing the toughness of Ti-5Al-2.5Sn alloy can be explained by the fracture mechanism. Of the events that lead to fracture (shown schematically in Fig. 11), void nucleation is the most influential [*5*]. Factors which promote void nucleation decrease toughness. In the present study, reduced toughness correlated with an increased number and decreased size of elognated dimples on the fracture surface. Closely spaced dimples

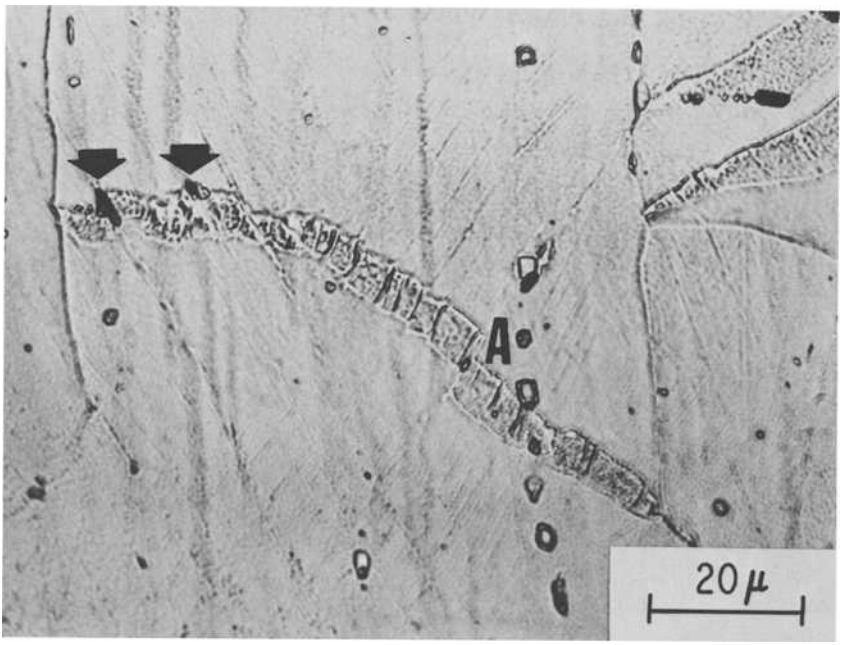

FIG. 10—*Offsets and void nucleation along primary twin boundaries in an optical micrograph of a sectioned air-cooled ELI Ti-5Al-2.5Sn tension specimen strained to 0.348 at 77K. The arrows point to voids along the primary twin boundary at offsets. The letter A indicates an offset without void nucleation. The tensile axis is vertical.*

correspond to a higher rate of void nucleation which results in lessened energy expense in void growth, and consequently reduced toughness.

Voids were nucleated at the intersections of severe shear deformation bands (slip bands or deformation twins) with crystallographic boundaries (grain or twin boundaries), and at the interfaces between iron-stabilized β-particles and the α-matrix. Ninety percent of the voids in the ELI plates formed at blocked slip bands: for air cooled stock, predominately at primary twin boundary intersections; for furnace cooled stock, predominately at α-grain boundary intersections. Void nucleation in the normal interstitial plates cooled at either rate was predominantly by decohesion at the β-particle-matrix interfaces and at the intersections of multiple twins.

Void nucleation at blocked slip bands is controlled by the magnitude of stress concentration at the ends of the bands where the voids form. The stress concentration is influenced by the distribution and length of the bands. The more coarse the slip band spacing (and hence the more dislocations or strain per slip band) and the longer the bands, the less macroscopic strain required for void formation. Previous investigations [*23,24*] have shown that reduced test temperature, increased interstitial level, and α_2

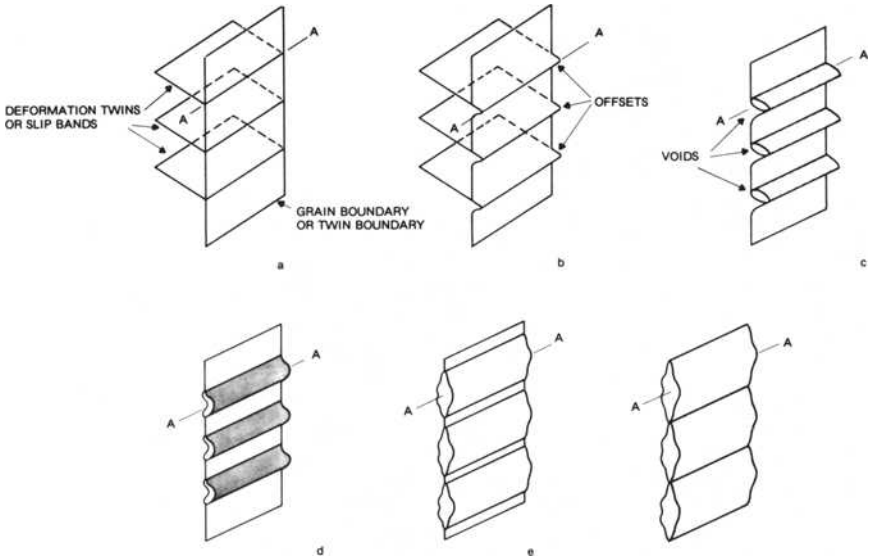

FIG. 11—*Schematic of the sequence of events during fracture by cigar-shaped voids forming elongated dimples.*

precipitation cause the character of slip in α-itanium alloys to become planar and more coarse. In the present study, these were the observed embrittling factors.

Thin foil TEM revealed extremely coarse, planar slip bands for both air-cooled and furnace-cooled normal interstitial Ti-5Al-2.5Sn plates deformed at 77 K ($-320°F$). In contrast, air-cooled ELI plate had planar but relatively fine homogeneous slip bands. Furnace cooling the ELI plate produced coarsening to an intermediate degree, an effect due to the ordering reaction evident in the diffraction patterns of Fig. 3. The degree of slip coarsening correlated with the degree of embrittlement. The grain size of the plates was not a significant factor in this study because of its essential uniformity. It is tempting to speculate, however, that grain refinement might further improve the toughness of Ti-5Al-2.5Sn alloy through its effect of reducing the stress concentration at the ends of the foreshortened slip bands or deformation twins.

Texture and Directionality

The fracture toughness directionality (LT versus LS specimen crack-plane orientation) is believed due to the variation in crystallographic texture among the plates tested. To explain the observed trends, refer to an

analysis of the resolved shear stresses for slip and for twinning in Appendix II.

The ELI plates possessed an annealed α-deformation texture. Void nucleation occurred primarily at blocked slip bands. The analysis of Appendix II predicts slip at lower stress intensity levels for LT oriented specimens than for LS oriented specimens. Slip band dislocation densities and stress concentrations therefore would be expectedly higher in the LT specimens. Preferential twinning is predicted for LS specimens by the analysis for resolved shear stresses for twinning (Appendix II). A higher incidence of twin intersections would be anticipated, having the effect of shortening slip band length and thereby reducing slip band stress concentration. These anticipated behaviors are in agreement with the observed toughness superiority of LS oriented specimens for the ELI plates.

The normal interstitial plates were β-processed textured. Void nucleation occurred at β particles and multiple twin intersections. Beta-particle decohesion would be expected to be independent of specimen orientation. Resolved shear stress analysis in Appendix II indicates that twinning occurs with near-equal ease on four of the five operative twin systems for both specimen orientations. An additional twin system is operative for LT specimens, which would increase void nucleation rate slightly for the LT specimen orientation. This explains the absence of significant directionality in the normal interstitial plates, with a hint of LS toughness superiority.

Conclusions

The mechanical properties of Ti-5Al-2.5Sn plate were evaluated over the temperature range from ambient to 20 K (−423°F). Decreases in test temperature and increases in interstitial level resulted in higher yield strength and decreased fracture toughness. Variation in cooling rate from the annealing temperature had no influence on strength or tensile ductility. The variation in cooling rate did not affect K_{Ic} of the normal interstitial plates, but K_{Ic} of the air-cooled ELI plate was 30 percent greater than that of the furnace-cooled ELI plate. The combination of specimen orientation and crystallographic texture caused variations in Young's modulus and K_{Ic}. LS orientation fracture toughness was 20 percent greater than LT K_{Ic} in the ELI plates, but the variations in the normal interstitial alloys were substantially less.

Fractography and metallographic sectioning were used to investigate the fracture mechanism. It was shown that the fracture mechanism was dimpled rupture where voids nucleated at the intersection of intense localized shear bands with crystallographic boundaries and at the interfaces between β-particles and the α-matrix. Increasing interstitial content, decreasing test temperature, and ordering caused by furnace-cooling from the annealing

temperature caused the slip band structure to become coarser. The higher strain per slip band increased the rate of void nucleation and as a result decreased fracture toughness. An analysis of the deformation systems active in the crack tip region in these textured plates was used to explain the variations in toughness with specimen orientation.

The results of this investigation suggest that the plane strain fracture toughness of Ti-5Al-2.5Sn alloy at cryogenic temperatures can be improved by having the lowest possible interstitial level, cooling rapidly from the annealing temperature to avoid ordering, and reducing the iron content to a maximum of 0.15 percent. It was suggested that a reduction in α-grain size and texture-stress state combinations which suppress multiple twinning may also improve K_{Ic}.

Acknowledgments

The work was performed in part under National Aeronautics and Space Administration Grant NGR-39-087-047. The authors would like to thank W. F. Brown, Jr. and W. D. Klopp of that organization for their helpful support and comments. The authors also appreciated the help of J. C. Williams, formerly of Rockwell International Science Center and presently of Carnegie-Mellon University, for his assistance in the ultrasonic determinations of elastic modulus.

APPENDIX I

Flow Curve Techniques

Flow stress-true plastic strain curves were developed at all test temperatures by fitting an empirical flow curve equation to the experimental data.

At 20 K (−423°F), only information from the load-extension record and the fracture event were available. At higher test temperatures, the load-extension record was supplemented with specimen diameter measurements taken periodically up to fracture.

Up to 0.1 strain where necking occurred, true stress and true strain were computed from the load-extension records using the classical relationships [25]

$$\text{true stress } (\sigma_t) = \frac{P}{A_o}(e + 1) \tag{3}$$

$$\text{true strain } (\epsilon) = \ln\ (e + 1) \tag{4}$$

Beyond 0.1 strain, diameter measurements were used to compute true stress directly as $\sigma_t = P/A$, and true strain from the relation

$$\epsilon = 2\ \ln\ (d_o/d) \tag{5}$$

True stress beyond maximum load was corrected for hydrostatic tension in the neck by multiplication with the Bridgman [*12*] correction factor

$$F = 1/[(1 + 2R/a)\ln(1 + a/2R)] \quad (6)$$

For use in this expression, a/R values were determined from room temperature tension specimens of air cooled Ti-5A1-2.5Sn plates. Neck diameter and curvature were measured over a range of strains on a $\times 20$ shadowgraph. The results are compared with Bridgman's data for steels [*12*] in Fig. 12. The scatter for both sets of data is enormous. Nevertheless, a least-squares regression line was drawn through each set, indicating an appreciable difference between the two classes of materials.

The equation for the Ti-5A1-2.5Sn regression curve is

$$a/R = -0.072 + 0.589\ \epsilon \quad (7)$$

In the present study, a/R values were assumed independent of test temperature, interstitial level, and cooling rate from the annealing treatment, and the values calculated from Eq 7 were used for all flow stress corrections. When a/R was negative, which occurs at strains below 0.122, a Bridgman correction factor of unity was used.

APPENDIX II

Crack Tip Deformation Mode Analysis

To examine the influence of texture and specimen orientation on K_{Ic}, a computer program similar to the one described by Thornburg [*26*] was written

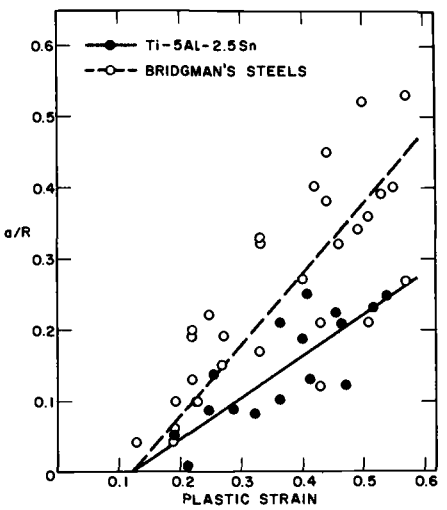

FIG. 12—*Comparison of room temperature* a/R *values as a function of strain for air cooled Ti-5Al-2.5Sn plates with those for Bridgman's steels* [12].

to describe the resolved shear stress on a given slip or twin system as a function of the position of the C-axis on a stereographic projection for an arbitrarily imposed stress state. The deformation systems included the four slip systems [prism, basal, pyramidal, and $\overrightarrow{c+a}$ (1011)] and five twin systems [$10\bar{1}2$), ($11\bar{2}1$), ($11\bar{2}2$), ($11\bar{2}3$), and ($11\bar{2}4$)] known to operate at cryogenic temperatures in α-titanium.

It was assumed that the criterion for deformation by slip is the critical resolved shear stress. The index used to evaluate the operation of a given slip system was the resolved shear stress divided by the critical resolved shear stress for that particular slip system. The critical resolved shear stresses determined by Paton et al [*24*] for titanium-6.6Al crystals at 77 K (−320°F) were used for the normalization. The index used for the activation of twin systems was a resolved shear stress criterion. There is no established critical resolved shear stress for twinning; however, in most cases, the twin system with the highest resolved shear stress is the first system to operate. Reed-Hill [*27*] has shown that in polycrystalline zirconium, the variation in number of twins for several twin systems is very similar in shape to the variation in the resolved shear stress. Thus, the resolved shear stress appears to be an adequate index to determine if a given twin system is operating.

To examine toughness variations between the LS and LT orientation fracture toughness specimens, a stress state typical of that ahead of a crack was used in the computer program. There are many elastoplastic finite element calculations which show the variation of the stresses with position and work-hardening characteristics. Rice et al [*28, 29*] have analyzed the crack tip stress fields of elastic-perfectly plastic (non work-hardening) material using both slip line field theory and finite element calculations. These stresses were normalized so that the maximum stress which is parallel to the applied load is equal to unity. The normalized stresses used to calculate the resolved shear stresses for the LS and LT orientation fracture toughness specimens are given in Table 6. For both specimen orientations, the maximum stress acts in the longitudinal plate direction and is the same so that equivalent levels of K_I are being compared.

The stereographic projections in Fig. 13 show the variation in the resolved shear stresses for slip normalized by the critical resolved shear stress for LT and LS orientation fracture toughness specimens. Figure 14 shows the resolved shear stress for twinning for the same stress states. Figure 13 shows that for alloys with an annealed α-deformation texture, specimens with an LT orientation will tend to deform by prism and pyramidal slip at a lower K_I level than specimens with an LS orientation, but higher K_I levels by basal slip. For both orientations, $\overrightarrow{c+a}$ slip seems to be fairly unlikely. Figure 14 shows that the resolved shear stress for twinning in plates with an α-annealing texture is fairly

TABLE 6—*Normalized stresses used for calculation of the resolved shear stresses for LS and LT orientation fracture toughness specimens.*

Stress Axis	LT Specimen	LS Specimen
Longitudinal	1.000	1.000
Transverse	0.607	0.804
Short-Transverse	0.804	0.607

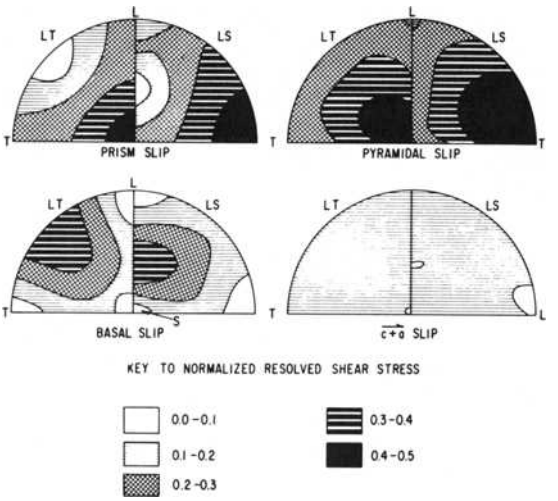

FIG. 13—*Stereographic projections showing the variation of normalized resolved shear stress for slip in LS and LT orientation fracture toughness specimens. L, T, and S indicate longitudinal, transverse, and short transverse plate directions, respectively.*

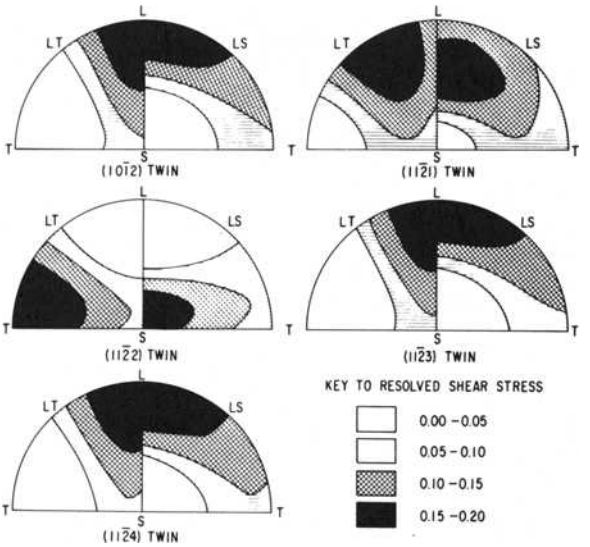

FIG. 14—*Stereographic projections showing the variation of resolved shear stress for twinning in LS and LT orientation fracture toughness specimens. L, T, and S indicate longitudinal, transverse, and short transverse plate directions, respectively.*

low except for $(11\bar{2}2)$ twinning. This twinning system is most likely to occur at lower K_I levels in the LS specimen than one with an LT orientation. Void nucleation in the ELI alloys occurs most frequently at the intersection of slip bands with twin boundaries or grain boundaries [5]. It is argued that a reduction in slip band length and a more even distribution of slip would delay void nucleation to higher strains and in turn improve K_{Ic}. Calculation of the resolved shear for slip for LS and LT fracture toughness specimens suggests that slip will occur at lower K_I levels in LT specimens than LS specimens. Thus, at the same K_I level, there will probably be more dislocations per slip band in LT specimens. The higher resolved shear stress for twins in the LS specimens suggests that the LS orientation will have a higher twin volume fraction than the LT specimen. A higher twin volume fraction of the $(11\bar{2}2)$ twins will tend to reduce the slip band length. These factors suggest that the LS K_{Ic} value will be higher than that for LT specimens for alloys with an α-annealing texture. This is consistent with the observed K_{Ic} values for the air-cooled and furnace-cooled ELI alloys.

The normal interstitial alloys have a β-processed texture. The resolved shear stresses on twin systems shown in Fig. 14 suggests that $(10\bar{1}2)$, $(11\bar{2}1)$, $(11\bar{2}3)$, and $(11\bar{2}4)$ twins are equally likely to occur for both LS and LT specimens with a β processed texture. Twins of the $(11\bar{2}2)$ system may also occur for LT specimens. Void nucleation in the normal interstitial alloys occurred most frequently at multiple twin intersections [5]. The resolved shear stress data on the twin systems suggest that twinning can occur on many twin systems for fracture toughness specimens with both LS and LT orientations. From this, one would expect that K_{Ic} would be similar for both orientations, as observed.

References

[1] Christian, J. L., Hurlich, A., Chafey, J. E., and Watson, J. F., *Proceedings,* American Society for Testing and Materials, Vol. 63, 1963, p. 578.

[2] Broadwell, R. G. and Wood, R. A., *Materials Research and Standards,* Vol. 4, 1964, p. 549.

[3] Shannon, J. L., Jr. and Brown, W. F., Jr., *Proceedings,* American Society for Testing and Materials, Vol. 63, 1963, p. 809.

[4] Curtis, R. E., Boyer, R. R., and Williams, J. C., *Transactions,* American Society for Metals, Vol. 62, 1969, p. 457.

[5] Van Stone, R. H., Low, J. R., Jr., and Shannon, J. L., Jr., "The Fracture Mechanism of Ti-5A1-2.5Sn at Cryogenic Temperatures," accepted for publication in *Metallurgical Transactions.*

[6] Olsen, R. H., *Metallography,* Vol. 5, 1972, p. 369.

[7] Larson, F. and Zarkades, A., "Properties of Textured Titanium Alloys," Report MCIC-74-20, Metals and Ceramics Information Center, Battelle Columbus Laboratories, Columbus, Ohio, June 1974.

[8] Blackburn, M. J., *Transactions,* American Institute of Mining, Metallurgical, and Petroleum Engineers, Vol. 239, 1967, p. 1200.

[9] Shannon, J. L., Jr. and Pierce, W. S., "An LVDT-Type Displacement Gage for Plane Strain Fracture Toughness Tests in Liquid Hydrogen," *NASA Tech Brief Journal,* LEW-13038, 1978.

[10] Shannon, J. L., Jr., Bubsey, R. T., and Pierce, W. S., "Plane Strain Fracture Toughness Assessment of Thick-Walled Liquid Hydrogen Transfer Pipe Made of Welded Centrifugally-Cast 21-6-9 Stainless Steel," to be published.

[11] Pierce, W. S. and Shannon, J. L., Jr., "Use of ASTM E-399 Displacement Gage for Plane Strain Fracture Toughness Tests in Liquid Hydrogen," *NASA Tech Brief Journal,* LEW-13039, 1978.

[12] Bridgman, P. W., *Studies in Large Plastic Flow and Fracture,* McGraw-Hill, New York, 1952.
[13] Monterio, S. N. and Reed-Hill, R. E., *Metallurgical Transactions,* Vol. 4, 1973, p. 1011.
[14] Basinski, Z. S., *Proceedings,* Royal Society of London, Vol. A240, 1957, p. 229.
[15] Kula, E. and DeSisto, T. in *Behavior of Materials at Cryogenic Temperatures, ASTM STP 387,* American Society for Testing and Materials, 1966, p. 3.
[16] Carman, C. M. and Katlin, J. M. in *Applications Related Phenomena in Titanium Alloys, ASTM STP 432,* American Society for Testing and Materials, 1968, p. 124.
[17] Conrad, H., Okasaki, K., Gadgil, V., and Jon, M. in *Electron Microscopy and Structure of Materials,* University of California Press, Berkeley, 1972, p. 438.
[18] Olsen, R. H. and Moreen, H. A., *Metallurgical Transactions,* Vol. 4, 1973, p. 701.
[19] Ogden, H. R., Maykuth, D. J., Finlay, W. L., and Jaffee, R. I., *Transactions,* American Institute of Mining, Metallurgical, and Petroleum Engineers, Vol. 197, 1953, p. 267.
[20] VanStone, R. H., Merchant, R. H., and Low, J. R., Jr. in *Fatigue and Fracture Toughness-Cryogenic Behavior, ASTM STP 556,* American Society for Testing and Materials, 1974 p. 93.
[21] Cox, T. B. and Low, J. R., Jr., *Metallurgical Transactions,* Vol. 5, 1974, p. 1457.
[22] Greenfield, M. A., and Margolin, H., *Metallurgical Transactions,* Vol. 3, 1972, p. 2649.
[23] Paton, N. E., Williams, J. C., and Rauscher, G. P., in *Titanium Science and Technology,* Plenum Press, New York, 1973, p. 1049.
[24] Paton, N. E., Baggerly, R. G., and Williams, J. C., "Deformation and Solid Solution Strengthening of Titanium Aluminum Single Crystals," Report SC 526.7FR, Rockwell International Science Center, 20 Jan. 1976.
[25] Dieter, G. E., Jr. in *Mechanical Metallurgy,* McGraw-Hill, New York, 1961, p. 237.
[26] Thornburg, D. A., "Cold-Rolling Texture Development in Titanium and Titanium-Aluminum Alloys," Ph.D. thesis, Department of Metallurgy and Materials Science, Carnegie-Mellon University, 1972.
[27] Reed-Hill, R. E. in *Deformation Twinning,* Gordon and Breach, New York, 1964, p. 295.
[28] Rice, J. R. and Rosengren, C. F., *Journal of the Mechanics and Physics of Solids,* Vol. 16, 1968, p. 1.
[29] Levy, N., Marcal, P. V., Ostergren, W. J., and Rice, J. R., *International Journal of Fracture Mechanics,* Vol. 7, 1971, p. 143.

R. Chait [1] *and P. T. Lum* [1]

Influence of Test Temperature on the Fracture Toughness and Tensile Properties of Ti-8Mo-8V-2Fe-3Al and Ti-6Al-6V-2Sn Alloys Heat Treated to High Strength Levels

REFERENCE: Chait, R. and Lum, P. T., **"Influence of Test Temperature on the Fracture Toughness and Tensile Properties of Ti-8Mo-8V-2Fe-3Al and Ti-6Al-6V-2Sn Alloys Heat Treated to High Strength Levels,"** *Toughness and Fracture Behavior of Titanium, ASTM STP 651*, American Society for Testing and Materials, 1978, pp. 180–199.

ABSTRACT: This paper examines the mechanical properties of two high strength titanium alloys as a function of test temperature, namely, the α/β titanium alloy Ti-6Al-6V-2Sn (Ti-662) as well as the metastable β-alloy Ti-8Mo-8V-2Fe-3Al (Ti-8823). Specifically, the paper characterizes the changes in fracture toughness and tensile properties at low and elevated test temperatures. The variation in fracture toughness is given by K_Q and W/A, while for the tensile properties, it is given by the yield and ultimate tensile strength, reduction of area, and elongation. For Ti-8823 material, the characterization was conducted on material that was given either a solution treated-and-aged or an age treatment directly after fabrication. Heat treatments for the Ti-662 alloy were either a solution-treated-and-age or solution-treated-and-overaged. Results are discussed in terms of fractographs taken from broken fracture toughness and tension specimens.

KEY WORDS: titanium, titanium alloys, mechanical properties, tensile properties, fracture toughness, fractography, low temperature tests, elevated temperature tests

Recent efforts [*1*] [2] have characterized important static mechanical properties of the metastable β titanium alloy, Ti-Mo-8V-2Fe-3Al (Ti-8823), and the α/β alloy, Ti-6Al-6V-2Sn (Ti-662), fabricated in heavy section by an extrusion operation which provided a large amount of continuous hot

[1] Army Materials and Mechanics Research Center, Watertown, Mass. 02172. Lum is presently employed by AIRCO, Inc., Murray Hill, N. J.

[2] The italic numbers in brackets refer to the list of references appended to this paper.

Copyright© 1978 by ASTM International www.astm.org

working. These mechanical properties, obtained at room temperature, were utilized in these studies to provide a comparison of through-the-section behavior after heat treatment. It was shown, for example, that for Ti-8823 receiving a large amount of continuous working, aging immediately after hot working results in higher and more uniform strength, ductility, and fracture toughness through the section when compared to solution-treated-and-aged material. Additional work on Ti-8823 with the same processing history, again at room temperature, detailed the effect of strain rate on tensile properties and relative fracture toughness [*2*]. It was shown that an increase in the strain rate is accompanied by an increase in not only yield and tensile strength but ductility and fracture toughness. The present study extends the alloy's characterization and examines the test-temperature influence on tensile and fracture toughness properties of Ti-8823 and Ti-662 alloys.

Materials and Test Procedures

The chemical compositions of the Ti-662 and Ti-8823 alloys are shown in Table 1. These alloys were processed in heavy section beginning with a reduction from 711-mm (28-in.) diameter ingot to 508-mm (20-in.) diameter billet, followed by extrusion at 871 and 927°C for the Ti-662 and Ti-8823, respectively, which continuously reduced the material approximately 84 percent and produced a cylindrical hollow having an outside diameter (OD) of 299 and 83-mm (11¾ and 3¼-in.) wall. The extrusion process is very similar to that utilized to produce oil pipe [*3*].

Following extrusion, a section of each billet was heat treated to provide high strength levels. Two heat treatments were selected for each alloy: solution-treated-and-aged (STA) and solution-treated-and-overaged (STOA) for the Ti-662 alloy, and a common STA and direct aged (DA) without any intermediate solutionizing for the Ti-8823 alloy. Temperatures and times for these heat treatments are given in Table 2.

Cylindrical tension specimens having a 6.4-mm (0.252-in.) diameter gage section were machined from the heat treated billet at the inner

TABLE 1—*Composition.*

Alloy	Element (weight percent)									
	Al	V	Mo	Fe	Sn	Cu	C	O	H	N
Ti-6Al-6V-2Sn (Ti-662)	5.58	5.67	...	0.72	2.01	0.57	0.024	0.16	0.006	0.015
Ti-8Mo-8V-2Fe-3Al (Ti-8823)	3.08	8.08	7.80	2.07	...	...	0.035	0.133	0.006	0.010

TABLE 2—*Heat treatment.*

Alloy	Condition	Solutionizing Temperature and Time Prior to Water Quench	Aging Temperature and Time Prior to Air Cooling
Ti-662 [a]	STA	871°C, 3 h	538°C, 4 h
	STOA	871°C, 3 h	690°C, 6 h
Ti-8823 [b]	STA	802°C, 1½ h	538°C, 8 h
	DA		510°C, 8 h

[a] Blocking, piercing, and extrusion temperature 871°C.
[b] Blocking, piercing and extrusion temperature 927°C.

diameter (ID) location. Material commitments to other programs precluded evaluation of other through-the-thickness locations. Specimens at the ID were taken in the longitudinal (LR) and transverse (CR) direction. In most instances, one specimen from each direction was tested at each of the following test temperatures: −79, 20, 204, and 315°C and the average value was utilized for evaluation purposes. The test was performed on a $534 \cdot 10^3$N (120 000-lb) capacity universal hydraulic testing machine at a platen displacement of 0.133 mm/min (0.005 in./min).

Standard full-size Charpy toughness specimens were also machined from the heat treated billets. Again, because of material commitments, it was not possible to get a full complement of specimens. For Ti-662 (STA), Ti-662 (STOA), and Ti-8823 (STA), specimens were taken from a single location: ID, OD, or midwall (MD) in the LR orientation. Since Ti-8823 (DA) exhibited very uniform properties through the thickness [*1*], Charpy specimens were utilized from all three locations. The Charpy specimens were precracked under fatigue loading at room temperature and tested to failure at the following test temperatures in three-point bending to determine the conditional plane strain fracture toughness parameter, K_Q: Ti-662 (STA) and Ti-8823 (STA)—196, −40, 20, and 93°C; Ti-662 (STOA)—previous temperatures plus 365°C; Ti-8823 (DA)—previous temperatures plus 204 and 365°C. The precracking procedure involved initiation of the crack in compression and subsequent growth in tension, a method which gave uniform crack fronts for high strength steels as well as titanium alloys [*4*].

Results and Discussion

Behavior Under Tensile Loading

Yield strength variation with temperature is detailed in Fig. 1. It is shown for Ti-8823 that lowering the test temperature to −79°C raises

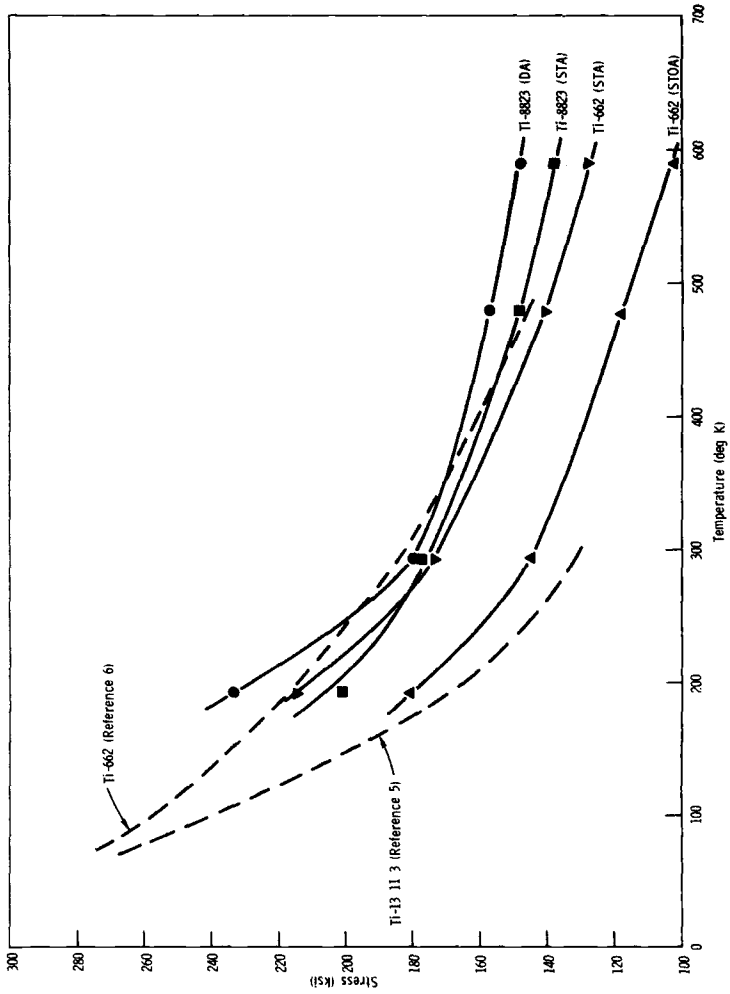

FIG. 1—*The effect of test temperature on the yield strength of Ti-662 and Ti-8823 alloys. (1 ksi=6.89 MPa.)*

the yield strength for the DA materials about 344 MPa (50 ksi) above that for room temperature. For Ti-8823 material in the STA condition, the increase is about 138 MPa (20 ksi). Temperature also has a marked influence on the yield strength of Ti-662 in both the STA and STOA condition. Lowering the test temperature from room temperature to −79°C increases the yield strength about 276 MPa (40 ksi) for both the STA and STOA material. As shown in Fig. 1, the increase in yield strength at the low temperatures for both the Ti-8823 and Ti-662 alloys is consistent with the results of previous studies dealing with the effect of test temperature on the tensile properties of Ti-662 and another metastable β-alloy, Ti-13V-11Cr-3Al [*5,6*]. The ultimate tensile strength variation with test temperature is detailed in Fig. 2. Essentially, this variation follows the trends just mentioned for the yield strength behavior of Ti-8823 and Ti-662.

The variation in yield strength with test temperature can provide important information on deformation mechanisms. First, however, it is important to distinguish between the thermal component (σ^*) and the athermal component (σ_u) to the flow stress. As summarized by Conrad [*7*], σ^* is very dependent on strain rate and temperature and is associated with short-range obstacles and dislocation motion past them; σ_u reflects only the temperature dependence of the elastic modulus and is associated with the longer range internal stress field. The total flow stress (σ) is thus given by

$$\sigma = \sigma^* + \sigma_u \tag{1}$$

To study thermally activated deformation, Conrad [*7*] has suggested eliminating σ_u by obtaining the difference between the flow stress at some test temperature, T (σ_T), and some reference test temperature, say room temperature (σ_{RT}), to form the relationship

$$\Delta\sigma^* = \sigma_T - \sigma_{RT} \tag{2}$$

This approach has been utilized to compare the temperature dependence of the thermal component of high strength maraging steel with that of various irons and steels [*8*]. Since $\Delta\sigma^*$ variation with temperature was independent of alloy type, it was concluded that the principal strengthening mechanism in maraging steels is athermal in nature and associated with the presence of longer range internal stresses of the kind associated with precipitated particles. Utilizing the same approach, it has been shown that for a number of titanium alloys, $\Delta\sigma^*$ was independent of alloy content over a range of test temperatures [*9*]. The trend line from Ref *9* is shown in Fig. 3. Using a Ti-6Al-4V alloy of a single composition, it was also shown that microstructural variation had no effect on $\Delta\sigma^*$. These observations appear to be substantiated by the behavior of the alloys of concern in the present study. As shown in Fig. 3, there is satisfactory agreement with the results of Ref 9.

Turning to the tensile ductility behavior, elongation (EL) and reduction

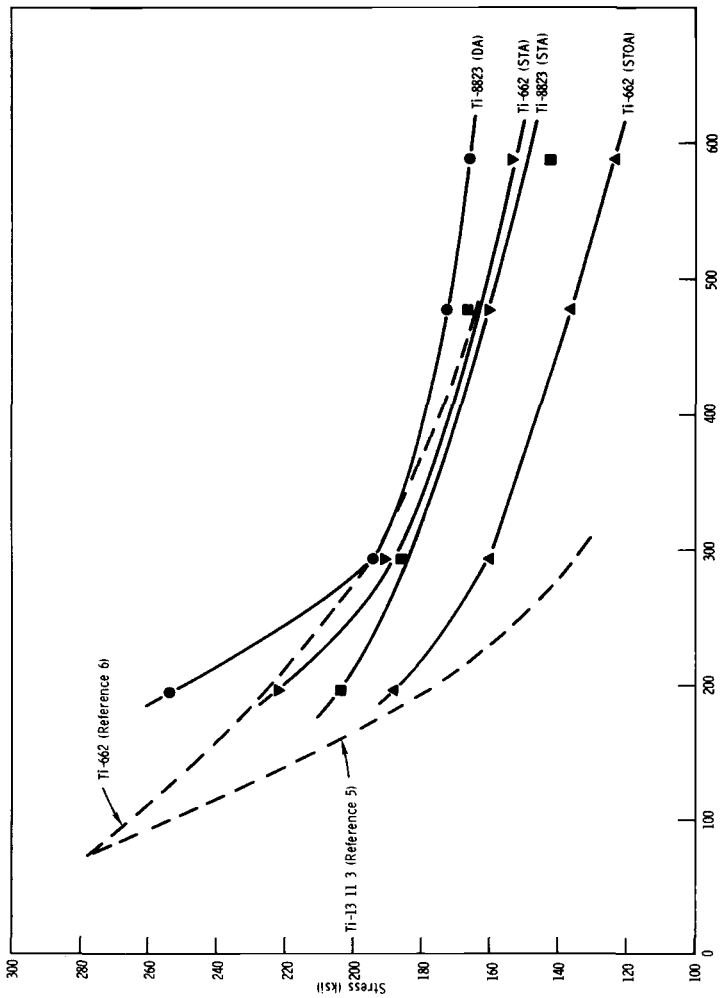

FIG. 2—*The effect of test temperature on the ultimate tensile strength of Ti-662 and Ti-8823. (1 ksi=6.89 MPa.)*

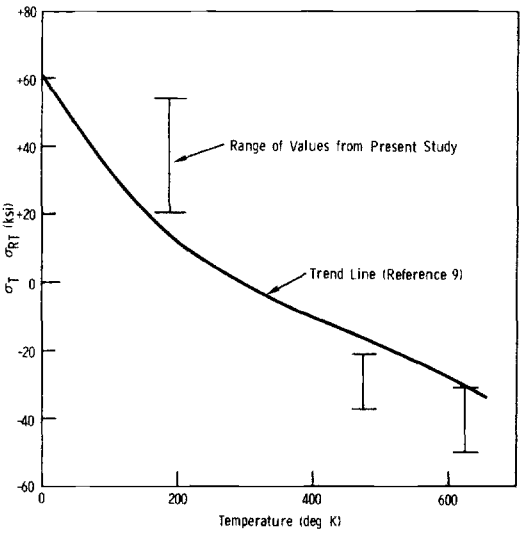

FIG. 3—*The effect of test temperature on the thermal component of the flow stress. (1 ksi=6.89 MPa.)*

of area (RA) values as a function of test temperature are shown in Fig. 4. For Ti-8823 and Ti-662 alloys, both measures of ductility diminish to practically zero as the temperature approaches −79°C. Increasing the test temperature beyond room temperature leads to considerable increase in ductility. At 315°C this increase levels off at the following approximate values: Ti-662 (RA~50 percent, El~20 percent); Ti-8823 (RA~30 percent, El~10 percent). Note that at the maximum test temperature there is little effect of heat treatment.

These changes in ductility are reflected in the appearance of the fracture surface of broken tension specimens. Macroscopic examination of these specimens shows that the increase in tensile ductility at the elevated temperatures is accompanied by an increase in the extent of shear-type fracture (shear-lip) as shown in Figs. 5 and 6 for Ti-8823 (DA) and Ti-662 (STA), respectively. Examination of the fracture surface at the higher magnification provides information on the mode of fracture. It is seen in Fig. 7 that for Ti-8823, there is a greater amount of intergranular fracture at −79°C than at 315°C. For Ti-662 shown in Fig. 8, the lower test temperature induces a low energy tear type of fracture at the expense of the dimple type of matrix failure.

Fracture Toughness Behavior

The K_Q fracture toughness values obtained from precracked Charpy specimens tested over a range of test temperatures are shown in Fig. 9 for

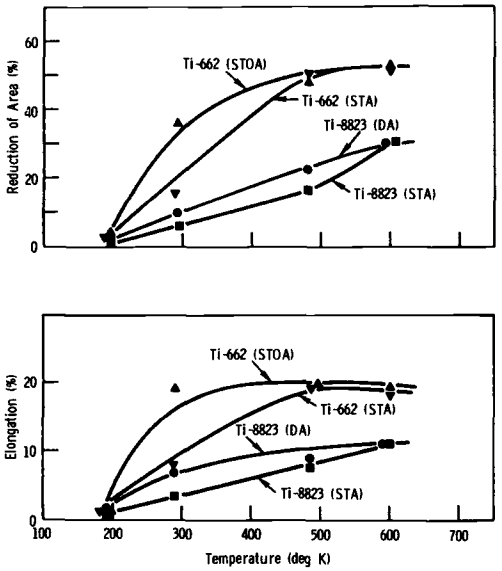

FIG. 4—*The effect of test temperature on the ductility (reduction of area and elongation) of Ti-662 and Ti-8823 alloys.*

Ti-662 and Ti-8823 alloys. Note that while Ti-662 (STOA) exhibits a better toughness at the lowest and highest temperatures, as might be expected from the relative strength values, there is a temperature region $<127°C$ where the toughness falls below that of Ti-8823 (DA) due to the lower rate of increase in K_Q with test temperature for Ti-662 in the -196 to $-40°C$ range. Over this temperature range, $\Delta K_Q \simeq 6.4$ MPa $\sqrt{m}$ (7 ksi $\sqrt{in.}$) for Ti-662 (STOA), while for Ti-8823 (DA) $\Delta K_Q \simeq 18.2$ MPa $\sqrt{m}$ (20 ksi $\sqrt{in.}$). The same comments can be made for a relative comparison of Ti-8823 (STA) and Ti-662 (STA). This trend of the lower temperature sensitivity of Ti-662 may be characteristic of the fracture toughness behavior of this type of α/β alloy at low temperatures. For Ti-6Al-4V, Steigerwald [*10*] notes little changes in K_{Ic} between -73 and $20°C$. Additional data in the literature [*11,12*] show that between -196 and $20°C$ for the same alloy, $\Delta K_{Ic} \simeq 7.3$ to 8.2 MPa $\sqrt{m}$ (8 to 9 ksi $\sqrt{in.}$). For Ti-662, $\Delta K_Q \simeq 5.5$ MPa $\sqrt{m}$ (6 ksi $\sqrt{in.}$) over the same temperature range [*6*]. Perhaps the explanation for this behavior rests with the fracture mode of the α/β alloys compared with that of the Ti-8823 metastable β-alloy in the temperature range of concern. For this purpose, the fracture surfaces of broken Ti-662 (STA) and Ti-8823 (DA) K_Q specimens were examined. For Ti-8823 (DA), Fig. 10 shows the marked decrease in intergranular type of fracture with increasing test temperature accounting for the increase in K_Q. In contrast (Fig. 11), there appears to be

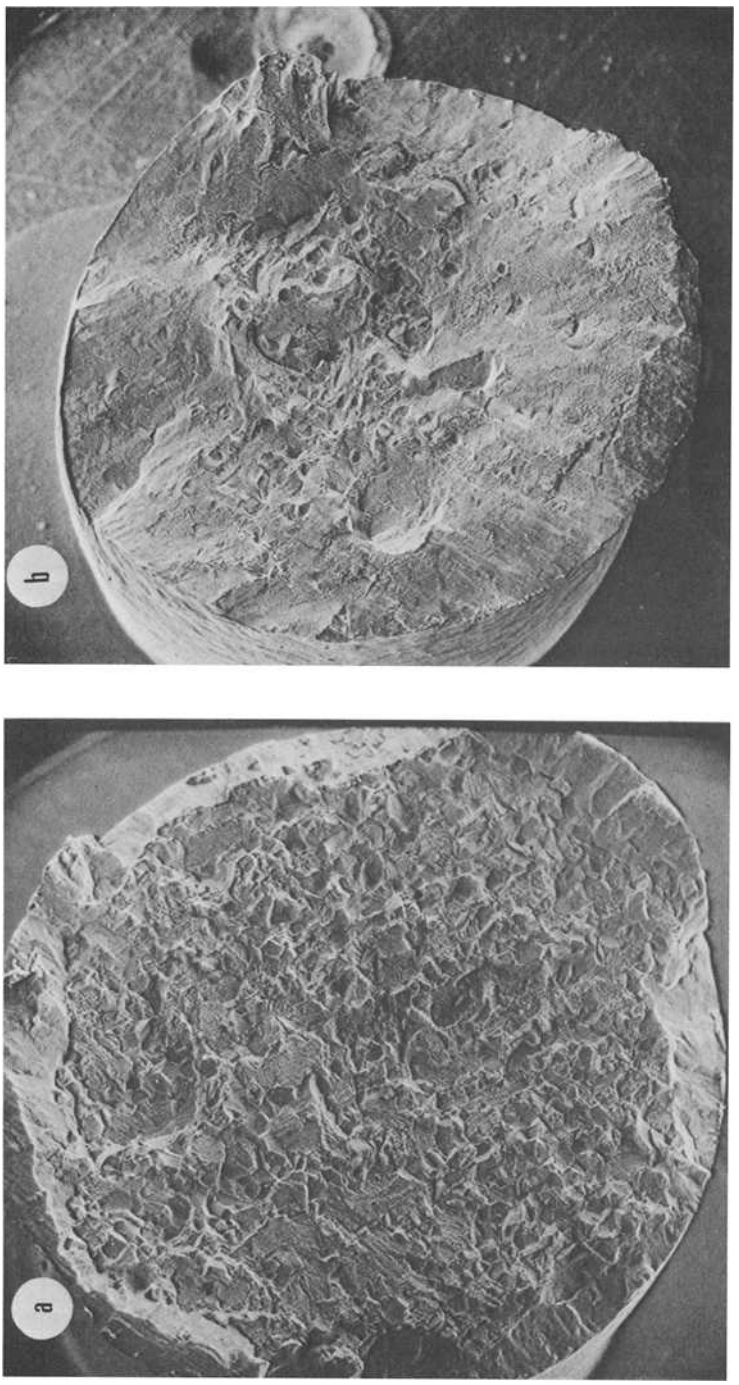

FIG. 5—*Low magnification view of Ti-8823 (direct age) tension specimens broken at two different test temperatures.* (a) *−79°C, and* (b) *315°C.* ×*20.*

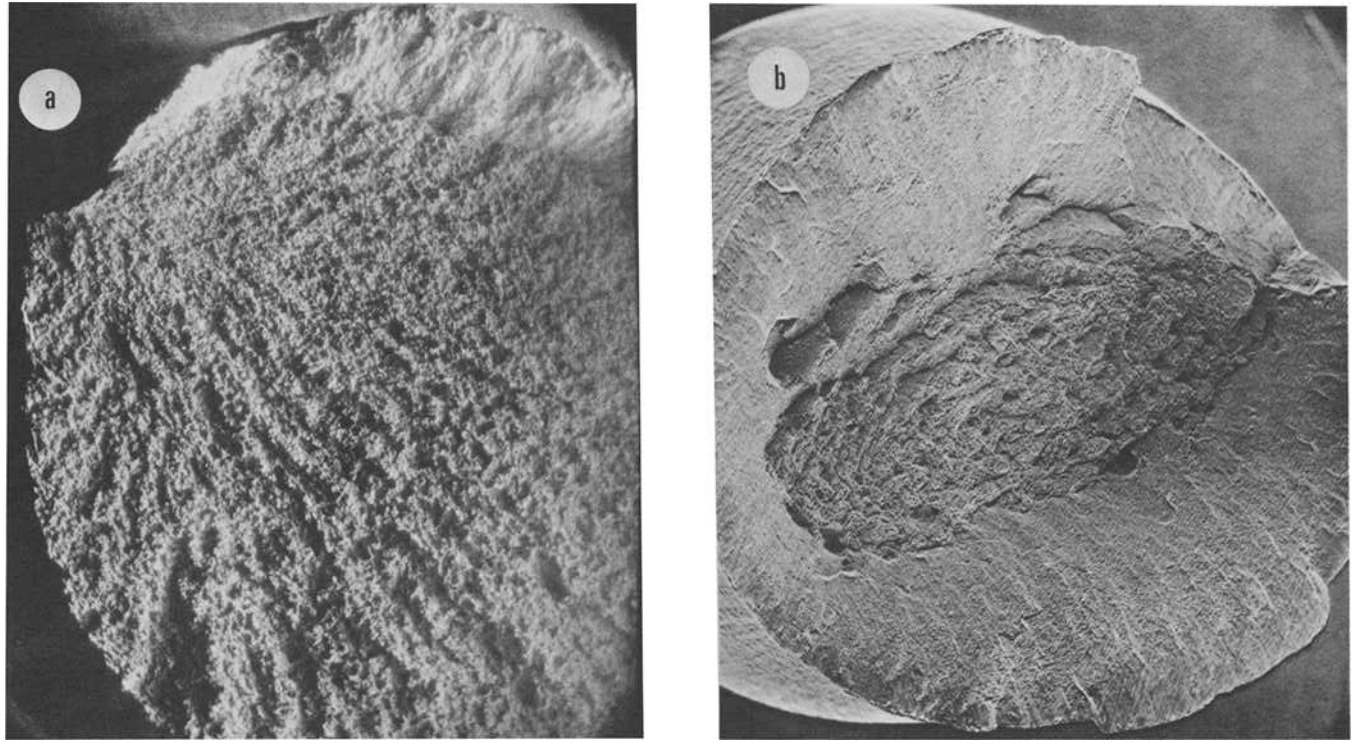

FIG. 6—*Low magnification view of Ti-662 (STA) tension specimens broken at two different test temperatures.* (a) *—79°C, and* (b) *315°C.* ×*20.*

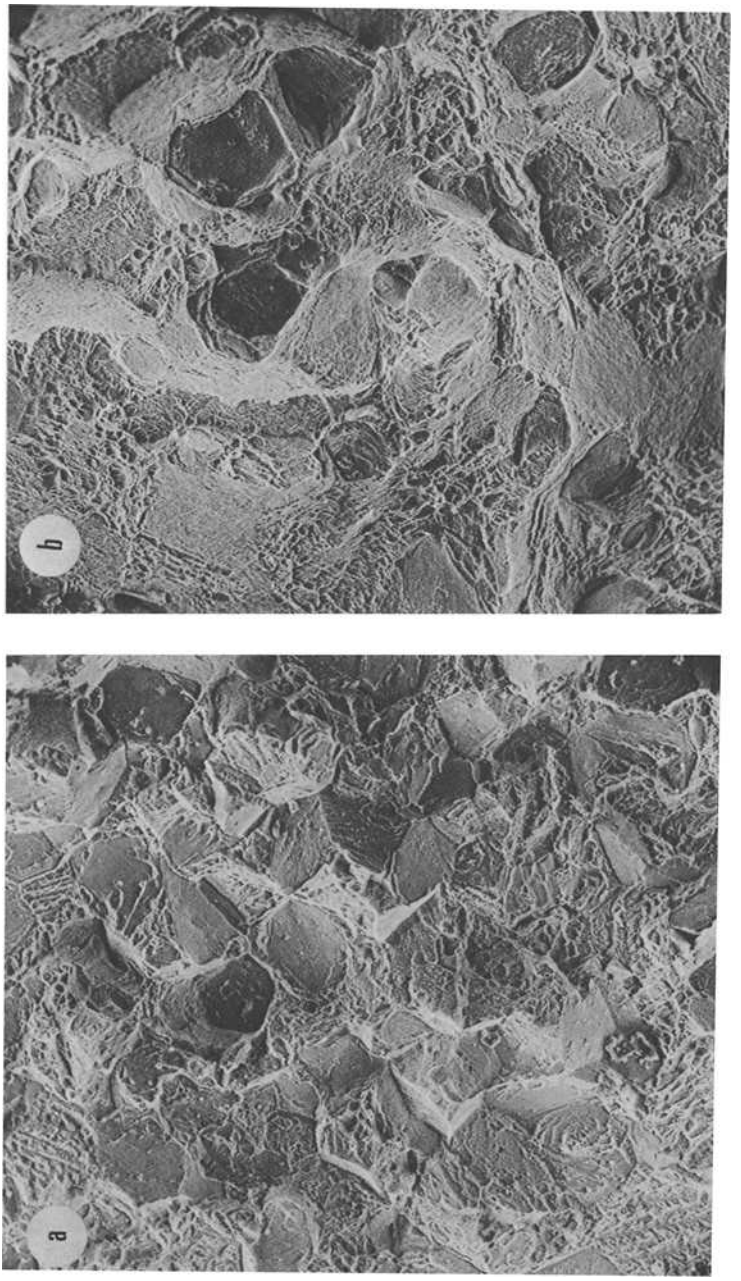

FIG. 7—*Comparison of the fracture surfaces of Ti-8823 (direct age) tension specimens tested at two different test temperatures.* (a) *−79°C, and* (b) *315°C.* ×100.

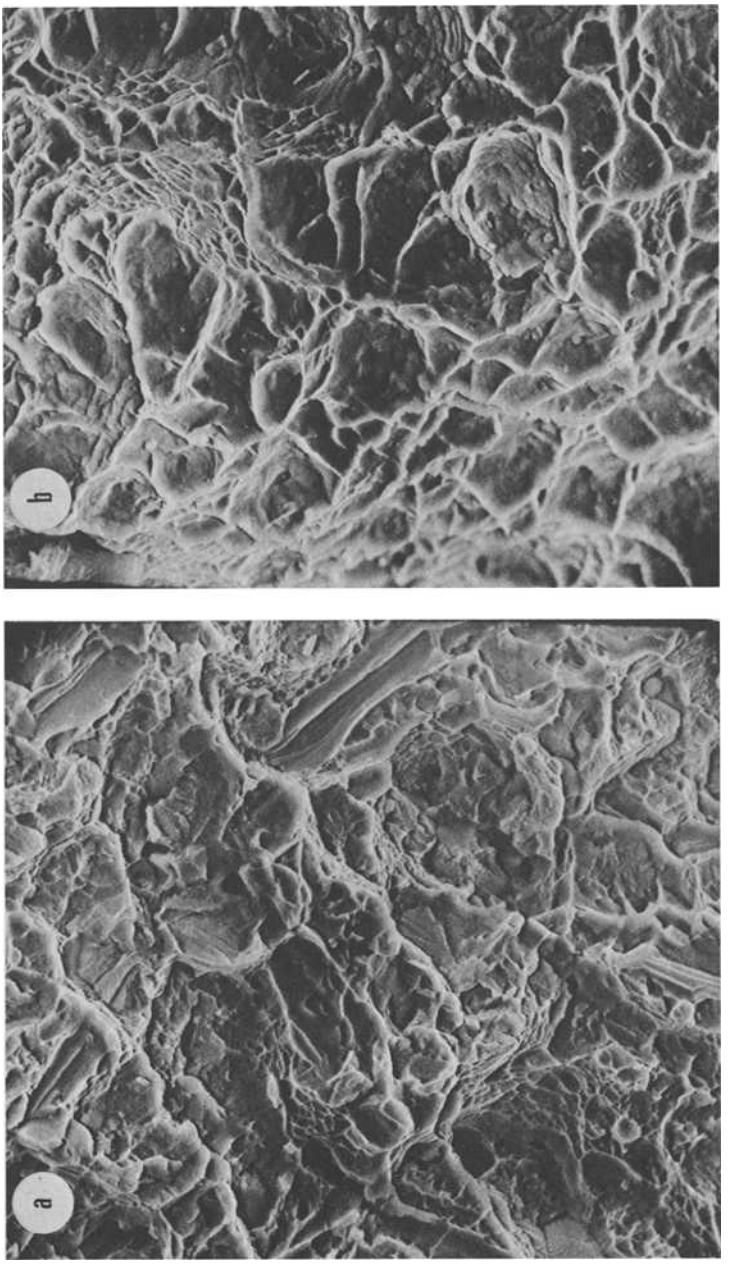

FIG. 8—*Comparison of the fracture surfaces of Ti-662 (STA) fracture toughness specimens tested at two different temperatures.* (a) *—79°C, and* (b) *315°C.* ×*1000.*

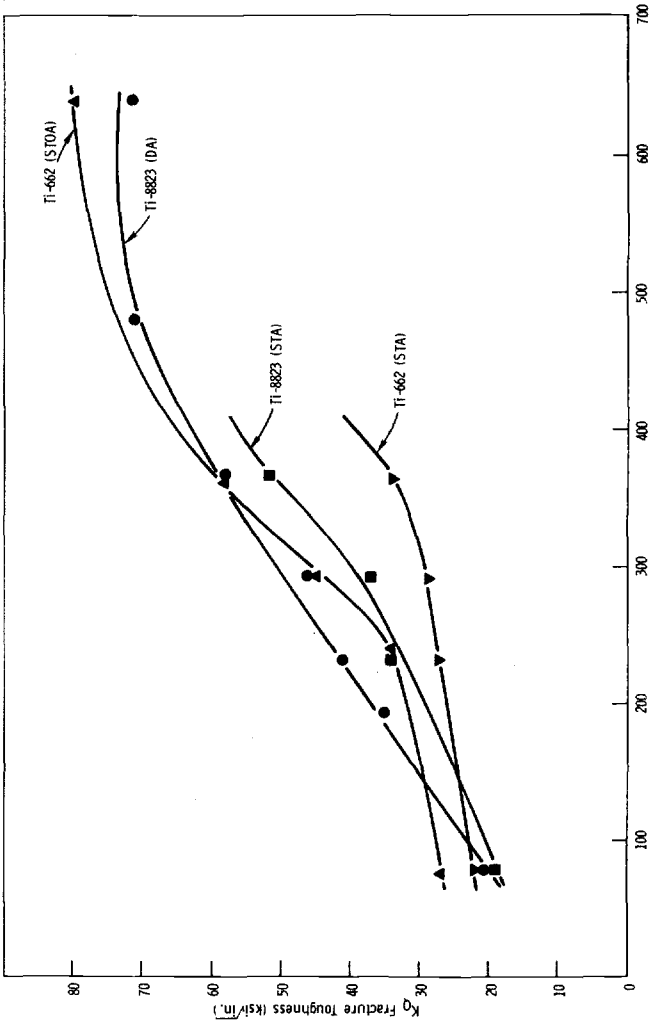

FIG. 9—*The effect of test temperatures on fracture toughness* (K_Q) *of Ti-662 and Ti-8823 alloys.* (*1 ksi*$\sqrt{in.}$ *= 0.91 MPa*$\sqrt{m}$.)

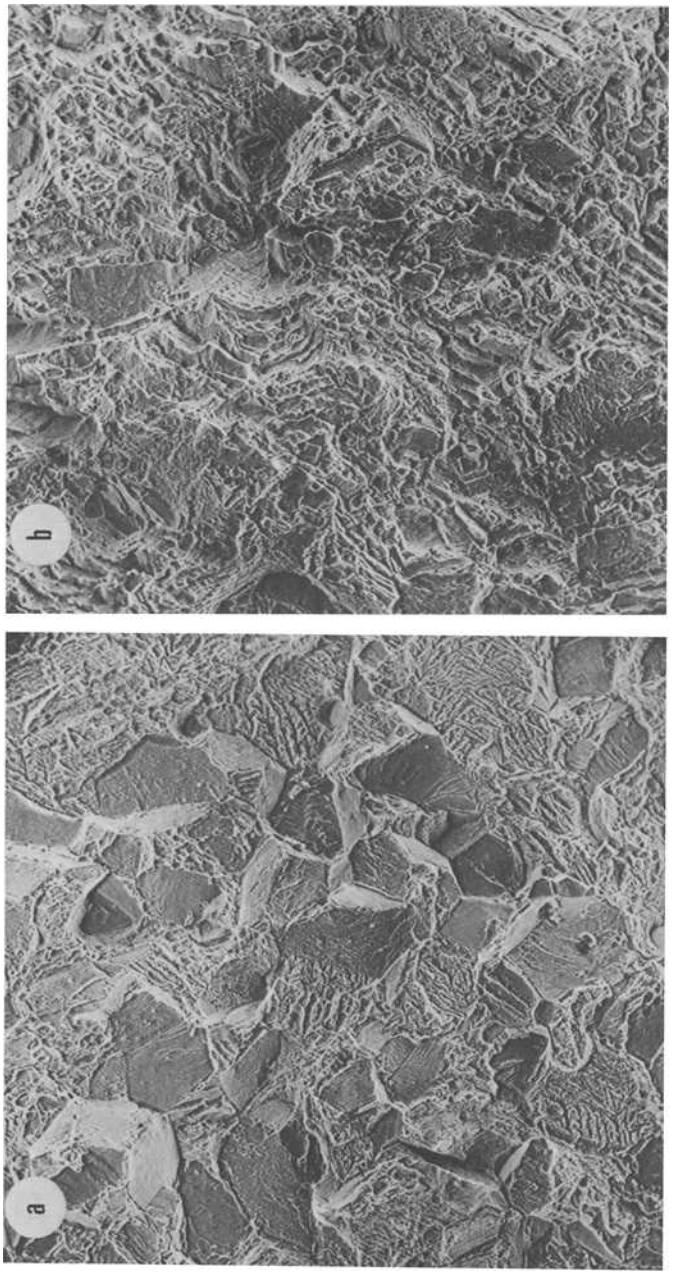

FIG. 10—*Comparison of the fracture surfaces of Ti-8823 (direct age) fracture toughness specimens tested at two different temperatures.* (a) *−40°C, and* (b) *240°C.* ×*100.*

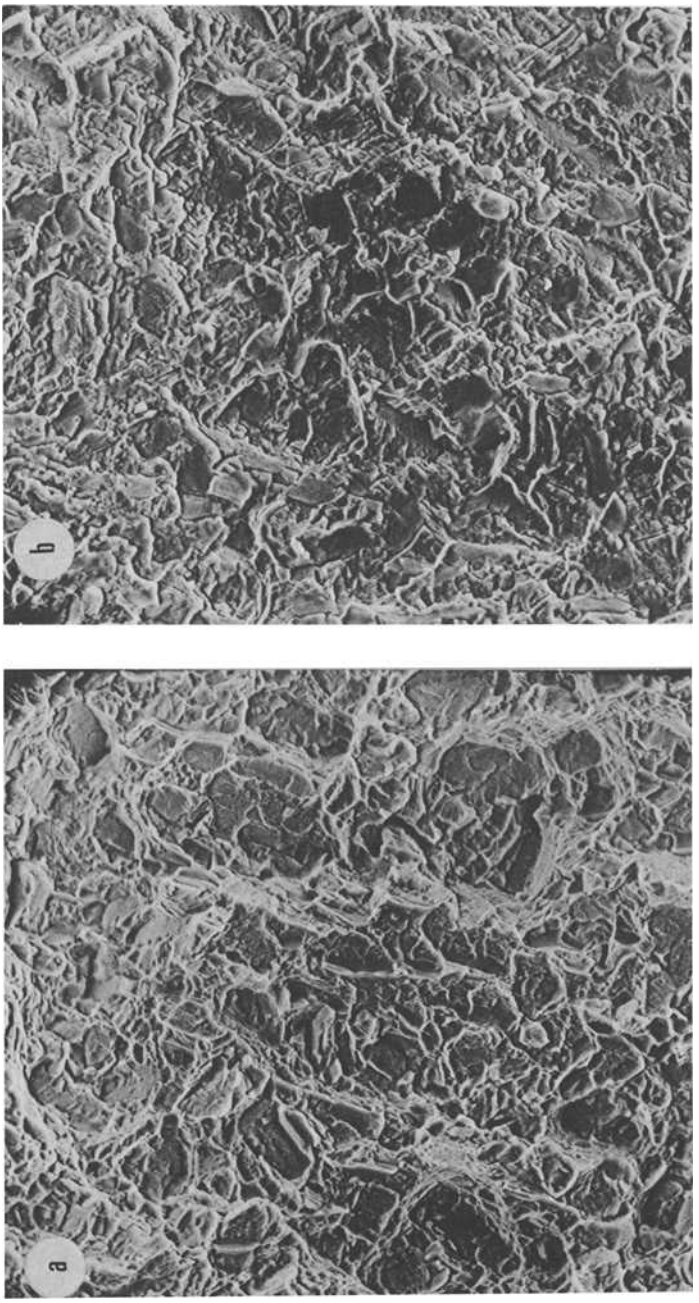

FIG. 11—*Comparison of the fracture surfaces of Ti-662 (STA) tension specimens tested at two different test temperatures.* (a) —40°C, *and* (b) 93°C. ×500.

little difference between the fracture modes associated with Ti-662 (STA) in the temperature region where there is no significant change in K_Q values.

From the slow bend tests that were conducted for K_Q determination, it was possible to obtain an additional measure of fracture toughness known as W/A (total fracture energy, W, divided by the net or uncracked area, A). The variation in W/A with test temperature is shown in Fig. 12 for both the Ti-8823 and Ti-662 alloys. The curves here are similar in shape to those shown in Fig. 9 for K_Q as a function of test temperature.

It is interesting to calculate K_Q from W/A values according to the plane-strain relationship

$$K_Q^2 = \frac{E}{2(1-\nu^2)} \times (\mathrm{W/A}) \tag{3}$$

where E is the modulus of elasticity, and ν is Poisson's ratio. This relationship is based on the fact that W/A is approximately twice G_{Ic}, the strain energy release rate [*13*]. At the low test temperatures, there was excellent agreement between K_Q and K_Q calculated from W/A values ($K_{Q(W/A)}$). For example at $-196°C$ the following comparison is noted in MPa $\sqrt{\text{m}}$: Ti-662 (STOA) [$K_Q=30$, $K_{Q(W/A)}=32$], Ti-662 (STA) [$K_Q=24$, $K_{Q(W/A)}=24$], Ti-8823 (STA) [$K_Q=21$, $K_{Q(W/A)}=28$], Ti-8823 (DA) [$K_Q=23$, $K_{Q(W/A)}=23$]. At 365°C, toughness tests were conducted on two of the four heat-treated conditions with the following results: Ti-662 (STOA) [$K_Q=88$, $K_{Q(W/A)}=100$], Ti-8823 (DA) [$K_Q=78$, $K_{Q(W/A)}=90$]. The lack of better agreement at the elevated temperatures is expected since W/A incorporates the energy for the entire fracture process whereas K_Q is based on maximum load for onset of rapid crack extension. The latter, being a limited crack extension, consumes a smaller portion of the overall fracture energy as the test temperature increases. Therefore, with increasing test temperature

$$K_Q \leq K_{Q(W/A)}$$

It has been shown that when the fracture surfaces were flat, indicating a near plane strain condition ($K_Q \simeq K_{Ic}$), there was satisfactory agreement between K_Q and $K_{Q(W/A)}$ [*14*]. Therefore, the agreement, or lack of it, between K_Q and $K_{Q(W/A)}$ can also be viewed in terms of the ability of the Charpy specimen to meet the following plane strain specimen thickness requirement established by ASTM Test for Plane-Strain Fracture Toughness of Metallic Materials (E 399).

$$B \geq 2.5\ (K_Q/\sigma_{ys})^2 \tag{4}$$

As shown in Fig. 13, the plane-strain thickness requirement is met by the Charpy specimen at the low test temperatures. However, at elevated temperatures such as 365°C, the Charpy specimen is not thick enough to provide plane strain conditions, with the net result being that $K_Q < K_{Q(W/A)}$.

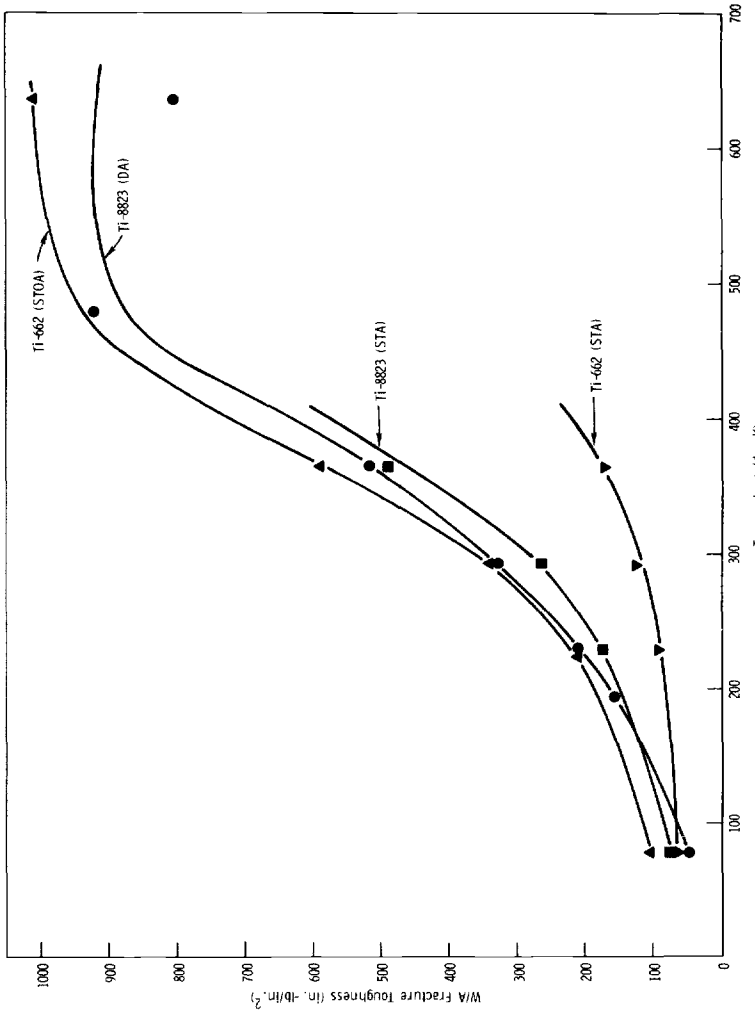

FIG. 12—*The effect of test temperature on fracture toughness* (W/A) *of Ti-662 and Ti-8823 alloys.* ($1\ ft{\cdot}lb/in.^2 = 0.59 \cdot 10^{-3}\ 5/m^2$.)

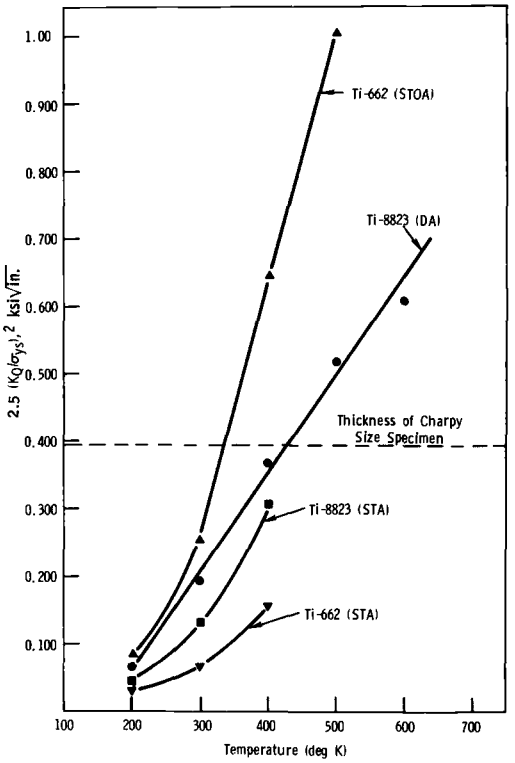

FIG. 13—*Plane strain thickness requirements as a function of test temperature.* (*1 in.* = *25.4 mm.*)

Finally, the various test temperatures made possible a wide range of yield strength and K_Q fracture toughness values as we have seen. The variation in fracture toughness with yield strength is shown in Fig. 14. Here, data from the present study have been supplemented with pertinent data from the literautre. In the case of the α/β alloys (Ti-662 and Ti-64), data taken from the literature [*6,10,11*] were also obtained at several test temperatures. For the metastable β-alloys, supplemental data [*15,16*] were available only at room temperature. In any event, the expected trend is evident, a decrease in fracture toughness with an increase in yield strength. Note the scatter band that is formed by the data of the present study also satisfactorily contains those data points obtained from the literature.

Conclusions

From the effort which has examined the mechanical property behavior of two high strength titanium alloys as a function of test temperature, the following conclusions can be drawn.

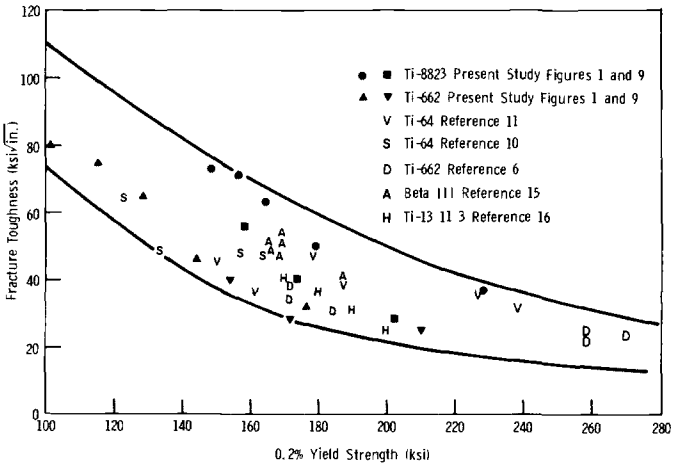

FIG. 14—*Variation in fracture toughness with yield strength. (1 ksi√in.=0.91 MPa√m, and 1 ksi=6.89 MPa.*

1. The yield and tensile strength of both the α/β alloy Ti-662 and metastable β-alloy Ti-8823 increase significantly toward the low test temperatures.

2. Over the range of test temperatures examined in this study, the thermal component of the flow stress does not appear to be affected by heat treatment or the type of alloy. This is in agreement with earlier studies conducted on other titanium alloys and detailed in the literature.

3. The negligible tensile ductility at the low test temperatures is accompanied by an increase in the intergranular and low energy tear mode of failure for Ti-8823 and Ti-662 alloys, respectively.

4. With the increase in strength at low temperatures comes a decrease in the fracture toughness. However, in the low test temperature region, the sensitivity of fracture toughness to temperature changes is less for Ti-662 than it is for Ti-8823.

5. In the low temperature region, there is good agreement between actual K_Q fracture toughness values and K_Q values obtained from W/A. At the higher temperatures, the agreement diminished due to a departure from plane strain conditions.

6. The data from this study obtained over a range of test temperatures detailed the expected decrease in fracture toughness with the increase in yield strength for the Ti-662 and Ti-8823 alloys. The scatter band that described this behavior also satisfactorily described the behavior of the same or similar alloys based on data taken from the literature.

Acknowledgments

The authors gratefully acknowledge the assistance of A. F. Connelly, who obtained the fractographs used in this study. Also acknowledged is the cooperation of T. S. DeSisto who offered many helpful comments during the course of the overall program of which the present effort was a part.

References

[1] Chait, R. and DeSisto, T. S., "An Evaluation of Some High Strength Titanium Alloys Processed in Heavy Sections," AMMRC PTR 75-3, Army Materials and Mechanics Research Center, Watertown, Mass., Sept. 1975.
[2] Chait, R., *Journal of Testing and Evaluation*, Vol. 4, Sept. 1976, p. 359.
[3] Avery, D., *Metal Progress*, Vol. 111, Feb. 1977, p. 52.
[4] Rollins, K. A., "On the Precracking Procedures for Fracture Toughness Deternation," Technical Note AMMRC TN 72-24, Army Materials and Mechanics Research Center, Watertown, Mass., Sept. 1972.
[5] Hickey, C. F., *Proceedings*, American Society for Testing and Materials, Vol. 62, 1962, p. 11.
[6] DeSisto, T. S. and Hickey, C. F., *Proceedings*, American Society for Testing and Materials, Vol. 65, 1965, p. 641.
[7] Conrad, H., *Journal of Metals*, July 1964, p. 582.
[8] Conrad, H., *Transactions*, American Society for Metals, Vol. 57, 1964, p. 747.
[9] Frederick, S. F. and Hanna, W. D., *Metallurgical Transactions*, Vol. 1, Feb. 1970, p. 347.
[10] Steigerwald, E. A., *Engineering Fracture Mechanics*, Vol. 1, 1969, p. 473.
[11] Vishnesky, C. and Steigerwald, E. A. in *Fracture Toughness Testing at Cryogenic Temperatures, ASTM STP 496*, American Society for Testing and Materials, 1971, p. 3.
[12] Fowlkes, C. W. and Tobler, R. L., *Engineering Fracture Mechanics*, Vol. 8, 1976, p. 487.
[13] Priest, A. H. et al, "The Fracture Toughness of a Series of Experimental High Strength Steels," BISRA Report MG/E/404/66, British Iron and Steel Research Association, 1966.
[14] Ronald, T. M. F., Hall, J. A., and Pierce, C. M., *Metallurgical Transactions*, 1972, Vol. 3, p. 813.
[15] Adair, A. M. and Roberson, J. A., "The Influence of Processing Variables on the Structure and Properties of Extruded Beta III Titanium," Technical Report ARML-TR-70-277, Air Force Materials Laboratory, Dayton, Ohio, March 1971.
[16] Heil, W. H., "New Developments in High Strength Titanium Alloys," Lecture No. 8, Titanium Course, New York University, New York, N. Y., Sept. 1969.

R. E. Smelser,[1] *J. L. Swedlow,*[1] *and J. C. Williams* [1]

Analysis of Local Stresses and Strains in Ti-6Al-4V Widmanstätten $\alpha + \beta$ Microstructures*

REFERENCE: Smelser, R. E., Swedlow, J. L., and Williams, J. C., **"Analysis of Local Stresses and Strains in Ti-6Al-4V Widmanstätten $\alpha + \beta$ Microstructures,"** *Toughness and Fracture Behavior of Titanium, ASTM STP 651,* American Society for Testing and Materials, 1978, pp. 200–215.

ABSTRACT: The application of continuum mechanics to the analysis of fracture in structural materials has been helpful in understanding macroscopic behavior in these materials. However, in many classes of structural material, among these titanium alloys, microstructure has been shown to have an effect on fracture even under circumstances of constant yield stress. In such instances, macroscopic continuum mechanics are of limited value since no microstructural scale variations in stress and strain are considered. In the present study we have used finite element analysis to calculate variations in local stress and strain distributions on a scale comparable to that of the microstructural features. This paper describes the methods used to make these calculations, illustrates some of the results for one microstructure, and suggests how these results influence our understanding of fracture in two phase microstructures such as those observed in $\alpha + \beta$ alloys.

KEY WORDS: titanium, titanium alloys, finite element analysis, fracture properties, microstructure, J-integral

The deformation and fracture behavior of $\alpha + \beta$ titanium alloys is somewhat different than that of carbon steels and aluminum alloys because the alloys contain virtually no hard second-phase particles. Instead, titanium alloys consist of a mixture of two ductile phases. Moreover, the macroscopic mechanical behavior of these two-phase alloys does not necessarily

* Original experimental data were measured in U. S. customary units.

[1] Graduate student and professor, respectively, Department of Mechanical Engineering, and associate professor, Department of Metallurgy and Materials Science, Center for the Joining of Materials, Carnegie-Mellon University, Pittsburgh, Pa. 15213.

Copyright© 1978 by ASTM International www.astm.org

bear any obvious relation to the properties of the individual microstructural constituents. Yet it is well known that variations in microstructure at a constant macrostrength can lead to significant variations in overall tensile ductility and fracture toughness. In some instances, the ductility and toughness vary in an opposite sense. This leads to the suggestion that crack initiation and crack propagation may be influenced by different microstructural features. Therefore, it would be useful to know the distribution of local stresses and strains in these two-phase microstructures. Such knowledge would provide a necessary first step to a more basic understanding of the processes of flow, crack initiation, and crack propagation. In particular, it would be useful to have a quantitative description of the interaction between the ductile phases, their mechanical properties, and their microstructural configuration.

On the other hand, there is a fairly sizeable technology on the mechanics of ductile behavior in metals. Within the last decade or so, some powerful techniques have been devised and verified whereby complex problems in elastoplasticity may be solved. Utilizing the computer as a primary tool for attacking such problems, it is now relatively straightforward to perform elastoplastic analysis. Therefore attention has turned to selection of appropriate problems for detailed study, their modeling, and sensible interpretation of results.

Given this interest in tracking the interaction between ductile phases in titanium and the capacity to perform the requisite analyses, it was decided to pursue the behavior for a specific microstructural configuration. In this paper, we report some initial results for an intact section of the microstructure, in terms of both elastic and elastoplastic response. Also, the elastic behavior of a partially cracked microstructure is described.

Microstructure Description

The microstructure selected for study is a transformed β-structure in Ti-6Al-4V. This structure consists of colonies of parallel Widmanstätten α-plates separated by narrow regions of β-phase as illustrated in Fig. 1. The thermal and processing histories which led to this microstructure are described in an earlier publication [*1*].[2] Also, as described elsewhere, the α-β interfaces in this material contain another constituent known as the interface phase [*2*] which consists of finely distributed α-phase oriented differently than in the Widmanstätten α-laths. This is shown in Fig. 2. The details of the origin of the interface phase are not clear [*3*], but for our purposes it is sufficient to identify it as a region of fine α-particles of separate orientation. Such a region can act as a barrier to plastic deformation

[2] The italic numbers in brackets refer to the list of references appended to this paper.

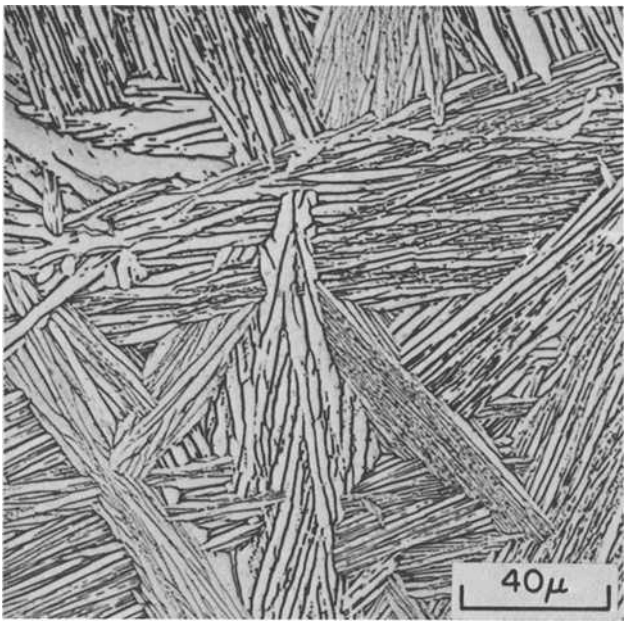

FIG. 1—*Light micrograph showing Widmanstätten colony structure in Ti-6Al-4V; 1035/15 min/air cooled + 705/4 h/air cooled.*

and, because of the fine particle size, can have an intrinsic high yield stress. Both of these features may lead to a stress concentration at the α-β interfaces and, therefore, must be incorporated into an analysis of the type described in this paper.

To characterize this microstructure, we consider a typical section as indicated in Fig. 3 and have measured the sizes (width) of the α, β, and I (interface) constituents. The sizes used are given in Table 1. Initial estimates of the elastic properties of each phase are shown in Table 2. These values were taken to be reasonable estimates based on data available in the literature or from other sources [*4,5*]. Similarly, post-yield properties were adopted as shown in Table 3.

TABLE 1—*Sizes of microstructural constituents.*

Phase	Width, μm	Width WRT I
α	1.85	12
β	0.30	2
Interface (I)	0.15	1

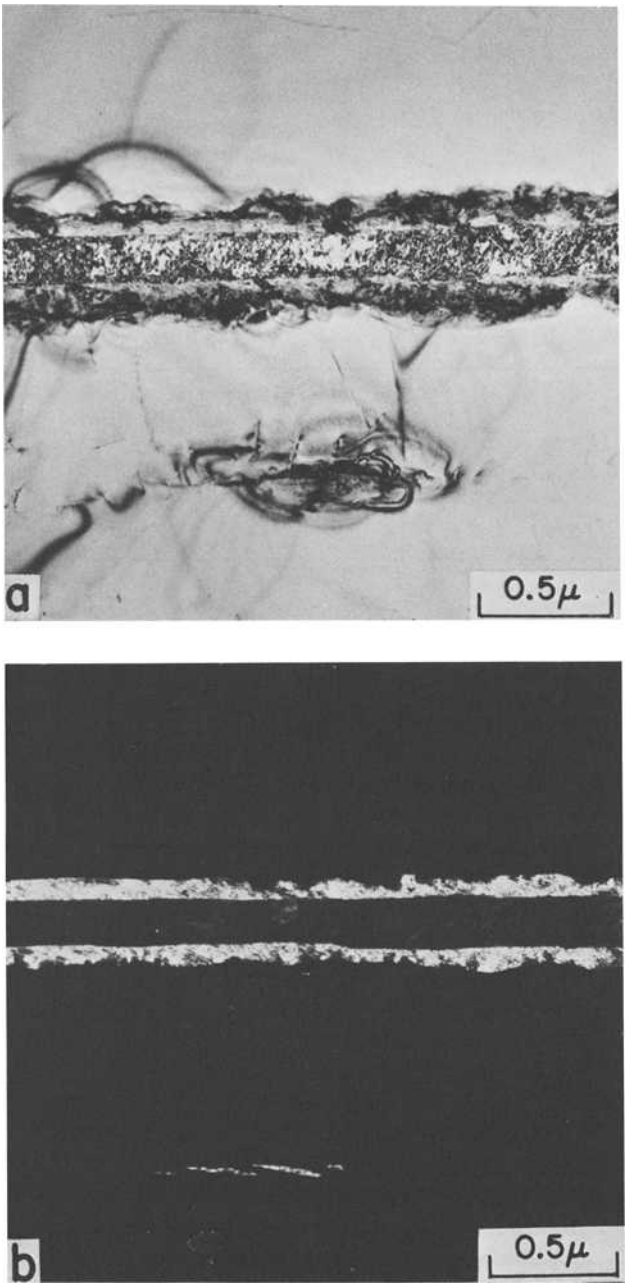

FIG. 2—*Thin foil electron micrograph of material shown in Fig. 1.* (a) *Bright field, showing* α *and* β *laths and interface phase.* (b) *Dark field micrograph showing interface phase.*

TABLE 2—*Elastic properties of microstructural constituents.*

Phase	Elastic Modulus, lb/in.^{2}	Yield Stress, lb/in.^{2}	Poisson's Ratio
α	17.5×10^6	115×10^3	0.33
β	13.0	130	0.33
I	15.5	175	0.33

Conversion factor—
1 lb/in.^{2}=6.89 kPa.

TABLE 3—*Post-yield properties of microstructural constituents.*

Phase	Ultimate Tensile Stress, lb/in.^{2}	Stress, in./in.
α	123×10^3	0.20
β	145	0.25
I	191	0.05

Conversion factors—
1 lb/in.^{2}=6.89 kPa, and
1 in./in.=1 mm/mm.

Overview of Computational Procedure

The relatively recent development of computational mechanics is described thoroughly elsewhere and a detailed review is beyond the scope of this paper. Certain central features may be noted, however, and the interested reader is referred to the established literature [*6*].

Briefly, the approach is as follows. Instead of dealing directly with some domain over which a complex, multiaxial state of stress and strain is expected, the domain to be analyzed is broken into a large number of small pieces. Each piece, or *element,* is allowed to deform in a relatively simple manner. In the simplest of cases, for example, an element will deform only as though it were strained in each of two directions and in simple shear.[3] The magnitude of each strain component is the information ultimately determined in the analysis.

These three types of deformation are taken to describe a local portion of the overall strain field. As a result, the continuous distribution of strain which would exist in theory is replaced by a stair-step representation. In general, the more refined the discretization of the domain, that is, the greater the number of elements used, the more accurately the continuous

[3] This paper is limited to two dimensions, namely, plane stress or plane strain. Similar considerations pertain to three-dimensional analysis.

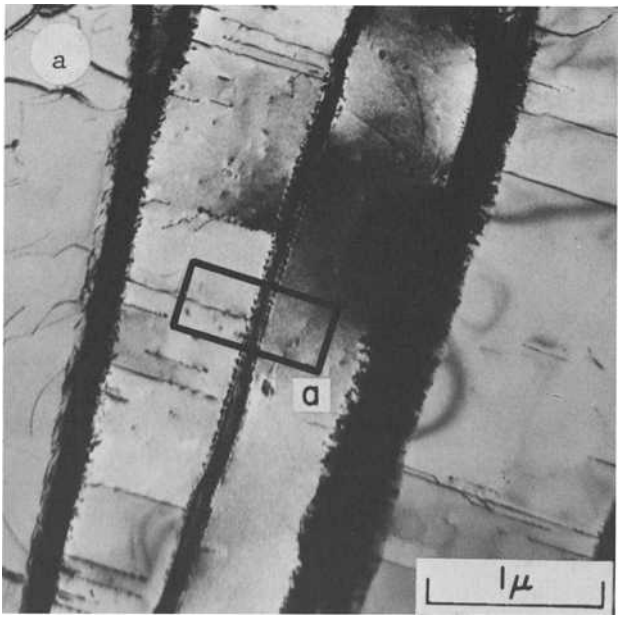

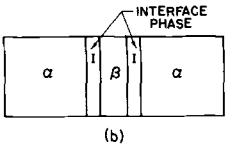

FIG. 3(a)—*Thin foil transmission electron micrograph showing a typical α-β lath structure, Box a, selected for analysis.* (b) *Idealization of the Widmanstätten microstructure of* (a) *used in subsequent analyses.*

distribution of strain is represented. More complex elements exist, of course, but this description is pertinent to the work reported here.

The elements are typically triangles or quadrilaterals, connected at *nodes* through which the forces causing deformation are transmitted. In the simple case of a triangle, the nodes are located at the vertices. It then becomes necessary to relate the forces acting at each node of a triangle to the deformation state within. This is done by means of the principle of virtual work or, equivalently, the theorem of minimum potential energy. The result, for any one element, is a set of linear algebraic equations which relate the nodal forces to the corresponding displacements. It is important to point up that these equations depend only on the size and shape of that element and on the properties of the material within it.

Recalling that the original domain is to be represented by an assembly or array of elements, it remains only to impose two conditions:

1. At any (nodal) point where elements are connected, the forces accruing from each of the elements must be in equilibrium with any applied loads
2. The displacement at that node must be common to all connecting elements, that is, compatibility is enforced

These conditions result in a typically large set of linear algebraic equations for which extraordinarily efficient solution methods have been devised. In the analyses reported next, we treat 412 simultaneous equations and obtain their solution in about 20 s of computer time.

This efficiency in itself makes the finite element method, as it is called, attractive for engineering purposes. In addition, it is feasible to represent the material properties as varying from one element to the next so that the material need not be taken as homogeneous throughout the domain.

Finally, it is a straightforward step to have the variation in material behavior dictated by the degree to which any one element has yielded, and thereby to represent inelastic behavior. The procedure used in the present work follows the Prandtl-Reuss flow rule. The details are presented elsewhere [7], but the overall sense follows the pattern described here. It is worth noting that the procedure requires an initial elastic deformation and that the material subsequently work-hardens. Actual tensile data may be used to represent the material, and elastic unloading is automatically taken into account wherever it may occur.

Elastic Analysis, Structure Intact

Because the section of the microstructure isolated for analysis is expected to behave in a manner independent of its precise location (diagonally in Fig. 3(*a*)), "loading" was specified in terms of boundary motion rather than stress. In this way, any neighboring section of the microstructure is compatible with the one shown in Fig. 3(*b*), on all four boundaries.

The microstructural geometry selected for analysis (Fig. 3(*b*)) thus incorporates the essential features of the lamellar structure such as the periodicity and the relative size of the phases. The model was next discretized for finite element analysis, Fig. 4. The map is not highly refined because this was a preliminary analysis. The anticipated rapid changes of stress near the interfaces required that a greater number of elements be placed in these regions. Representative material properties (Table 2) were selected from available data and an elastic analysis performed.

Figure 5 presents the results of the finite element analysis for uniform extension. The loading is shown in the upper right corner of the figure. The figure indicates that the α-phase is the first to yield and undergo plastic deformation. It should be noted that while the yield stress of the α and β

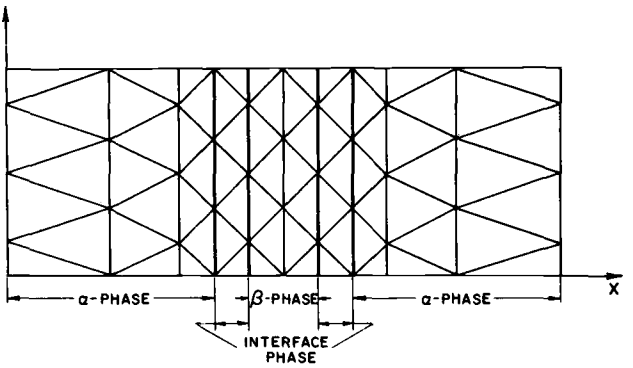

FIG. 4—*Simplified finite element map of the Widmanstätten microstructure model.*

phases differ by about 12 percent, their normalized stresses under uniform extension differ by about 35 percent. This is due to the fact that the α-phase is much stiffer than the β-phase (see Table 2). The last component of the microstructure to yield is the interface phase. One consequence of the interface remaining elastic after both the α and β phases have yielded might be the initiation of fracture in the interface region releasing the stored elastic energy.

The results of a uniform shear displacement on the upper surface are presented in Fig. 6. Two types of constraint were studied. In Case 1, only boundary displacements were specified. Case 2 had an additional constraint

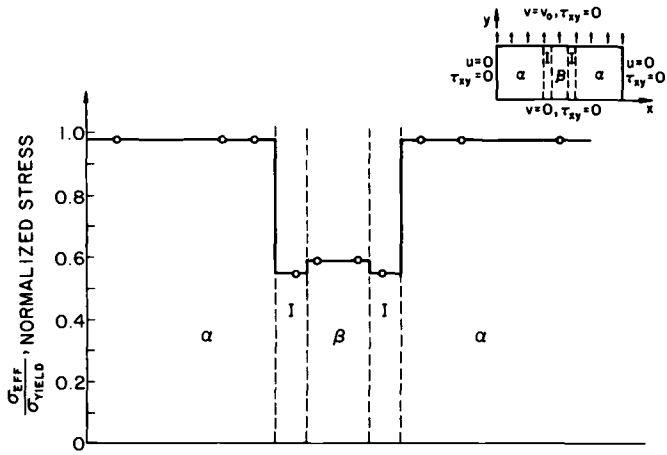

FIG. 5—*Stress distribution for the elastic finite element analysis for uniform extension of the Widmanstätten model.*

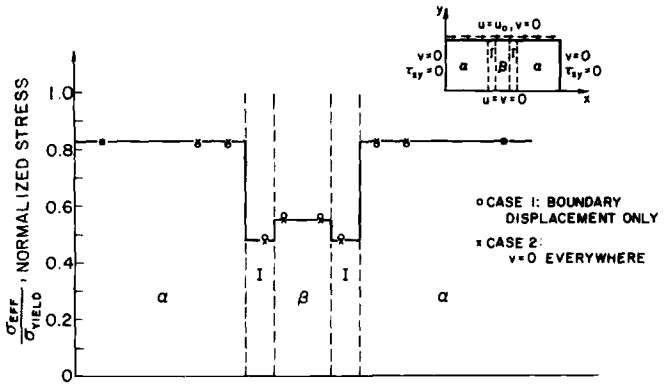

FIG. 6—*Stress distribution for the elastic finite element analysis for simple shear of the Widmanstätten model.*

applied to the interior nodes. Here the vertical displacements were specified to be zero. This leads to a strain distribution which corresponds to analytically defined simple shear. The strain field for Case 1 showed slight "numerical noise." This noise results from the differing material properties: the boundary constraints are not transmitted to the interior. Figure 6 again shows that the α-phase will yield first while the β-phase and interface will remain elastic. The ratio of the normalized stresses of the α and β phases is lower than that for the case of simple extension.

These preliminary computations point to a possible failure mechanism similar to that postulated for crack problems. In crack problems, stress analysis indicates the existence of an elastic zone close to the front of the crack. This elastic zone is flanked by regions of intense plastic deformation. Crack propagation is associated with the release of stored elastic energy ahead of the crack and its dissipation in the plastic regions off to the sides. An analogous situation is seen in Figs. 5 and 6. Here the α-phase is seen to yield first with the β and interface phases remaining elastic. This sets up an energy source-energy sink interaction similar to that for propagating cracks. It may be inferred that microstructural failure can begin within the β-interface regions resulting in energy release which is then dissipated in the yielded α-phase.

Elastoplastic Analysis, Structure Intact

The results of the elastic analysis indicated that regions of elastic energy storage and plastic energy dissipation could exist within the Widmanstätten microstructure. On the basis of this finding, a plastic analysis of the structure (Fig. 4) was pursued. This was carried out to determine whether

plastic flow localization was possible within any of the microstructural regions. The analysis was performed using the finite element elastoplastic flow procedure just outlined [7].

To carry out the analysis, it was necessary to generate stress-strain curves for each microstructural phase. The assumed elastic properties are shown in Table 2, while the assumed plastic properties are shown in Table 3. The Ludwik formula

$$\sigma/\sigma_t = 1 + (\epsilon^{(p)}/\epsilon)^n \tag{1}$$

in conjunction with the Consideré condition was used to determine the

$$d\sigma/d\epsilon = \sigma \tag{2}$$

proportional limit and to fit smooth curves through the data of Table 3. These curves are shown in Fig. 7 using the normalized octahedral stress and octahedral plastic strain. With these curves, an elastoplastic analysis for uniform extension of the isolated section was carried out. The results are presented in Figs. 7 through 9.

Figure 7 indicates the ability of the analysis to track the input stress-strain curve. Here, the octahedral stress (normalized) and plastic strain in each constituent are plotted for a succession of load increments. It is seen that initially the β and interface phases overshoot the yield value of one (open symbols, Fig. 7). However, the numerical procedure is self-correcting [7] and, within a maximum of 12 load steps for the β-phase, the computation is again following the prescribed curve. Thus, the overshoot produces errors only in the initial stages of yielding.

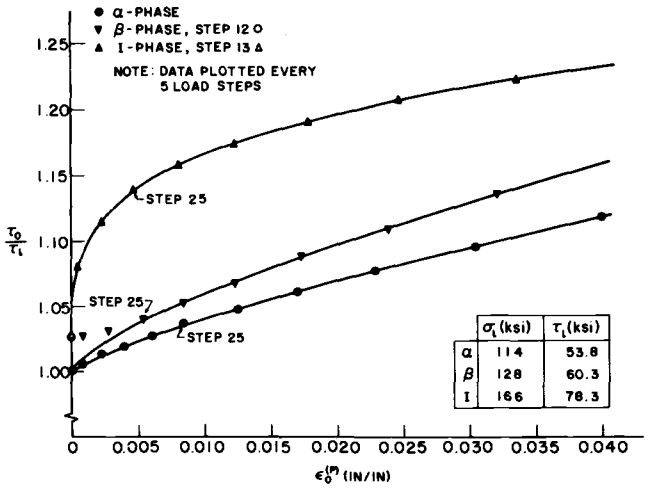

FIG. 7—*Octahedral stress-strain curves for the plastic behavior of the microstructural constituents.*

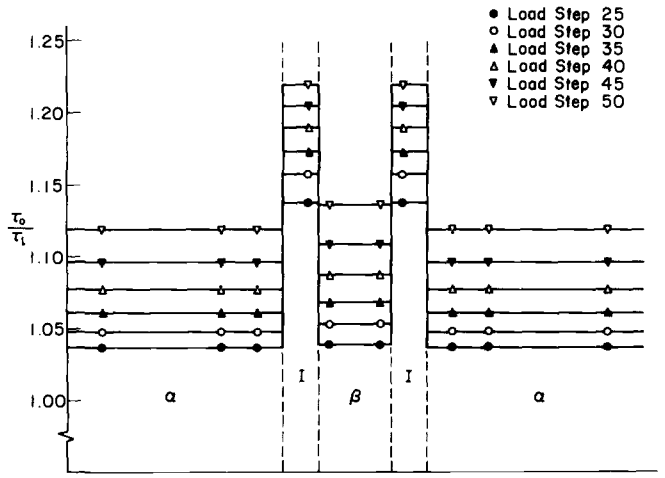

FIG. 8—*Octahedral stress distribution for the elastoplastic analysis of uniform extension of the Widmanstätten model.*

One may also note in Fig. 7 the development of stress gradients across the section (for example, stress levels at Step 25). This is seen more easily in Fig. 8 where the normalized octahedral stress has been plotted as a function of distance across the section for selected load steps. It is seen that the differences in the stresses of the various phases remain relatively constant as deformation proceeds. This is not the case for the strains however.

Figure 9 clearly shows that as the deformation proceeds strain gradients

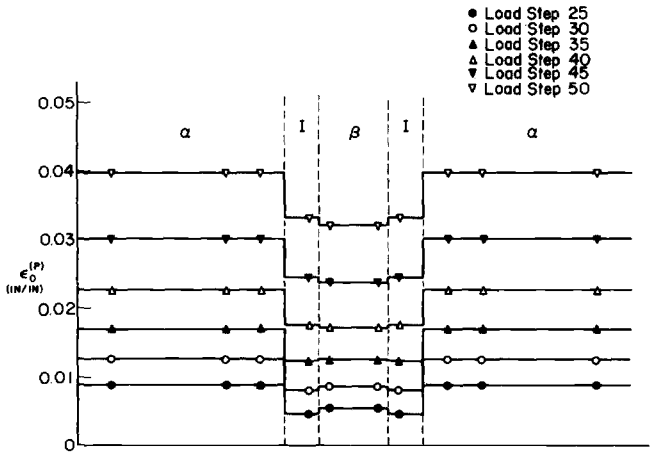

FIG. 9—*Octahedral plastic strain distribution for the uniform extension of the Widmanstätten model.*

are accentuated. This implies that flow localizations may be possible within the α-phase. From Table 3, the ultimate tensile strain for the interface phase is reached at an octahedral plastic strain level of 0.06 mm/mm (0.025 in./in.), for the case treated. Thus, early in the deformation history the interface phase may fail causing increased plastic strain in the adjoining α and β phases. This low ductility of the interface phase also has implications for crack growth in this microstructure. However, the evaluation of such failure mechanisms must await further experimental observation coupled with refined modeling.

Elastic Analysis, Cracked Structure

An observed mode of failure within the Widmanstätten colonies is fracture of the bond region between the α and β platelets, Fig. 3. To analyze this type of failure, cracks were introduced in the model along the α-interface phase boundary and the β-interface phase boundary, Fig. 10. The introduction of cracks into multimaterial domains presents special problems not encountered in homogeneous bodies. The stresses near the crack tip

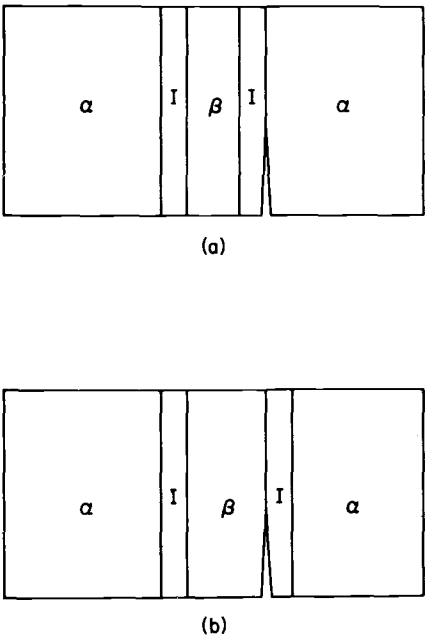

FIG. 10—*Schematic representation of the finite element maps for cracked microstructures.* (a) *Crack on α-interface boundary.* (b) *Crack on β-interface boundary.*

are intensified by both a geometric discontinuity and a material discontinuity. This introduces K_I and K_{II} stress intensification for single-mode loading first demonstrated by Williams [*8*]. In addition to this phenomenon, he pointed up that the stresses behave in an oscillatory manner as the crack tip is approached. Further analysis by Rice and Sih [*9*] has given explicit forms for the stress intensity factors for some simple geometries.

In view of the complexity of the analyses for K_I and K_{II}, other procedures are desirable to allow one to characterize crack tip stress fields. Recently, Stern and Hong [*10*] have presented a contour integral method which requires an auxiliary stress and displacement field for obtaining the stress intensity factors. Also, Lin and Mar [*11*] have described a special crack tip element for use in determining bimaterial stress intensity factors. While these methods yield K_I and K_{II} independently, complicated procedures are required for their implementation.

Another method of characterizing the crack tip stress field for homogeneous bodies is the J-integral [*12*], which is equal to the elastic energy release rate, G, in nonyielding bodies. Smelser and Gurtin [*13*] have shown that the J-integral extends from single material domains without change to a bimaterial body provided the crack lies along a straight interface. This result is of value in that it presents a single parameter characterization of the crack tip stress field. Also it can be shown that J for a bimaterial is equal to the energy release rate for the crack extending along the interface. Using the near tip stress fields of Rice and Sih [*9*], the value of J is found to be

$$J=\frac{\pi}{16}(\lambda_1+\lambda_2)(k_1^2+k_2^2)$$

where

$$\lambda_\alpha=\begin{cases}\dfrac{4(1-\nu_\alpha)}{\mu_\alpha} & \text{(plane strain)}\\[2ex] \dfrac{4}{\mu_\alpha(1+\nu_\alpha)} & \text{(plane stress)}\end{cases}$$

μ_α and ν_α are the shear modulus and Poisson's ratio for material α. The J-integral may be computed with little effort. Such an analysis has been carried out for the configuration of Figure 10.

The map for this analysis is shown in Fig. 11. Modest detail is provided along the crack flanks. Conditions of symmetry were imposed along the vertical and lower horizontal sides and a uniform shear free displacement was given to the upper horizontal face. The J values for various a/w ratios are shown in Fig. 12. As a/w increases, it is observed that the J curve becomes flat. This is due to the fact that the crack is extending into an approximately uniform stress field. This is in contrast to an edge notched

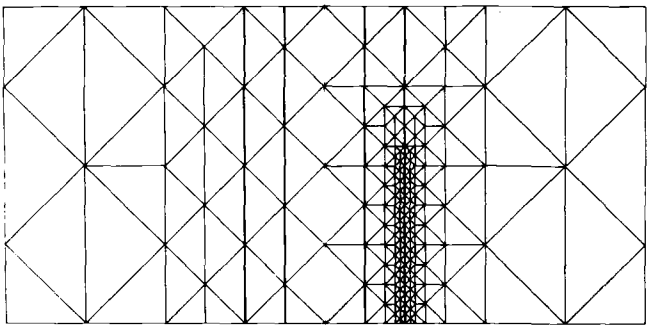

FIG. 11—*Detailed finite element map of the Widmanstätten microstructure for the analysis of cracked microstructures.*

specimen, for example, where the crack extends into an increasing stress field and J increases with increasing a/w.

It is seen from Fig. 12 that the J values for cracks located on the α-interface boundary and the β-interface boundary are approximately equal. This implies that the crack has equal propensity to extend along either

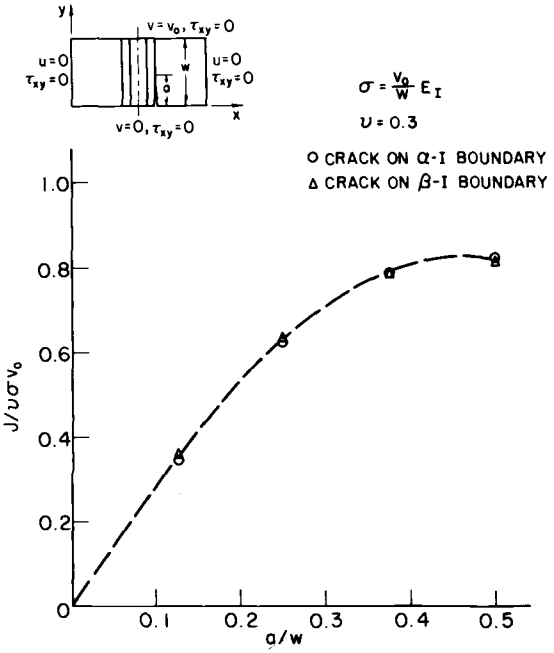

FIG. 12—*Plot of the J-integral versus* a/w *for cracked microstructures indicating equal propensity for crack extension on either the α-interface or β-interface boundary.*

boundary. It should be noted that in Fig. 10 the proportions of the α and β phase are different. This will not influence the J value since the far field stresses and strains are reasonably unaffected by the geometry change and it is these values from which J is calculated. Thus, while it may be possible for cracking to initiate on either boundary, crack extension appears equally probable for each side.

Concluding Remarks

It should be evident that computational mechanics offers significant opportunity for simulating microstructural behavior. Information outlined here for the three simple cases studied to date is consistent with experimental observations. Other cases, notably elastoplastic analysis of a cracked microstructure, are in progress and will be reported when available.

The nature of the results at this stage points to another significant aspect. Moving forward with this sort of interactive, observational *cum* computational study of microstructural behavior is of necessity iterative. We have used here some relatively simple models and representative material data, but have nevertheless inferred certain aspects of localized failure mechanisms. These results will require further experimental observation to establish the degree to which our inferences are correct. Improvements to the model, and especially more detailed material data [*7*], should follow to provide a better simulation of microstructural behavior. Pursuit of this research is anticipated so that, eventually, the computation becomes a meaningful analogue to physical behavior.

Acknowledgments

This work was supported by the Material Research Laboratory Section of the National Science Foundation, through the Center for the Joining of Materials at Carnegie-Mellon University.

References

[*1*] Chesnutt, J. C,. Rhodes, C. G., and Williams, J. C. in *Fractography—Microscopic Cracking Process, ASTM STP 600,* C. D. Beachem and W. R. Warke, Eds., American Society for Testing and Materials, 1976, p. 99.

[*2*] Rhodes, C. G. and Williams, J. C., *Metallurgical Transactions,* Vol. 6A, 1975, p. 1670.

[*3*] Margolin, H., Levine, E., and Young, M., *Metallurgical Transactions,* Vol. 8A, 1977, p. 373.

[*4*] Paton, N. E., Rauscher, G. P., and Williams, J. C. in *Titanium Science and Technology,* Vol. 2, R. I. Jaffee and H. M. Burte, Eds., Plenum Press, 1973, p. 1049.

[*5*] Williams, J. C. and Rhodes, C. G., unpublished research, Rockwell International, 1974.

[6] Zienkiewicz, O. C. in *The Finite Element Method in Engineering Science,* McGraw-Hill, New York, 1971; Cook, R. D. *in Concepts and Applications of Finite Element Analysis,* Wiley, New York, 1974; and Gallagher, R. H. in *Finite Element Analysis Fundamentals,* Prentice-Hall, Englewood Cliffs, N. J., 1975, are among the standard texts available. See also periodicals such as *Computers and Structures* and *Numerical Methods in Engineering* for on-going developments.

[7] Swedlow, J. L., *Computers and Structures,* Vol. 3, 1973, pp. 879-898.

[8] Williams, M. L., *Bulletin of the Seismological Society of America,* Vol. 49, 1959, pp. 199-204.

[9] Rice, J. R. and Sih, G. C., *Journal of Applied Mechanics,* Vol. 32, 1965, pp. 418-423.

[10] Stern, M. and Hong, C-C., *Advances in Engineering Science,* Proceedings of the 13th Annual Meeting, Society of Engineering Science, Hampton, Va., 1-3 Nov. 1976, NASA Cp-2001, Vol. 2, pp. 699-710.

[11] Lin, K. Y. and Mar, J. W., *International Journal of Fracture,* Vol. 12, 1976, pp. 521-531.

[12] Rice, J. R., *Journal of Applied Mechanics,* Vol. 35, 1968, pp. 379-386.

[13] Smelser, R. E. and Gurtin, M. E., *International Journal of Fracture,* Vol. 13 1977.

R. W. Judy, Jr.[1] *and R. J. Goode* [1]

Screening Test Method Development for Fracture Resistance Measurements in Thin-Gage Titanium

REFERENCE: Judy, R. W., Jr. and Goode, R. J., **"Screening Test Method Development for Fracture Resistance Measurements in Thin-Gage Titanium,"** *Toughness and Fracture Behavior of Titanium, ASTM STP 651,* American Society for Testing and Materials, 1978, pp. 217–226.

ABSTRACT: Titanium sheet products in gages less than 12.5 mm are used for many lightweight, highly efficient structures. Since these materials are very expensive, in many cases their use requires that very careful attention be given to the prevention of crack growth and fracture. One result of this design approach is that minimum allowable fracture resistance values are specified for mill products; screening tests for quality assurance are required to certify that these minimum values of fracture resistance are met for each sheet of material. The dynamic tear (DT) test was developed for this purpose for heavier section materials (16 mm and thicker) for steels, aluminum alloys, and titanium alloys. Correlations of DT energy values with linear-elastic fracture mechanics parameters enables the determination of K_{Ic} values on a routine basis by methods that are quicker and less expensive than direct measurement of K_{Ic}. Additionally, the DT test can be used to measure fracture resistance properties of materials in the elastic-plastic and plastic ranges, which is not possible by linear-elastic methods. Past studies of the effect of specimen dimensions on measured DT energy values have shown that the fracture resistance of materials can be expressed in terms of a constant R_p. Using the relationships developed for heavier section materials, a study involving several titanium alloys in thicknesses ranging from 2.5 to 12.7 mm showed that the fracture behavior of thin-section titanium alloys could be rationalized by these methods.

KEY WORDS: titanium, titanium alloys, fractures (materials), dynamic tests

Screening tests for fracture resistance measurements are necessary to certify the quality of mill products. Historically, most products requiring

[1] Head, Structural Mechanics Section, and head, Metals Performance Branch, respectively, Engineering Materials Division, U. S. Naval Research Laboratory, Washington, D. C. 20375.

Copyright© 1978 by ASTM International www.astm.org

minimum levels of fracture resistance have been heavy section steels (25 mm thick or greater), and the Charpy V-notch (C_v) test or similar methods have been used for the purpose of routine quality control checks. Higher strength steels, aluminum alloys, and titanium alloys are not amenable to C_v methods, however, and an additional complication arises for gages thinner than the standard C_v specimen thickness.

Since the design of many of the modern, lightweight titanium structures relies heavily on the tolerance of the base material to contain cracks and other defects sufficiently large to be found by routine inspection at reasonable intervals, the importance of having adequate fracture resistance becomes apparent. It is one thing to determine fracture resistance of thin-gage titanium alloys by highly sophisticated fracture mechanics techniques; it is quite another thing to be assured that all of the material that goes into production of a large number of manufactured items has at least the minimum value of fracture resistance assumed in the design of the structure. Thus, there is a definite need for a simple, inexpensive test which can be conducted routinely on large quantities of material with simplified analysis of test results.

The dynamic tear (DT) test was developed for quality control of materials to be used in applications requiring high levels of fracture resistance. Standard test methods have been established for the 16-mm-specimen [*1*][2] and the 25-mm-specimen (ASTM Test for Dynamic Tear Energy of Metallic Materials (E 604-77)); both of these test methods are finding wider use in materials procurements. A major advantage of the DT test, in addition to its low cost and convenience, is its capability to measure fracture resistance of materials with fully plastic and elastic-plastic properties. Past research has shown that the DT test can be used to define the fracture resistance of materials in the 2.5 to 15-cm thickness range, and the results can be rationalized independent of thickness by using established methods. Extension of this technology to include thin-section titanium alloys is the subject of this paper.

Materials

The materials studied in this investigation included three commercial titanium alloys, each represented by several thicknesses in the range of 2.3 to 12.7 mm. The alloys were Ti-6Al-2Cb-1Ta-0.8Mo (6-2-1-0.8), Ti-6Al-4V (6-4), and Ti-6Al-6V-2.5Sn (6-6-2.5), which represent conditions of lowest strength combined with highest fracture resistance, intermediate strength and fracture resistance, and highest strength and lowest fracture resistance, respectively. The chemical composition of each sheet of material is shown in Table 1. Of particular importance for the fracture

[2] The italic numbers in brackets refer to the list of references appended to this paper.

TABLE 1—*Chemical composition of thin-gage titanium sheet materials.*

Alloy	Thickness, mm	C, %	N, %	Fe, %	Al, %	V, %	Cu, %	Sn, %	Cb, %	Mo, %	Ta, %	O, %	H, ppm
Ti-6Al-2Cb-1Ta-0.8Mo	2.5	0.02	0.012	0.05	5.9	...	...	...	1.95	0.81	0.94	0.077	66
	3.2	0.02	0.012	0.05	5.9	...	...	...	1.95	0.81	0.94	0.077	64
	4.8	0.02	0.011	0.05	5.9	...	...	...	2.05	0.82	0.96	0.082	71
	6.4	0.02	0.012	0.05	5.9	...	...	...	1.95	0.81	0.94	0.072	85
	9.5	0.02	0.012	0.05	5.9	...	...	...	1.95	0.81	0.94	0.074	62
	12.7	0.02	0.012	0.05	5.9	...	...	...	1.95	0.81	0.94	0.078	81
Ti-6Al-4V	2.3	0.01	0.012	0.18	6.3	4.0	...	...	...	...	...	0.133	120
	2.3	0.02	0.014	0.18	6.2	4.1	...	...	...	...	...	0.109	53
	3.2	0.02	0.012	0.16	6.0	4.0	...	...	...	...	...	0.113	50
	3.2	0.02	0.012	0.16	6.0	4.0	...	...	...	...	...	0.113	50
	6.4	0.02	0.008	0.18	5.9	3.9	...	...	...	...	...	0.113	86
	12.7	0.02	0.016	0.17	6.6	4.0	...	...	...	...	...	0.190	55
	12.7	0.02	0.008	0.18	5.9	3.9	...	...	...	...	...	0.113	46
Ti-6Al-6V-2Sn	2.3	0.02	0.012	0.68	5.6	5.5	0.69	2.1	...	...	...	0.124	...
	3.2	0.02	0.030	0.68	5.6	5.7	0.72	2.2	...	...	...	0.180	53
	6.4	0.01	0.013	0.63	5.5	5.6	0.63	2.0	...	...	...	0.178	53
	12.7	0.02	0.010	0.70	5.5	5.6	0.70	2.1	...	...	...	0.169	51

resistance property is the interstitial oxygen content. In general, two ranges of oxygen content are available in commercial alloys—commercial purity (CP) grade (oxygen content in excess of 0.015 weight percent) and extra-low interstitial (ELI) grade (oxygen) content in the 0.12 to 0.15 weight percent range). Materials of both types were included in this study, and all materials were tested in the as-rolled condition.

Dynamic Tear Test

The DT specimen, Fig.1, is an edge-notched bar which is loaded dynamically in three-point bending by machines of pendulum or falling weight type. Specimens are dimensioned according to material thickness; standard configurations for two thicknesses have been established. Energy to fracture the specimen at specified loading rates and temperatures is measured in standard tests. Various analysis procedures based on the DT test have been evolved over the past several years, including ratio analysis diagrams (RADs) for steels, aluminum alloys, and titanium alloys. It is emphasized that the DT test is intended for engineering use in providing material characterizations, rather than as a tool for precise scientific investigations. For this reason, every effort to simplify test procedures and to minimize test costs has been made.

A relation between DT energy values and specimen cross-section dimensions was established in past studies [*2-4*]. The DT test ductile fracture equation

$$E = R_p\,(\Delta a)^2\,B^{1/2}$$

where the terms are defined in Fig. 1, has been shown to apply for steels

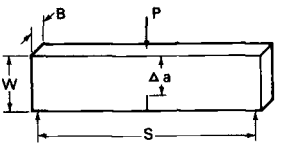

ENERGY = $R_pB^{0.5}\Delta a^2$
WHERE R_p=CONSTANT

STANDARD SPECIMENS

B	Δa	W	S
(CM)	(CM)	(CM)	(CM)
1.6	2.9	4.1	16.5
2.5	7.6	12.1	41

FIG. 1—*DT specimen.*

and aluminum alloys in sections above 7 mm. The constant, R_p, which is the index of material resistance to fracture, is a geometry-independent parameter. It is important to note that the equation applies only for fully plastic and elastic-plastic fracture conditions. Plane-strain fracture is best handled by linear-elastic fracture mechanics. Use of the R_p parameter to measure fracture resistance allows mechanical constraint effects and metallurgical effects to be considered independently.

A test method for characterizing thin-section materials was developed from the DT test to provide continuity between the technology developed for thicker materials. The approach to the problem was to establish that the ductile fracture equation did apply for titanium alloys. Standard 16-mm DT specimen plan dimensions, Fig. 2, were utilized so that existing equipment could be used for the experimental part of the study. Lamination techniques, as shown in Fig. 2, were necessary to prevent specimen buckling and to provide sufficient energy to get a good measurement. In past studies, it was shown that the energy per laminate was constant, using aluminum alloy 5086-H32, and therefore that an averaging method could be used [*4*].

Fracture Resistance of Thin-Section Titanium

The initial phase of the investigation was to determine whether the DT test ductile fracture equation (Fig. 1) applied to thin titanium alloys as it did for thicker-section materials; the second phase was to define the fracture resistance of each of several sheets of material in various thicknesses. In the initial phase, a 12.7-mm-thick sheet of each composition was sectioned to half and quarter thicknesses. The sections were laminated to form DT specimens; specimens were configured to vary systematically Δa for each thickness of each material. In the second phase, tests were conducted with DT specimens of the type shown in Fig. 2 for each thickness of each material. All tests were conducted at 0°C in a 392-Nm capacity pendulum-type machine.

To determine the conformance of the test results to the ductile fracture equation, the following procedure was used.

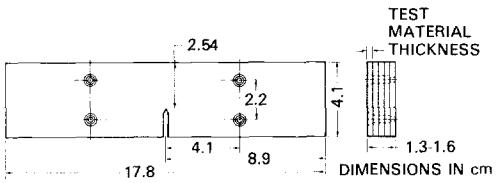

FIG. 2—*Specimen configuration for DT tests of thin-gage titanium alloys.*

1. For each specimen, substitute the measured energy and the specimen dimensions into the equation $E = R_p \Delta a^2 B^{1/2}$ to calculate a value of R_p.

2. Average all values of R_p for each test material to give a characteristic R_p for the material.

3. Determine a value of "predicted" energy for each specimen tested by use of the specimen dimensions and the characteristic R_p value.

4. Compare measured energy with predicted energy. The results obtained from this procedure are shown for the three materials individually in Fig. 3 and combined in Fig. 4. Since the full-thickness sheet of 6-6-2.5 has a plane-strain level of fracture resistance, these data do not conform to the equation, and the data are not included in Figs. 3 and 4. The data group reasonably well around the 1:1 lines in both figures, which indicates that the equation is applicable for the 12.7-mm sheet materials.

The second phase of the investigation was concerned with measuring the fracture resistance of each material in various thicknesses. Values of R_p determined by DT tests of each thickness of the available materials of the three alloys are presented in Table 2, along with the tension test data.

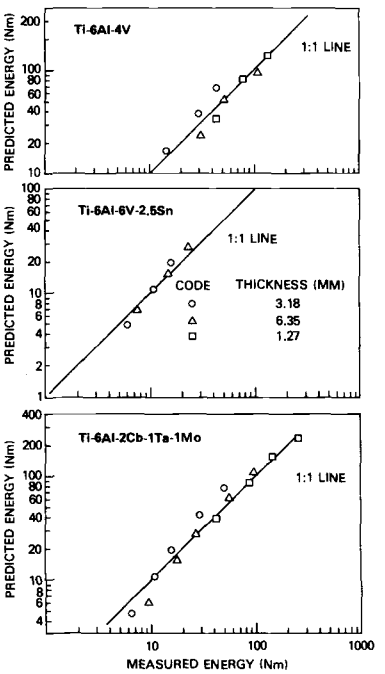

FIG. 3—*Comparison of measured DT energy values for specimen of various dimension with values predicted from the ductile fracture equation using an average value of* R_p. *Results are shown separately for each of the three materials.*

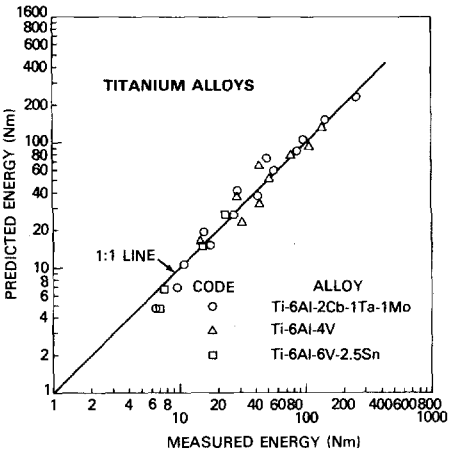

FIG. 4—*Data shown in Fig. 3 combined on a single plot.*

Ratio Analysis Diagrams

Establishing that the ductile fracture equation applies to thin-section titanium alloys allows use of existing analysis techniques for interpreting basic material characterization data. For thicker-section materials, the RAD, Fig. 5, is a format which has been verified for this purpose and contains all of the parameters necessary for a simplified assessment of the fracture properties of thin-section titanium alloys.

TABLE 2—*Properties of thin-gage titanium alloys.*

Alloy	Thickness, mm	Yield Strength, MPa	R_p, MNm/m$^{5/2}$	Grade [a]
Ti-6Al-2Cb-1Ta-0.8Mo	2.5	843	1.27	. . .
	3.2	829	1.56	. . .
	4.8	891	2.30	. . .
	6.4	868	2.40	. . .
	9.5	871	2.16	. . .
	12.7	878	2.08	. . .
Ti-6Al-4V	2.3	923	0.73	CP
	2.3	967	0.84	ELI
	3.2	967	1.48	ELI
	3.2	967	1.20	ELI
	6.4	936	2.14	ELI
	12.7	996	0.65	CP
	12.7	943	1.82	ELI
Ti-6Al-6V-2.5Sn	2.3	1069	0.86	ELI
	3.2	1122	0.26	CP
	6.4	1078	0.36	CP
	12.7	1039	0.53	CP

[a] CP=commercial purity (oxygen content >0.15 percent), and ELI=extra low interstitial (oxygen content <0.12 percent).

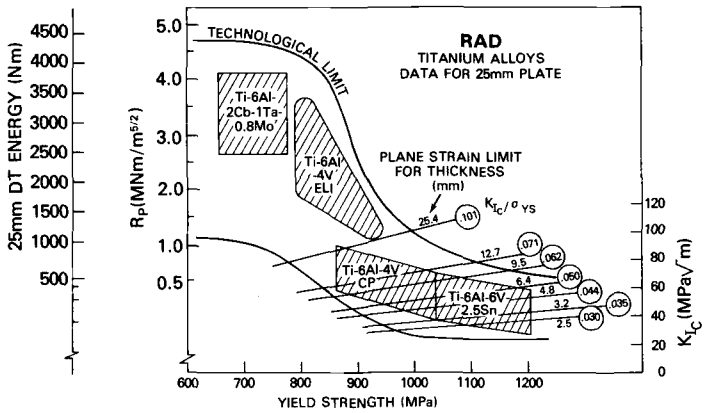

FIG. 5—*RAD for thick section (25 to 76-mm) titanium alloys.*

The RAD is based on a correlation of K_{Ic} with DT energy for 25 to 76 mm thick plate material [*5*], which fixed the relative position of the K_{Ic} and DT energy scale. The technological-limit line represents the highest values of fracture resistance measured to date either by DT tests over the entire yield-strength range or by K_{Ic} tests in the elastic fracture range; the lower bound represents the lowest levels of fracture resistance. The scale of R_p was added by calculating its position from the 25-mm DT energy scale.

The K_{Ic}/σ_{ys} ratio is the indicator of material performance with respect to fracture of plane-strain materials, because in all of the fracture mechanics equations used for analysis of flaw tolerance of structures, this ratio is proportional to applied stress (σ/σ_{ys}) and flaw size for fracture. Furthermore, the K_{Ic}/σ_{ys} ratio is the materials property input to these equations. All other variables represent conditions imposed by external loads and size and shape of the flaw. For this reason, K_{Ic}/σ_{ys} ratio lines are used to index the RAD into regions of expected fracture behavior for given material thicknesses. For purposes of determining a minimum allowable value of R_p, the most useful ratio line is the plane-strain limit, which is determined for a given thickness by $B = 2.5\ (K_{Ic}/\sigma_{ys})^2$. Thus, given a material thickness from other considerations, the minimum K_{Ic}/σ_{ys} ratio to avoid a plane-strain condition is established and the indexed value of R_p is established as well. Conservatism can be introduced by requiring a margin on the allowable K_{Ic}/σ_{ys} and hence by a margin on R_p.

Comparison of Thin and Thick-Section Properties

The R_p data are plotted on the titanium RAD in Figs. 6, 7, and 8 for the 6-2-1-0.8, 6-4, and 6-6-2.5 alloys, respectively. Plane-strain limits are

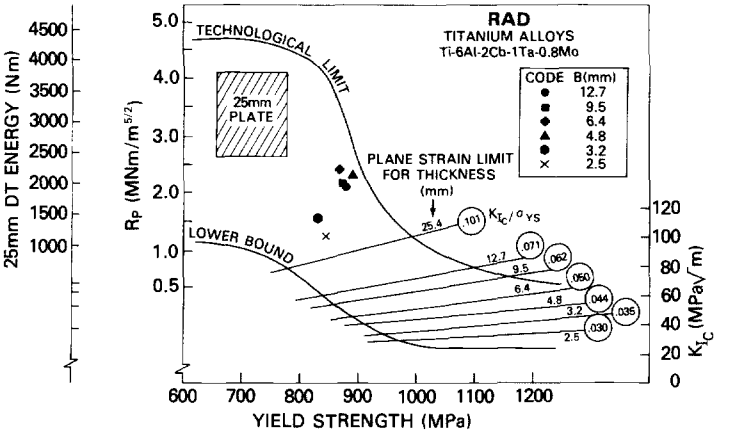

FIG. 6—*RAD comparison of fracture properties of thin-section Ti-6Al-2Cb-1Ta-0.8Mo with data for 25 to 76-mm plate materials.*

shown as K_{Ic}/σ_{ys} ratio lines corresponding to the thicknesses of materials tested in the study. Also on each RAD, a comparison is made of the fracture resistance data zone for 25-mm and thicker plate materials with the individual data for thin-gage titanium materials; all of the data represent properties of material in the as-rolled condition. Each data point in Figs. 6 through 8 represents a separately produced sheet of material, so that the range of data shown is indicative of the metal quality and thickness considered. In general, metal quality in titanium alloys is controlled by the

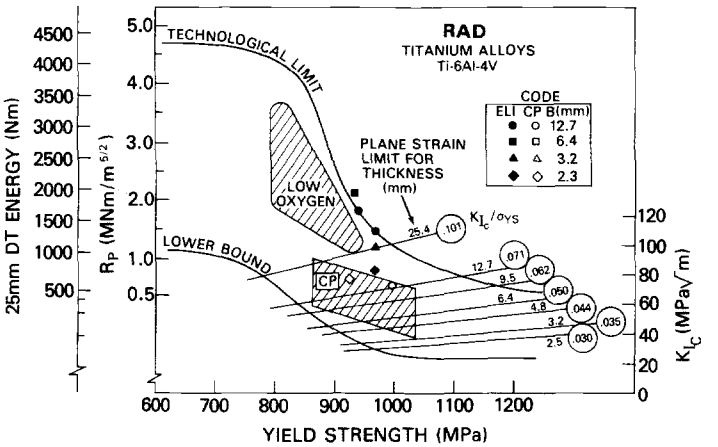

FIG. 7—*RAD comparison of fracture properties of thin-section Ti-6Al-4V with data for 25 to 76-mm plate materials.*

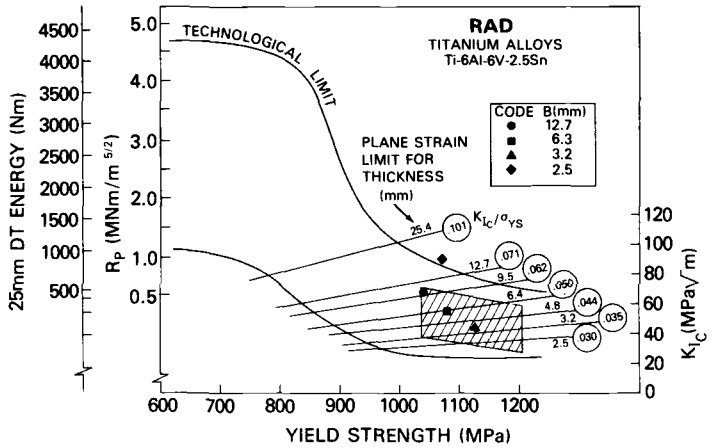

FIG. 8—*RAD comparison of fracture properties of thin-section Ti-6Al-6V-2.5Sn with data for 25 to 76-mm plate materials.*

interstitial oxygen content; that is, lower oxygen content generally results in lower strength and higher fracture resistance.

Values of yield strength and R_p for different sheets of material of 6-2-1-0.8 alloy are plotted on the RAD in Fig. 6. As this alloy system was developed to have high fracture resistance, all of the data points fell well above their respective plane-strain limit lines. All of the 6-2-1-0.8 sheets were rolled from the same ingot, which had an oxygen content corresponding to the ELI product category. Comparison of the properties of thin-gage material with the data zone for 25-mm plate material shows that the increased work of rolling the material to the thinner gage results in higher strength and lower fracture resistance. However, because the K_{Ic}/σ_{ys} ratio for plane-strain behavior also decreases as the thickness decreases, plane-strain fracture is not a problem with this alloy system.

Of the 6-4 alloys (Fig. 7), two specimens were standard commercial quality; the remainder were ELI grade with oxygen contents of 0.12 to 0.15 weight percent. In Fig. 7, it can be noted that the sheet of 12.7-mm-thick ELI grade 6-4 alloy is significantly higher in fracture resistance than the 12.7-mm-thick CP grade 6-4 material. (These points are coded by circles.) Such differences can be caused by processing effects (forging and rolling temperatures) as well as oxygen content; however, there is no reason to expect that the two specimens were produced by significantly different mill practices. In the other ELI grade versus CP grade comparison in 6-4 materials (2.5-mm thickness), the difference which might be attributable to interstitial oxygen content is not as pronounced as it is in the 12.7-mm-thick sheets. Comparing the properties of each grade with previously determined data zones for thicker material of each type shows that the two specimens of CP grade material correspond very well, but the ELI grade

showed the same trend as did the 6-2-1-0.8 alloy; that is, higher yield strength and decreased fracture resistance result from rolling 6-4 plate to thinner sections.

In the 6-6-2.5 alloy, the only specimen of ELI grade material was the 2.3-mm-thick sheet, which also had the highest fracture resistance. Of the four sheets tested, only the 12.7-mm-thick sheet had plane-strain properties. The plane-strain K_{Ic}/σ_{ys} limits for the 6.4 and 3.2-mm thicknesses are below the data in each case, so that elastic-plastic behavior is predictable for each material. The CP specimens compared very favorably with the existing data base for this alloy system.

Summary

When high performance titanium structures are designed to sustain damage due to the growth of small defects for a finite lifetime, it becomes imperative to have simplified tests to screen production material on the basis of fracture resistance. The DT test was developed for this purpose with the emphasis on heavy-section material. Use of an equation relating DT specimen dimensions to measured fracture energy permits extension of this method to screening application for thin-section titanium alloys. In this investigation, it was shown that the equation developed for plate materials applied to three 12.7-mm-thick titanium alloys which were selected to cover a range of yield strength and fracture resistance levels. Using existing RAD methods, it was also shown that the properties of sheet materials of the same compositions and ranging in thickness from 2.3 to 12.7 mm compared reasonably well to previously defined fracture resistance properties of thicker materials of the same composition. This work demonstrated validity of the approach to screening thin-gage titanium alloys on the basis of fracture resistance. The low cost of the DT test, relative to fracture mechanics tests and the convenience of conducting the test and interpreting results, make it an ideal test for checking large quantities of materials to ensure a specified value of fracture resistance.

References

[1] Puzak, P. P. and Lange, E. A., "Standard Method for the 1-In. Dynamic Tear Test," NRL Report 6851, Naval Research Laboratory, 13 Feb. 1969.

[2] Judy, R. W., Jr. and Goode, R. J. in *Fracture Toughness Evaluation by R-Curve Methods, ASTM STP 527,* American Society for Testing and Materials, 1973, p. 48.

[3] Judy, R. W., Jr. and Goode, R. J. in *Progress in Flaw Growth and Fracture Toughness Testing, ASTM STP 536,* American Society for Testing and Materials, 1973, p. 377.

[4] Judy, R. W., Jr. and Goode, R. J., *Metals Engineering Quarterly,* Vol. 13, No. 4, 19 Nov. 1973.

[5] Judy, R. W., Jr., Freed, C. N., and Goode, R. J., *Titanium Science and Technology,* Vol. 2, 1973, pp. 1393-1409.

G. S. Hall,[1] *S. R. Seagle,*[1] *and H. B. Bomberger* [1]

Effect of Specimen Width on Fracture Toughness of Ti-6Al-4V Plate*

REFERENCE: Hall, G. S., Seagle, S. R., and Bomberger, H. B., **"Effect of Specimen Width on Fracture Toughness of Ti-6Al-4V Plate,"** *Toughness and Fracture Behavior of Titanium, ASTM STP 651,* American Society for Testing and Materials, 1978, pp. 227–245.

ABSTRACT: From a group of 96 specimens ranging in thickness from 15 to 38 mm (0.60 to 1.50 in.), a regression equation was obtained for Ti-6Al-4V plate relating the fracture toughness, K_Q, of 205-mm (8-in.) wide specimens to the variables of specimen thickness and fracture toughness, K_Q, for 76-mm (3-in.) width. The fracture toughness value of Ti-6Al-4V plate can be increased appreciably in thin specimens by using an oversized width specimen. The magnitude of this toughness increase diminishes as the thickness increases and approaches 38-mm (1.5-in.). Oversizing the specimen results in a significant reduction in the stress at instability at 2 percent crack extension. The specimen strength ratio, R_{sc}, essentially remains the same while K_{max} and the P_{max}/P_Q ratio increase.

Crack-growth-resistance curves constructed from load versus crack-opening-displacement curves for the two different width specimens are similar. This indicates the fracture behavior is the same and not altered with increased specimen width. Furthermore, K values for oversized specimens can be calculated from the loads at the appropriate crack extension in smaller standard size specimens, and vice versa.

KEY WORDS: titanium, fracture properties, toughness, titanium alloys, thickness, mechanical properties

Plate of the Ti-6Al-4V alloy in thicknesses up to 76 mm (3 in.) is produced to a guaranteed fracture toughness for critical applications. Except for the thinner plate, test procedures basically follow those of ASTM Test

* Original experimental data were measured in U. S. Customary units.

[1] Senior research engineer, manager-commercial sales development, and director, Metallurgy and Research, respectively, RMI Company, Niles, Ohio 44446.

Copyright© 1978 by ASTM International www.astm.org

for Plane-Strain Fracture Toughness of Metallic Materials (E 399-74). Because of the high toughness (77 MPa $\sqrt{m}$, >70 ksi $\sqrt{in.}$) and moderate strength (792 MPa, >115 ksi, yield strength) of Ti-6Al-4V plates, specimens from thin plate, 32 mm (1.25 in.) thick and less, normally do not meet the plane-strain sizing requirements of the ASTM procedure. Users still require fracture toughness tests for these thin plates as a means of ensuring a tough product. To obtain more useful information from thin specimens, increased specimen widths are allowed by some materials specifications. Recommended specimen widths for thinner plates range from 76 mm (3 in.) to greater than 152 mm (6 in.). Justification [*1*][2] for this oversizing is to ensure that the crack will propagate through an elastic stress field, thus satisfying a requirement of linear elastic fracture mechanics.

Because of test geometry effects, larger fracture toughness numbers, K_Q[3] are obtained from the 205-mm (8-in.) compared to the 76-mm (3-in.) wide specimen. This dependence of fracture toughness on specimen width complicates data analysis. A need exists for correlating fracture toughness values between the standard 76-mm (3-in.) wide specimens and the wider specimens. This work presents the background for correlations based on (*a*) regression analysis, and (*b*) analysis of crack-growth-resistance curves constructed from load versus crack-opening-displacement (COD) curves.

Material

The material used in this study was 16 to 38-mm (0.625 to 1.500-in.) thick, Ti-6Al-4V plate. The Ti-6Al-4V alloy chemical composition range for the 48 plates was 0.10 to 0.13O with aluminum and vanadium ranging from 5.8 to 6.1 percent and 3.8 to 4.0 percent, respectively. The production α-β processed plates were recrystallized annealed [*2*] and met guaranteed minimum tensile properties of 896-MPa (130-ksi) ultimate strength, 792-MPa (115-ksi) yield strength, and 10 percent elongation. The toughness specification for these plates was 77 MPa $\sqrt{m}$ (70 ksi $\sqrt{in.}$) minimum.

Procedure

Fracture toughness testing employed compact tension specimens in both the LT and TL crack-plane orientations for each plate. Specimen thicknesses were at least 90 percent of the plate thickness. Test procedures and

[2] The italic numbers in brackets refer to the list of references appended to this paper.

[3] K_Q is used to designate the stress intensity calculated on the basis of the load at 95 percent secant offset from the linear portion of the test record and the initial crack length of the specimen.

calculations were those of ASTM Test E 399-74 except where changes were mandated by material specifications. These changes allowed specimen width to range from 76 to 205 mm (3 to 8 in.) for plates 16 mm (0.625 in.) thick and greater.

Selected fracture toughness data from 16, 32, and 76-mm (0.625, 1.250, and 1.500-in.) thick plate were used in constructing crack-growth-resistance curves from load versus COD curves for 76 and 205-mm (3 and 8-in.) wide specimens. The following polynominal equation by Brown [*3*] for plane-stress displacements, $Ev\ B/P$, at the crack mouth was used for determining the change in crack length during fracturing of the specimen

$$\log e\ (Ev\ B/P) = 2.21 + 1.86\ (a/W) + 7.44\ (a/W)^2 - 13.71\ (a/W)^3 + 11.04\ (a/W)^4$$

where

E = modulus of elasticity, MPa, (psi),
v = COD at crack mouth, mm (in.),
B = specimen width, mm (in.),
P = load, N (lb),
a = crack length, mm (in.), and
W = specimen width, mm (in.).

A value of 16.5×10^6 psi (113.7×10^3 MPa) was used for the modulus of elasticity, E, of Ti-6Al-4V. Load versus COD curves were reduced to crack-growth-resistance curves incrementally along the fracture curve. Using the inverse slope from the origin to points on the curve, and from the aforementioned equation, relative crack lengths were calculated. Incremental crack extensions were determined by subtracting the measured initial crack length from the calculated relative crack length. The K values were determined from the standard compact tension specimen fracture toughness equation using the load at the same incremental points on the test record and the relationship between the relative crack length at that load and specimen width and thickness. As a measure of K level required for initial crack extension, the load at which deviation occurred from the straight line of the test record was used along with the measured initial crack length to obtain the stress intensity value, K_o, for onset of fracture. Calculations of stress intensity values and their respective crack extension, Δa, were then used to construct the crack-growth-resistance curves for the various specimens.

Regression Analysis Results

From a group of 96 specimens, including both test directions, a regression equation was obtained for relating fracture toughness values of 205-

mm (8-in.) wide specimens to specimen thickness and the fracture toughness values of 76-mm (3-in.) wide specimens. The specimen thickness range was 15 to 38 mm (0.585 to 1.498 in.) Fracture toughness value ranges for 76 and 205-mm (3 and 8-in.) wide specimens were 64.0 to 97.9 and 73.0 to 115.4 MPa $\sqrt{m}$ (58.3 to 88.9 and 66.4 to 105.0 ksi $\sqrt{in.}$), respectively.

Low K_Q values from very early production plate were included in this analysis to give a larger data range. The regression equation obtained from these data was

$$K_{Q8} = 28.2 - 14.6\,(B) + 0.93\,K_{Q3}$$
$$(31.0) - (0.63)(B) + 0.93\,K_{Q3}\ (\text{MPa}\sqrt{m})$$

where

K_{Q8} = fracture toughness of 205-mm (8-in.) wide specimen, MPa $\sqrt{m}$ (ksi $\sqrt{in.}$),
B = specimen thickness, mm (in.), and
K_{Q3} = fracture toughness of 76-mm (3-in.) wide specimen, MPa $\sqrt{m}$ (ksi $\sqrt{in.}$).

Specimen thickness was the strongest dependent variable. This equation explains 79 percent of the total variability and on this basis is considered excellent. The fit for this equation is also considered excellent. The standard error of the estimate is ± 4.2 MPa $\sqrt{m}$ (± 3.8 ksi $\sqrt{in.}$). For a narrow range of plate thicknesses, there was not sufficient sample size to analyze statistically the fracture toughness relationship between 205 and 76-mm (8 and 3-in.) wide specimens. Specimen test direction had no effect on the dependent variable. The correlation equation just presented indicates that fracture toughness number, K_Q, of Ti-6A1-4V plate can be increased appreciably in thin plate by using an oversized width specimen. The magnitude of the increase diminishes as the thickness increases and approaches 38 mm (1.5 in.). This is not surprising since this thickness meets plane-strain conditions per ASTM Test E 399-74 for these particular Ti-6A1-4V plates. For the most part, fracture toughness tests on Ti-6A1-4V plate less than 32 mm (1.25 in.) thick measure a combination of plane-strain and plane-stress fracture. This by itself results in larger toughness numbers.

Selected Data for Analysis

Selected data covering the plate thicknesses of interest were used for detailed analysis. Table 1 contains the description, tensile properties, and fracture toughness information normally reported for these tests. Also included are the specimen strength ratio, R_{sc}, and K_{max} for the various frac-

TABLE 1—*Tensile and fracture properties of selected Ti-6Al-4V plate.*

Heat No.	Nominal Plate Thickness, in. (mm)	Companion Tensile Properties			Test Plane Orientation	Specimen Dimensions		$\frac{P_{max}}{P_Q}$	R_{sc}	K_{max}, ksi$\sqrt{in.}$ (MPa$\sqrt{m}$)	K_Q, ksi$\sqrt{in.}$ (MPa$\sqrt{m}$)
		UTS, ksi (MPa)	YS, ksi (MPa)	El, %		Width, W, in. (mm)	Thickness, B, in. (mm)				
802549	0.625 (16)	136 (937)	123 (847)	14	LT	3.011 (76.48)	0.585 (14.86)	1.36	1.03	105.0 (115.4)	77.0 (84.6)
					LT	7.999 (203.17)	0.595 (15.11)	1.83	0.95	152.9 (168.0)	83.5 (91.8)
		143 (985)	131 (903)	13	TL	3.010 (76.45)	0.625 (15.88)	1.14	0.93	101.6 (111.6)	88.9 (97.7)
					TL	7.994 (203.05)	0.625 (15.88)	1.44	0.86	150.6 (165.5)	105.0 (115.4)
895116	1.250 (32)	131 (903)	120 (827)	14	LT	3.005 (76.33)	1.227 (31.17)	1.12	0.82	79.8 (87.7)	71.1 (78.1)
					LT	8.010 (203.45)	1.228 (31.19)	1.70	0.87	137.5 (151.1)	82.0 (90.1)
		134 (923)	125 (861)	14	TL	3.006 (76.35)	1.253 (31.83)	1.03	0.85	85.5 (94.0)	82.6 [a] (90.8)
					TL	8.000 (203.20)	1.253 (31.83)	1.41	0.75	122.9 (135.1)	86.9 (95.5)
895116	1.500 (38)	131 (903)	122 (841)	14	LT	3.010 (76.45)	1.480 (37.59)	1.03	0.84	82.2 (90.3)	80.0 [a] (87.9)
					LT	8.035 (204.10)	1.498 (38.05)	1.48	0.78	118.2 (129.9)	79.7 (87.6)
		134 (923)	125 (861)	14	TL	3.008 (76.40)	1.495 (37.97)	1.04	0.81	81.5 (89.6)	78.7 [a] (86.5)
					TL	8.022 (203.76)	1.481 (37.62)	1.37	0.70	112.5 (123.6)	82.2 (90.3)

NOTE—UTS=ultimate tensile strength, YS=yield strength, and EL=elongation.
[a] K_{Ic} per ASTM Test E 399-74.

ture toughness tests. The K_{max} value is calculated on the basis of maximum load and initial crack length. This toughness value is similar to apparent fracture toughness, K_{app}, obtained from transitional fracture toughness tests [*4*]. The tensile properties shown are typical for this type of Ti-6A1-4V plate. Some strength directionality is evident in the thinner plate. This is fairly typical for thinner plate. For each plate, higher yield strengths were obtained for the transverse compared to the longitudinal test direction. The transverse test direction also resulted in higher fracture toughness, K_Q. Fracture toughness values for all specimens from the thin plate are not K_{Ic} because of insufficient specimen thickness and exceeding the ratio of maximum load to the 95 percent secant offset load, P_{max}/P_Q, of 1.10. For the two thicker plates, all specimens were thick enough to satisfy the crack size and thickness requirement of $\geq 2.5\ (K_Q/YS)^2$. For 76-mm (3-in.) wide specimens in the thicker plates, only the LT direction 76-mm (3-in.) wide specimen of the 32-mm (1.250-in.) thick plate did not satisfy the P_{max}/P_Q ratio of ≤ 1.10. The P_{max}/P_Q ratios of all 205-mm (8-in.) wide specimens were greater than 1.10 and sufficiently larger than those obtained for the 76-mm (3-in.) wide specimens. The P_{max}/P_Q ratios of the TL test direction specimens tended to be lower than the LT test direction. The exception was for 76-mm (3-in.) wide specimens from the 38-mm (1.50-in.) thick plate, where all P_{max}/P_Q ratios were low. The directionality differences in P_{max}/P_Q ratio for the data from the same specimen widths in Table 1 are the result of lower P_Q for the LT direction specimens compared to the TL direction specimens. The specimen strength ratios, R_{sc}, were higher for the thin plate compared to the two thicker plates and reflect a stress at the crack tip near the yield strength. Specimens from this plate were not sufficiently thick to satisfy the sizing requirement of ASTM Test E 399-74. The R_{sc} of specimens from the 32 and 38-mm (1.25 and 1.50-in.) thick plates reflect lower stress at the crack tip and approach 80 percent of the yield strength. For these specimens, the ASTM crack size and thickness requirements were met. Comparison of the R_{sc} of 76 and 205-mm (3 and 8-in.) wide specimens shows little, if any, differences. The net section stress divided by the yield strength did appear to normalize the R_{sc} ratio. Some of the small differences in the R_{sc} ratio were accounted for by small variations in crack length to width, a/W, ratios between the 76 and 205-mm (3 and 8-in.) wide specimens. Fracture toughness, K_Q, except for the thick plate, in Table 1, showed increased values for the 205 mm (8 in.) compared to 76-mm (3-in.) wide specimens. This was also the case for K_{max}. The 76-mm (3-in.) wide specimens for the 38-mm (1.50-in.) plate met all of the validity requirements of ASTM Test E 399-74 and by definition measured plane strain, K_{Ic}. Therefore, for thicker plate the small difference in fracture toughness, K_Q, between 76 and 205-mm (3 and 8-in.) wide specimens was not surprising.

The rationale for using the wider specimens is that at instability cracks propagate through an elastic stress field (net section stress <80 percent yield strength). For the Ti-6Al-4V plate considered in this paper, a 76-mm (3-in.) wide specimen is on the low side in width for satisfying this requirement. The net section stress calculation is based on the load at 95 percent secant offset and the relative crack length at that point in the fracture process. At the 95 percent secant offset load, the crack has extended 2 percent of its initial length. This 2 percent extension plus the initial crack length is the relative crack length. Net section stresses and the ratios to yield strength are shown in Table 2. For the 76-mm (3-in.) wide specimens, the net section stress to yield strength ratios were nearly all greater than 0.8, while these ratios for the 205-mm (8-in.) wide specimens were less than two thirds of the yield strength. This gives assurance that for the larger width specimen, the crack is propagating through an elastic stress field at the particular part of the fracture process of interest. For mixed-mode failures, the larger width, compared to the 76-mm (3-in.) wide specimen, results in fracture toughness, K_Q, satisfying more ideally the elastic stress analysis provision.

Crack-Growth-Resistance Curves

Although a difference in fracture toughness number, K_Q, between 76 and 205-mm (3 and 8-in.) wide specimens is obtained, the fracture behavior

TABLE 2—*Comparison of net section stress and ratio to yield strength of standard and wider Ti-6Al-4V compact tension specimens.*

Nominal Plate Thickness, in. (mm)	Test Plane Orientation	Nominal Specimen Width, in. (mm)	Net Section [a] Stress, ksi (MPa)	Ratio of Net Section Stress to Yield Strength
0.625 (16)	LT	3 (76)	96.8 (666.9)	0.79
		8 (205)	65.8 (453.4)	0.53
	TL	3 (76)	111.8 (770.3)	0.85
		8 (205)	82.7 (569.8)	0.63
1.250 (32)	LT	3 (76)	92.4 (636.6)	0.77
		8 (205)	65.6 (451.9)	0.55
	TL	3 (76)	108.0 (744.1)	0.86
		8 (205)	69.6 (481.6)	0.56
1.500 (38)	LT	3 (76)	103.8 (715.2)	0.85
		8 (205)	65.1 (448.5)	0.53
	TL	3 (76)	103.1 (710.4)	0.82
		8 (205)	66.8 (460.3)	0.53

[a] On the basis of load at 95 percent secant offset and relative crack length (initial crack length plus 2 percent).

for both size specimens is simliar. This is shown by crack-growth-resistance curves (Figs. 1 through 6) developed from the test records of the fracture-toughness specimens noted in Table 1. Construction of these curves was described earlier and in more detail elsewhere [5]. Use of the value 113.7×10^3 MPa (16.5×10^6 psi) for the modulus of elasticity in the dimensionless displacement factor worked well for these Ti-6Al-4V specimens. The present study and Jones and Brown [5] show that differences between relative and actual crack extension from contributions of crack tip plastic flow and the outward curved shape of the actual crack were not significant. For the crack-growth-resistance curves shown in Figs. 1 through 6 and following the work just presented, the initial portion of the curves is shown as dashed lines. As described in Ref 5, the uncertainties of this analysis make the initial portion of crack-growth-resistance curve impossible to determine with useful accuracy. To help in constructing the curves in this initial

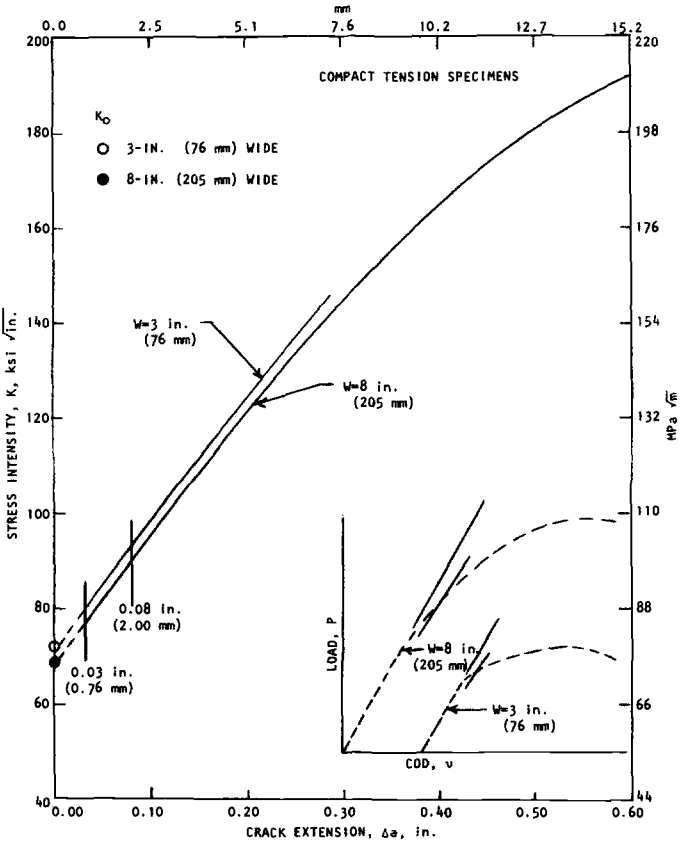

FIG. 1—*Crack-growth-resistance curve for LT test plane of 16-mm (0.625-in.) thick Ti-6Al-4V plate.*

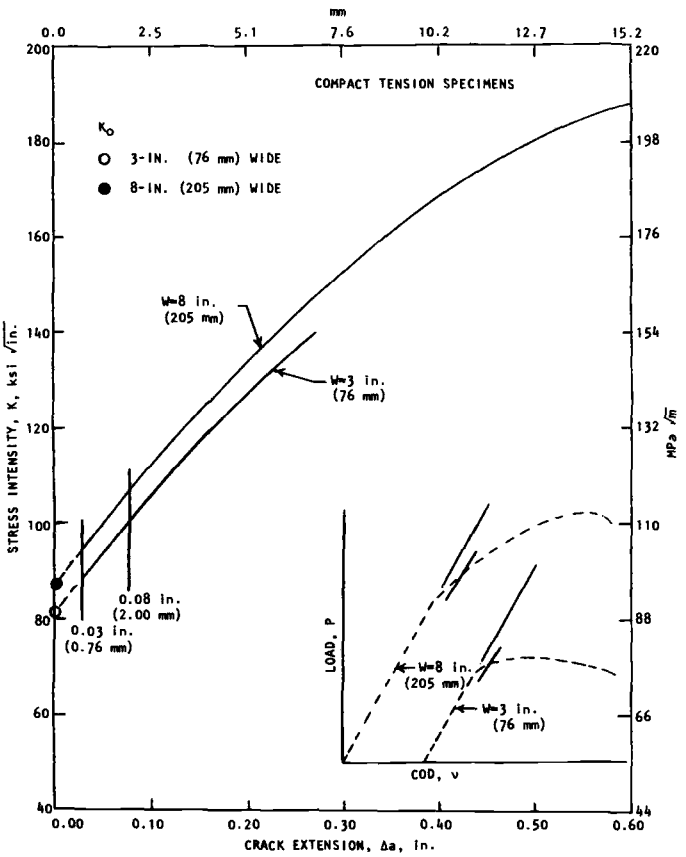

FIG. 2—*Crack-growth-resistance curve for TL test plane of 16-mm (0.625-in.) thick Ti-6Al-4V plate.*

region, the stress intensity value, K_o, at the onset of fracture was calculated. These values are shown on the left-hand side of the figures. The crack-growth-resistance curves were determined up to the maximum load obtained for the specimens. The average crack extensions to maximum load were 0.71 and 1.91 mm (0.280 and 0.750 in.) for the 76 and 205-mm (3 and 8-in.) wide specimens, respectively. For simplicity in presentation, the crack-growth-resistance curves (Figs. 1 through 6) only show crack extension to 1.52 mm (0.60 in.). The crack-growth-resistance curves shown in Figs. 1 through 6 tend to become more linear with increasing thickness. Superimposed on the figures are representatives of the load-COD test records of the various specimens. All of the test records for the 205 and 76-mm (8 and 3-in.) wide specimens of the thin plate show very high ascending curves and large differences between P_{max} and P_Q loads. It has been

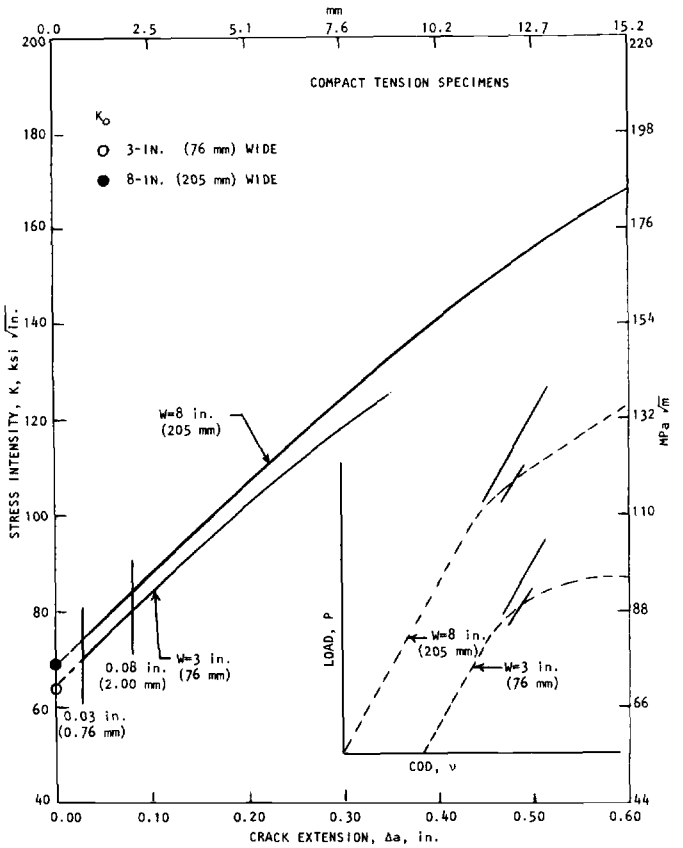

FIG. 3—*Crack-growth-resistance curve for LT test plane of 32-mm (1.250-in.) thick Ti-6Al-4V plate.*

documented [5] that these types of test records result in K_Q dependence on specimen geometry and size. The P_{max}/P_Q ratios of all of these specimens are greater than that allowed (≤ 1.10) under ASTM Test E 399-74. The test records for the 76-mm (3-in.) wide specimens of the 32 and 38-mm (1.25 and 1.50-in.) thick plate are relatively flat in comparison to the others. Only the 76-mm (3-in.) wide LT specimen from the 32-mm (1.25-in.) thick plate gave a P_{max}/P_Q ratio higher than the maximum allowed (1.12 versus 1.10). Under ASTM Test E 399-74, three out of four of these 76-mm (3-in.) wide specimens from the two thicker plates met plane-strain requirements. All of these test records showed evidence of stable crack growth.

Vertical lines representing 2 percent crack extension for 76 and 205-mm (3 and 8-in.) wide specimens are shown on the crack-growth-resistance

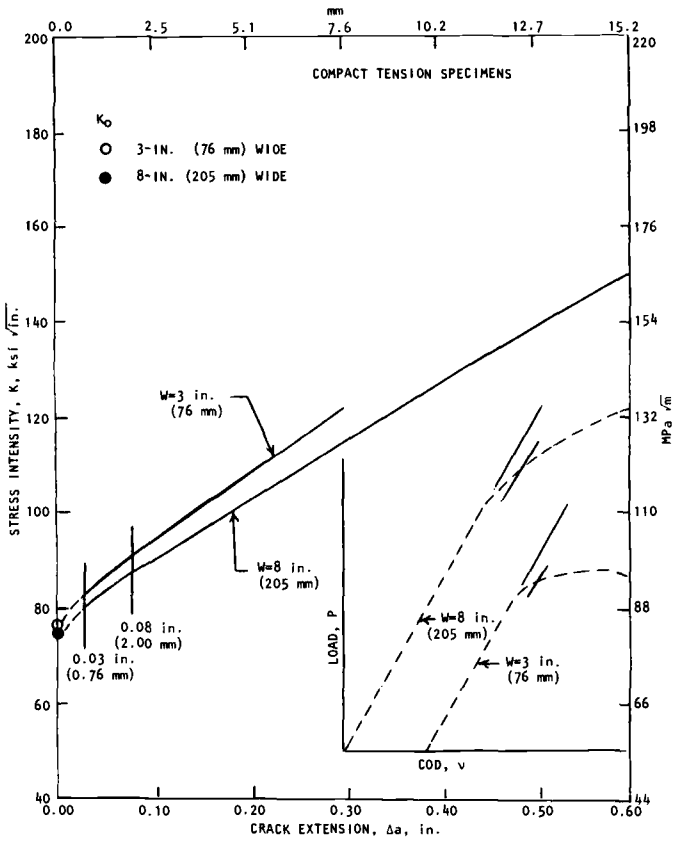

FIG. 4—*Crack-growth-resistance curve for TL test plane of 32-mm (1.250-in.) thick Ti-6Al-4V plate.*

curves in Figs. 1 through 6. In each figure, the stress intensity values, K, at these crack extensions on the crack-growth-resistance curves are similar for 76 and 205-mm (3 and 8-in.) specimen widths. Average stress-intensity values, K, at 0.76 and 2.0-mm (0.030 and 0.080-in.) crack extension from the crack-growth-resistance curves are shown in Table 3 along with fracture toughness, K_Q and K_o, previously discussed. Because the relative crack length is greater than the initial crack length, the K values at representative 2 percent crack extension (relative crack length) are higher than the K_Q values.

Figures 1 through 6 demonstrate the minimal influence of width on K for crack extensions of 0.76 and 2.0 mm (0.030 and 0.080 in.). These crack extensions are 2 percent of the initial crack length for 76 and 205-mm (3 and 8-in.) wide specimens. The reason for higher K_Q for the 205-mm

TABLE 3—*Comparison of stress intensity values for selected Ti-6Al-4V plates.*

Nominal Plate Thickness, in. (mm)	Test Plane Orientation	Nominal Specimen Width, in. (mm)	ksi $\sqrt{\text{in.}}$ (MPa $\sqrt{\text{m}}$) K_Q	K_o[a]	Avg K[b] at 0.030-in. (0.76 mm) Crack Extension	Avg K[b] at 0.080-in. (2.0-mm) Crack Extension
0.625 (16)	LT	3 (76)	77.0 (84.6)	72.5 (79.7)	78.5 (86.3)	92.0 (101.1)
		8 (205)	83.5 (91.8)	67.0 (73.6)		
	TL	3 (76)	88.9 (97.7)	81.6 (89.7)	93.0 (102.2)	105.5 (115.9)
		8 (205)	105.0 (115.4)	87.8 (96.5)		
1.250 (32)	LT	3 (76)	71.1 (78.1)	63.5 (69.8)	72.5 (76.7)	82.5 (90.7)
		8 (205)	82.0 (90.1)	69.5 (76.4)		
	TL	3 (76)	82.6 (90.8)	76.4 (84.0)	82.5 (90.7)	89.0 (97.8)
		8 (205)	86.9 (95.5)	74.6 (82.0)		
1.500 (38)	LT	3 (76)	80.0 (87.9)	75.6 (83.1)	78.0 (85.7)	85.0 (93.4)
		8 (205)	79.7 (87.6)	71.7 (78.8)		
	TL	3 (76)	78.7 (86.5)	73.5 (80.8)	79.0 (86.8)	86.5 (95.1)
		8 (205)	82.2 (90.3)	73.3 (80.5)		

[a] Onset of fracture.
[b] Taken from crack-growth-resistance curves.

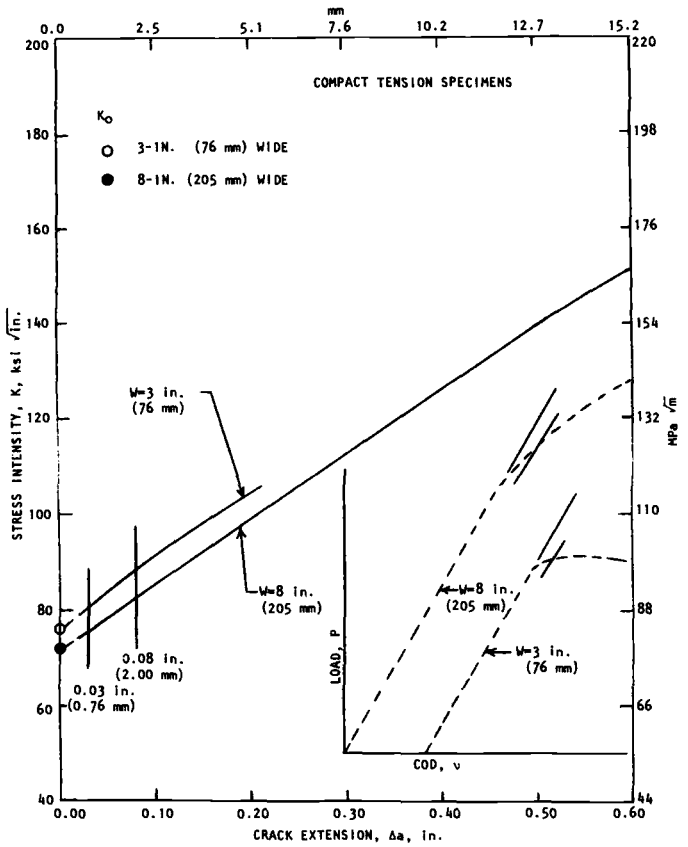

FIG. 5—*Crack-growth-resistance curve for LT test plane of 38-mm (1.500-in.) thick Ti-6Al-4V plate.*

(8-in.) wide specimen compared to 76-mm (3-in.) wide specimens is that from the use of the 95 percent secant offset and resulting 2 percent crack extension from the longer initial crack, K_Q is determined farther into the fracture process. In measuring the fracture for a longer time, greater spread between the load at 2 percent crack extension, P_Q, and the maximum load, P_{max}, is also obtained for the wider specimen compared to the 76-mm (3-in.) wide specimen. This resulted in increased P_{max}/P_Q ratios for the wider specimen.

Modified Secant Offset Procedure

Because of the same relative fracture behavior of 76 and 205-mm (3 and 8-in.) wide specimens, consideration can be made for calculating K values

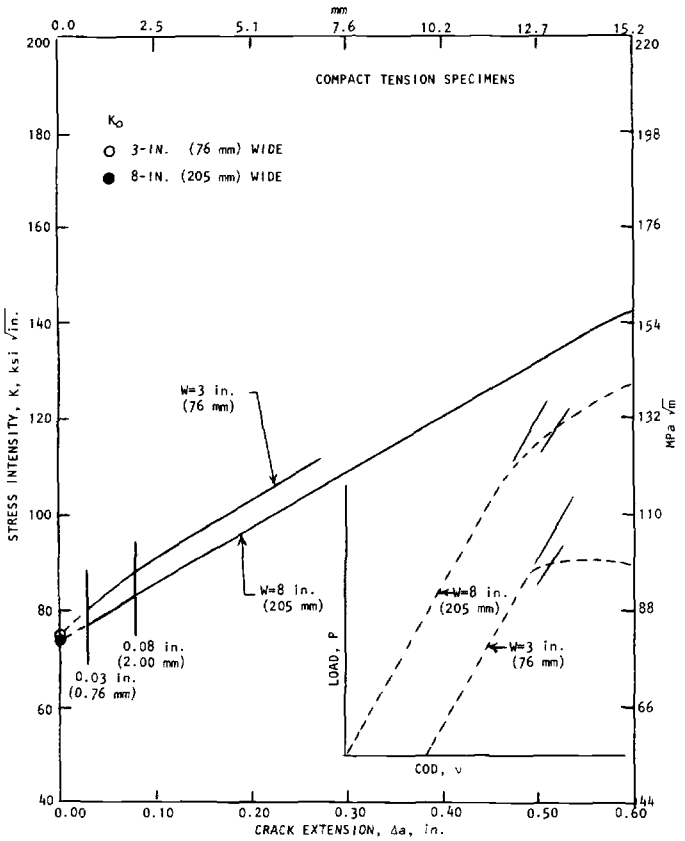

FIG. 6—*Crack-growth-resistance curve for TL test plane of 38-mm (1.500-in.) thick Ti-6Al-4V plate.*

following a modified calculation procedure. The loads at 0.76-mm (0.030-in.) crack extension for 205-mm (8-in.) wide specimens and 2.0-mm (0.080-in.) crack extension in 76-mm (3-in.) wide specimens can be determined from the test records. Under ASTM Test E 399-74, these crack extensions are obtained at 95 percent secant offset from test records of 76 and 205-mm (3 and 8-in.) wide specimens, respectively. The analytical procedure for obtaining crack-growth-resistance curves from test records was reversed and the percent secant offset required for 0.76-mm (0.030-in.) crack extension was determined for 205-mm (8-in.) wide specimens and for 2.0 mm (0.080 in.) for the 76-mm (3-in.) wide specimens. These average percent secant offsets determined from individual test records were 98.2 percent (range of 97.9 to 98.5 percent) and 87.5 percent (range of 86.2 to 88.1 percent) for 0.76 and 2.0-mm (0.030 and 0.080-in.) crack ex-

tension in 205 and 76-mm (8 and 3-in.) wide specimens, respectively. Using loads for these secant offsets from the test records, the initial crack length, specimen width, and thickness in the K equation for the compact tension specimen allows estimating the 76-mm (3-in.) wide fracture toughness number, K_Q, from 205-mm (8-in.) wide fracture toughness specimen test records and the 205-mm (8-in.) wide fracture toughness number, K_Q, from 76-mm (3-in.) wide specimen test records. This type of approach on other types of fracture toughness specimens has been reported [6]. Estimated fracture toughness, K_Q, determined from the fracture toughness test records of the data shown in Table 1 are presented in Table 4. These are compared with actual K_Q for the respective width fracture toughness specimens. The average difference between K_Q and estimated K_Q for 76-mm (3-in.) wide specimens is less than the difference between K_Q and estimated K_Q for the 205-mm (8-in.) specimens.

From data on 76 and 205-mm (3 and 8-in.) wide specimens, estimated fracture toughness K_Q was calculated at 87.5 and 98.2 percent secant offset. These specimens were from some of those previously used for the regression analysis. Estimated K_Q values are compared with actual fracture toughness K_Q data in Table 5 along with estimated K_Q values from the regression equation. The results show that reasonable estimates can be made with the regression equation and by using 87.5 and 98.2 percent secant offsets on 76 and 205-mm (3 and 8-in.) wide specimen test records. Differences between estimated and actual K_Q values are small. The average difference between the 76-mm (3-in.) wide K_Q and estimated K_Q from the modified

TABLE 4—*Comparison of actual and estimated* K_Q *(modified secant offset method) for selected Ti-6Al-4V plates.*

Nominal Plate Thickness, in. (mm)	Test Plane Orientation	Nominal Specimen Width, in. (mm)	ksi$\sqrt{\text{in.}}$ (MPa$\sqrt{\text{m}}$)					
			K_Q		Estimated K_Q		Difference	
0.625 (16)	LT	3 (76)	77.0	(84.6)	73.0	(80.2)	4.0	(4.4)
		8 (205)	83.5	(91.8)	85.3	(93.7)	1.8	(1.9)
	TL	3 (76)	88.9	(97.7)	92.2	(101.3)	3.3	(3.6)
		8 (205)	105.0	(115.4)	93.6	(102.9)	11.4	(12.5)
1.250 (32)	LT	3 (76)	71.1	(78.1)	75.4	(82.9)	4.3	(4.4)
		8 (205)	82.0	(90.1)	73.8	(81.1)	8.2	(9,0)
	TL	3 (76)	82.6	(90.8)	81.9	(90.0)	0.7	(0.8)
		8 (205)	86.9	(95.5)	83.6	(91.9)	3.3	(3.6)
1.500 (38)	LT	3 (76)	80.0	(87.9)	75.3	(82.7)	4.7	(5.2)
		8 (205)	79.7	(87.6)	80.8	(88.8)	1.1	(1.2)
	TL	3 (76)	78.7	(86.5)	77.9	(85.6)	0.8	(0.9)
		8 (205)	82.2	(90.3)	80.7	(88.7)	1.5	(1.6)

TABLE 5—*Summary of* K_Q *and estimated* K_Q *for 14 Ti-6Al-4V plates.*

	ksi$\sqrt{in.}$ (MPa$\sqrt{m}$)				
Nominal [a] Specimen Width, in. (mm)	Avg K_Q	Avg Estimated K_Q [b] (Modified Secant Offset)	Avg Individual Difference (Actual versus Estimated K_Q)	Avg Estimated K_Q [c] (Regression Equation)	Avg Individual Difference (Actual versus Estimated K_Q)
8 (205)	81.2 (89.2)	76.1 (83.6)	6.4 (7.0)	80.1 (88.0)	3.7 (4.1)
3 (76)	72.0 (79.1)	74.2 (81.5)	3.6 (4.0)	72.2 (79.3)	3.6 (4.0)

[a] Sample size of 28 for each group of data.
[b] Estimated 8-in. (205-mm) wide fracture toughness value from 3-in. (76-mm) wide test record and estimated 3-in. (76-mm) wide fracture toughness value from 8-in. (205-mm) wide test record.
[c] Calculated on the basis of regression equation.

secant offset method is also small. The average difference of about 6.6 MPa $\sqrt{m}$ (6 ksi $\sqrt{in.}$) between actual versus estimated K_Q from the modified secant offset method for 205-mm (8-in.) wide specimens is reasonable on the basis of scatter in fracture toughness data. The error [7] due to imprecision of physical measurements for compact tension specimens can be as much as 2 percent of the fracture toughness value, while the standard deviation in interlaboratory tests, using compact tension specimens, was reported in the same reference to be from 2.60 to 3.75 percent.

Discussion

This work provided techniques for estimating 76 or 205-mm (3 or 8-in.) wide fracture toughness values from actual 205 or 76-mm (8 or 3-in.) wide fracture toughness results. This is a useful operation in that varying fracture toughness specimen widths have been used to test material. The presented techniques allow normalizing the fracture toughness data to either that associated with 76 or 205-mm (3 or 8-in.) wide specimens. In this manner, data can be analyzed to assess probabilities in meeting guaranteed fracture toughness.

Similar analysis could be done on any widths of specimens. The regression equation resulted in closer estimates to actual data than the use of the modified secant offset method. Both methods gave acceptable estimates based on scatter normally associated with fracture toughness data. The latter is more desirable because it is applied to the individual specimen test record and follows procedures already used.

The crack-growth-resistance curves for 76 and 205-mm (3 and 8-in.)

wide specimens showed similar fracture behavior for the same material. Because of its longer initial crack length and resulting crack extension, the 205-mm (8-in.) wide specimen was measured further by the fracture process and resulted in higher K_{max} than the 76-mm (3-in.) wide specimen. At the same crack extension, the K values were similar for 76 and 205-mm (3 and 8-in.) wide specimens. However at 2 percent crack extension (ASTM Test E 399-74), the longer crack length of the 205-mm (8-in.) wide specimens resulted in higher K_Q compared to 76 mm (3-in.) wide specimens. This was particularly true for thinner specimens which resulted in mixed-mode failures. For specimens near 38-mm (1.5-in.) thickness, very small increases in toughness were obtained in increasing the width from 76 to 205 mm (3 to 8 in.). These specimens (38 mm [1.5-in.] thick, 76 mm [3-in.] wide) satisfied the ASTM plane-strain validity requirements. Stable crack extension was, however, apparent in the test records from these specimens. This study did not determine if the thickness and crack length requirement of being equal to or greater than the sizing parameter, 2.5 $[K_Q/\mathrm{YS}]^2$, was sufficient to give the lower limiting value of fracture toughness. It has been suggested [*8*] that the coefficient of this parameter be raised from 2.5 to 5.0.

For thin plate ($\leq$32 mm [1.25 in.] thick) testing according to ASTM Test E 399-74 resulted in validity violations and plane-strain toughness, K_{Ic}, was not obtained. At the present time, there are no inexpensive accepted test procedures for mixed-mode fracture toughness testing which would lend themselves for use as a quality control test. Use of plane-strain test procedures under ASTM Test E 399-74 for quality control work is in itself expensive, and other test methods [*9*] are being reviewed to reduce this cost. Acceptable plane-stress and transitional fracture toughness tests, [*4, 10*] including R-curve determinations (for example, ASTM Recommended Practice for R-Curve Determination (E 561-76T)) would be even more expensive at present than testing according to ASTM Test E 399-74. Because of cost considerations, testing thin plate, which results in mixed-mode failures, under procedures of ASTM Test E 399-74 is justified. This will be particularly true when sufficient data have been generated and statistical treatment of the historical data can be established. On this basis, these tests on thin plate give assurance that plate of adequate fracture toughness is consistently produced.

A width to thickness, W/B, ratio for compact tension specimens greater than allowed by ASTM Test E 399-74 ($\leq$4.0) was shown to have merit for tests for thin plate. The 205-mm (8-in.) wide specimens resulted in net section stress below two thirds of the yield strength, whereas the 76-mm (3-in.) wide specimens showed difficulty in meeting net section stress less than 80 percent of the yield strength. Therefore, from the use of the 205-mm (8-in.) wide specimen, the crack is propagating through an elastic

stress region, at the point of interest for calculation of fracture toughness, K_Q. Ratios of P_{max}/P_Q were higher for these 205-mm (8-in.) wide specimens than allowed by ASTM Test E 399-74. Recent work on aluminum alloys [*1*] has suggested that the validity provision of P_{max}/P_Q to be equal to or less than 1.10 is not required for wide specimens. For this consideration it must be shown that the specimen results in a net section stress below 0.7 of the yield strength. The higher K_Q number associated with the 205-mm (8-in.) wide specimen compared to the 76-mm (3-in.) wide specimen has no real meaning unto itself as to the fracture toughness of the plate. The 205-mm (8-in.) wide specimen measures farther into the fracture process than the 76-mm (3-in.) wide specimen.

The use of the modified secant offset method allows a useful estimate of 76-mm (3-in.) wide fracture toughness K_Q from test records of 205-mm (8-in.) wide specimens and vice versa. The estimated 76-mm (3-in.) wide K_Q (98.2 percent secant offset) made from 205-mm (8-in.) wide specimens is at a net section stress less than two thirds of the yield strength, while the estimated 205-mm (8-in.) wide K_Q (87.5 percent secant offset) from 76-mm (3-in.) wide specimens is at a net section stress greater than 80 percent of the yield strength. On the basis of the crack propagating through an elastic stress field, the estimated 76-mm (3-in.) wide fracture toughness K_Q from the 205-mm (8-in.) wide specimen test record is the better of the two. This type of approach in describing fracture toughness is similar to that proposed earlier [*5*] in the development of ASTM Test E 399-74. It was suggested that fracture toughness should be determined on a fixed increment of crack extension rather than on a percentage of the initial crack length in order to eliminate specimen size dependence.

Conclusions

1. Reasonable correlations were developed for comparing K_Q of 76 and 205-mm (3 and 8-in.) wide compact tension fracture toughness specimens. One method was from a regression equation and the other from a modified secant offset method.

2. The regression equation resulted in closer estimates to actual data, however, the modified secant offset method is preferred because it is applied on the basis of individual test records and follows procedures similar to those of ASTM Test E 399-74.

3. Crack-growth-resistance curves for 76 and 205-mm (3 and 8-in.) wide specimens show similar fracture behavior. The wider specimens, because of the greater crack extension from longer crack length, measure the fracture process farther.

4. The higher K_Q number of the 205 mm (8-in.) compared to the 76-mm (3-in.) wide specimen is the result of specimen size difference. This

effect in high toughness-moderate strength Ti-6Al-4V specimens is related to stable crack growth.

References

[1] Kaufman, J. G. and Nelson, F. G. in *Fracture Toughness and Slow Stable Cracking, ASTM STP 559,* American Society for Testing and Materials, 1974, pp. 74-85.

[2] "The Fracture Toughness of RMI Ti-6Al-4V Plate," Technical Bulletin, RMI Company, Niles, Ohio, 11 June 1974.

[3] Brown, W. F., Jr., "Note for ASTM E-24, Sub. I on Effects of Some Dimensional Variables for Compact Tension Specimens," NASA, Lewis Research Center, Cleveland, Ohio, 23 Sept. 1969.

[4] *Damage Tolerant Design Handbook,* Section 5, MCIC-HB-01, Metals and Ceramics Information Center, Battelle, for Air Force Materials Laboratory, Dayton, Ohio. Sept. 1973.

[5] Jones, M. H. and Brown, W. F., Jr., "The Influence of Crack Length and Thickness in Plane Strain Fracture Toughness Tests," NASA TM X-1860, NASA, Lewis Research Center, Cleveland, Ohio, Aug. 1969.

[6] Donald, J. K. et al, "Size Requirements for Fatigue-Cracked Fracture Toughness Screening Specimens," Final Report AMMRC CTR 74-72, Del Research Corporation, Hellertown, Pa. for The Metals Properties Council, Inc., Dec. 1974.

[7] Orange, T. W., "Some Effects of Experimental Error in Fracture Testing," NASA TM X-68285, NASA, Lewis Research Center, Cleveland, Ohio, Aug. 1973.

[8] Brown, W. F., Jr. and Srawley, J. E. in *Review of Developments in Plane Strain Fracture Toughness Testing, ASTM STP 463,* American Society for Testing and Materials, 1970, pp. 216-248.

[9] "Rapid Inexpensive Tests for Determining Fracture Toughness," NMAB-328, Report of The Comittee on Rapid Inexpensive Tests for Determining Fracture Toughness, National Materials Advisory Board, National Research Council, National Academy of Sciences, Washington, D.C., 1976.

[10] Section 9.5.1.5, *MIL-HDBK-5B,* Change Notice 2, "Plane Stress and Transitional Fracture Toughness," Dept. of Defense, Washington, D.C., 31 Aug. 1973.

J. F. Throop [1] *and R. R. Fujczak* [1]

Fracture Resistant Titanium-Aluminum Laminate*

REFERENCE: Throop, J. F. and Fujczak, R. R., **"Fracture Resistant Titanium-Aluminum Laminate,"** *Toughness and Fracture Behavior of Titanium, ASTM STP 651,* American Society for Testing and Materials, 1978, pp. 246–266.

ABSTRACT: In an exploratory program for the development of damage tolerant materials for aircraft and helicopter structures, it has been found that laminated panels composed of mill-annealed Ti-6Al-4V sheet and alclad 2024-T3 sheet provided unusual fatigue and fracture resistance. Lamination of these two materials by explosive bonding results in a damage-tolerant fatigue resistant laminate.

Notched-beam specimens were fatigue cycled in pure bending at 30 Hz. The value of stress intensity factor range for crack propagation rates of 2.54×10^{-9} m/cycle (10^{-7} in./cycle) or less appears to be about 17.5 $MN/m^{3/2}$ (16 $ksi\sqrt{in.}$) For values of ΔK less than 35 $MN/m^{3/2}$ (32 $ksi\sqrt{in.}$) the fatigue crack propagation rate measured in the laminate is smaller than that of either the aluminum alloy or the titanium alloy. Room temperature fracture toughness tests of fatigue precracked beams made of equal thickness layers of the two materials give values higher than those of the component alloys. An interlaminar shear strength of 99 MN/m^2 (14.3 ksi) was measured.

While complete evaluation of this laminate will require extensive testing, the early indications are that the damage tolerance is superior to that of either of the component metals because of the energy absorbing capacity provided by the laminated construction. Crack growth is retarded by the ductile cladding which forms the welded interfaces, and impact energy is absorbed in deformation and delamination. Moreover, because of favorable residual stresses the laminate appears to have a higher threshold for fatigue crack propagation than either of the component metals. This permits a larger defect size to be sustained without fatigue crack propagation at a given stress level, or a higher stress level to be endured with a given defect size.

* Original experimental data were measured in U. S. customary units.

[1] Mechanical engineers, Benet Weapons Laboratory, LCWSL, Watervliet Arsenal, Watervliet, N. Y. 12189.

Copyright© 1978 by ASTM International www.astm.org

KEY WORDS: laminates, titanium, aluminum, fatigue (materials), fracture properties, residual stress, explosive welding

Nomenclature

HK	Knoop hardness at 50-g load
τ	Shear stress in the bond layer
A_T	Cross-sectional area of titanium
A_A	Cross-sectional area of aluminum
σ_T	Residual stress in titanium
σ_A	Residual stress in aluminum
E_T	Elastic modulus of titanium alloy
E_A	Elastic modulus of aluminum alloy
ϵ_T	Initial strain in the titanium
ϵ_A	Initial strain in the aluminum
t_T	Thickness of the titanium sheet
t_A	Thickness of the aluminum sheet
L	Length of the laminate specimen
ΔK	Cyclic range of stress intensity factor
Δa	Increment of crack length
da/dN	Fatigue crack growth rate per cycle
N	Number of fatigue cycles applied
γ	Gradient of interfacial tensile strength
r	Radius of the crack tip plastic zone
K_{max}	Maximum value of stress intensity factor during cycle
S_y	Yield strength of the material at the crack tip
K_Q	Apparent fracture toughness
K_{Ic}	Fracture toughness, here calculated from J_{Ic}
J_{Ic}	Rice's path independent integral
C_v	Energy absorbed in Charpy V-notch impact

Prior study of the fatigue behavior of metal laminates [*1*][2] indicated that fatigue crack propagation is retarded by a "crack blunting" effect at each interface in furnace-brazed steel laminates if the brazing provides a ductile bond layer. Also, in explosively bonded aluminum laminates it was found that the alclad layer on the structural alloy sheet provides a ductile bond layer which permits crack blunting and causes fatigue crack arrest followed by cyclic delamination of the bond layer. Both crack blunting and cyclic delamination serve to increase the fatigue life beyond that for solid plate of equal thickness. Fracture toughness test results for these alumium laminates were about the same as for the weaker (T-L) orientation of the solid plate.

Wright et al [*2-4*] have shown that the impact and fracture resistance of metal laminates is superior to that of the corresponding homogeneous

[2] The italic numbers in brackets refer to the list of references appended to this paper.

plate, especially when fracture occurs in the "crack arrest" configuration with the crack advancing normal to the layers. This is attributed to the energy absorption involved in deformation and delamination. The concept was developed analytically for all-brittle systems by Cook and Gordon [*5*] and may be extended to ductile systems in fatigue. In the "crack divider" orientation, with the crack advancing into the edges of the layers, the ductile bond layers may also absorb energy by deformation so as to make the laminate more fracture resistant than a solid plate.

The purpose of this present exploratory study has been to establish whether or not these principles will apply to fatigue of bimaterial systems. The laminate system chosen for investigation consisted of alclad 2024-T3 aluminum alloy and mill-annealed Ti-6Al-4V alloy sheets explosively bonded. It will be shown that such a laminate results in significantly improved fatigue resistance and higher Charpy impact and fracture toughness than those of the component alloys. These improvements are attributed both to the effects of energy absorption of the soft interfaces and to a new phenomenon involving residual stresses induced by the explosive bonding process in a bimetallic system.

Materials and Lamination Process

The laminate consists of alternate layers of alclad 2024-T3 aluminum alloy and mill-annealed Ti-6Al-4V alloy sheets. The sheets of both alloys are 2 mm (0.080 in.) thick and intimately welded to each other by explosive bonding in such a manner that the aluminum alloy layers are left in a state of residual compression and the titanium alloy layers are left in a state of residual tension. A laminate plate with an odd number of layers in this condition is self-equilibrating. It is preferable to have both outside layers be aluminum alloy, since their compressive residual stress helps to prevent fatigue crack initiation at the surface. Also, the alclad surface may serve to provide environmental protection for the laminate.

The laminating process is described in a report by Pattee and Linse [*6*]. A Ti-6Al-4V sheet and an alclad 2024-T3 sheet are welded to the base component as a pair in each detonation. The titanium sheet is placed closer to the base component. The initial base component is an alclad 2024-T3 sheet laid on a steel anvil. Subsequently, the base components are the previously welded laminate and the steel anvil. The residual stresses are induced in the process because the titanium sheets have different density and elastic modulus than the aluminum sheets and are therefore accelerated and stretched differently during the detonation which welds them together. Upon coming to rest after welding, the titanium is left in a state of residual tension and the aluminum is left in a state of residual compression. Some bowing of the panels occurs during welding, and straightening or flattening

is required after each welding operation. Ten welding operations (21 layers) were performed before edge delamination became a problem in the flattening operation.

Specimens and Test Procedures

Configurations

Fatigue and fracture toughness tests were made with notched-beam specimens 19 mm thick by 38 mm deep by 203 mm long (¾ by 1.5 by 8 in.). The crack arrest configuration was made from 21-layer laminates as shown in Fig. 1(*a*). The crack divider configuration was made from 10-layer laminates as shown in Fig. 1(*b*). These two configurations correspond to those used previously by Wright et al [*2–4*] in impact studies of metal laminates.

Interlaminar Shear

The opposing forces of compression residual stress in the aluminum layers and tension residual stress in the titanium layers require an interlaminar shear stress in the alclad layer which bonds them. As mentioned earlier, the straightening process needed when a large number of layers

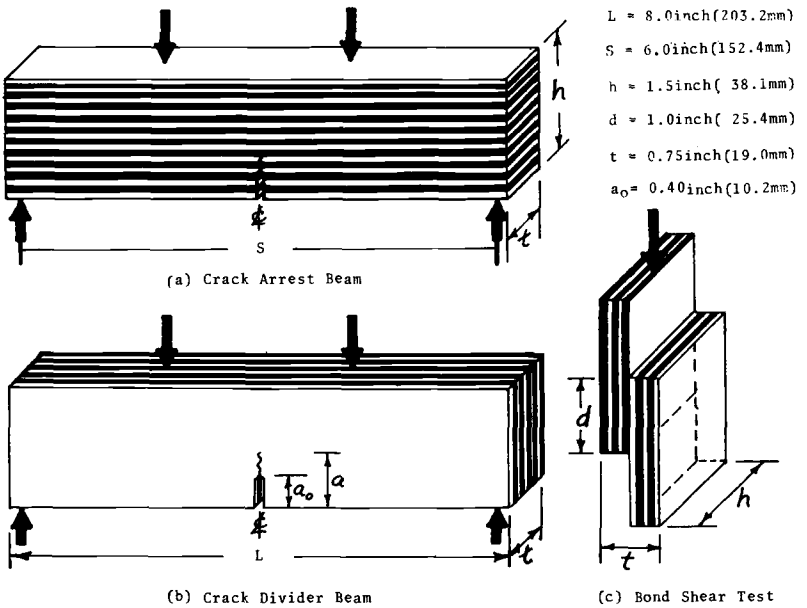

FIG. 1—*Specimens of the titanium-aluminum laminate.*

are bonded may cause delamination at the edges of panels during production. The resistance of the bond layer to shear was measured in a specimen machined from a 10-layer laminate and loaded as shown in Fig. 1(*c*).

Hardness Gradients

The aluminum cladding on the 2024-T3 sheets serves as a soft interlayer between the sheets of structural alloys. A hardness traverse was made of each of several bond layers by taking microhardness readings with a 50-g load on a Knoop indentor. Hardness readings of the virgin sheets used for laminating were also made. Figure 2 is a plot of the hardness variation across a typical bond layer. It shows that the hardness of the alclad layer and the hardness of the aluminum and titanium layers was increased relative to the hardness of the virgin sheets as a result of the explosive bondings. The hardness readings from a typical traverse are listed in Table 1. Thickness measurements also showed that the thickness of the sheets had been reduced by approximately 10 percent during the explosive process.

The hardness gradients in Fig. 2 are steep, indicating that the tensile strength gradients through the interface are also steep. McCartney et al [7] have discussed the strength gradient in regard to conditions for laminate interfaces to arrest fractures. They stated that the two parameters that ap-

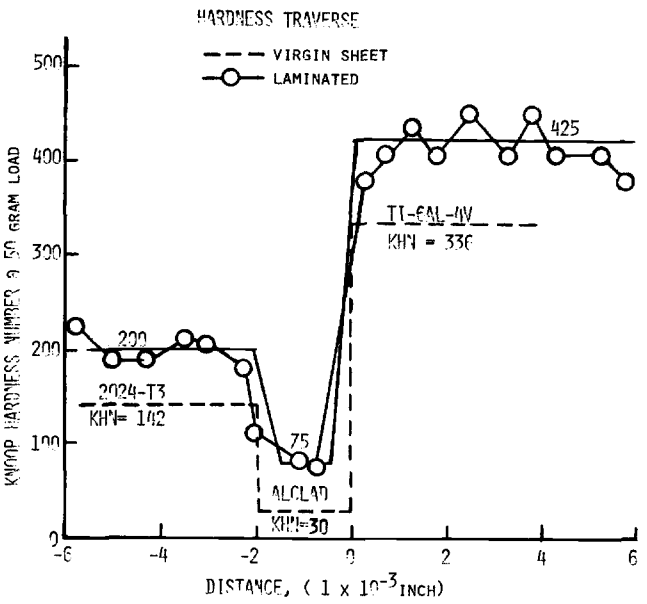

FIG. 2—*Hardness traverse of the laminate bond layer.* 1×10^{-3} *in.* $= 2.54 \times 10^{-6}$ *m.*

TABLE 1—*Hardness traverse of bond layer.*

Material	Distance [a]		Hardness [b]
	in.	mm	HK
2024-T3	−0.650	−16.5	208
	−0.575	−14.6	222
	−0.500	−12.7	188
	−0.425	−10.8	188
	−0.350	−8.89	211
	−0.300	−7.62	206
	−0.225	−5.72	175
	−0.200	−5.08	108
Alclad	−1.00	−2.54	80
	−0.070	−1.78	76
Ti-6Al-4V	+0.030	0.762	382
	+0.070	1.78	408
	+0.125	3.18	438
	+0.175	4.45	409
	+0.250	6.35	453
	+0.325	8.26	409
	+0.375	9.53	453
	+0.425	10.80	408
	+0.525	13.3	408
	+0.575	14.6	382
	+0.675	17.1	453

[a] Distance measured from edge of Ti-6Al-4V sheet.
[b] HK at 50-g load on Knoop indentor.

pear to govern the phenomenon of crack arrest by delamination at the interface ahead of a crack are (*a*) the fracture strength gradient across the interface, and (*b*) the plastic-zone size at the crack tip. They showed for AISI 4337M steel that a gradient steeper than 6.9×10^6 MN/m^3 (1 ksi/μm) would cause delamination and arrest of supercritical cracks in the Charpy impact test but a gradient of more than 3.45×10^8 MN/m^3 (50 ksi/μm) is required to cause crack arrest and delamination in cyclic fatigue loading. The steeper gradient is required in cyclic loading because of the smaller plastic zone size involved in the propagation of subcritical cracks in fatigue. The application of this concept will be discussed later.

Residual Stress Evaluation

Residual stress present in the individual layers was evaluated by means of X-ray diffraction measurements. The readings were taken on the edges of the lamina in a 21-layer crack arrest specimen and in a 10-layer crack divider specimen. They were made with an electronically controlled goniometer with digital readout from a minicomputer to a printer [*8*]. The

TABLE 2—*Residual stresses in the 21-layer laminate.*

Material	Stress		Material	Stress	
	ksi	MN/m²		ksi	MN/m²
2024-T3	−4.1	−28.3	Ti-6Al-4V	...	...
	...	...		+18.0	124.1
	−16.6	−114.4		...	...
	...	...		+14.7	101.4
	−15.2	−104.8		...	...
	...	...		+11.8	81.4
	−18.5	−127.6		...	...
	...	...		+14.1	97.2
	−6.5	−44.8		...	...
	...	...		+15.2	104.8
	−12.0	−82.7		...	...
	...	...		+14.2	97.9
	−13.5	−93.1		...	...
	...	...		+9.4	64.8
	−18.0	−124.1		...	...
	...	...		+23.4	161.3
	−17.0	−117.2		...	...
	...	...		+16.0	110.3
	−9.8	−67.6		...	...
	...	...		+16.2	111.7
	−16.6	−114.4		...	...
Avg Al=	−13.4	−92.4	Avg Ti=	+15.3	105.5

NOTE—The minus sign denotes compression.

measurements from the 21 and 10-layer specimens showed that the aluminum layers are under residual compression stress which is balanced by residual tension stress in the adjacent layers of titanium alloy. Values measured in a 21-layer specimen are listed in Table 2.

Residual Stress Analysis

It became apparent to the investigators that the laminate behavior was being influenced greatly by the presence of the residual stresses in the individual layers, not only in regard to straightening and edge delamination during the lamination process but also in the crack propagation and fracture characteristics in the fatigue, fracture, and impact tests. Some understanding of the presence of these self-equilibrating systems of stresses may be gained from the equations of forces and moments as discussed by Trathen [9] in the consideration of so-called statically indeterminate structures.

In the example in Fig. 3, for instance, the equations for stresses and strains are

$$\sigma_T A_T + \sigma_A A_A = 0 \tag{1}$$

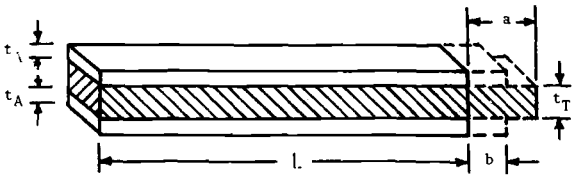

FIG. 3—*A bimaterial laminate with residual stresses. The central strip is stretched an elastic amount "a" that is greater than the simultaneous stretch "b" of the two outer strips, which are half as thick. These deformations are held while the two outer strips are bonded to the central strip all over the surfaces of contact. The resulting laminate is released, and it recovers elastically to a self-equilibrated condition, with compressive residual stress in the outer layers and tensile residual stress in the central layer. This can happen in the explosive bonding of two materials of different densities and elastic modulus values.*

$$(\sigma_T/E_T) - (\sigma_A/E_A) = \epsilon_T - \epsilon_A \tag{2}$$

$$\tau = \frac{\sigma_T t_T}{L} = \frac{2\sigma_A t_A}{L} \tag{3}$$

For the laminate under consideration, A_T, σ_T, and E_T are the cross-sectional area, the residual tensile stress, and the elastic modulus of the high modulus material. Similarly, A_A, σ_A, and E_A are the cross-sectional area, the residual compression stress, and the elastic modulus of the low-modulus material. Here τ is the average interlaminar shear stress acting in the bond layer. The initial strains in the two materials at the time of bonding are ϵ_T and ϵ_A, respectively, t_T and t_A are their thicknesses, and L is the length of the assembly. In the example, t_A is taken as one-half of t_T so as to give equal cross-sectional areas, since the areas of aluminum and titanium layers in the 21-layer laminate are approximately equal.

From Eq 1, if the cross-sectional areas are equal the residual stresses in the two materials must be equal and opposite. Taking E_T as 116 000 MN/m² (16 800 000 psi) and E_A as 71 000 MN/m² (10 300 000 psi) for titanium and aluminum alloys respectively in Eq 2, if the initial strain, ϵ_T, is 0.002 m/m (0.002 in./in.) greater than the initial strain, ϵ_A, the residual stresses in the example would be a tensile stress σ_T of 88 MN/m² (12 770 psi) and a compression stress σ_A of 88 MN/m² (12 770 psi). These are approximately the same as the residual stresses found in the multilayered titanium-aluminum laminates that were tested. Further, from Eq 3, if the length of the assembly under consideration is 10 times the thickness, t_T, the opposing residual stresses will be held in equilibrium by an interlaminar shear stress of 8.8 MN/m² (1 277 psi). The measured shear strength of the bond layer in the titanium-aluminum laminate exceeds this by a factor of 10 or more. These equations then give a reasonable estimate of the stresses and strains involved in laminating by explosive bonding.

Fatigue Tests

Fatigue crack growth was measured in bending specimens as shown in Fig. 1(*a*) and (*b*). The fatigue path may be seen in Fig. 4 for the two different orientations: (*a*) the crack arrest type specimen, and (*b*) the crack divider type specimen. In the crack arrest specimens, the notch was machined so that some cyclic crack propagation could occur in a given layer before the crack would reach an interface. Some specimens were tested with the initial notch in an aluminum layer (Fig. 4(*a*)) and others with the initial notch in a titanium layer. In the crack divider specimens the crack growth was observed to have a nearly continuous crack front across the interfaces at the bond layers between the adjacent aluminum and titanium layers (Fig. 4(*b*)). This suggests that the bond is good between the two different metals.

The specimens were cycled from zero to maximum load in pure bending at 30 Hz in a fatigue machine set-up as shown in Fig. 5. The loading was applied to produce tension at the notch. The crack growth was measured periodically with graduated microscopes reading to 0.05 mm (0.002 in.). It was measured at notches at the mid-span of beam specimens 203 mm (8 in.) long, thereby avoiding difficulties arising from any delamination at the edges of the fabricated panels from which the specimens were made. In some cases, through-bolts were used to prevent delamination of the specimen edges during machining. These bolts were left in the specimens to prevent any edge flaws from entering which would spoil the performance tests at the mid-span cross section. In larger panels, or longer span beams, this would not be necessary.

Fracture Toughness and Impact

After the fatigue crack had been propagated to the desired depth, the specimen was removed and placed in a universal testing machine for the fracture toughness test, also in the 4-point bending configuration. The crack divider specimens were tested in accordance with ASTM Test for Plane-Strain Fracture Toughness of Metallic Materials (E 399-74) with the exception that the 4-point loading was used and appropriate formulas for this type of loading were used to analyze the results. The crack arrest specimens were tested and analyzed in the same manner for purposes of comparison, although it is recognized that the laminated nature of the specimen should require a more appropriate formulation for stress intensity factor of the notched laminated beam in this configuration. Because the crack arrest configuration is capable of resisting large deflections before fracture, the load-line deflection under one of the load points was monitored using a linear variable differential transformer and plotted versus

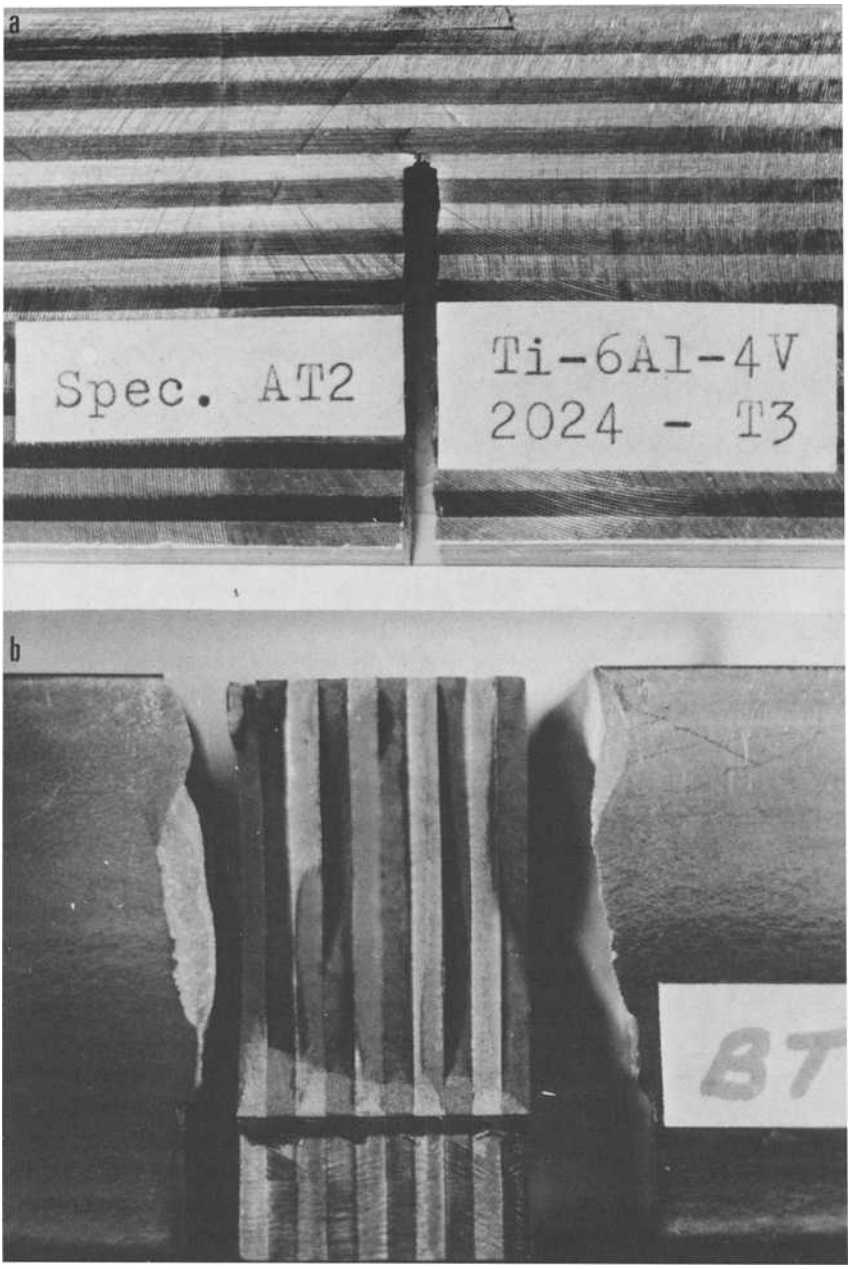

FIG. 4—*The two specimen configurations that were tested.* (a) *Crack arrest configuration.* (b) *Crack divider configuration.*

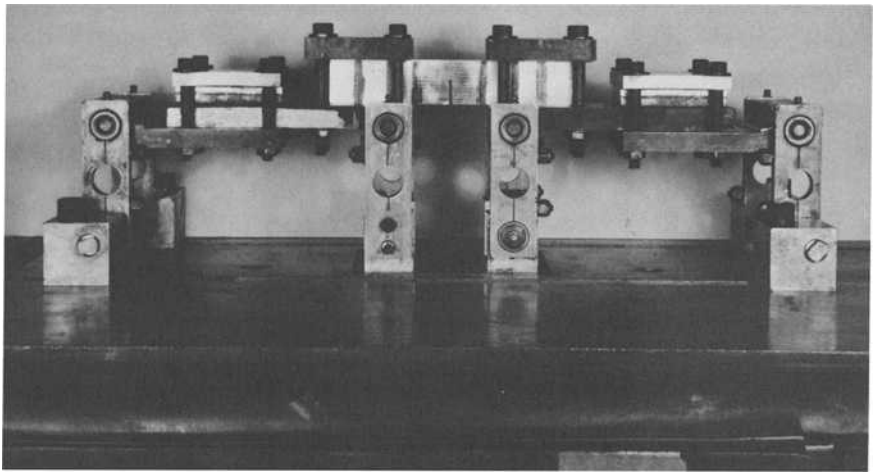

FIG. 5—*The notched-beam fatigue test set-up.*

load on an X-Y recorder. This enabled evaluation of K_{Ic} values from the J-integral approach for comparison with fracture toughness K_Q values. The values are listed as apparent fracture toughness in Table 3.

Charpy impact tests of V-notched specimens of both crack arrest and crack divider configuration were made. Tests were made at room temperature and −40°C (−40°F). The results, listed in Table 4, may be compared with the usual published results for V-notch Charpy impact tests of metals since the standard 10-mm (0.4-in.) specimens were used. The laminate results differ somewhat in that the notch tip in some specimens was in a titanium layer while in other specimens the notch tip was in an aluminum layer. The test results are listed separately in the table.

Results

Residual Stresses

The X-ray measurements from a 21-layer specimen gave an average compressive residual stress of 92 MN/m² (13 400 psi) in the 11 aluminum layers and an average tensile residual stress of 105 MN/m² (15 300 psi) in the 10 titanium layers. Table 2 lists the values for the individual layers. Results from a 10-layer specimen confirmed the presence of similar residual stresses in the 10-layer panels. These averaged 86.2 MN/m² (12 500 psi) in both tension and compression.

TABLE 3—*Apparent fracture toughness,* K_Q, *test results.*

Configuration	Specimen	K_Q		K_{1c} from J_{1c}	
		ksi$\sqrt{\text{in.}}$	MN/m$^{3/2}$	ksi$\sqrt{\text{in.}}$	MN/m$^{3/2}$
Crack divider	BT2	53.1	58.2	59.7	65.4
	BT3	58.6	64.2	60.9	66.7
	BT4	62.5	68.5	60.5	66.3
	BT5	49.4	54.1	54.0	59.2
	BT6	45.3	49.6	49.0	53.7
	BT7	53.8	59.0	54.1	59.3
	avg	53.8	58.9	56.4	61.8
Crack arrest: fatigued through 2024-T3; failure of Ti-6Al-4V					
	AT3	72.3	79.2	91.7	100.5
	AT5	69.9	76.6	90.0	98.6
	AT6	66.4	72.8	94.6	103.7
	avg	69.5	76.2	92.1	100.9
Crack arrest: fatigued through Ti-6Al-4V; failure of 2024-T3					
	AT4	24.8	27.2	65.2	71.5
	AT7	37.9	41.5	94.0	103.0
	AT8	30.7	33.6	55.5	60.8
	AT9	44.5	48.8	73.5	80.6
	avg	34.5	37.8	72.1	79.0

Interlaminar Shear Strength

The test of a specimen as shown in Fig. 1(*c*) from a 10-layer panel gave the shearing strength of the bond layer as 98.5 MN/m^2 (14 290 psi).

Hardness Tests

The virgin hardness values in Knoop Hardness Numbers (HK) were 30 for the alclad bond layer, 142 for the 2024-T3, and 336 for the Ti-6Al-4V. The *in-situ* hardnesses were 75, 200, and 425, respectively, as a result of the explosive bonding (see Fig. 2).

Fatigue Tests

A graph of fatigue crack propagation rate da/dN plotted versus ΔK on log-log scales is shown in Fig. 6. The upper bound of crack rates for all the titanium-aluminum specimens tested is shown as line (c) on the graph and is expressed by the equation

$$da/dN = 7.094 \times 10^{-19}\ \Delta K^{8.056} \tag{4}$$

It represents the upper bound for the data from ΔK of 17.5 to 36 MN/m$^{3/2}$ (16 to 33 ksi$\sqrt{\text{in.}}$) and da/dN from 2.54×10^{-9} to 2.54×10^{-6} m (10^{-7} to about 10^{-4} in.) per cycle. This upper bound for the laminate represents

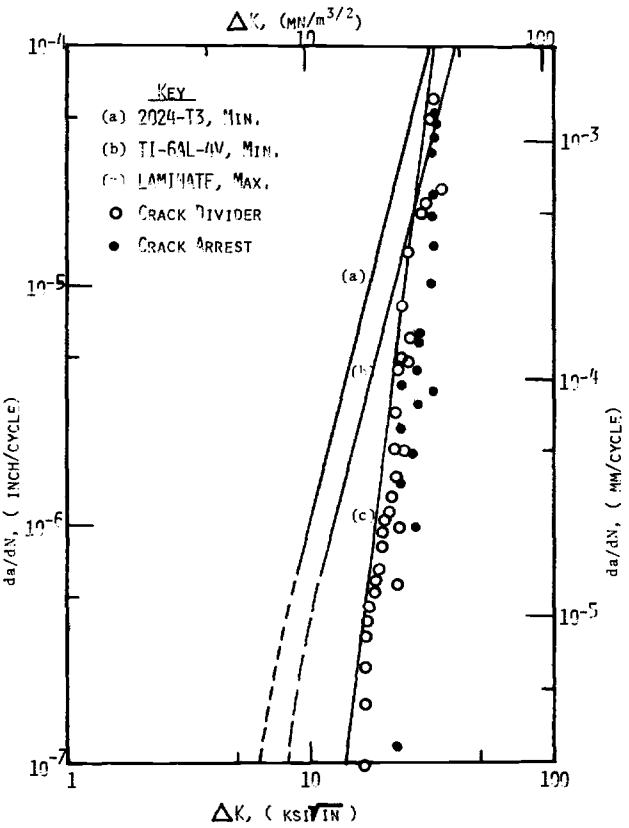

FIG. 6—*Fatigue crack rate versus range of* K.

slower crack rates than the lower bounds shown as line (a) and line (b) for the 2024-T3 and the Ti-6Al-4V, respectively. These represent the lower bounds of data published in recent literature [*10–12*]. For the 2024-T3 [*10*] this may be expressed as

$$da/dN = 1.76 \times 10^{-12}\ \Delta K^4 \tag{5}$$

for values of ΔK between 11 and 44 MN/m$^{3/2}$ (10 and 40 ksi$\sqrt{\text{in.}}$) and for sheet thickness from 2.3 to 3.2 mm (0.090 to 0.125 in.). For the Ti-6Al-4V alloy [*11*], the lower bound for mill-annealed plate may be expressed as

$$da/dN = 7.04 \times 10^{-13}\ \Delta K^4 \tag{6}$$

for values of ΔK between 11 and 66 MN/m$^{3/2}$ (10 and 60 ksi$\sqrt{\text{in.}}$) and for plate thicknesses of 25.4 to 31.8 mm (1.00 to 1.25 in.).

The most significant feature in Fig. 6 is the higher apparent threshold of the laminate, attributable to the presence of the residual compression stress in the aluminum layers. The effect of this residual stress is to reduce the effective range of K during the cyclic loading of the laminate. This effect is most pronounced at small crack depths or low values of ΔK where most of the fatigue life of a component is spent. It therefore can result in a large extension of the fatigue life of a component.

In the fatigue tests of the crack divider configuration, the cracks were propagated from an initial notch depth of about 10 mm (0.4 in.) until they reached near mid-depth of the beam, about 19 mm (0.75 in.). The specimens were then set aside for subsequent static tests of fracture toughness. A graph of typical crack growth Δa versus cycles is shown in Fig. 7 for given initial values of ΔK.

In the fatigue tests of the crack arrest configuration, cyclic delamination of the bond layer ensued when the crack reached the bond layer in all cases except Specimen AT-2 which will be discussed later. The alclad bond layer was about 0.05 mm (0.002 in.) thick. A graph of typical crack growth Δa versus cycles for various initial values of ΔK is shown in Fig. 8. The difference in the aluminum and titanium propagation rates is particu-

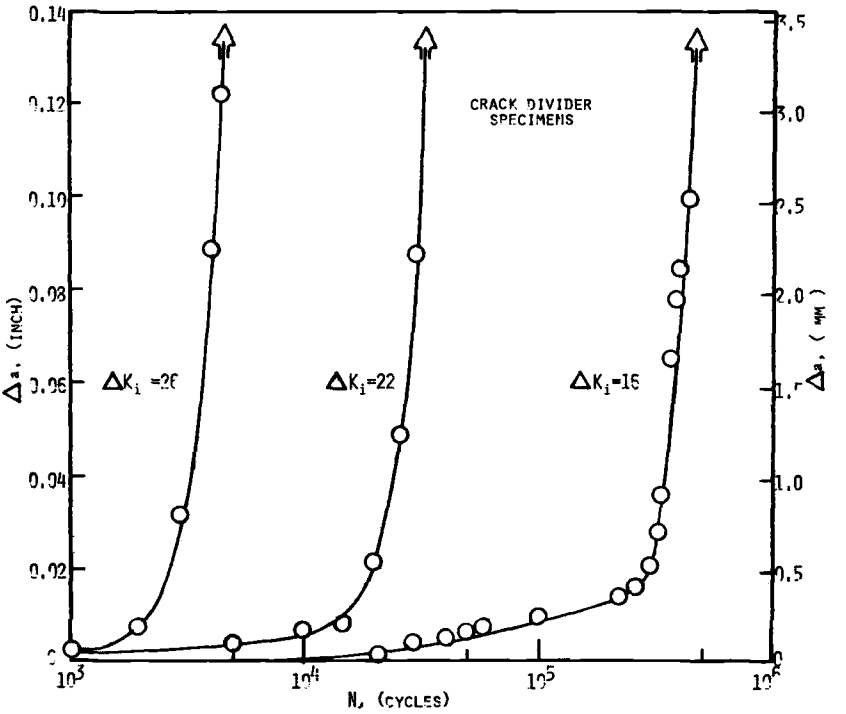

FIG. 7—*Crack propagation in crack divider specimens at given initial* K*-range.*

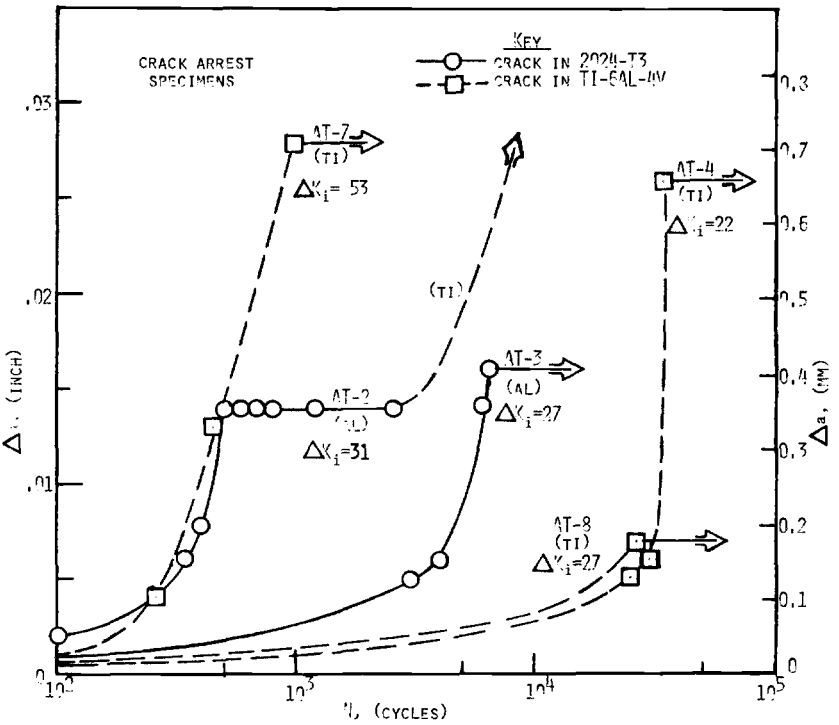

FIG. 8—*Propagation and arrest in crack-arrest specimens at given inital* K*-range.*

larly noticeable in Specimen AT-3 with the crack in the aluminum and Specimen AT-8 with the crack in the titanium. Both specimens had an initial ΔK of 30 MN/m$^{3/2}$ (27 ksi$\sqrt{\text{in.}}$). To grow 0.13 mm (0.005 in.), the crack in the titanium took six times more cycles than the crack in the aluminum.

The end of each curve designates the point where the crack reached a bond layer. The propagation was generally arrested at that point, followed by slow cyclic delamination. In Specimen AT-2, however, the crack grew from the aluminum layer into the bond layer and cyclic delamination began but the crack continued into the adjacent titanium layer. At 13 861 cycles it was part way through the titanium layer when the layer fractured and the fatigue machine shut off because of the increased amplitude of deflection. This was the only case among these titanium-aluminum laminate specimens in which the fatigue crack traversed the bond layer and continued part way through the adjacent layer. In Fig. 8 the dashed line representing the continued crack growth in the titanium layer of Specimen AT-2 is approximately parallel to that for crack growth in the titanium layer of

Specimen AT-7 which had its initial notch in the titanium layer. When the crack in Specimen AT-7 reached the bond layer, however, its advance was arrested. Cyclic delamination began, and the specimen was set aside for fracture toughness testing.

Crack Arrest Criterion

Following the reasoning of McCartney et al [7], since the gradient of strength from the titanium to the alclad in Specimen AT-7 is greater than that from the aluminum alloy to the alclad in Specimen AT-2 one might expect the fatigue crack in Specimen AT-7 to be arrested where that in Specimen AT-2 might not be. The gradient γ of interlaminar tensile strength may be approximated by dividing the difference between the tensile strength of the structural alloy and the bond layer by one quarter of the thickness of the bond layer. The width of the plastic zone may be approximated by the equation for the radius of the plastic zone ahead of the crack

$$r=\left(\frac{1}{2\pi S_y^2}\right)K_{\max}^2 \tag{7}$$

Here $K_{\max}$ is the stress intensity factor at maximum cyclic load when the crack tip just reaches the bond layer, and S_y is the yield strength of the layer in which the crack is growing. In another phase of this investigation, a tentative criterion for crack arrest by delamination at bond layers in laminates of alclad 6061-T6 is expressed as

$$\gamma \times r = 54.3 \tag{8}$$

when γ is expressed in MN/m^2 and r is in mm units ($\gamma \times r = 0.31$ when γ is expressed in ksi/μm and r is in inch units). This provides a design estimate of the likelihood of crack arrest.

In Specimen AT-2, the gradient from the 2024-T3 to the alclad is 2.8×10^7 MN/m^3 (4 ksi/μm) and the yield strength of the 2024-T3 is 310 MN/m^2 (45 ksi). Solving for r from Eq 8 gives 1.98 mm (0.078 in.) and solving for K from Eq 7 gives $K_{\max}$ of 34.5 MN/m$^{3/2}$ (31.5 ksi $\sqrt{\text{in.}}$) as the value that must be exceeded to cause crack arrest at the bond. The ΔK applied to Specimen AT-2 was 34 MN/m$^{3/2}$ (31 ksi$\sqrt{\text{in.}}$), but considering the compressive residual stress in the aluminum layer it is likely that the $K_{\max}$ is less than that. Hence, it is likely that the crack would not be arrested at this interface.

In Specimen AT-7 the gradient from the titanium layer to the alclad is 7.76×10^7 MN/m^3 (11.25 ksi/μm) and the yield strength is 924 MN/m^2 (134 ksi) for the Ti-6Al-4V in the explosive bonded condition. Equation 8 gives a value of 0.71 mm (0.028 in.) for r in the titanium and from Eq 7

the value of K_{max} for crack arrest is 61 MN/m$^{3/2}$ (56 ksi$\sqrt{in.}$) The ΔK applied to Specimen AT-7 was 58 MN/m$^{3/2}$ (53 ksi$\sqrt{in.}$), but considering the tensile residual stress in the titanium layer it is likely that the K_{max} is greater than that. Hence, it is likely that the crack would be arrested at the interface.

These approximations indicate that in these titanium-aluminum laminate beam specimens, the crack arrest criterion will be exceeded when the crack is in the 2024-T3 layer because of its lower yield strength and its smaller strength gradient to the alclad bond layer. It is important to realize that the stress intensity factor increases with the square root of crack depth under constant cyclic loading and therefore r in Eq 7 increases with crack depth. Hence in multilayer laminates, the product $\gamma \times r$ will exceed the criterion for crack arrest at one of the successive bond layers. It is inevitable, then, that the crack will be arrested at a bond layer by delamination if there are enough layers for this to occur, as long as the bond layer is weaker in tension than the structural layer. This means that McCartney et al [7] were correct in saying that interior cracks will be contained in the grid of bond layers in a laminated material. This aspect deserves further study.

The graph in Fig. 9 shows a solid line and data points giving the relation between the initial ΔK and the cycles to grow the crack 0.127 mm (0.005

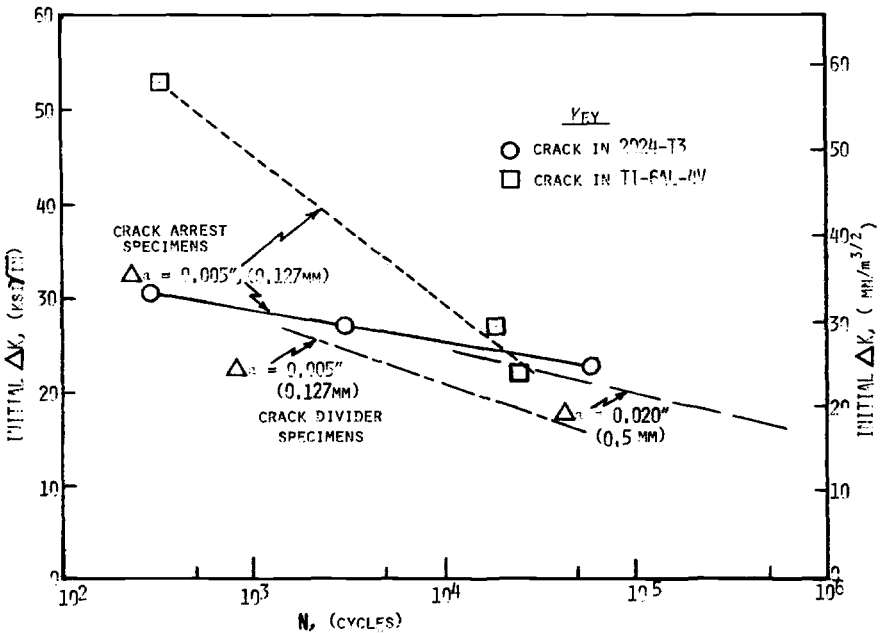

FIG. 9—*Fatigue cycles for given crack growth versus initial range of* K.

in.) in the aluminum layers of the crack arrest specimens. The dotted line shows the relationship for the same crack growth in the titanium layers. This steeper line indicates that a larger ΔK is required for a given crack growth in the Ti-6Al-4V layers. The greater resistance to crack propagation in the titanium layers can be attributed to its higher yield strength which, in spite of the tensile residual stress, results in smaller plastic zone size and slower crack rate than in the aluminum layers.

Also, the dashed lines in Fig. 9 pertain to the crack divider specimens for crack growth of 0.127 and 0.5 mm (0.005 and 0.020 in.). The graph shows that the ΔK which will produce 0.5 mm (0.020 in.) growth in the crack divider specimens at a given number of cycles will produce only 0.127 mm (0.005 in.) crack growth in the aluminum layers of the crack arrest specimens. This reduced rate in the aluminum layers can be attributed to the compressive residual stress.

Fracture Toughness

The results of the fracture toughness tests are listed as apparent fracture toughness in Table 3. The K_Q tests did not give valid K_{Ic} results, mainly because specimen thickness greater than 19 mm (3/4 in.) would be required. The values of K_{Ic} obtained from the J_{Ic} analysis of the data may be a more appropriate measure of the toughness for the crack arrest specimens. It is also recognized that the stress intensity factor for a homogeneous notched beam may be improper for a bimaterial laminate, especially for the crack arrest configuration. The values listed were computed as though the specimen were a homogeneous beam of the same dimensions and failure load and, therefore, are called "apparent fracture toughness."

Considering the K_{Ic} values from the J_{Ic} analysis to represent the fracture toughness of the laminate, the average for the crack divider configuration is 61.8 MN/m$^{3/2}$ (56.4 ksi$\sqrt{\text{in.}}$) while that for the crack arrest specimens failing in the titanium layer is 100.9 MN/m$^{3/2}$ (92.1 ksi$\sqrt{\text{in.}}$) and that for crack arrest specimens failing in the aluminum layer is 79 MN/m$^{3/2}$ (72 ksi$\sqrt{\text{in.}}$). These may be compared to published values of K_{Ic} of 51.5 MN/m$^{3/2}$ (47 ksi$\sqrt{\text{in.}}$) for 25.4 mm (1-in.) thick mill-annealed Ti-6Al-4V as shown by Lewis et al [*12*].

They may also be compared to a K_{Ic} of 29 MN/m$^{3/2}$ (26.5 ksi$\sqrt{\text{in.}}$) for 19 mm (3/4-in.) thick 2024-T3 and 17.5 MN/m$^{3/2}$ (16 ksi$\sqrt{\text{in.}}$) for the S-L, 21.9 MN/m$^{3/2}$ (20 ksi$\sqrt{\text{in.}}$) for the T-L and 25.2 MN/m$^{3/2}$ (23 ksi$\sqrt{\text{in.}}$) for the L-T orientations in 102 to 140-mm (4 to 5.5-in.) thick 2024-T851 plate as reported by Staley [*13*]. The test results demonstrate an improvement in fracture toughness as a result of the laminating. This is

compatible with the large increase in energy absorbing capacity shown by the Charpy impact test results for the crack arrest configuration.

Charpy Impact Results

The results of Charpy impact tests of standard notched specimens at room temperature and at −40°C (−40°F) are listed in Table 4. The average for the crack divider specimens is 14.4 Nm (10.6 ft/lb) at both temperatures. The overall average for the crack arrest specimens is 84.7 Nm (62.3 ft/lb), and the cold temperature results are no lower than the room temperature results. Some of the crack arrest specimens did not fracture completely in the test and are so marked. The results may be compared with 6.8 Nm (5 ft/lb) for the 2024-T3 alloy and with 20.4 Nm (15 ft/lb) for mill-annealed Ti-6Al-4V presented elsewhere [*14*].

Discussion

From the results presented in the preceding section, it appears that the interlaminar shear strength is more than sufficient to sustain the residual stresses and the addition of active bending stresses. This means that little

TABLE 4—*Charpy impact test results.*

Configuration	Specimen	C_V, −40°C		C_V, Room Temperature	
		ft·lb	Nm	ft·lb	Nm
Crack divider:	B2	11.0	15.0	11.3	15.4
	B4	11.1	15.1	11.1	15.1
	B6	10.0	13.6	9.6	13.1
	B7	10.6	14.4	10.2	13.9
	avg	10.7	14.5	10.6	14.4
Crack arrest: notch in the Ti-6Al-4V					
	A2T	...	...	45.0	61.2
	A4T [a]	...	...	75.4	102.5
	A6T	52.5	71.4	...	...
	A7T	71.0	96.6	...	...
	avg	61.8	84.0	60.2	81.9
Crack arrest: notch in the 2024-T3					
	A2A [a]	...	...	70.0	95.2
	A4A	...	...	40.8	55.5
	A6A [a]	69.6	94.6	...	...
	A7A [a]	74.4	101.2	...	...
	avg	72.0	97.9	55.4	75.4

NOTE—Crack arrest: overall average=62.3 ft·lb (84.7 Nm).

[a] Specimens so marked did not fracture completely.

difficulty should be experienced from edge delamination except in the straightening process that is required for a large number of layers. It is now believed that a heat treatment for stress relieving the titanium and solution treating the aluminum can be used periodically during bonding and straightening to avoid some of the problems encountered in those steps.

Despite those problems, the residual stresses developed in the laminate are assets that improve the fatigue performance over those of the component alloys by raising the threshold for fatigue crack propagation and reducing the crack propagation rate. The interfaces at the alclad bond layers also provide fatigue crack retardation and crack arrest, and they absorb energy in delamination under either cyclic or impact loading. The laminate appears, therefore, to be a good candidate for a damage tolerant material for aircraft and helicopter structures. At present the cost of production limits its consideration to very critical components where the particular attributes of the laminate can be exploited to an advantage.

Conclusions

1. Explosive bonding of alternate sheets of mill-annealed Ti-6Al-4V and alclad 2024-T3 produces a laminate in which the fatigue crack rates, fracture toughness, and impact resistance are superior to those of the component alloys.
2. The ductile bond layers in this laminate absorb energy in fatigue and impact and result in crack arrest and progressive delamination.
3. The explosive bonding process produces residual stresses that are favorable to improved fatigue and fracture resistance. Compressive residual stress in the 2024-T3 layers increases the threshold for fatigue crack propagation and reduces the fatigue crack propagation rate.
4. Optimization of geometry and residual stress state can produce a fatigue and fracture resistant damage-tolerant laminate for critical structural applications.

Acknowledgments

We express our appreciation to R. T. Abbott for his work in testing and data analysis, C. Albrecht for special machining operations, Mrs. T. Brassard for microhardness measurements, K. Loomis for X-ray stress evaluation, and Miss E. Fogarty for typing this manuscript. We also appreciate the counseling and assistance of T. E. Davidson and others of his staff. This work was performed under funding from the Army Air Mobility Research and Development Laboratory, Moffett Field, Calif.

References

[1] Throop, J. F. and Miller, J. J., "Fatigue Behavior of Metal Laminates," *1974 Army Science Conference Proceedings*, Vol. III, AD785672, also Watervliet Arsenal Technical Report WVT-TR-75035, June 1975.

[2] Embury, J. D., Petch, N. J., Wraith, A. E., and Wright, E. S., *Transactions*, American Institute of Mining, Metallurgical, and Petroleum Engineers, Vol. 239, Jan. 1967, pp. 114-118.

[3] Almond, E. A., Embury, J. D., and Wright, E. S. in *Interfaces in Composites, ASTM STP 452*, American Society for Testing and Materials, 1969 pp. 107-129.

[4] Almond, E. A., Petch, N. J., Wraith, A. E., and Wright, E. S., *Journal of the Iron and Steel Institute*, Oct. 1969, pp. 1319-1323.

[5] Cook, J. and Gordon, J. E., *Proceedings*, Royal Society of London, Vol. 282A, 1964, pp. 508-520.

[6] Pattee, H. E. and Linse, V. D., "Explosive Welding of Laminated Specimens," Final Report to Watervliet Arsenal, Battelle Columbus Labs, 28 June 1976.

[7] McCartney, R. F., Richard, R. C., and Trozzo, P. S., *Transactions*, American Society for Metals, Vol. 60, 1967, pp. 384-394.

[8] Capsimalis, G., Haggerty, R. F., and Loomis, K., "Computer Controlled X-Ray Stress Analysis for Inspection of Manufactured Components," Watervliet Arsenal Technical Report WVT-TR-77001, 1977.

[9] Trathen, R. H. in *Statics and Strength of Materials*, Wiley, New York, 1954, pp. 284-293.

[10] Wygonik, R. H. in *Damage Tolerant Materials Handbook*, Battelle Columbus Labs, 1975, p. 8-1-20 (9/73).

[11] Harrigan, M. J. in *Damage Tolerant Materials Handbook*, Battelle Columbus Labs, 1975 p. 8.4-7 (12/72) and 8.4-8 (1/75).

[12] Lewis, R. E., Bjeletich, J. G., Morton, T. M., and Crossley, F. A. in *Cracks and Fracture, ASTM STP 601*, American Society for Testing and Materials, 1976, pp. 371-390.

[13] Staley, J. T. in *Properties Related to Fracture Toughness, ASTM STP 605*, American Society for Testing and Materials, pp. 71-103.

[14] *Aerospace Structural Metals Handbook*, J. Wolf and W. F. Brown, Eds., Mechanical Properties Data Center, Belfour Stulen, Inc., 1972, Code 3203 and Code 3707.

R. L. Tobler [1]

Low Temperature Fracture Behavior of a Ti-6Al-4V Alloy and Its Electron Beam Welds

REFERENCE: Tobler, R. L., **"Low Temperature Fracture Behavior of a Ti-6Al-4V Alloy and Its Electron Beam Welds,"** *Toughness and Fracture Behavior of Titanium, ASTM STP 651,* American Society for Testing and Materials, 1978, pp. 267–294.

ABSTRACT: The effects of electron beam welding on the fracture behavior of a recrystallization annealed, extra-low-interstitial Ti-6Al-4V alloy have been investigated at temperatures in the ambient-to-cryogenic range. Plane strain fracture toughness (K_{Ic}) and subcritical crack growth parameters were measured using compact specimens 10 to 25.4 mm thick. These parameters can be used to predict the safe operating lifetimes of cryogenic pressure vessels and other welded Ti-6Al-4V structures.

At intermediate stress intensity factors and within the data scatter for replicate tests, the growth rates of fatigue cracks sited in the fusion and heat-affected zones of electron beam weldments were temperature insensitive and nearly equivalent to rates for the base metal. However, electron beam welding introduced a zone of low fracture toughness at the heat-affected-zone/fusion-zone boundary. The K_{Ic} value for this boundary zone at liquid nitrogen temperature (76 K) was 51 MPa/m$^{1/2}$, 16 percent lower than the base metal. The base metal fracture toughness increases between 4 and 295 K, with an abrupt transition to higher K_{Ic} values occurring at temperatures between 76 and 125 K. Static load cracking, temperature effects, and specimen orientation effects on the fracture behavior of this titanium alloy are central topics of discussion.

KEY WORDS: titanium, electron beam welding, fatigue (materials), fracture properties, low temperature tests, mechanical properties, titanium alloys

Favored for their high strength-to-weight ratios, Ti-6Al-4V alloys have become the principal construction materials for cryogenic pressure vessels in aerospace electrical, propulsion, and reaction control systems [*1*].[2] Such

[1] Cryogenics Division, Institute for Basic Standards, National Bureau of Standards, Boulder, Colo. 80302.

[2] The italic numbers in brackets refer to the list of references appended to this paper.

Copyright© 1978 by ASTM International www.astm.org

pressure vessels are designed using low safety factors (~ 1.5), and they may experience service temperatures as low as 20 K (−423°F). Typically, spherical vessels are constructed by welding hemispherical forgings.

Although welding is essential in fabricating these components, weld zones represent a potential source of flaws. Microcracking or porosity may occur during weld metal solidification, and heat conducted to the base metal may induce microstructural transformations with resultant mechanical property degradation. In the case of Ti-6Al-4V alloys, low ductility and toughness in gas metal-arc or gas tungsten-arc welds derive from oxygen and nitrogen contamination [*2*]. Thicker sections are necessary to guarantee structural reliability if the weld mechanical properties undermatch those of the base metal.

Disregarding its high cost, electron beam welding offers significant technical advantages compared to arc welding. The kinetic energy of high velocity electrons converts to intense heat upon collision with the structural component. The highly localized heating produces narrow, moderately tapered, deeply penetrating fusion zones. Consequently, factors such as distortion, residual stress, total heat input, and heat-affected zone (HAZ) sizes are minimized. Also, electron beam welding is performed in vacuum, reducing the possibility of contamination by impurities [*3*].

Room temperature tensile and fatigue data for Ti-6Al-4V electron beam welds in 25.4 to 50.8 mm thicknesses are available, but most results decribe unflawed specimen behavior [*4, 5*]. Fracture mechanics parameters are now needed to predict the low temperature performance of large structures which cannot be guaranteed to be flawless. Such data for an extra-low-interstitial (ELI) Ti-6Al-4V alloy in the recrystallization annealed condition are presented here. Fracture toughness (K_{Ic}), fatigue crack rate (da/dN), and static load cracking parameters are reported for the unwelded and the electron beam welded alloy, at selected temperatures between 295 and 4 K (70 and −453°F).

Material and Specimen Preparation

Material

The ELI Ti-6Al-4V alloy stock was received in the form of a 1-m-diameter hemisphere with a 51-mm wall thickness. The hemisphere had been recrystallization annealed at 1200 K (1700°F) for 4 h, furnace cooled to 1033 K (1400°F) in 3 h, cooled to 756 (900°F) in 3/4 h, and air cooled to room temperature. Table 1 lists the chemical analysis. The tensile and elastic properties at room and liquid nitrogen temperatures

TABLE 1—*Mill analysis (in weight percent) ELI, recrystallization annealed Ti-6Al-4V.*

Ti	Al	V	Fe	O	C	N	H
Bal	5.91	3.94	0.103	0.110	0.018	0.014	52 ppm

were measured using established techniques [*6-8*], and the results are shown in Table 2. Some fracture mechanics data were previously reported for this same heat of material [*8*].

Electron Beam Welds

Several pairs of arc-shaped bars were machined from stock and electron beam welded. Most of these bars were 90 cm in arc length and 3.8 by 5.1 cm in cross-sectional area. Two bars having 18 by 5-cm cross-sectional areas were also welded, but the larger integral heat sink offered by this geometry apparently did not affect the fracture properties.

The double-rabbeted, self-backing, self-aligning, square-groove joint used for these welds is shown in Fig. 1(*a*). The specimens were chemically cleaned and then mounted between aluminum chill plates in a rotary indexing fixture. Circumferential welding was accomplished in vacuum at 4×10^{-2} Pa (3×10^{-4} torr), using tack, penetration, and cosmetic passes. The specimens were rotated under a vertical electron beam, at a gun-to-work distance of 32.4 cm. Other machine settings, determined from trial runs on scrap pieces, are listed in Table 3. The completed welds were annealed in air at 811 K (1000°F) for 50 h, simulating a stress-relief heat treatment that is applied to welded pressure vessels.

Figure 1(*b*) and (*c*) illustrate an etched weld cross section, and a compact specimen of the ML orientation (discussed next). The fracture specimens were machined such that the flawed seam at the weld root (which is typical for this type of joint preparation) was removed by notching. Based on commercial ultrasonic inspections and metallographic evidence, these laboratory specimens are representative of production quality electron beam welds.

Specimens

The compact specimen was chosen because it offered a high K_{Ic} measurement capability for its size, and a geometry compatible with that of the welded stock. This specimen is described in the ASTM Test for Plane-Strain Fracture Toughness of Metallic Materials (ASTM E 399-74). Specimen thicknesses, B, ranged from 10 to 25.4 mm, and width, W, ranged

TABLE 2—*Mechanical properies of ELI recrystallization-annealed Ti-6Al-4V alloy.*

Temperature, K (°F)	0.2% Yield Strength MPa	(ksi)	Ultimate Strength MPa	(ksi)	Elongation, %	Reduction in Area, %	Young's Modulus GPa (10^6 psi)	Poisson's Ratio
295 (70)	830	(120.5)	890	(129.1)	14.0	41.2	1.11 (16.1)	0.323
76 (−323)	1363	(197.7)	1429	(207.3)	9.6	16.4	1.21 (17.5)	0.310

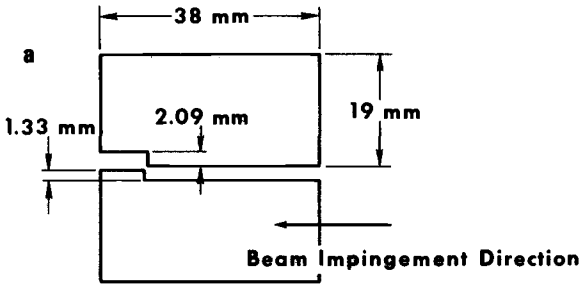

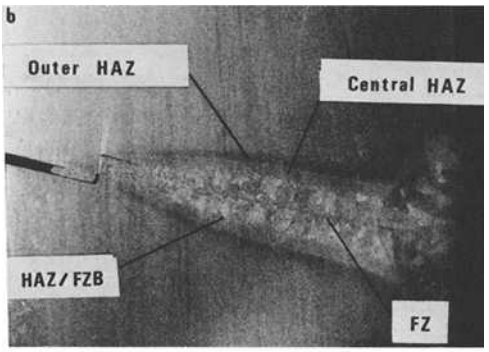

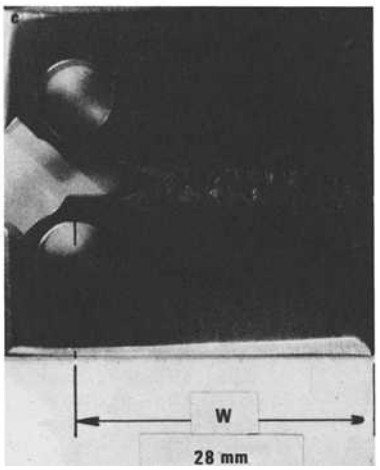

FIG. 1—*Electron beam weld joint preparation* (a), *the cross section of a completed weld* (b), *and a compact specimen of the ML orientation* (c).

TABLE 3—*Electron beam welding variables.*

Operation	Accelerating Voltage, kV	Beam Current, mA	Focus	Travel Speed, mm/s (in./s)
Tack pass	115	15	sharp	4.8 (0.189)
Penetration pass [a]	150	45	sharp	4.8 (0.189)
Cosmetic pass [a]	120	25	sharp, +100	3.5 (0.138)

[a] Using two complete revolutions (720 deg) of the specimen.

from 28 to 50.8 m. The W/B ratio was 2, except as noted in the text. Without exception, the planar specimen dimensions were proportional to W, as per ASTM Method E 399-74, and knife edges for clip gage retention were machined integral to the notch. The knife edges were located at the specimen edge, and not at the loadline as in previous work [*8*].

Orientation

Reference axes for specimen orientation are defined in Fig. 2. The letter R represents the radial direction of the original forging, while M and L represent circumferential (meridional and latitudinal) directions. Base metal specimens were machined in as many as six orientations, designated

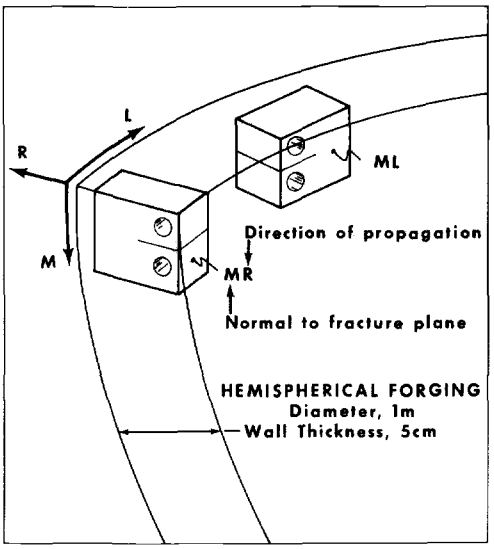

FIG. 2—*Notation for reference axes and specimen orientations.*

RL, LR, RM, MR, LM, or ML. The first letter of each designation identifies the direction normal to the fracture plane, and the second letter identifies the direction of crack propagation. Weld specimens were tested only in MR and ML orientations where the cracks propagate radially or equatorially.

Microstructure

The recrystallization annealed base metal microstructure of primary α and intergranular β (or transformed β phase) is shown in Fig. 3. Although nearly equiaxed, the microstructure viewed along the R axis is distinguishable from those of the M and L axes. The latter microstructures are equivalent, having an average primary α grain diameter of approximately 0.013 mm.

A microstructural traverse of the weld is shown in Fig. 4. At distances 4 mm or greater from the fusion zone centerline, the base metal microstructure is unaltered by welding. The outer HAZ (3 to 3.5 mm from the fusion line) etches darkly, while the center of the HAZ shows primary α in a highly permutated matrix. The HAZ/fusion-zone boundary structure is aged acicular α, and the fusion zone is aged martensitic α.

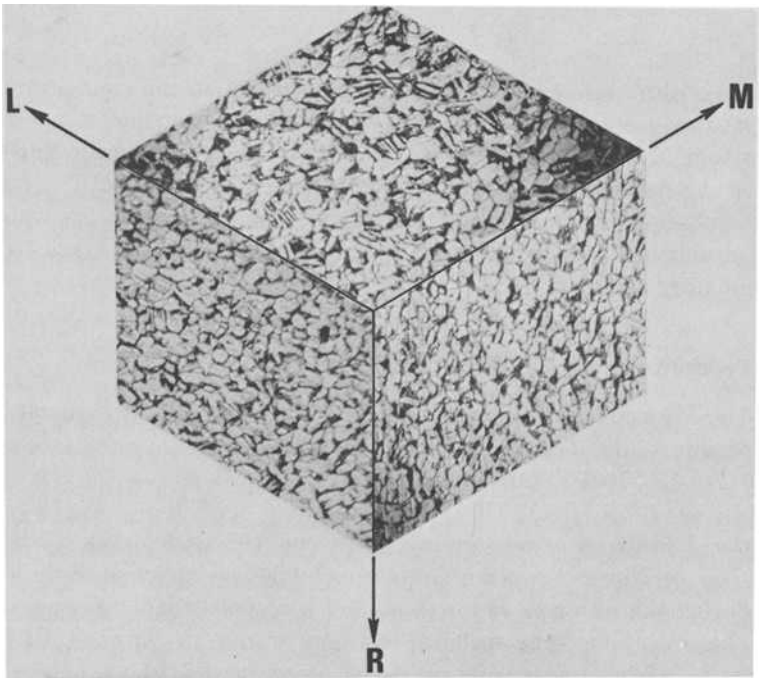

FIG. 3—*Recrystallization annealed base metal microstructure,* $\times 170$.

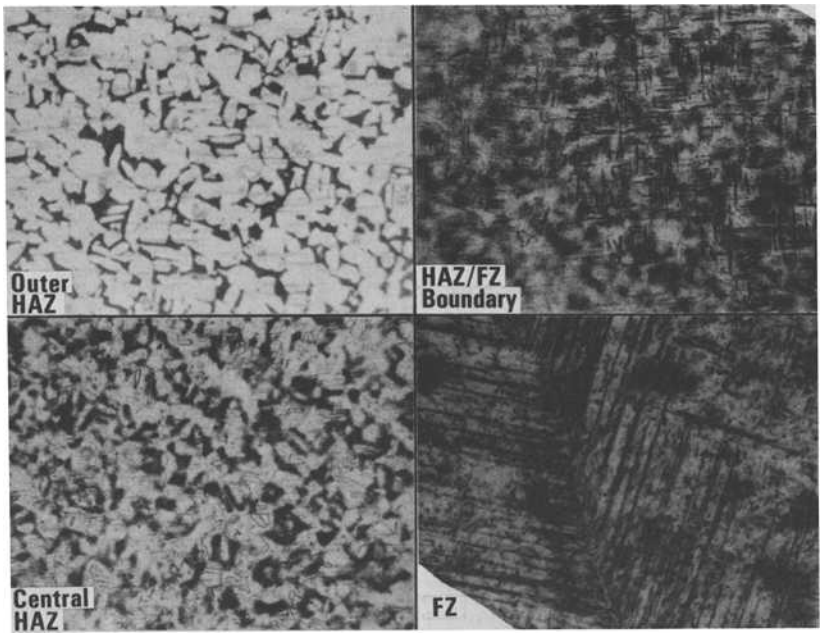

FIG. 4—*Electron beam weld microstructures,* $\times 170$.

Three critical weld locations were tested: (*a*) the fusion zone centerline, FZ, (*b*) the center of the HAZ, and (*c*) the macroscopically visible HAZ/fusion-zone boundary, HAZ/FZB. Notches parallel to the fusion line were sited in the desired zones, after etching each specimen blank. The fatigue cracks subsequently propagated parallel to the notch plane, to within 3 deg. No difficulty was encountered in maintaining the fatigue cracks within their intended zones.

Test Procedure

A 100-kN capacity servohydraulic testing machine and cryostat were used in this study. Test environments included unconditioned laboratory air at 295 K (70°F), ethanol and dry ice at 195 K (−108°F), liquid nitrogen at 76 K (−323°F), liquid helium at 4 K (−453°F), and evaporated nitrogen at temperatures between 195 and 108 K (108 and −200°F). A chromel-constantan thermocouple was attached to the specimen during the nitrogen vapor tests, and a servomechanical temperature controller maintained the specified test temperature to within ±3 K. The apparatus and techniques were previously described [*8, 9*].

Fracture Toughness

The fracture toughness specimens were precracked at their K_{Ic} test temperatures and fractured at a stress intensity factor increase rate of approximately 1 MPa/m$^{1/2}$/s. The critical stress intensity factors were calculated according to ASTM Method E 399-74. In most cases the linear-elastic test criteria were satisfied. However, the room temperature specimens consistently failed to meet the thickness requirement

$$B \geq 2.5\ (K_Q/\sigma_{ys})^2 \tag{1}$$

where σ_{ys} is the uniaxial yield strength of the material, and K_Q is the conditonal fracture toughness. Nonlinear behavior at room temperature proved unavoidable, because specimens of a thickness meeting Eq 1 could not be manufactured from the available stock. For this reason, J-integral tests were previously applied in estimating a room temperautre K_{Ic} for the base metal [*8*].

Fatigue Crack Growth

Considerable amounts of fatigue crack growth data were obtained during the precracking of fracture toughness specimens where the maximum fatigue stress intensity factor did not exceed 34 MPa/m$^{1/2}$. Additional specimens were tested at 295 and 76 K, solely for fatigue crack growth rates at higher stress intensity factors. All fatigue tests were conducted under controlled load, using a sinusoidal load cycle at frequencies, F, from 10 to 30 Hz. The ratio, R, of minimum/maximum load was 0.1. A digital indicator was used to monitor continuously the peak loads, which were accurate to ± 2 percent of the specified values.

Fatigue crack growth was monitored by measurements of deflection per unit load (δ/P). Correlations between average crack length and δ/P were obtained experimentally, following previous techniques [*8*]. Changes in clip gage sensitivity and Young's modulus with temperature were accounted for by plotting the base metal data versus $EB\delta/P$, or by shifting the weld specimen room temperature calibration curves [*9*]. The crack growth rate measurement procedure then involved recording δ versus P periodically duing fatigue. Crack length, a, was inferred from the empirical correlations and plotted versus cycles, N. Computer programs were used to fit the a-versus-N curves with third-order polynomials, to differentiate the curves for da/dN data, and to calculate the corresponding stress intensity factor ranges, ΔK, from the peak fatigue stress intensity factors ($\Delta K = K_{max} - K_{min}$).

Static Load Cracking

A series of specimens were sustained in inert environments at constant load to determine whether time-dependent crack growth culminating in fracture could occur. These base metal ($B=25.4$ mm) and weld specimens ($B=10$ mm, $W/B=2.75$) were precracked as for K_{Ic} testing, and then loaded within 15 s to a specified stress intensity factor. Most specimens were instrumented with a clip gage so that cracking could be monitored by deflection measurements.

For the base metal specimens, meaningful static load cracking rates were measured by unloading after moderate crack extensions of no more than 2 mm. The procedure involved: (*a*) sustaining the specimens at constant load for hold times, Δt, ranging from 15 to 10^5 s, (*b*) unloading and heat-tinting the specimens to oxidize their crack surfaces, and (*c*) fracturing the specimens into halves to measure the crack extension. Tinting was accomplished by heating with an acetylene torch. After specimen fracture, increments of static load crack extension were identifiable as straw-blue oxidized areas located between the fatigue crack and the untinted ligament.

An average crack extension, Δa, was obtained from three measurements with a traveling microscope at 25, 50, and 75 percent of specimen thickness. The cracking rate, $\Delta a/\Delta t$, was then calculated and plotted versus the nominal value of K at the initial crack length and static load. For compact specimens, K increases continuously with crack extension under constant load so the $\Delta a/\Delta t$-versus-K relationships are only approximate. However, the calculations were performed for Δa values from 1 to 2 mm, and differences between the initial and final K values were not greater than 5 percent.

Results

Fracture Toughness

Tables 4 through 7 list the fracture toughness results at each temperature, along with notes relating to validity requirements. In several cases, a/W exceeded 0.55. Although this deviates from the ASTM Method E 399-74 specifications, the K_Q results were not always in disagreement with valid K_{Ic} data, as indicated by the results at 76 K. This near equivalence is indicated in the tables by the statement $K_Q \cong K_{Ic}$.

The base metal fracture toughness results are plotted in Fig. 5, along with previous data for the LR orientation, which includes a room temperature K_{Ic} estimate derived by J-integral tests [*8*]. The ML and LR orientations exhibit a similar temperature dependence. At temperatures between 295 and 125 K, K_{Ic} remains at relatively high shelf levels. Then, a 33 to 45 percent decrease of K_{Ic} occurs on cooling between 125 and 76 K.

TABLE 4—*Fracture toughness of Ti-6Al-4V base metal specimens in the ML orientation.*
(Specimen thickness B=*20.3 at* T=*76 K;* B=*25.4 at T > 76 K).*

Temperature, K	(°F)	Specimen Number	a/W	$2.5(K_Q/\sigma_{ys})^2$, mm	K_Q, MPa/m$^{1/2}$	K_{Ic}, MPa/m$^{1/2}$	K_{Ic}, ksi/in.$^{1/2}$
295	(70)	2	0.500	30	91.4	$K_Q \neq K_{Ic}$	
		3	0.525		84.7	$K_Q \neq K_{Ic}$	
		63	0.570		94.0	$K_Q \neq K_{Ic}$	
		67	0.655		93.9	$K_Q \neq K_{Ic}$	
195	(−109)	57	0.555	19	$K_Q \cong K_{Ic}$	91.4	83.1
		69	0.530		$K_Q = K_{Ic}$	87.5	79.6
176	(−143)	60	0.515	19	$K_Q = K_{Ic}$	95.6	87.0
130	(−226)	4	0.575	16	$K_Q \cong K_{Ic}$	86.4	78.6
		53	0.565		$K_Q \cong K_{Ic}$	95.6	87.0
		50	0.535		$K_Q = K_{Ic}$	95.6	87.0
108	(−266)	58	0.540	14	$K_Q = K_{Ic}$	85.6	77.9
76	(−323)	5	0.480	5	$K_Q = K_{Ic}$	65.0	59.1
		7	0.515		$K_Q = K_{Ic}$	60.8	55.3
		10	0.555		$K_Q \cong K_{Ic}$	65.6	59.7

On further temperature reductions to 4 K, the data for the LR orientation indicate only a slight decline of K_{Ic}. Thus, the recrystallization annealed and furnace cooled Ti-6Al-4V alloy exhibits a fracture transition at low temperatures which resembles the classical fracture transitions of other metals and alloys having body-centered cubic (bcc) or hexagonal crystal

TABLE 5—*Fracture toughness of Ti-6Al-4V base metal at 76 K as a function of orientation.*
(Specimen thickness, B,=*20.3 to 25.4 mm).*

Specimen Number	Orientation	a/W	K_Q, MPa/m$^{1/2}$	K_{Ic}, MPa/m$^{1/2}$	K_{Ic}, ksi/in.$^{1/2}$
5	ML	0.480	$K_Q = K_{Ic}$	65.0	59.1
7	ML	0.515	$K_Q = K_{Ic}$	60.8	55.3
10	ML	0.555	$K_Q \neq K_{Ic}$	65.6	59.7
40	MR	0.550	$K_Q = K_{Ic}$	65.3	59.4
36	MR	0.520	$K_Q = K_{Ic}$	61.7	56.1
48	MR	0.490	$K_Q = K_{Ic}$	59.1	53.8
31	LR [a]	0.515	$K_Q = K_{Ic}$	60.9	55.4
35	LR	0.500	$K_Q = K_{Ic}$	59.9	54.5
41	LR	0.520	$K_Q = K_{Ic}$	56.0	51.0
32	LM	0.530	$K_Q = K_{Ic}$	61.3	55.8
34	LM	0.540	$K_Q = K_{Ic}$	59.9	54.5
42	RM	0.525	$K_Q = K_{Ic}$	58.3	53.0
39	RM	0.515	$K_Q = K_{Ic}$	65.9	60.0
38	RL	0.625	$K_Q \cong K_{Ic}$	57.4	52.2
37	RL	0.525	$K_Q = K_{Ic}$	54.6	49.7

[a] Four additional specimens of the LR orientation were tested in Ref *8*.

TABLE 6—*Effect of thermal-mechanical treatments on the fracture toughness of Ti-6Al-4V (ELI) base metal.*

Treatment Prior to Test	Test Temperature, K	Test Temperature, (°F)	Specimen Number	Orientation	Thickness, mm	K_{Ic}, MPa/m$^{1/2}$	K_{Ic}, ksi/in.$^{1/2}$
SRA [a]: 533 K (500°F), 50 h	76	(−323)	11	MR	20.3	58.0	52.8
			12	MR	20.3	67.6	61.5
SRA: 811 K (1000°F), 50 h	76	(−323)	13	ML	25.4	60.9	55.4
			14	ML	25.4	65.4	59.5
Prestrained in biaxial tension (see text)	295	(70)	11	ML	15.7	52.0	47.3
			22	LM	15.7	55.1	50.1
	76	(−323)	33	ML	15.7	51.2	46.6
			44	LM	15.7	51.6	47.0

[a] Simulated stress-relief anneal, conducted in air.

TABLE 7—*Fracture toughness of stress-relief annealed Ti-6Al-4V electron beam welds.*

Location	Temperature, K	Temperature, (°F)	Specimen Number	Thickness, mm	a/W	Orientation	$2.5(K_Q/\sigma_{ys})^2$, mm	K_Q, MPa/m$^{1/2}$	K_{Ic}, MPa/m$^{1/2}$	K_{Ic}, ksi/in.$^{1/2}$
Fusion Zone (FZ)	295	(70)	7	14.0	0.520	MR	22	76.8	$K_Q \neq K_{Ic}$	
			8	14.0	0.470	MR		78.5		
	76	(−323)	2	14.0	0.475	MR	4	$K_Q = K_{Ic}$	59.1	57.8
			3	14.0	0.505	MR		$K_Q = K_{Ic}$	64.9	59.1
			4	14.0	0.515	MR		$K_Q = K_{Ic}$	55.0	50.0
			10	10.1	0.475	ML	4	$K_Q = K_{Ic}$	55.3	50.3
			55	14.0	0.470	ML		$K_Q = K_{Ic}$	61.4	55.9
			77	14.0	0.475	ML		$K_Q = K_{Ic}$	55.1	50.1
			88	14.0	0.560	ML		$K_Q \cong K_{Ic}$	56.3	51.2
Heat-affected zone (HAZ)	295	(70)	20	15.2	0.500	MR	23	83.7	$K_Q \neq K_{Ic}$	
			22	15.2	0.600	MR		81.8	$K_Q \neq K_{Ic}$	
			23	15.2	0.465	MR		72.4	$K_Q \neq K_{Ic}$	
	76	(−323)	25	15.2	0.535	MR	4	$K_Q = K_{Ic}$	58.2	53.0
			26	15.2	0.420	MR		$K_Q = K_{Ic}$	57.6	52.4
			27	15.2	0.490	MR		$K_Q = K_{Ic}$	55.7	50.7
HAZ/FZ boundary (HAZB)	295	(70)	4	10.1	0.595	MR	16	63.7	$K_Q \neq K_{Ic}$	
			1	10.1	0.560	MR		70.3	$K_Q \neq K_{Ic}$	
	76	(−323)	7	10.1	0.485	MR	3	$K_Q = K_{Ic}$	53.1	48.3
			9	10.1	0.435	MR		$K_Q = K_{Ic}$	52.3	47.6
			12	10.1	0.495	MR		$K_Q = K_{Ic}$	47.5	43.2

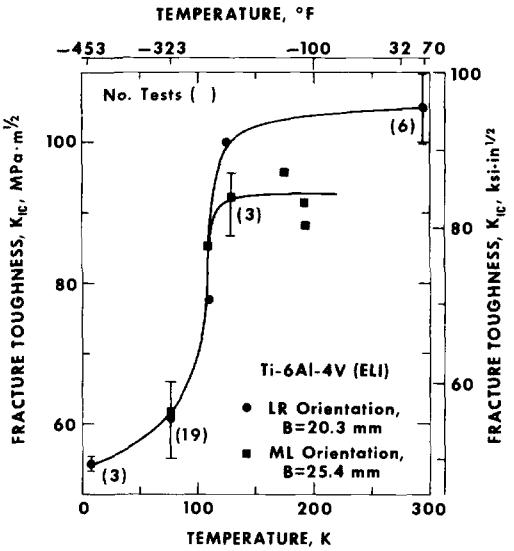

FIG. 5—*Temperature dependence of* K_{Ic} *for the base metal, indicating transitional behavior at 76 K≤T≤125 K.*

structures. The abrupt decrease of K_{Ic} in the interval 76 K $< T <$ 125 K suggests that a change in the fracture micromode may have occurred, but there was no attempt to verify this fractographically.

Some anisotropy in the base metal fracture toughness is evident at temperatures above the transition region. The shelf K_{Ic} values for the LR orientation range from 100 to 110 MPa/m$^{1/2}$, about 15 percent greater than shelf values for the ML orientation. However, orientation effects become immeasurable at lower temperatures. Data for six orientations at 76 K are listed in Table 5 and bracketed in Fig. 5. At this temperature, orientation effects are indistinguishable from the scatter of replicate tests, although it may be significant to note that the RL orientation yielded two of the lowest K_{Ic} values. Neglecting any minor effects, the 19 results for the base metal at 76 K can be statistically described: the K_{Ic} values range between 54.6 and 65.9 MPa/m$^{1/2}$, the mean value is 60.8 MPa/m$^{1/2}$, and the standard deviation is 3.0.

Other results in Table 6 show that stress-relief heat treatments such as applied to welded structures (533 or 811 K, 50 h, air cool) do not lower the base metal fracture toughness. However, extensive prestraining at room temperature can reduce the toughness of this Ti-6Al-4V alloy by as much as 50 percent, while virtually eliminating the temperature dependence of K_{Ic} over the ambient-to-cryogenic range. The data shown for the prestrained condition (Table 6, Fig. 6) represent specimens taken from sections of a fractured burst tank that was destructively tested at room tem-

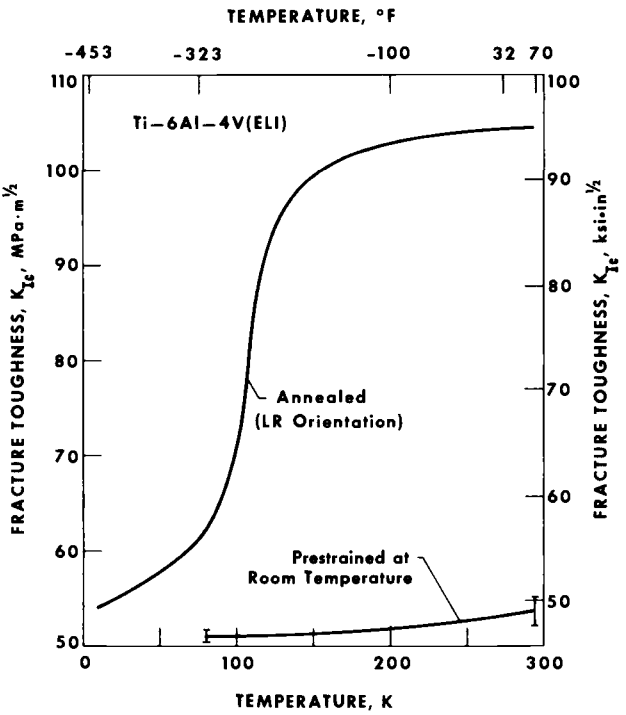

FIG. 6—*Effect of a room temperature prestrain in biaxial tension on the fracture toughness of the base metal.*

perature [*10*]. This tank exhibited a sizable volumetric expansion prior to fracture, and postmortem tension tests confirmed that the material was strain-hardened [*11*]. The exact amount of prestrain is unknown, but the K_{Ic} data obtained are valid according to the ASTM Method E 399-74 criteria.

Electron beam welding also reduces the fracture toughness of this titanium alloy. The weld data are listed in Table 7, and the average K_Q and K_{Ic} values at 295 and 76 K are compared in Fig. 7. The results show that the fusion zone and HAZs of welds at 76 K are nearly equivalent in toughness, with K_{Ic} averaging only 4 to 6 percent lower than the 60.8 MPa/m$^{1/2}$ average value for the base metal. However, the region of minimum toughness is located at the HAZ/FZB. There, K_{Ic} for three specimens at 76 K ranged from 47.5 to 53.1 MPa/m$^{1/2}$, averaging 16 percent lower than the unwelded base metal.

Fatigue Crack Growth Rates

Fatigue crack growth rates for the base metal at 295, 195, 76 and 4 K are shown in Figs. 8 and 9. These data were obtained for the LR and ML

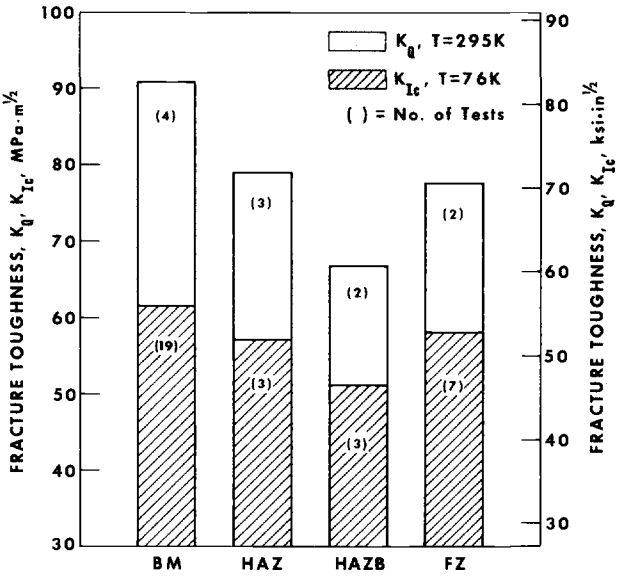

FIG. 7—*Average fracture toughness as a function of crack location in the Ti-6Al-4V base metal and its electron beam welds.*

orientations, as noted. Additional data for RL, LM, MR and RM orientations were also obtained at 76 K, during the precracking of K_{Ic} specimens. These additional data, obtained at ΔK values between 22 and 32 MPa/m$^{1/2}$, also fall within the scatterbands of Figs. 8 and 9. A comparison of all results reveals no measurable specimen orientation or temperature effects over the intermediate range of ΔK investigated.

Fatigue crack growth rates in electron beam welds were measured at 295 and 76 K. Figures 10 and 11 show the data obtained for FZ, HAZ, and HAZ/FZB specimens (ML and MR orientations). For a considerable portion of the ΔK ranges investigated, temperature effects are indistinguishable from the scatter observed in replicate tests. However, for ΔK greater than 30 MPa/m$^{1/2}$, the FZ and HAZ rates at 76 K appear to be somewhat faster than the bulk of results at 295 K. Stronger conclusions are not justified in view of the data scatter, and the restricted range of ΔK investigated for the HAZ/FZ boundary.

The scatterbands of Figs. 8 through 11 are superimposed for comparison in Fig. 12. The unshaded band represents the unwelded base metal results of Figs. 8 and 9 combined. The weld zone scatterbands nearly coincide with the base metal band. Therefore, despite the extensive microstructural transformations that are introduced, it appears that electron beam welding did not lead to measurable effects on the fatigue crack growth resistance of this alloy. The fatigue crack growth rates appear to be structure insensitive

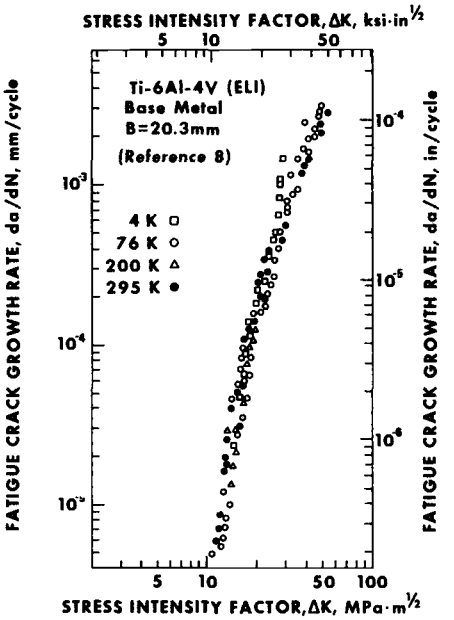

FIG. 8—*Fatigue crack growth rates for base metal specimens of the LR orientation* [8].

over a considerable range of intermediate ΔK values. Nevertheless, it is quite possible that minor effects due to microstructure are being masked by the data scatter in this study. Scatter for each of the base metal and weld zones corresponds to about a 2.5:1 uncertainty on the value of da/dN at a given ΔK value. Such uncertainty is reported to be typical for the present state of the art of da/dN testing [*12*].

Static Load Cracking

Several aspects of static load cracking in the base metal are illustrated by the test record and fracture surface of Fig. 13. The deflection at constant load reflects time-dependent crack extension which is most pronounced at the center of the specimen thickness (approximate plane strain conditions). Crack extension at the specimen edges (plane stress conditions) is retarded. Judging from the rate of increase of deflection, cracking in the base metal began without delay; that is, no incubation periods were observed in base metal tests at 295, 195, or 130 K. In two tests at 295 K, cracking led to complete fracture when the initial load was maintained indefinitely. This cracking process begins at stress intensity factors well below the "critical" levels associated with P_Q or the maximum loads of fracture test records.

The base metal cracking rates are highly sensitive to the applied stress

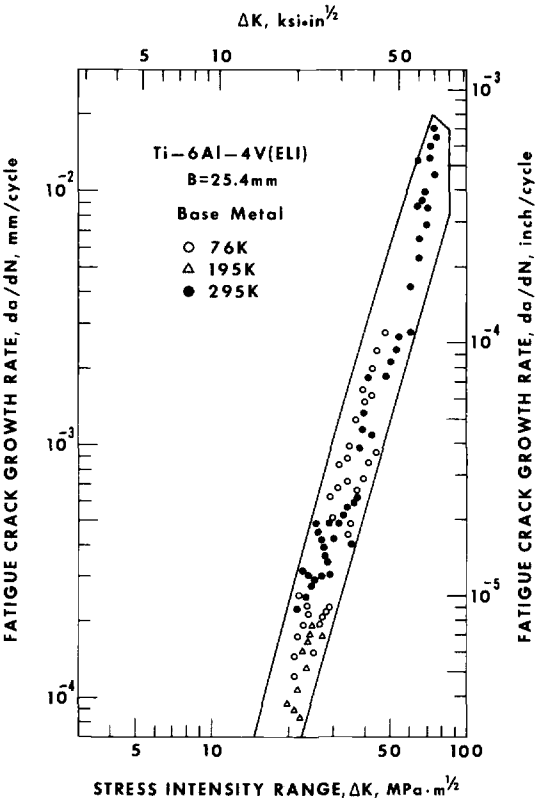

FIG. 9—*Fatigue crack growth rates for base metal specimens, primarily of the ML orientation.*

intensity factor. The rates can be described as power law functions of K, having the form

$$\frac{\Delta a}{\Delta t} = B(K)^m \tag{2}$$

Appropriate values for the parameters B and m were graphically determined from Fig. 13, using SI units. At room temperature,

$$\frac{\Delta a}{\Delta t} = 1.9 \times 10^{-56} (K)^{27} \tag{3}$$

and, at 195 K

$$\frac{\Delta a}{\Delta t} = 4.3 \times 10^{-72} (K)^{36} \tag{4}$$

As shown in Fig. 13, the rates at 195 K exhibit less scatter and are faster

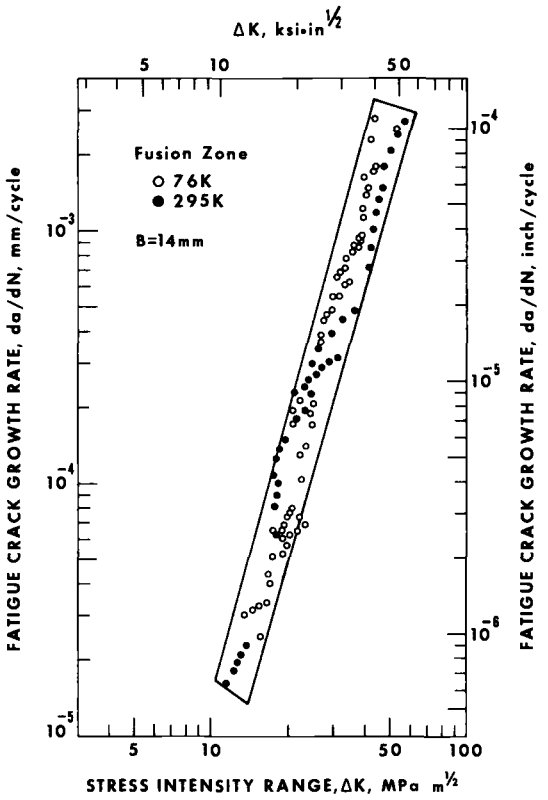

FIG. 10—*Fatigue crack growth rates for electron beam weld fusion zone specimens of the MR orientation.*

than those at room temperature. To demonstrate that these effects are not due to stress corrosion cracking, the chemistry of the environment was alternated. The cracking rates for two specimens submerged in ethanol at 295 K were not higher than those in room air at 295 K. Similarly, the data at 195 K are in excellent agreement, whether the environment is nitrogen vapor or a mixture of alcohol and dry ice. Therefore, the environments used here are believed to be chemically inert.

Although there are only two data points at 130 K, a decrease in static load cracking rates between 195 and 130 K is clearly indicated. Thus, the rates do not vary monotonically with temperature, but peak at some temperature between 295 and 130 K. One possible explanation for this trend is a change in the micromode of cracking, as suggested in discussion.

Three specimens tested at 295 K and at constant stress intensity factors ranging from 52 to 60 $MPa/m^{1/2}$ showed no evidence of cracking after

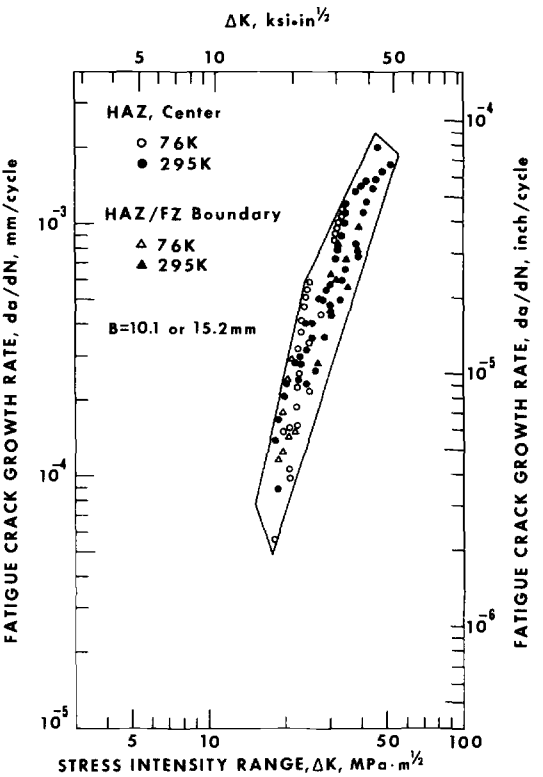

FIG. 11—*Fatigue crack growth rates for HAZ specimens of the MR orientation with cracks sited near the center (HAZ) and boundary (HAZB).*

holding 116 h. Accordingly, 60 MPa/m$^{1/2}$ can be taken as the apparent room temperature value of K_{Th}, the threshold stress intensity factor below which static load cracking was not observed in 116-h tests. Since all of the base metal static load cracking specimens were of the ML orientation, the ratio of K_{Th}/K_{Ic} at room temperature is estimated to be 0.7, or less. Some uncertainty is attached to this figure, since the reliability of a K_{Th} measurement increases at very long hold times [*13*]. Note also that the static load cracking rates are less sensitive to temperature variations at lower K; the linear trends of Fig. 13 appear to converge at $K \cong 63$ MPa/m$^{1/2}$. This prompts speculation that K_{Th} may not vary with temperature, but additional experiments of longer duration would be necessary to verify this.

Static load tests were also performed on specimens submerged in liquid nitrogen at 76 K. Three base metal specimens were loaded for 10 to 16 h at K/K_{Ic} ratios from 90 to 96 percent. As verified by heat-tinting, crack growth did not occur under these conditions. The absence of cracking at 76

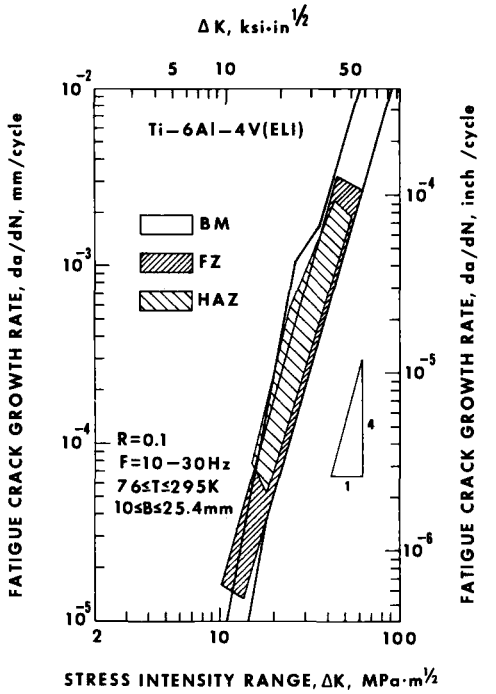

FIG. 12—*Comparison of fatigue crack growth rate scatterbands for base metal and weld zones.*

K may be a consequence of the declining trend observed below 195 K. Such a trend is consistent with the hypothesis that static load cracking is a thermally activated process which can be suppressed at cryogenic temperatures.

Fusion zone and HAZ boundary specimens from electron beam welds were also subjected to static load tests at 76 and 295 K. As noted earlier, the stock dimensions dictated the use of specimens smaller than the 25.4-mm thickness favored for the base metal, and a 10-mm weld specimen thickness was selected. The results are itemized in Table 8 and summarized as follows.

At 76 K, duplicate specimens from the weld zones were sustained for up to 16 h at K/K_{Ic} ratios between 90 and 98 percent. There was no evidence of static load cracking at this temperature.

The weld specimens did exhibit cracking at room temperature, but $\Delta a/\Delta t$ measurements could not be obtained. Problems were encountered in that an unknown amount of stable crack extension occurred during loading to the initial K value. For example, a crack extension of 0.07 mm was measured after heat-tinting one fusion zone specimen which had been sub-

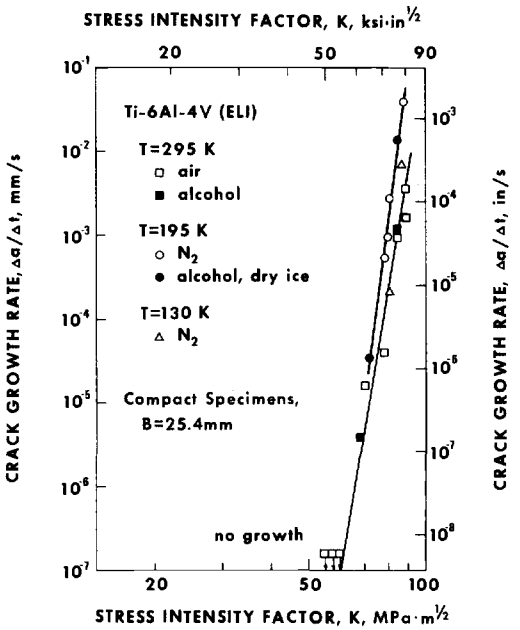

FIG. 13—*Static load cracking rates for the base metal at room and cryogenic temperatures.*

jected to a K value of 64 MPa/m$^{1/2}$ and promptly unloaded. Therefore, not all of the crack extension in static tests could be attributed to static load cracking. Moreover, crack arrest occurred in FZ tests, while fast fracture occurred at the HAZ/FZB.

Despite these testing difficulties, it seems clear that the HAZ boundary may be critical with respect to static load cracking resistance. One room temperature HAZ/FZB specimen fractured at an initial K value of 60.4 MPa/m$^{1/2}$, a level which had proved innocuous to base metal and fusion zone specimens. Presumably, the greater suspectibility to static load cracking at the HAZ boundary relates to the fact that the K_Q and K_{Ic} values are lowest there as well. Unfortunately, the scatter in results for HAZ/FZB specimens at room temperature is considerable, and good estimates of K_{Th} would require longer hold times.

Finally, there is evidence that an incubation period precedes cracking in the HAZ/FZB specimens. A delay of 10^3 s was noted in one test during which there was no sign of any crack growth; then, rapid cracking and fracture followed within an additional 20 s. Another specimen showed no time-dependent crack extension at all, but fractured spontaneously after 20 s at a stress intensity factor of 69.9 MPa/m$^{1/2}$. These observations sug-

TABLE 8—*Static load cracking results for electron beam welded Ti-6A1-4V specimens.*

Specimen and Crack Location		Temperature, K	Temperature, (°F)	Stress Intensity Factor, K MPa/m$^{1/2}$	Stress Intensity Factor, K (ksi/in.$^{1/2}$)	Hold Time, Δt, s	Result
Fusion zone	11	76	(−323)	56.9	(51.8)	18 000	no measureable crack growth
	13	76		55.1	(50.2)	36 000	
	12	295	(70)	73.9	(67.3)	36 000	Δa=1.10 mm (crack arrest)
	17	295		73.4	(66.8)	1 560	Δa=1.29 mm (crack arrest)
	10	295		68.1	(62.0)	3.42×10^5	Δa=0.51 mm (crack arrest)
	15	295		61.5	(56.0)	3.42×10^5	no measureable crack growth
	14	295		56.1	(51.1)	3.42×10^5	no measureable crack growth
	16	295		51.0	(46.4)	4.18×10^5	no measureable crack growth
HAZ/FZ boundary	7	76	(−323)	50.1	(45.6)	58 000	no measureable crack growth
	12	76		49.4	(45.0)	18 000	
	6	295	(70)	71.0	(64.6)	60	Δa=0.30 mm
	1	295		69.9	(63.6)	20	fracture
	2	295		69.0	(62.8)	1 020	fracture
	5	295		68.1	(62.0)	3.6×10^5	no measureable crack growth
	3	295		64.0	(58.3)	60	Δa=0.32 mm
	4	295		60.4	(55.0)	50	fracture

gest that different mechanisms may govern static load cracking in base and weld metal specimens.

Discussion

Campbell's review [*14*] of low temperature fracture behavior reveals few valid data for titanium alloys. In general, the existing literature does not associate transitional behavior with Ti-6Al-4V, but asserts that K_{Ic} decreases uniformly at low temperatures. Certainly, the normal grades having relatively high carbon, oxygen, nitrogen, and hydrogen contents exhibit low K_{Ic} values (35 to 43 MPa/m$^{1/2}$) and mild temperature dependences [*9,15*]. Why were transitions for ELI Ti-6Al-4V alloys not previously reported? Among other factors, the interval 76 K$<T<$125 K was never thoroughly investigated, and invalid results predating current testing standards sometimes obscured the true trend of K_{Ic} [*16-18*].

Although specimen orientation effects for the base metal were noted in the K_{Ic} data at temperatures above the transition region, this alloy shows nearly isotropic behavior. Considering the equiaxed nature of the recrystallized base metal microstructure (Fig. 3), one appreciates that several orientations tested here were virtually equivalent. Nevertheless, we assume that minor microstructural dissimilarities, perhaps texture effects, account for the slight anisotropy apparent in Fig. 5. It is not inconsistent to report no measurable orientation effects at low temperatures, in view of a possible fracture mode change. Analogously, fracture anisotropy in steels is most pronounced at temperatures above the transition region.

The virtual independence of fatigue crack growth rates with respect to temperature is supported by other work on Ti-6Al-4V alloys. The mill-annealed normal grades tested by Fowlkes and Tobler [*9*] and Wei and Ritter [*19*] show no measurable differences in rates at temperatures ranging between 4 and 563 K. Pittinato's data [*20*] for an ELI grade tested in gaseous helium also show little effect of temperature in the range 145 to 295 K. The subject of microstructural effects is, however, more controversial. Yoder et al [*21*] reported that a β-annealed, commercial-purity Ti-6A1-4V base metal microstructure offers superior resistance, with rates that are up to 10 times slower than rates for the same material in the mill-annealed condition. In contrast, Irving and Beevers [*22*] tested five microstructures of a Ti-6Al-4V alloy and concluded that the fatigue crack growth rates were structure-insensitive at ΔK values greater than 12 MPa/m$^{1/2}$. Similarly, Fig. 14 of the present study demonstrates that the electron beam weld fusion zone and base metal fatigue crack growth rates are nearly equivalent, despite the fact that these two zones represent aged martensitic α and equiaxed α microstructures, respectively. The present results are in harmony with Johnson and Paris' statement [*23*] that structure exerts only

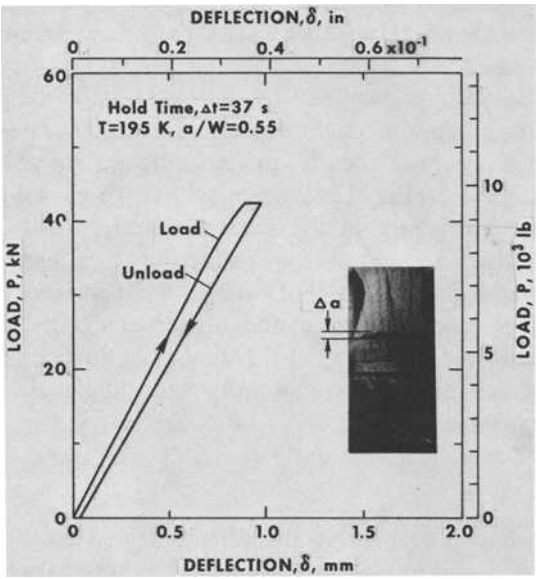

FIG. 14—*Static load fracture behavior of the base metal, showing the compact specimen fracture surface.*

a secondary influence on da/dN. In any event, we agree that microstructure and temperature effects may become quite significant at high ΔK values, as the maximum fatigue stress intensity factor approaches K_{Ic} [*24*]. Therefore, the statements in this report regarding fatigue crack growth behavior apply only to the ΔK ranges investigated. Hopefully, further advances in the art of fatigue crack growth testing will lead to a clarification of the effects of material and test variables.

A successful theory of static load cracking in titanium alloys at temperatures below the secondary creep regime (that is, at test temperature/melting-point ratios, T/T_m, of less than 0.4) must rationalize the observations that the resistance to fracture under static loading is reduced by electron beam welding, and that cracking rates at low temperatures (195 K) may be more severe than at room temperature. At the 50-ppm level of the present alloy, interstitial hydrogen may facilitate cracking by diffusing to and concentrating at regions of high stress [*25-30*]. Local fracturing is then assisted by reductions of fracture surface energy and cohesive strength. It is also known that primary creep occurs in Ti-6Al-4V alloys, at stress levels as low as 70 percent of the conventional yield strength [*31*]. Thus, primary creep in the crack-tip plastic zone of a compact specimen at room temperature is expected. But if we accept that interstitial hydrogen and creep effects are responsible for static load cracking in Ti-6Al-4V, it fol-

lows from the present results at 130 K that these processes must be operative at T/T_m ratios as low as 0.07.

If static load cracking is governed by thermally activated processes involving diffusion or creep, one might expect crack growth rates to decrease with decreasing temperature. Clearly, the base metal data at temperatures between 295 and 195 K (Fig. 13) do not follow the expected trend, but this may be due to a change in the micromode of fracture. Static load cracking in Ti-6Al-4V at room temperature involves mixed modes of dimpled rupture and cleavage [*27*]. Possibly, an increased constraint to plasticity at 195 K favors cleavage and higher cracking rates. Varying tendencies to crack branching may also play a role. Such effects, superimposed on those of a thermally activated process, could explain the observed temperature dependence.

Summary

The fracture behavior of a recrystallization annealed and furnace cooled ELI Ti-6Al-4V alloy and its electron beam welds is summarized as follows.

1. *Fracture Toughness*—At temperatures between 4 and 295 K, K_{Ic} for the unwelded base metal ranges from 54 to 105 MPa/m$^{1/2}$. An abrupt transition in K_{Ic} occurs between 76 and 125 K. Apparently, there is a slight degree of fracture anisotropy, but only at temperatures above the transition region. Electron beam welding leads to a 16 percent reduction in K_{Ic} at 76 K, the HAZ/FZB being the region of minimum fracture toughness in an electron beam weld.

2. *Fatigue Crack Growth Rates*—Within the data scatter of replicate tests, the Ti-6Al-4V base metal fatigue crack growth rates are insensitive to specimen orientation and temperature variations. Similarly, the microstructural transformations associated with electron beam welding appear to exert only a minor influence on the fatigue crack growth resistance of this material. These conclusions apply specifically to intermediate ΔK ranges, where the maximum fatigue stress intensity factor remains low as compared with K_{Ic}.

3. *Static Load Cracking*—Precracked base and weld metal specimens sustained at stress factors approaching K_{Ic} did not exhibit static load cracking in liquid nitrogen environments at 76 K. However, static load cracking did occur in inert environments at temperatures between 130 and 295 K. Cracking in the base metal begins without delay at K values greater than 60 MPa/m$^{1/2}$. In contrast, several HAZ/FZ boundary specimens exhibited an incubation period prior to cracking.

Acknowledgments

This work was sponsored by Kirtland Air Force Base, under Kirtland Order AFWL 75-177. The assistance of H. Vail (Chem-Tronics, Inc.) in

providing the electron beam welds and related technical information is gratefully acknowledged. The assistance of E. Ballinger and S. Naranjo in fracture testing and data reduction is also deeply appreciated.

References

[1] Johnson, R. E. in *The Science, Technology, and Application of Titanium*, R. I. Jaffee and N. E. Promisel, Eds., Pergamon, London, 1969, p. 1175.
[2] White, S. S. and Bakish, R. in *Introduction to Electron Beam Technology*, R. Bakish, Ed., Wiley, New York, 1962, Chapter 9, p. 125.
[3] Bennett, M. G., in *The Science, Technology and Application of Titanium*, R. I. Jaffee and N. E. Promisel, Eds., Pergamon, London, 1969, p. 1023.
[4] Stubbington, C. A., and Ballett, J. T. in *Titanium Science and Technology*, R. I. Jaffee and H. M. Hurte, Eds., Plenum, New York, 1975, p. 601.
[5] Groves, M. T. and Gerken, J. M. in *Electron and Ion Beam Science and Technology*, R. Bakish, Ed., Wiley, New York, 1966, p. 477.
[6] Reed, R. P., in *Advances in Cryogenic Engineering*, K. D. Timmerhaus, Ed., Vol. 7, Plenum, New York, 1962, p. 448.
[7] Naimon, E. R., Weston, W. F., and Ledbetter, H. M., *Cryogenics*, Vol. 14, 1974, p. 245.
[8] Tobler, R. L. in *Cracks and Fracture, ASTM STP 601*, American Society Testing and Materials, 1976, p. 346.
[9] Fowlkes, C. W., and Tobler, R. L., *Engineering Fracture Mechanics*, Vol. 8, 1976, p. 487.
[10] Gowan, J. G., and Stein, C., "Metallographic Analysis of Fracture Surfaces of the 20.7 cu. ft. Pressure Vessel for the ALL Cryogenic Storage Assembly," presented at the Titanium Materials Properties Seminar, Kirtland AFB, Albuquerque, N. Mex., Feb. 1975.
[11] Bania, P. J., "Ti-6Al-4V Pressure Vessel Toughness Evaluation," presented at the Titanium Materials Properties Seminar, Kirtland AFB, Albuquerque, N. Mex., Feb. 1975.
[12] Clark, W. G., Jr. and Hudak, S. J., Jr., *Journal of Testing and Evaluation*, Vol. 3, 1975, p. 454.
[13] Williams, D. N., *Metallurgical Transactions*, Vol. 5, 1974, p. 2351.
[14] Campbell, J. E. in *Fatigue and Fracture Toughness-Cryogenic Behavior, ASTM STP 556*, American Society for Testing and Materials, 1974, p. 3.
[15] Vishnevsky, C. and Steigerwald, E. A. in *Fracture Toughness Testing at Cryogenic Temperatures, ASTM STP 496*, American Society for Testing Materials, 1970, p. 3.
[16] Witzell, W. E., "Fracture Data for Materials at Cryogenic Temperatures," Tech. Rept. AFML-TR-67257, General Dynamics-Convair, AD 825264, 1967.
[17] Tiffany, C. F., and Lorenz, P. M., "An Investigation of Low Cycle Fatigue Failure Using Applied Fracture Mechanics," Tech. Doc. Rept. ML-TDR-64-53, Boeing, 1964.
[18] Hall, L. R., "Plane-Strain Cyclic Flaw Growth in 2014-T62 Aluminum and 6Al-4V (ELI) Titanium," N69-20265, NASA-CR-62396, Boeing, 1968.
[19] Wei, R. P. and Ritter, D. L., *Journal of Materials*, Vol. 7, 1972, p. 240.
[20] Pittinato, G. F., *Metallurgical Transactions*, Vol. 3, 1972, p. 235.
[21] Yoder, G. R., Cooley, L. A., and Crooker, T. W., Report of NRL Progress, 1975, p. 16.
[22] Irving, P. E. and Beevers, C. J., *Materials Science and Engineering*, Vol. 14, 1974, p. 229.
[23] Johnson, H. H. and Paris, P. C., *Engineering Fracture Mechanics*, Vol. 1, 1968, p. 3.
[24] Crooker, T. W., *Engineering Fracture Mechanics*, Vol. 5, 1973, p. 35.
[25] Yoder, G. R., Griffis, C. A., and Crooker, T. W., *Journal of Engineering Materials and Technology*, Vol. 96, 1974, p. 268.

[26] Williams, D. N., *Materials Science and Engineering,* Vol. 18, 1975, p. 149.
[27] Meyn, D. A., *Metallurgical Transactions,* Vol. 5, 1974, p. 2405.
[28] Troiano, A. R., *Transactions,* American Society for Metals, Vol. 52, 1960, p. 54.
[29] Gerberich, W. W., and Chen, Y. T., *Metallurgical Transactions,* Vol. 6A, 1975, p. 271.
[30] Liu, H. W., *Journal of Basic Engineering,* Vol. 92, 1970, p. 633.
[31] Odegard, B. C., and Thompson, A. W., *Metallurgical Transactions,* Vol. 5, 1974, p. 1202.